The application of Earth Observation for mapping soil saturation and the extent and distribution of artificial drainage on Irish farms

Robert O'Hara

Thesis submitted to the Maynooth University
in fulfilment of the requirements for the
Degree of Doctor of Philosophy

National Centre for Geocomputation,
Maynooth University Social Sciences Institute (MUSSI),
Maynooth University,
Maynooth, Co. Kildare, Ireland

Head of Department: Professor Chris Brunsdon
Research Supervisors: Dr Tim McCarthy, Dr Stuart Green
September 2019


Maynooth
University
National University
of Ireland Maynooth

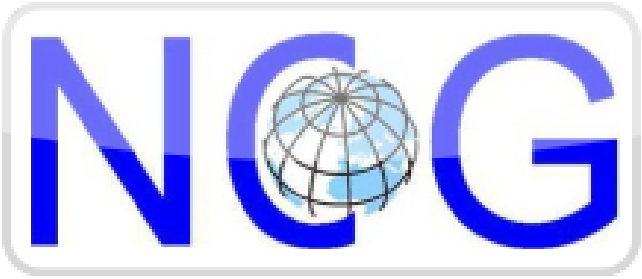
NCG


eagasc
Agriculture and Food Development Authority


Wf
P
Walsh Fellowships Programme

Contents

List of Tables

This page is intentionally blank

List of Figures

Acronyms and abbreviations

These common acronyms or abbreviations are used throughout the following thesis:

ATI	Apparent Thermal Inertia
DEM	Digital Elevation Model
DM	Dry Matter
DSM	Digital Surface Model
EO	Earth Observation
EPA	Environmental Protection Agency
ESA	European Space Agency
FAO	Food and Agriculture Organisation of the United Nations
GPR	Ground Penetrating RADAR
GNSS	Global Navigation Satellite System
ISIS	Irish Soil Information System
MODIS	Moderate Resolution Imaging Spectroradiometer
MVS	Multiview stereopsis
NDVI	Normalised Difference Vegetation Index
NDWI	Normalised Difference Water Index
OPW	Office of Public Works
PA	Precision Agriculture
PMVS	Patch-based Multiview stereopsis
RF	Random Forest
RS	Remote Sensing
SAR	Synthetic Aperture RADAR
SfM	Structure from Motion
SM(C)	Soil Moisture (Content)
SVM	Support Vector Machine
SWIR	Shortwave Infra-red
TI	Thermal Inertia
TIR	Thermal Infrared
TWI	Topographic Wetness Index
UAS	Unmanned Aerial System
UAV	Unmanned Aerial Vehicle
UN-SPIDER	United Nations Space-based Information for Disaster Management and Emergency Response
USGS	United States Geological Survey
VI	Vegetation Index
VNIR	Visible Near Infra-red

This page is intentionally blank

Declaration

This thesis has not been submitted in whole or in part to this or any other university, for any other degree, and is, except where otherwise stated, the original work of the author.

Signed:

Robert O'Hara

September 2019

This page is intentionally blank

Acknowledgements

For my sons, Jonas & Henrik

I am hugely indebted to my supervisors, Dr Stuart Green (Spatial Analysis Unit, Teagasc) and Dr Tim McCarthy (National Centre for Geocomputation, Maynooth University) for their guidance, encouragement and patience in helping me reach this point. Also to Dr Conor Cahalane and Dr Paul Gibson (Department of Geography, Maynooth University) for their support and assistance at different stages. Thanks to Prof. Owen Fenton and Dr Pat Touhy (Teagasc) for their time and input. Also to Dr Ian Thomas for providing LiDAR data from the Agricultural Catchments Programme. I would like to thank my departmental colleagues in the Spatial Analysis Unit: Dr Shafique Matin, Dr Guy Serbin, Richa Marwaha, Mohana Lognakrishnan and Dr Gabriela Afrasinei.

I am extremly grateful to Teagasc for funding this research under the Walsh Fellowship Programme. Also, for their financial assistance in facilitating a period at Sveriges lantbruksuniversitet, Umeå, Sweden in 2017. I am also thankful to the Postgraduate Travel Fund at Maynooth University for funding attendance at the 5th EnMAP hyperspectral summer school, Universität Trier, Trier, Germany in April 2016.

Sincerest gratitude to my parents Frank & Nano O'Hara, family and friends for their unwavering support and encouragement.

Slutligen, och speciellt, till min älskade fru Karin för hennes kärlek och tålamod och för att hon, utan alltför många protester, hållit ställningarna och styrt skutan mot land.

This page is intentionally blank

Abstract

Artificial drainage is required to make wet soils productive for farming. However, drainage may have unintended environmental consequences, for example, through increased nutrient loss to surface waters or increased flood risk. It can also have implications for greenhouse gas emissions. Accurate data on soil drainage properties could help mitigate the impact of these consequences. Unfortunately, few countries maintain detailed inventories of artificially-drained areas because of the costs involved in compiling such data. This is further confounded by often inadequate knowledge of drain location and function at farm level. Increasingly, Earth Observation (EO) data is being used map drained areas and detect buried drains. The current study is the first harmonised effort to map the location and extent of artificially-drained soils in Ireland using a suite of EO data and geocomputational techniques.

To map artificially-drained areas, support vector machine (SVM) and random forest (RF) machine learning image classifications were implemented using Landsat 8 multispectral imagery and topographical data. The RF classifier achieved overall accuracy of 91% in a binary segmentation of artifically-drained and poorly-drained classes. Compared with an existing soil drainage map, the RF model indicated that ~44% of soils in the study area could be classed as "drained". As well as spatial differences, temporal changes in drainage status where detected within a 3 hectare field, where drains installed in 2014 had an effect on grass production. Using the RF model, the area of this field identified as "drained" increased from a low of 25% in 2011 to 68% in 2016. Landsat 8 vegetation indices were also successfully applied to monitoring the recovery of pasture following extreme saturation (flooding). In conjunction with this, additional EO techniques using unmanned aerial systems (UAS) were tested to map overland flow and detect buried drains. A performance assessment of UAS structure-from-motion (SfM) photogrammetry and aerial LiDAR was undertaken for modelling surface runoff (and associated nutrient loss). Overland flow models were created using the SIMWE model in GRASS GIS. Results indicated no statistical difference between models at 1, 2 & 5 m spatial resolution ($p < 0.0001$). Grass height was identified as an important source of error. Thermal imagery from a UAS was used to identify the locations of artifically drained areas. Using morning and afternoon images to map thermal extrema, significant differences in the rate of heating were identified between drained and undrained locations. Locations of tiled and piped drains were identified with 59 and 64% accuracy within the study area.

Together these methods could enable better management of field drainage on farms, identifying drained areas, as well as the need for maintenance or replacement. They can also assess whether treatments have worked as expected or whether the underlying saturation problems continues. Through the methods developed and described herein, better characterisation of drainage status at field level may be achievable.

This page is intentionally blank

Chapter 1 Introduction

Artificial drainage facilitates farming on wet soil, making farms on marginal soils more efficient and profitable. However, installing drains is a significant intervention in the hydrology of a field, one which can have unintended or unpredictable environmental consequences. Knowing where drains are located, and what the current drainage status of a field is, could help mitigate some of the negative environmental impacts. This thesis, conducted under the Teagasc DrainMap project (project number 6522), assessed potential applications for Earth Observation (EO) data in conjunction with state-of-the-art machine learning and geocomputational techniques to map the extent and distribution of artificially-drained fields on Irish grassland farms. The project focused on multi-scale, multi-sensor EO data, taking advantage of recent advances in machine learning digital image classification and the availability of unmanned aerial systems (UAS) as platforms for low-altitude remote sensing (RS). The opening section of the thesis defines salient terms and concepts relating to both soil- and artificial drainage. The rationale for the study is then presented in detail, outlining the local and broader context of the research, the need and timeliness of the study and an examination of why an EO data was the best-suited approach.

1.1 Soil drainage versus field drainage

1.1.1 Soil drainage

Soil drainage describes the ability of soil to remove excess water under the force of gravity. This natural property effectively determines whether soils are favourable to certain types of farming, and whether farming may be detrimental to water- and environmental quality (Shukla, 2011). Texture and structure are the principal soil properties affecting soil drainage, by regulating the volume of available pore space (porosity) and influencing the speed at which water can be transported. Extrinsic factors can also play a role, for example, local landscape position, water table depth and prevailing climate (Anderson & Burt, 1978; Batey, 2009; Moore *et al.*, 1993; Potter, 1991; K. Price, 2011). Land use and management practices can also play a role (Batey, 2009; Potter, 1991).

Mineral soils with a high percentage of silt and clay are typically characterised by low porosity and compacted structure that reduce their ability to transmit water. Hence, they are termed "poorly-drained" or "heavy" soils ("heavy" being an agricultural description for these soils being sticky and difficult to work). Poorly-drained soils may also be found in lowland settings with shallow groundwater, or where groundwater exudes from surface seepage or springs. Conversely, "well-drained" soils generally have a coarser texture (i.e. higher sand content) and a greater porosity that permits freer movement of water. These soils are also not disadvantaged in terms of landscape position or groundwater breakout.

Figure 1-1 A Digital Globe scene of grassland within the Border, Midland and Western region of Ireland depicting drained and poorly drained conditions. Poorly drained conditions are exemplified by extensive growth of water tolerant species. Evidence for cleaning out surface drains can be seen in the bottom right of the image (circular mounds of excavated soil).

Poor soil drainage may be recognised through ponding of water at the surface following heavy or persistent rainfall. It may also be noticeable from poor crop yields or through the growth of water-tolerant vegetation (see Figures 1-1 & 1-2), or where poaching (hoof damage) is observed (see Figures 1-6). There may also be instances where there are no visible signs of a problem, but where a problem exists. In such instances, EO data can be of use (see Section 1.6 below). Limited soil drainage and excessive soil moisture (SM) are recognised as significant biophysical constraints on agricultural production, often requiring expensive countermeasures to make soils workable and profitable. In many parts of Ireland, for example, the combination of wet climate (high rainfall and low evapotranspiration) and poor soil drainage are a considerable constraint on farm system viability (Schulte *et al*., 2012). Galvin considered a large proportion of Irish soils to be impermeable, with infiltration rates of < 0.1 mm day^{-1} (Galvin, 1983). A subsequent study by Diamond and Shanley (2003) highlighted spatial and temporal variability in infiltration rates across the country (Diamond & Shanley, 2003). It was observed how infiltration rates (mm/hr) were lower on moderately-, imperfectly- and poorly-drained soils during winter as a consequence of higher volumes of antecedent soil moisture. A synopsis of their findings for different soil types is included in Table 1-1 below.

Table 1-1 Measured infiltration rates for Irish soil types during dry (summer) and wet (winter) conditions (Diamond & Shanley, 2003).

Location	Drainage	Texture		Infiltration rate (mm/hr)	
		Horizon A	Horizon B	Summer	Winter
Gurteen	Well	Loam	Loam	114	8.7
Cappoquin	Well	Loam	Loam	160	3.7
Midleton	Well	Loam	Loam	103	22
Dundalk	Well	Loam	Stony	96	122
Clonmel	Well	Loam	Clay loam	30	10.3
Birr	Moderate	Sandy loam	Sandy loam	53.7	11.3
Kilcock	Imperfect	Loam	Clay loam	96.3	6
Castlecomer	Poor	Clay loam	Clay loam	5.3	1.7

Figure 1-2 Two views of typical heavy soils within the study area (County Leitrim) showing extensive growth of water tolerant species within the sward.

Soil drainage is conventionally mapped using *in-situ* field observations, for example, of water table depth, soil wetness and landscape position. Characteristics such as colour, gleying and mottling are also important. Colour is a useful indicator of anaerobic soil conditions from periodic or continuous saturation. Gleying is a process of iron reduction in waterlogged, anaerobic soils which leads to conversion of iron from its oxidised (ferric) state to a reduced (ferrous) state. In the ferrous state it is soluble in water and can be leached to lower soil horizons giving gleyed soils a characteristic grey or bluish colour. Mottling is a process where secondary colours develop that are not associated with the parent material, but rather from soil wetness. Traditional soil surveys are now combined or replaced with digital, remotely-sensed data such as satellite imagery and digital elevation data. These are typically analysed within a geographic information system (GIS) and modelled using predictive machine learning or statistical inference (McBratney *et al.*, 2003; Mulder *et al.*, 2011).

Soil drainage is frequently conceptualised as a linear progression between moisture extremes, with the number of intervals defined by timing, duration and depth of saturation characteristics. The number of intervals is not prescribed. The United States Department of Agriculture (USDA), for example, recognises seven classes (excessively-, somewhat excessively-, well-, moderately well-, somewhat poorly-, poorly- and very poorly-drained). A recent 1:250,000 scale Irish Soil Information System (ISIS) (2014) recognises five drainage classes (excessively-, well-, moderately-, imperfectly- and poor) (R. Creamer *et al.*, 2014). The indicative soil drainage map produced at soil association level from the ISIS dataset is illustrated in Figure 1-3. This map depicts an overview of dominant soil drainage class for the dominant soil group within a soil association. While it provides a useful assessment of

dominant drainage properties at catchment scale, the scale at which the ISIS map was created, and the means by which it was created, makes it ill-suited to mapping drainage condition at field- or farm level (Creamer *et al*., 2016).

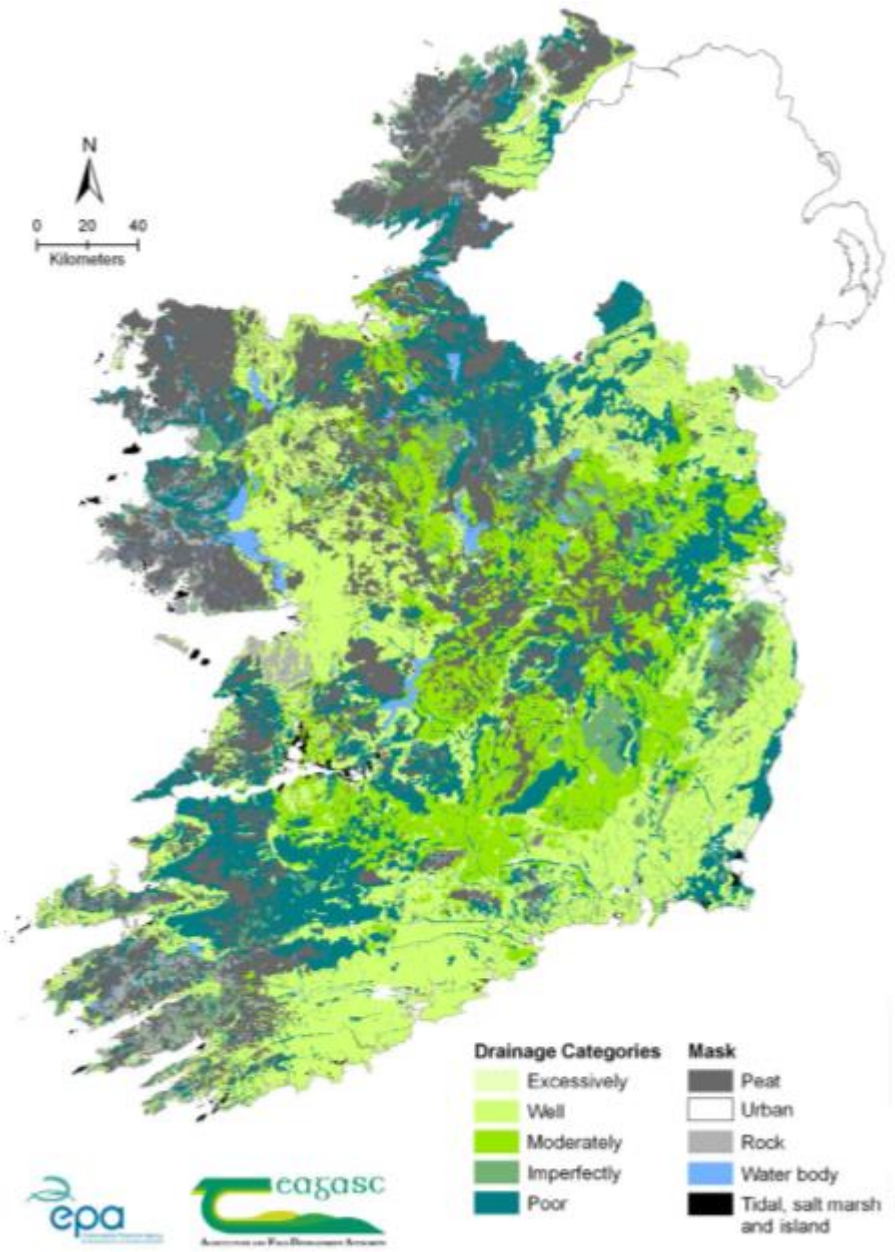

Figure 1-3 Indicative soil drainage classification based on the Irish Soil Information System. Source: (R. Creamer *et al.*, 2016).

Under an earlier soil map prepared by Teagasc/ Environmental Protection Agency (EPA) for the Forest Inventory and Planning System Irish Forest Soils project (FIPS-IFS), broader soil drainage classifications were assigned based on a combination of field observations and an interpretation of satellite imagery, digital elevation data (Fealy *et al*., 2009). This soil classification system subdivided soils based on whether they were mineral or organic. Mineral soils were further categorised into calcareous/ non-calcareous, well-drained/ poorly-drained and shallow/ deep. The "poorly-drained" soil class of the FIPS-IFS map was defined as being equivalent to “imperfectly-“, “poorly-“ or “very poorly-drained” classes in conventional soil classification terms. The FIPS-IFS map, which has a nominal working scale of 1: 50,000; suggested the national figure for poorly-drained soils was ~50% of soils.

The expense of conducting field surveys for soil mapping means data are generally sparse, and consequently soil maps tend to have coarse spatial resolution. National datasets, for example, may have minimum mapping unit (MMU) of several hectares. Global datasets may have MMU of several kilometres. These datasets have a role in regional or global modelling of physical processes, but have no use for precision farming where the coarse resolution will tend mask subpixel or sub-unit variation in soil type. An example of a very coarse soil map is the 10 km - < 50 km resolution Harmonized World Soil Database (2008) which proposed 67% of soils globally have a moderate, severe or very severe limitation in respect to “oxygen availability to roots” (a proxy indicator of drainage status). Figure 1-4 illustrates these constraint areas for Ireland, where areas of moderate to severe constraint can be identified in the North-Western part of the island (the Border, Midland and Western region). At these coarse scales, it is difficult to account for the very high spatial variation in soil drainage type. It

is also not possible to represent locations where poorly drained soils have been artificially drained.

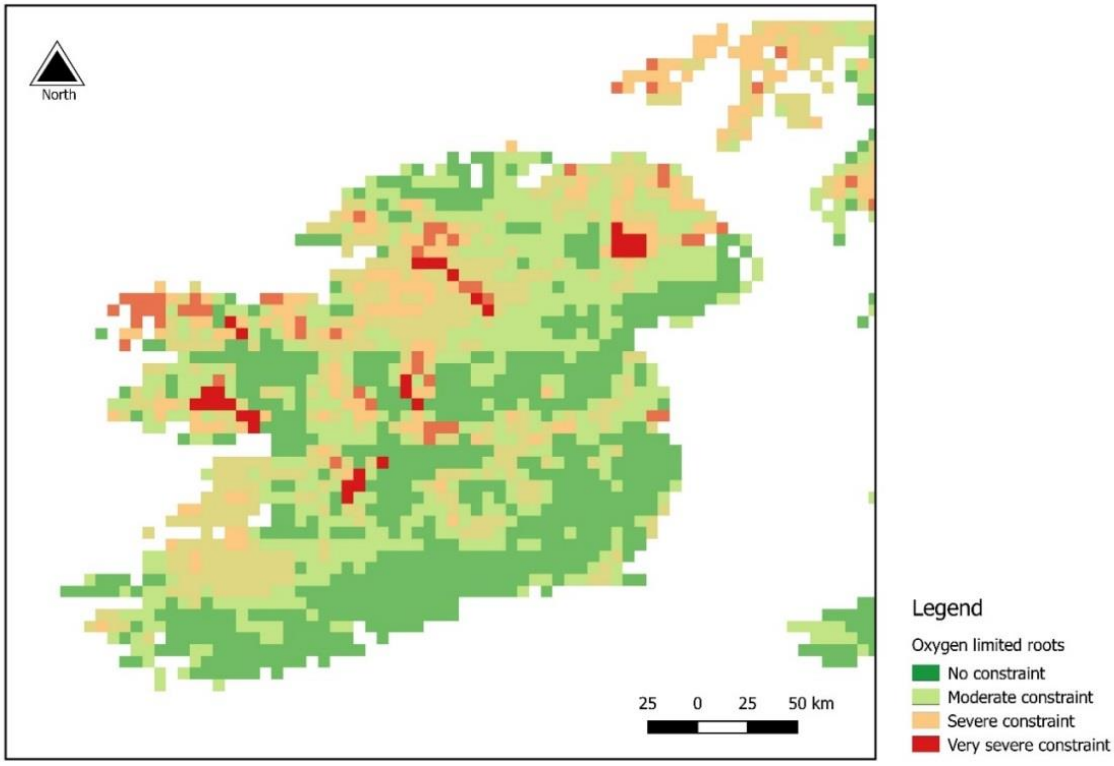

Figure 1-4 The Harmonized World Soil Database map indicating the extent of constraint based on "oxygen availability to roots" for Ireland. The map highlights areas of "moderate" to "very severe" constraint the Border, Midlands and Western Region, is the study area for the research described in Chapter 4.

1.1.2 Artificial drainage

Artificial drainage are used to stabilise fluctuating groundwater levels and expedite the transport of excess water from the root zone of plants. This improves soil aeration and structure and making the soils more productive for agriculture (Armstrong & Garwood, 2006). Drains may also extend the length of the growing season relative to undrained conditions and

increase crop yield. Drier soils improve accessibility/ trafficability of fields (for livestock and machinery) and can reduce the risk of surface damage (poaching) and soil compaction (Smedema *et al*., 2004).

An artificial drainage system is an integrated system that typically comprises of a subsurface network of drains, that collects and siphon off excess water, and a main drainage system (usually open ditches) which receive water from subsurface systems (Figure 1-5). Depending on the nature of the underlying drainage issue, two broad types of subsurface drainage systems (groundwater and shallow) are commonly deployed in Ireland, often in combination (Tuohy *et al.*, 2017). Groundwater drainage systems are a network of piped drains that allow groundwater to flow into permeable layers where it can infiltrate into the water table. Shallow drainage systems are required where infiltration is impeded at all depths, so drainage channels (for example, mole drains) are created that increase movement of water within the soil profile. After artificial drainage, water transport within a field may be significantly different from its natural state. Studies suggest artificial drainage typically changes the hydrological characteristics of a soil by at least one drainage class (Van Orshoven *et al*., 2014). For example, an imperfectly-drained soil may become a moderately drained soil but it is unlikely to become a well-drained soil. For a period after drainage, an artificially drained soil will no longer carry the same risk of saturation. The duration of this improvement depends on the type of drainage system installed, the level of post-installation maintenance and whether an installed system has addressed the original drainage impediment (Tuohy *et al*., 2013a, 2013b; Tuohy *et al*., 2015; Tuohy *et al*., 2016; Tuohy *et al*., 2017).

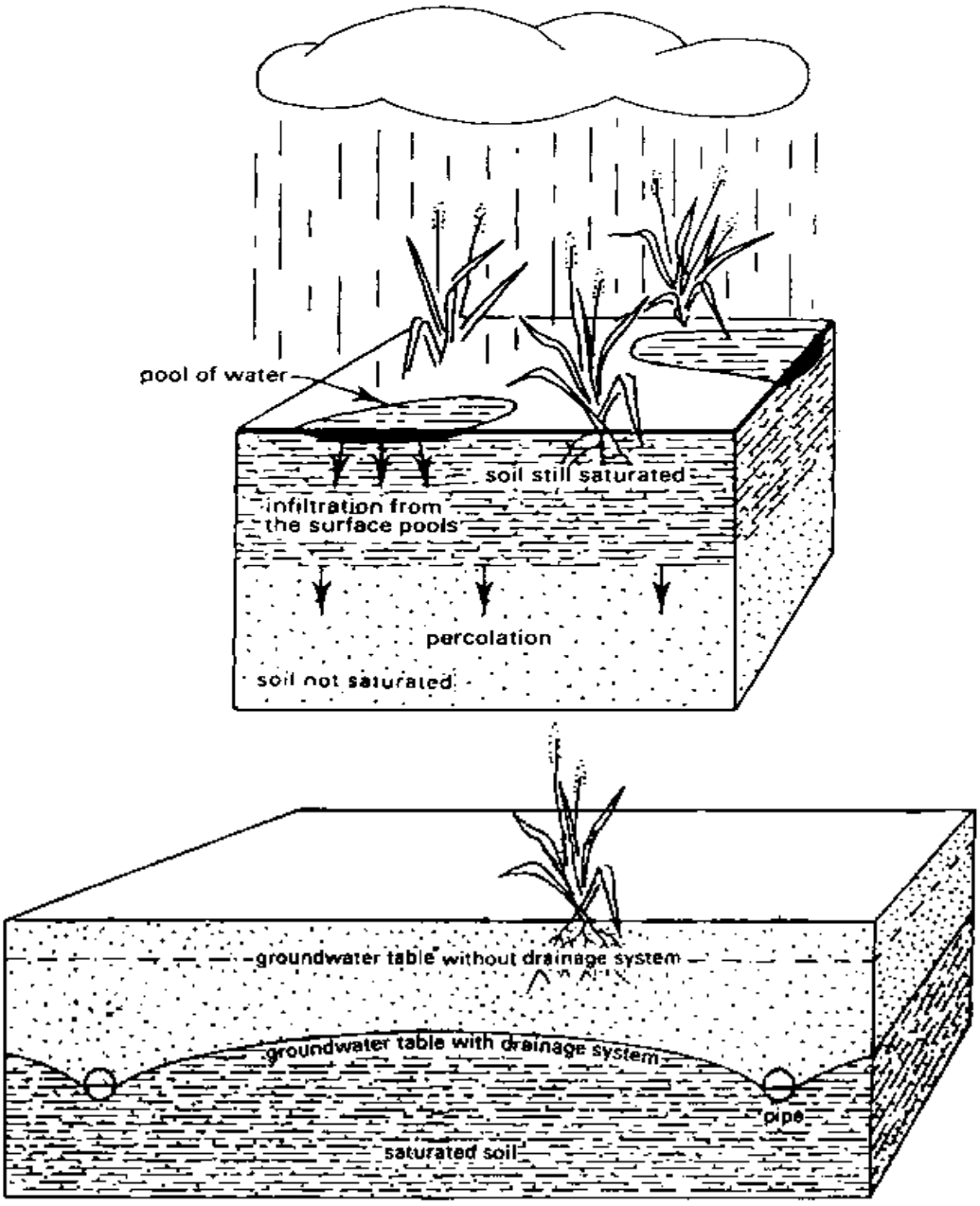

Figure 1-5 (top) Idealised view of poorly drained soil where restricted drainage reduces the infiltration of rainwater and results in ponding at the surface; (bottom) An installed subsurface drainage system controls groundwater depth keeping the root zone aerated and increasing rooting depth.

Source: www.fao.org/docrep/r4082e/r4082e07.htm#chapter%206%20%20%20drainage# (accessed 12 December 2018).

1.2 Rationale for the study

1.2.1 Environmental impacts

As noted previously, artificial drainage makes farming on wet soil more efficient and more profitable, however the installation of drainage can have unintended environmental consequences, for example, on water quality (Daly *et al*., 2002; Ibrahim *et al*., 2013; Skaggs *et al*., 1994; Withers *et al*., 2014, Blann *et al*., 2009) or on greenhouse gas (GHG) emissions (Clagnan *et al*., 2018; Rafique *et al*., 2011). It has also been linked with increased streamflow and flood risk (Armstrong & Garwood, 2006; Potter, 1991; Schilling & Helmers, 2008) and greater soil erosion (Gramlich *et al.*, 2018). The direction of impact can be both positive and negative. For example, installing drains on low infiltration soils may decrease instances of surface pooling and overland flow which is an important pathway for phosphorous (P) loss to surface waters However, this reduction may be compounded by an increased volume of nitrate (N) losses in drain flow (Ibrahim *et al*., 2013).

To mitigate potential impacts, it is beneficial for farmers, agronomists, hydrologists, ecologists, catchment managers and policymakers to have accurate and up-to-date information on soil drainage, including the location of artificially-drained areas. Maps of current drainage conditions at field scale could provide relevant stakeholders with a better understanding of inter- and intra-farm variability in, for example, grassland production, soil degradation, surface water pollution and GHG emissions (Clagnan *et al.*, 2018; Paul *et al.*, 2018; Schulte *et al.*, 2012; Shalloo *et al.*, 2004). More accurate accounting of soil drainage could also improve predictive modelling of, for example, grass production (Fitzgerald *et al.*, 2008) soil moisture

estimates (Schulte *et al.*, 2005; Schulte *et al.*, 2015) or operational decision-making for farm operations such as slurry spreading (Kerebel *et al.*, 2013a, 2013b; Kerebel & Holden, 2016).

1.2.2 Lack of relevant data

As noted previously, where soil drainage classifications are included in existing soil maps they are typically at very coarse resolution, are too spatially aggregated and do not account for the presence of artificial drainage. They do not, therefore, accurately represent drainage conditions at field- or even farm level. A 2005 study reported just eleven of 161 countries (7%) investigated had sub-national information on the location of artificially-drained areas (Feick *et al.*, 2005). Even more surprisingly, considering the long history of agricultural drainage in Western Europe, only four of these countries were EU member states (Estonia, France, Germany and Latvia). Most estimates of the extent of artificial drainage are therefore speculative at best. Current best estimates suggest ~130-167 million hectares (ha) of rain-fed farmland globally (but predominantly in Europe and North America) have some artificial drainage treatment in place (Blann *et al*., 2009; Feick *et al*., 2005; Schultz *et al*., 2007; Smedema *et al*., 2000; Smedema *et al*., 2004). This area is expected to increase with growing demand for agricultural produce encouraging the reclamation of marginal lands (Ayars & Evans, 2015).

Ireland does not currently collect detailed spatial information on artificial drainage. Neither is there an archive of existing drainage systems. Thus, there is no clear record of the extent or distribution of artificially-drained soils. Yet, artificial drainage is ubiquitous in some areas of the country. Centrally-organised land drainage schemes, particularly during the twentieth century,

have been crucial for agricultural production (Duffy, 2007). It was estimated that ~2 million ha of farmland (or ~30% of the country) had drainage installed between 1940 and 1980 based on the allocation of drainage grants (Bruton & Convery, 1982). This included drainage of ~1,170,000 ha under the Land Project (1949), ~200,000 ha under the Farm Modernisation Scheme (1974-1985), and ~182,500 ha as part of the Western Drainage Scheme (1979-1986)[1]. Unfortunately, it is not always evident that drainage works were always subsequently undertaken once grants were issued. An audit of arterial drainage schemes in Leitrim/Roscommon in the 1980's and 1990's reported low instances of land drainage followed arterial drainage within these counties, with < 25% of the estimated 12,000 ha of benefitting lands showing any physical sign of improvement (Burdon, 1986). Government subsidised drainage projects are no longer carried out in Ireland, but drain installation and cleaning continues to be undertaken privately. Under European Community (Environmental Impact Assessment) (Agriculture) Regulations 2011 (S.I. No. 456/2011), reporting of land drainage is only required where area of the proposed works exceeds 15 ha, or where drainage may have a significant effect on the environment (DAFM, 2013b). As the average field size in Ireland is ~ 2.5 ha (J. Zimmermann, 2018, personal communication, 18 January), most drainage projects fall well below the notification threshold and consequently go unrecorded. This lack of relevant data on the location of artificial drainage is a considerable knowledge-gap affecting agricultural production and environmental protection which the DrainMap project has attempted to address.

[1] Report available at www.esri.ie/pubs/BKMNEXT23.pdf (accessed 12 December 2018).

The requirement for accurate drainage data has resulted in a strong research interest internationally for developing efficient methods of mapping drainage characteristics. Traditional fieldwork methods can be labour-intensive, expensive and ill-suited to large area reconnaissance. This is an area where EO or other remote sensing (RS) methods can be employed to great effect without engaging in expensive and labour-intensive fieldwork, for example, in physically probing or digging to locate broken drainage pipes. Several studies have demonstrated the effectiveness of remote sensors, on satellite, aerial or terrestrial vehicles for mapping drainage over different scales under different land cover and land uses. Much of this work has focussed on North America where the focus is mapping subsurface drain tiles (B. S. Naz *et al.*, 2009; Verma *et al.*, 1996). More recently, there have an increasing number of studies in Europe, notably Germany, the Czech Republic and Denmark (Beucher *et al.*, 2017; Møller *et al.*, 2018; Møller *et al.*, 2017; Tetzlaff, Kuhr, Vereecken*, et al.*, 2009; Tetzlaff, Kuhr, & Wendland, 2009; Tlapáková *et al.*, 2017; Tlapáková *et al.*, 2015).

Mapping of surface drainage (open ditches) is relatively straightforward, thanks largely to the availability of laser scanning technology, or LiDAR (Light Detection And Ranging). LiDAR is an active RS technology which uses light in the form of a pulsed laser to measure distance between the sensor and an object. A major advantage of LiDAR is that the light pulses can penetrate dense canopy to create detailed topographical models of the underlying surface. Previous studies have demonstrated how surface ditches (Cazorzi *et al.*, 2012; Prosdocimi *et al.*, 2015; Roelens *et al.*, 2018) and microtopographic pathways can be extracted from LiDAR point clouds. The definition of surface microtopography is an important ability for understanding overland flow and how and where agricultural nutrients might be transported

from agricultural fields (Heathwaite *et al.*, 2005; Sonneveld *et al.*, 2006). In several recent papers, precursors to aspects of this study discussed in Chapter 5, LiDAR accurately mapped surface pathways for phosphorous (P) loss in mixed agricultural catchments (I. Thomas, Jordan*, et al.*, 2016; I. Thomas, Mellander*, et al.*, 2016; I. A. Thomas *et al.*, 2017). Defining pathways within fields, breakthroughs between fields and delivery points for runoff into surface waters were important outcomes from these studies, allowing targeted remedial measures for nutrient loss to be established. Though accurate, the cost of acquiring LiDAR data is a major stumbling block to the wider adoption of this method for modelling overland flow and P loss. In Chapter 5, a low-cost alternative is proposed for mapping surface drainage in intensively managed grassland that uses structure-from-motion (SFM) photogrammetry from an unmanned aerial system (UAS).

1.2.3 Timeliness

The timeliness of developing efficient drain mapping procedures for Ireland was emphasised by a recent EPA report on the quality of Irish inland and coastal waters (EPA, 2018). The report found an 11% increase in waterbodies with high P concentrations since 2015. Coastal waters also had higher nitrogen (N) and P loads compared with previous reports. If unaddressed, these trends would put Ireland in breach of their obligations under the European Union Water Framework Directive (WFD) (EPA, 2018). The primary goal of the WFD is to prevent deterioration of waterbodies and protect, enhance and restore them with the aim of achieving at least “good” status. The proposed measures to achieve WFD objectives are set out in the River Basin Management Plan for Ireland 2018-2021 published by the Department of Housing, Planning and Local Government (DHPLG, 2018). This management plan called for a renewed focus on compliance with the Good Agriculture Practice Regulations (Statutory

Instrument No. 65 of 2018 [European Union (Good Agricultural Practice for Protected of Waters) (Amendment) Regulations 2018]), with a greater emphasis on measures to intercept and break nutrient transport pathways and prevent sediment and nutrient losses. It is not clear to what degree intensification programs currently underway (Food Harvest 2020 (DAFF, 2011) and Food Wise 2025 (DAFM, 2015)) are driving these increasing trends. These programs proposed substantial increases in primary production (to increase by 65% to a value of €10 billion per annum by 2025) to supply a projected 85% increase in agri-food exports in the same period. It was always feared that any increase in production would have a negative impact on surface water (eutrophication and sedimentation) as well as increased groundwater vulnerability (Farrelly *et al.*, 2014). Improving nutrient management in sensitive areas and a greater application of technological innovations to mitigate these impacts were the recommendations of an independent analysis on likely environmental impacts from intensification (Farrelly *et al*., 2014). The EO techniques explored in subsequent chapters can contribute to the implementation of these measures by providing a better understanding of the spatial distribution of field drainage conditions (Chapter 4) and providing more affordable means of high-resolution surface mapping (Chapter 5) and detecting drains and drained areas (Chapter 6).

Another aspect of timeliness is recent technological advances in data and data processing. There is a greater availability of moderate resolution EO imagery, from the USGS Landsat 8 and ESA Sentinel 2 missions, that provide an unprecedented opportunity for satellite mapping of drainage. Supplementing moderate resolution satellite data is very high spatial- and temporal-resolution datasets from UAS, permitting targeted, on-demand imagery of precision

agricultural mapping and monitoring. There are also on-going developments in digital image processing that now offer enhanced classification ability, allowing researchers to taking full advantage of the massive volumes of imagery now available (Behmann *et al.*, 2015; Rogan *et al.*, 2008; Tuia *et al.*, 2011). Machine learning (ML) classification algorithms for land cover classification are well-established, for example, Support Vector Machine (SVM) (Cortes & Vapnik 1995) and Random Forests (RF) (Breiman, 2001) and can be implemented using free or open-source software such as R or Python. Both ML algorithms are recognised for their high accuracy in classifying multispectral data with limited training data. Their robustness and effectiveness under varying environmental conditions have been demonstrated in extensive review studies over the past decade (Ali *et al.*, 2015; Belgiu & Drăguţ, 2016; Gislason *et al.*, 2006; Huang *et al.*, 2002; Lary *et al.*, 2016; Mountrakis *et al.*, 2011; Pal, 2005; Pal & Mather, 2005; Rodriguez-Galiano *et al.*, 2012).

This section has established the rationale for the current study. Ireland does not currently record the location of drainage works and there is no data on the extent or distribution of drained soils. To understand the potential environmental impacts that can arise from artificial drainage in the wider context of climate change, agricultural intensification and environmental sustainability there is a need to accurately map drainage regimes on Irish farms.

1.3 Consequences of poor soil drainage on agricultural production

In the preceding section, the impact of poor soil drainage on the efficiency and profitability of farms was highlighted. This section examines some of the consequences of poor soil drainage, with particular reference to grassland production in Ireland or similar climates. The European Union definition on whether soil drainage is severely limiting for agricultural production is if soils are wet within 80 cm of the surface for > 6 months per year, or within 40 cm for > 11 months per year. Also, if groundwater is present within 15-40 cm of the surface, or if the soil has gley characteristics within 40 cm of the surface. Additionally, soil maybe characterised as excessively wet if the number of days with SM at or above field capacity is ≥ 230 days. Field capacity (FC) is the maximum amount of water a soil can retain solely under the force of gravity (Van Orshoven *et al.*, 2014). Above FC there is a surplus of water (negative soil moisture deficits (SMD)), below FC there is a deficit (positive SMD). In the wettest parts of North-West Europe, including western and upland areas of Ireland, >300 days per year above FC would not be unusual.

1.3.1 Grass production

The impact of saturation on growth has been demonstrated in several studies. In a laboratory study, McFarlane *et al.* demonstrated how perennial ryegrass on soils saturated had reduced root and leaf biomass after 14-21 days (McFarlane *et al.*, 2004). After 28 days, there was a 70% reduction in overall biomass with a concomitant reduction of 30–50% in photosynthetic activity. A subsequent study reported a decline in leaf extension rate and biomass as soil saturation increased (Laidlaw, 2009). Such experimental results are supported by several field-based studies where reduced grass yields were recorded on wet, poorly drained soils.

For example, Ryan (1974) reported a reduction in grass yield of 2 t ha^{-1} yr^{-1} on wet soils relative to drained soils (Ryan, 1974). Brereton & Hope-Cawdery (1988) found a 16-36% reduction in grass yield on wet soils (Brereton & Hope-Cawdery, 1988). Baker *et al.* (1988) reported a 16% reduction in yield for poorly drained fields compared with drained fields, the equivalent to 1-5 t ha^{-1} yr^{-1}, (Baker *et al*., 1988).

Some of these studies have suggested the impact on yields from saturation is greatest during spring, when grass growth should be reaching its peak phenological stage. For example, the Brereton & Hope-Cawdery study noted previously identified a 38-59% reduction in spring/ early summer yield on wet soils (Brereton & Hope-Cawdery, 1988). Tyson *et al.* (1992) reported an 11% reduction in spring grass yield on wet soils (Tyson *et al*., 1992). In a comprehensive study of contrasting farm production between wet and dry soil regimes, Shalloo *et al*. (2004) demonstrated the relative inefficiency of farming systems on heavy soils under high rainfall when compared with comparable systems in free-draining/low rainfall areas (Shalloo *et al*., 2004). The study indicated lower dry matter (DM) production for wetter farms, but also a lower stocking rate (1.89 vs. 2.34 cows ha^{-1}), lower milk production (5781 vs. 6421 kg per cow), a shorter grazing season (149 vs. 250 days) and lower proportion of grass in the diet (40% vs. 70%). The net result was lower overall profitability. Subsequent studies have also confirmed reduced performance on heavy soil farms, for example through increased housing time during winter or wet weather with a greater reliance on silage (Fitzgerald *et al*., 2008; Sharma *et al.*, 2018).

1.3.2 Soil degradation

Wet soils are at high risk from soil compaction from livestock and heavy machinery (Batey, 2009; Earl, 1997). This can result in slower movement of water through soil, which may further compound existing drainage issues in the root zone. The compaction or compression of wet, malleable soils can degrade soil structure by reducing porosity. The reduction in pore space can reduce aeration which can reduce the ability of plants to take up oxygen, water and nutrients. It can also impact soil microbial activity, limiting the ability of micro-organisms and earthworms to decompose and cycle organic matter and nutrients efficiently. Roots are less able to penetrate compacted soils, restricting plant utilisation of water and nutrients. Poaching is also a risk, where the sward cover is removed. An example of the poaching damage livestock can do on wet soils is illustrated in Figure 1-6. Compaction is a particular issue where there is shallow groundwater. Irish soil compaction studies have indicated that soils are only trafficable to heavy machinery when groundwater depth is maintained below 320 mm (Brereton & Hope-Cawdery, 1988), or when soil moisture deficit (SMD) is 10 mm (Vero *et al.*, 2014). Soil microbial activity may also be impacted by the colder soil temperatures and anoxic/hypoxic conditions brought about by excessive soil water (Porporato *et al.*, 2003). Studies have shown how microbial activity is reduced when there are extremes volumes (high and low) of SM (Barros *et al.*, 1995; Richter *et al.*, 2018; Unger *et al.*, 2009).

Figure 1-6 Example of saturation issues (poaching) developing on heavily trafficked soil.

1.3.3 Surface water pollution

Nutrient loss via overland flow is a high risk on poorly-drained soils. Overland flow describes the natural movement of water over land, toward a surface water body. It is generated by two different physical processes (Davie, 2008):

- Infiltration excess (or Hortonian) overland flow occurs where rainfall intensity exceeds soil infiltration capacity. Water accumulates on the surface soil and moves under gravity along hydrological pathways.
- Saturation excess overland flow occurs where soil saturation exceeds its maximum level due to groundwater uplifting, baseflow and lateral subsurface water discharge.

In either case, the associated P loss that accompanies overland flow in agricultural catchments from diffuse sources (for example, fertiliser application or manure) is a major contributor of eutrophication both nationally and internationally (Carpenter *et al.*, 1998; Hughes *et al.*, 2005; Sharpley *et al.*, 2015; Toner *et al.*, 2005). The deterioration in water quality can result in reduced biodiversity and destroyed ecosystems (Bilotta *et al.*, 2007; Sharpley *et al.*, 1994). A recent EPA report has identified an increase in nutrient enrichment of Irish surface- and coastal waters since 2014 (EPA, 2018). As will be demonstrated in Chapter 3, overland flow and flooding are strongly linked to rainfall depth and the level of antecedent SM. With increased precipitation likely under predicted climate change scenarios, there is an increased risk of greater eutrophication levels increased surface runoff (Sinha *et al.*, 2017). Under current climate models for Ireland, an overall increase of ~11% in winter rainfall is predicted over the coming decades, largely in the North-West part of Ireland, where rainfall increases of ~20% are predicted by 2050 (Sweeney *et al.*, 2008).

1.3.4 Flooding

When the intensity of rainfall exceeds the infiltration capacity of the soil onto which it falls, or when soils become saturated and cannot accept more water, it will begin to pool at the surface and pluvial floods may develop. Additionally, groundwater may begin to rise, breaking the surface and flooding large areas. The effect of flooding, whatever the source, on farm operations and production can be long-lasting. There is an immediate threat to farm infrastructure, buildings and yards from water damage, as well as a threat to materials (silage or hay) and livestock. The lasting impact, after surface water has receded, is the effect on growth and utilisation where soils remain saturated once surface flooding has receded.

1.3.5 Greenhouse gas emissions

The agricultural sector in Ireland is a leading emitter of GHG, in the form of nitrous oxide (N_2O) and carbon dioxide (CO_2). These are gaseous compounds are capable of trapping and holding radiation in the atmosphere and are linked to climate change. The type of soil drainage that may occur on a farm can have a considerable impact on the volume of emissions. For example, intensively managed grasslands are a potential large source of N_2O from N applications and urine excretion by grazing animals. In areas of high rainfall where waterlogged soils are common, there is a high risk of denitrification. This is the conversion of nitrate (NO^3) into nitric oxide (NO), nitrous oxide (N_2O) and finally nitrogen gas (N_2) by soil bacteria in wet soils. N_2O emissions from grazed grasslands are estimated to be ~28% of total anthropogenic N_2O emissions, which is estimated to account for ~6% of predicted global warming (Rafique *et al*., 2011). Well-drained soils conversely pose little risk of significant denitrification loss. Studying grassland in Southern Ireland, Rafique and colleagues (Rafique *et al*., 2011) found N_2O emissions increased as soils became wetter with maximum N_2O emissions occurring at 60–80% water-filled pore space.

The drainage of organic peat soils can remove natural carbon (C) sinks while simultaneously releasing captured C back to the atmosphere. Research also suggests, however, that the draining poorly-drained mineral soils can increase levels of soil organic carbon (SOC) by encouraging deeper rooting in plants and through the formation of stable soil aggregates (Kiely *et al.*, 2017; Freibauer *et al.*, 2004; Lal, 2004). Recent research has reported that clay-rich soils >30 cm deep might therefore become important long-term carbon stores (Torres-Sallan *et al.*, 2017). Such storage could offset increasing agricultural emissions of C and

suitable soils could have greater economic potential for C sequestration than in continued primary production (Coyle *et al.*, 2016).

Figure 1-7 DigitalGlobe image of Ireland showing specific areas of interest discussed in Chapters 4-6, including the Border, Midlands and Western region, test site Farm A (see Chapter 4); Arable B, Co. Louth (see Chapter 5) and Rathcoffey, Co. Kildare (see Chapter 6). Source: DigitalGlobe, ArcGIS base map.

1.4 Introduction to the study area

This section provides an broad overview of the principal area of interest for this study, the Border, Midlands and Western (BMW) region of the Republic of Ireland (Figure 1-7). The focus is on establishing the agri-environmental context, including prevailing climate, land use and agricultural production.

1.4.1 Climate

Ireland generally has a temperate, humid climate strongly influenced by prevailing westerly winds and a maritime location (Keane & Sheridan, 2001). Rainfall is spatially and seasonally variable with the highest volumes falling in western coastal regions as well as uplands areas nationally. Annual rainfall can vary from < 800 mm to > 2500 mm. The wettest months are October to January, with April typically the driest month. Annual temperatures display strong geographic influences, with a distinct NNE to SSW gradient in mean annual temperature (from 9°C in the NNE to 10.6°C in the SSW). Inter-annual temperature fluctuations are typically minor and rarely stray too far from expected values. As a consequence, evapotranspiration is relatively stable across the island, approximately 400-450 mm yr^{-1} (Keane & Sheridan, 2001). This disparity between the rates of rainfall and evapotranspiration means that a considerable volume of water must be recycled annually by drainage, either as surface runoff or within the soil matrix. The spatial variability in temperature and rainfall and their impact on SM influence the type of land use and management that is practised on farms. This can have a considerable impact on profitability. For example, using ten years of precipitation and grass yield data from Solohead Research Farm, Co. Tipperary (2001-2010), Humphreys *et al.* (2012) demonstrated the reduction in net profitability under increasingly wet conditions (Figure

1-8). In wetter years (i.e. those with high annual rainfall that resulted in longer periods of wet soils), net farm profits were reduced by ~25% (or €400 ha^{-1}) relative to drier years (Humphreys *et al.*, 2012).

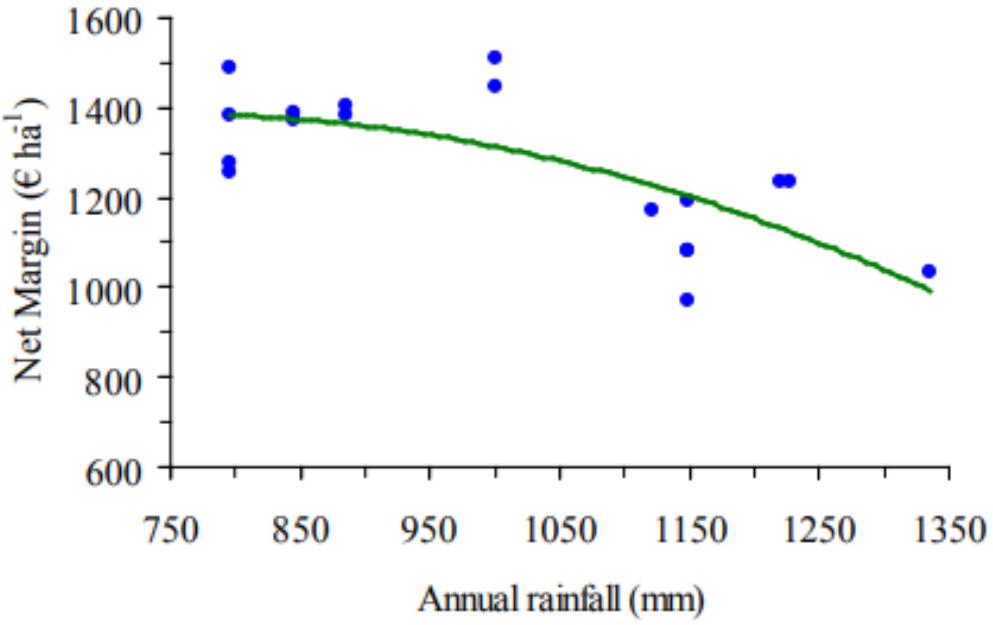

Figure 1-8 The impact of high rainfall on farm profitability at Solohead Research Farm, Co. Tipperary between 2001 and 2010. Increasingly higher rainfall volume had a negative impact on net profit per ha amounting to nearly €400 ha^{-1} between very wet and dry years. Source: (Humphreys *et al.*, 2012)

1.4.2 Agricultural production

1.4.2.1 Overview

Approximately 4.45 million ha or 63% of the total land area of the Republic of Ireland is used for agriculture, with ~ 3.38 million ha used for grazing or silage production and a further 0.53 million ha as rough grazing/ commonage (see Table 1-2). Based on recent figure, a little ust over half (52%) of the 137,500 farms in the Republic of Ireland are located in the Border,

Midlands and Western (BMW) region, where sheep and beef are the dominant enterprises (CSO, 2016). In the same statistics, the average farm size in the BMW region was typically 5 ha smaller than the national average (~27 ha vs ~32 ha).

Table 1-2 Total area farmed in the Republic of Ireland (by land use and region) (June 2017). Source: CSO StatBank database.

Land use	Region	Area (x1000 ha)
Pasture	State	2177.3
	Border	364.7
	Midland	214.2
	West	436.8
	Dublin plus Mid East	203.6
	Mid-West	309.3
	South-East	314.2
	South-West	334.5
Hay	State	211.8
	Border	29.6
	Midland	33.1
	West	37.3
	Dublin plus Mid East	24.6
	Mid-West	40.9
	South-East	25.1
	South-West	21.3
Grass silage	State	1206.4
	Border	174.9
	Midland	141
	West	198.9
	Dublin plus Mid East	85.8
	Mid-West	166.2
	South-East	177
	South-West	262.5
Rough grazing	State	530
	Border	148.5
	Midland	37.5
	West	120.3
	Dublin plus Mid East	31.2
	Mid-West	38.1
	South-East	30.7
	South-West	123.6

1.4.2.2 Grass production

Cheap and abundant, grass accounts for ~90% of livestock feed through grazing or silage. It is the foundation of the Irish meat and dairy industries, which had a combined worth of €6.8 billion in export value in 2017 (DAFM, 2018). Growth is highly seasonal, typically beginning in early spring, when soil temperatures are consistently >6°C. Rapid growth follows in spring (March/April) with a peak in May. There is a prolonged decline in growth over the remainder of the season. This trend is influenced by soil and climate at local levels. High inter- and intra-farm variability in growth patterns would not be unusual. Latitudinal temperature gradients also have a major role in season start and duration (McEniry *et al.*, 2013). Figure 1-9 below shows a national grass growth curve for Ireland for the period 2016-2018 (up to November 2018) based on individual farm data contributing to the PastureBase database. Inter-annual variation in mean grass growth is very obvious during late winter to spring in each year. This is largely an effect of weather variation between years. For example, in 2016 extensive winter rainfall and subsequent floods delayed the start of the growing season over large areas of the country until May (the impact of winter floods on grass production is discussed in Chapter 3). In 2018, the dual impact of a wet winter/ spring delaying growth is evident, but also the impact of a widespread drought during the summer.

National Farm Survey data reports average grass production over the island is ~9 t dry matter (DM) ha^{-1} yr^{-1} but could potentially be as high as 16 t DM ha^{-1} yr^{-1} through more efficient farm management (Hanrahan *et al.*, 2018). Of the grass produced, only 60-65% is utilised, (~7 t DM ha^{-1} yr^{-1}) (Dillon *et al.*, 2017). One reason for the lower volume of grass utilised is where access for grazing or silage harvesting is restricted on wet fields (Creighton *et al.*, 2011).

Unutilised grass is a wasted resource and the costs incurred purchasing supplementary feed is a double-blow to farm profitability (Ramsbottom *et al.*, 2015). There are programs currently underway to raise awareness and educate livestock farmers on the economic benefits of increasing levels of sward utilisation to 10 t DM ha^{-1} yr^{-1} in order to meet current levels of needs and to support ambitious industry targets for meat and dairy production over the coming decade (Teagasc, 2017).

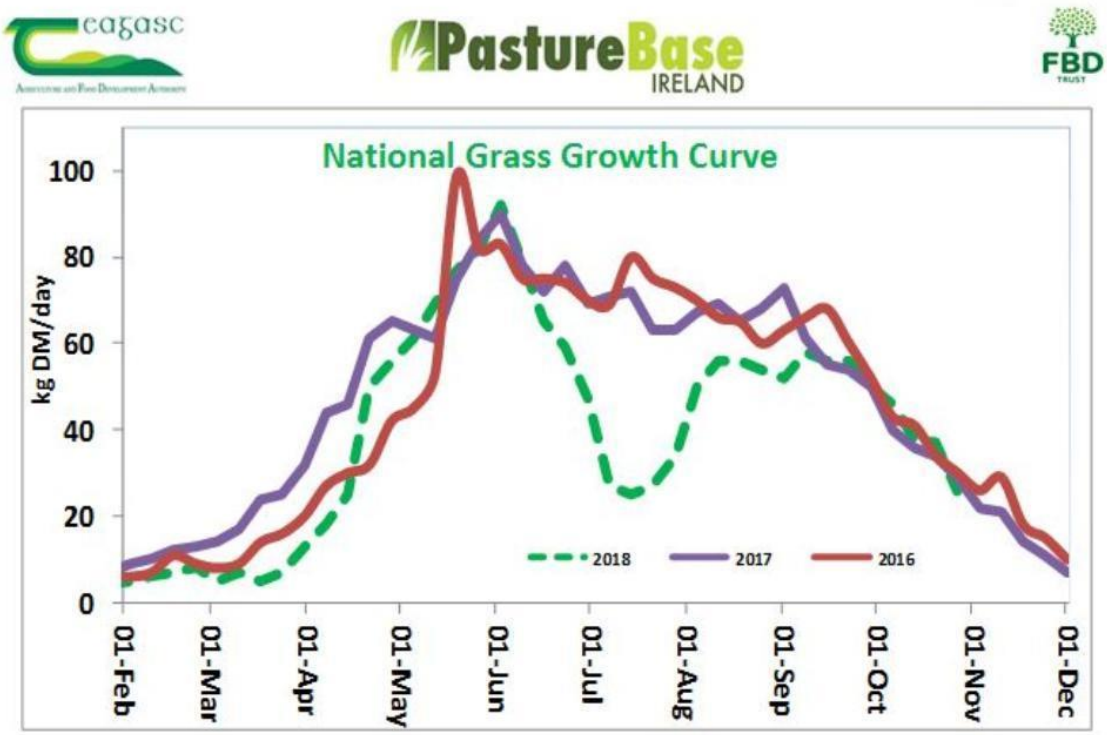

Figure 1-9 National grass growth curves from January 2016 to November 2018. Values are based on grass measurements uploaded to PastureBase Ireland from farms across Ireland. The phenological development of grass is immediately evident despite considerable inter-annual variation. Source: Teagasc/ PastureBase[2]

[2] www.teagasc.ie/crops/grassland/pasturebase-ireland/grass-curve. Accessed 12 December 2018

Farmers must also contend with disruptions from extreme weather events, both in the present-day and for predicted climate change scenarios expected over the coming decades. The expectation is that Irish winters will become wetter over the coming century (resulting in greater soil saturation) while drier summers bring greater occurrences of summer drought (Holden & Brereton, 2002).

As was witnessed in 2018, each of these scenarios put considerable strain on grass production and extended housing periods can quickly use up fodder supplies. Since the beginning of the current project in 2013/14, there have been three severe fodder shortages nationally: During winter 2013, a prolonged cold winter lasted into early summer which delayed cattle turnout for several weeks in the worst affected areas. Winter silage stores were exhausted and fodder had to be imported at an estimated cost of ~€500 million to the State. In spring 2016 extensive winter floods again delayed turnout for several weeks in affected areas and had a longer impact of grass production (Chapter 3). The total estimated cost of providing emergency and replacement fodder during this crisis was ~€756,500 (NDFEM, 2016). A wet summer in 2017 required animals to be housed for long periods during the grazing season. This had a double impact, of depleting saved fodder stores while preventing silage harvesting. Emergency fodder was imported at a cost of €1.5 m. Wet weather during winter and spring 2018 was compounded by extensive summer droughts in 2018. At the time, the reduced grass production was expected to create fodder shortages in winter 2018/2019. A Teagasc survey[3] in October 2018 reported that ~33% of farmers nationally had a fodder shortage (with an average deficit of ~15%, the equivalent of 3 weeks' worth of feed based on a 145-day

[3] https://www.agriland.ie/farming-news/the-results-are-in-on-the-teagasc-2019-fodder-survey/. Accessed 7 February 2019.

winter). In February 2019, ~25% of farmers reported insufficient fodder to meet feed requirements until the expected end of the winter housing period[4]. Ultimately, there were sufficient fodder supplies to avert a crisis, however prolonged wet or cold weather conditions in late spring (March/ April) 2019 could have delayed turnout and precipitated an emergency.

1.5 Introduction to Earth observation

Remote sensing (RS) is the science of observing and recording phenomena from a distance to obtain information about it. Earth observation (EO) is a particular branch of RS that uses satellite and aerial (manned or unmanned) platforms to measure reflected or emitted electromagnetic (EM) radiation. EM energy, in the form of visible an invisible light, propagates as a transverse wave consisting of dual electric and magnetic components. EM waves can be described in relation to their wavelength (measured in nm) and frequency (measured in Hz) (Equation 1.1). A generalised presentation of the EM spectrum is illustrated in Figure 1-10.

Typically EO is concerned with measuring EM radiation in the visible, infrared (short- and longwave) and microwave regions. The transmissivity of the Earth's atmosphere to EM radiation varies by wavelength. Only specific bands can pass through because atmospheric gases and water molecules act as selective absorbers. The wavelengths at which EM radiation can pass through, wholly or partially, are known as atmospheric windows. The important windows occur in the visible and near infrared region (300 – 1000 nm), with narrower bands in the infrared region centred at 1300 nm, 1600 nm and 2200 nm. Wavelengths in the microwave region (> 5000 μm) can pass unhindered.

[4] https://www.independent.ie/business/farming/beef/beef-advice/quarter-of-farmers-still-facing-a-fodder-deficit-on-their-farms-37780490.html. Accessed 7 February 2019.

$$c = f\lambda \qquad \text{(Eqn. 1.1)}$$

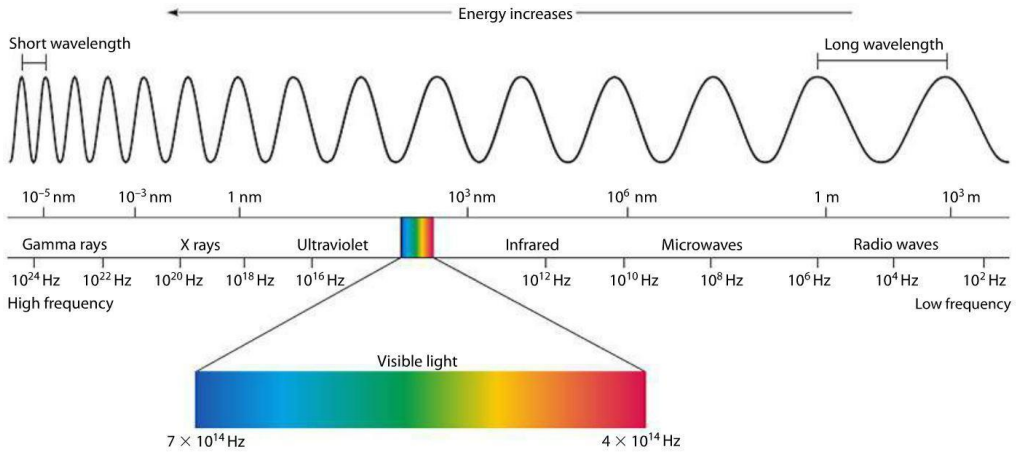

Figure 1-10 The EM radiation spectrum showing the position of each of the main regions in terms of wavelength (nm) and frequency (Hz).

EO satellite sensors must operate within these atmospheric windows, as demonstrated for Landsat 7, Landsat 8 and Sentinel 2 in Figure 1-11. Once EO data is recorded, it must then be processed to remove the effect of atmospheric scattering of EM waves. This is wavelength dependant, with radiation in shorter wavelengths more readily scattered that longer wavelengths). Removal of the atmospheric component within reflectance signals ensure only surface reflectance is recorded in images. Failure to remove this scattering effect can impact subsequent analysis. EO data providers now provide most data already processed to this stage (referred to as Level 2A). There are other illumination effects that are present, for example, when natural surfaces reflect light anisotropically. The radiance measured a a sensor is a function of viewing and illumination geometry (known as a bidirectional reflectance distribution function, BRDF) (Jones & Vaughan, 2010).

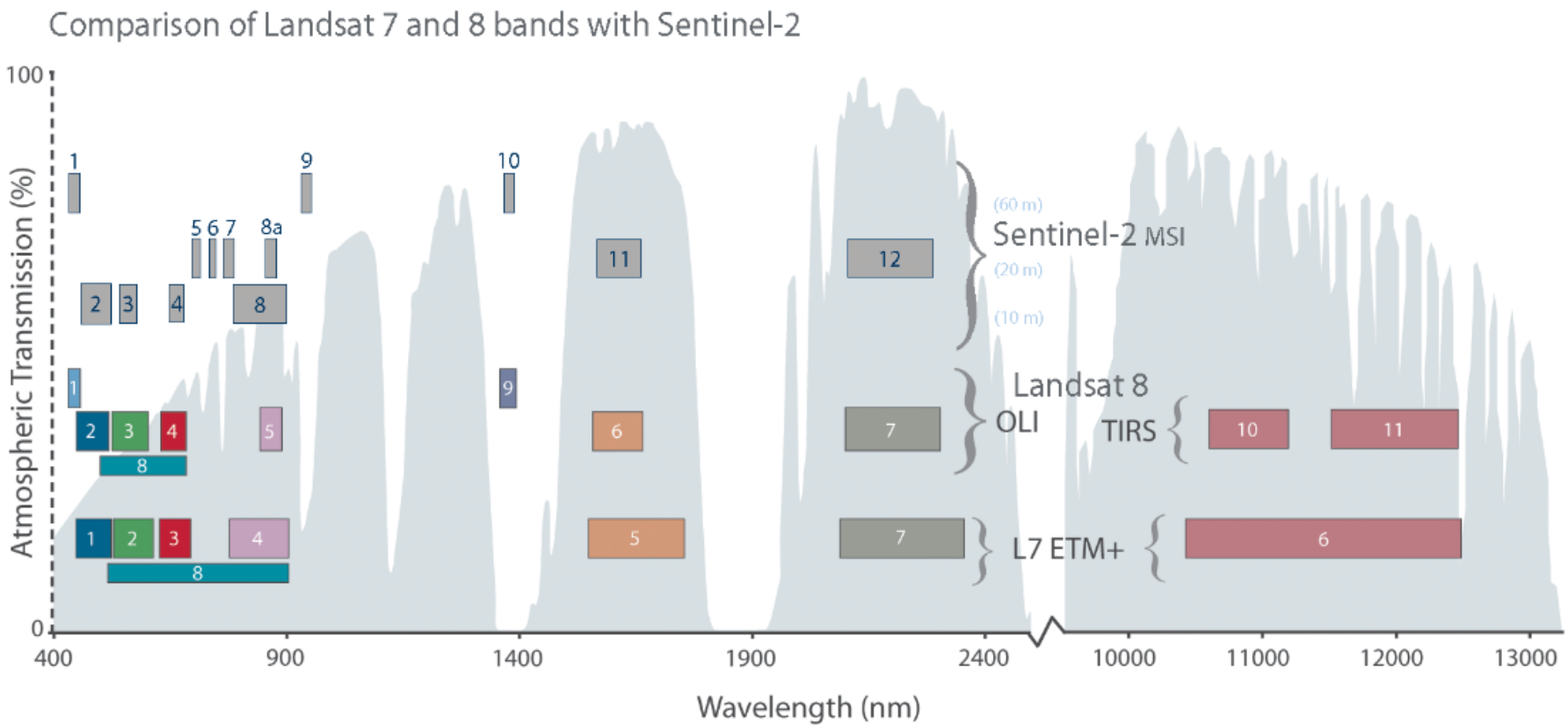

Figure 1-11 A comparison of the spectral band position and bandwidth for Landsat 7 & 8 and Sentinel 2 with respect to atmospheric windows. Source: USGS[5]

[5] Available at https://landsat.gsfc.nasa.gov/sentinel-2a-launches-our-compliments-our-complements/; accessed 12 December 2018

1.5.1 Role of EO in Precision Agriculture

The objective of this research was to determine spatial patterns in overlying grass canopy relating to in-field drainage conditions using a suite of EO data. Identifying and targeting spatial variation in crop or soil properties is a principle of Precision Agriculture (PA), a farm management concept that identifies different management zones. It is characterised by the collection and analysis of high resolution, site-specific data to support farming decisions, increase agricultural output and reduce costs and waste (Gebbers & Adamchuk, 2010; Mulla, 2013; Stafford, 2000). PA is considered by the European Union to be an important milestone for achieving sustainable food security (Schrijver, 2016). Historically, EO satellite platforms have played a key role in PA by providing a wide range of data on soil- and vegetation properties. Satellite platforms have several advantages for monitoring agricultural land use (Moran *et al.*, 1997), for example: they are capable of sensing differences in surface properties using different parts of the EM spectrum; they can measure different surface properties (for example, plant health, soil moisture, surface roughness, surface temperature etc.) and they allow cheap, synoptic collection of data at different scales. The shortcomings of EO platforms for agricultural monitoring are equally well-established (Atzberger, 2013; Bontemps *et al.*, 2015). These include, for example, the wavelength-dependent attenuation of EM radiation in visible and infrared regions, extensive occlusion by clouds and cloud shadow and poor temporal resolution (historically). The requirement for better spatial-, spectral- and temporal resolution data for agricultural monitoring was a key purposes behind the development of the ESA Sentinel 2 mission (Malenovský *et al.*, 2012). In comparison with similar (non-commercial) EO missions such as Landsat 8, the Sentinel 2 mission has unprecedented spatial resolution (10m, 20m, 60m), spectral resolution (13 spectral bands between 443-2190 nm) and a shorter revisit time (2-3 days at mid latitudes). Commercial

missions such as QuickBird or WorldView can provide very high spatial resolution (<1 m) data, however, the cost per scene makes mapping over large areas prohibitively expensive.

There is increased availability of hyperspectral imagery for EO mapping. These images typically have a narrower bandwidth (~ 10-20 nm) than broadband sensors and may consist of hundreds of individual bands. The number of bands can help identify and distinguish spectrally similar materials. In the recent past, the Hyperion sensor on-board the EO-1 satellite provided access to hyperspectral data. Several new hyperspectral sensors are expected to launch in the coming decade. For example, EnMAP (Environmental Mapping and Analysis Program) is expected to launch in 2020 providing on-demand VNIR data at 30 m resolution over 240 spectral bands (420-2450 nm) (Guanter *et al.*, 2015). The Italian PRISMA (PRecursore IperSpettrale della Missione Applicativa) was launched during 2019 and will also have ~250 bands at 30 m spatial resolution (66 VNIR bands between 400 and 1010 nm; and 171 SWIR bands between 920 and 2505 nm) (Pignatti, 2013). Although hyperspectral sensors have a superior ability to quantify vegetation stresses based on small changes in several hundred spectra, the volume of data provided can be a challenge to manage and analyse (Transon *et al.*, 2018). They often have poor temporal resolution and typically have a narrow swath width and so cover less ground than multispectral sensors. Both EnMAP and PRISMA have just 30 km footprints compared to the 185 km and 290 km swath widths of Landsat 8 and Sentinel 2 respectively.

1.5.2 Vegetation indices

Combining spectral bands, for example, through ratioing or differencing, can enhance surface reflectance signals by minimising variation caused by solar irradiance and topographical background effects (Jackson & Huete, 1991). Commonly known as vegetation indices (VI), these image processing techniques typically combine red and NIR reflectance to monitor spatial and temporal variation in vegetation cover and vegetation health. Variant indices using different bands have also been developed (see J. Xue & Su, 2017 for a comprehensive review). A popular VI is the normalised difference vegetation index (NDVI) (Equation 1.2) using red and NIR bands. The NDVI has a normalised, dimensionless output ranging from -1 to 1, where negative values (approaching -1) correspond to open water, no vegetation (bare rock, soil, cement etc.) is around 0, and verdant, healthy vegetation (for example, grass cover in Ireland during spring) has high values approaching 1 (Rouse *et al.*, 1974) (Figure 1-12).

$$NDVI = \frac{NIR-RED}{NIR+RED} \quad \text{(Eqn.1.2)}$$

where NIR and RED are surface reflectance values measured by an EO satellite or aerial sensor.

The normalised difference water index (NDWI) (Equation 1.3), is complementary to the NDVI but is computed using NIR and SWIR bands (Gao, 1996), with SWIR reflectance negatively related to leaf water content (Tucker, 1979). This VI also has a dimensionless output from -1 to +1. High NDWI values correspond to high vegetation water content or vegetation fraction cover. Low NDWI values correspond to low vegetation water content and low vegetation

fraction cover. When stressed, NDWI values for plants tend to decrease as less water is taken up from the roots (Figure 1-12).

$$NDWI = \frac{NIR - SWIR}{NIR + SWIR} \quad \text{(Eqn. 1.3)}$$

where NIR and SWIR are surface reflectance values measured by an EO satellite or aerial sensor.

DigitalGlobe RGB image of area of Co. Cavan

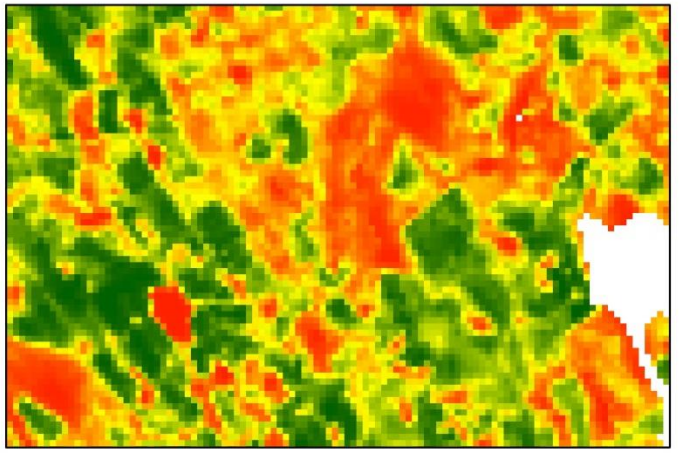

Same area viewed as a Landsat 8 NDVI image

N

NDVI

High : 0.93

Low : 0.13

NDWI

High : 0.61

Low : -0.20

High values for NDVI (green) and NDWI (blue) represent healthy vegetation canopy.

Mid values for NDVI and NDWI (yellow) represent stressed vegetation canopy

Low values for NDVI and NDWI (red) represent bare earth or artifical surfaces

km

0 0.5 1

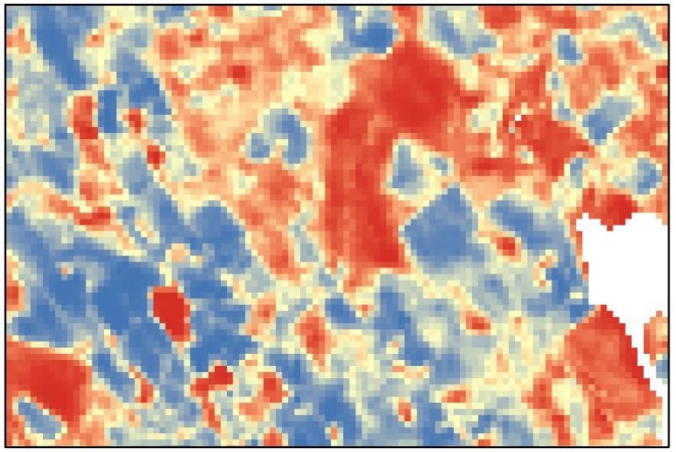

Same area viewed as a Landsat 8 NDWI image

Figure 1-12 A DigitalGlobe image with corresponding Landsat 8 NDVI and NDWI images shown in colour ramps for visualisation purposes.

1.5.3 Unmanned aerial systems

Unmanned aerial systems (UAS), otherwise known as unmanned aerial vehicles (UAV), remotely piloted aircraft systems (RPAS), or more commonly drones, are increasingly used as low-altitude remote sensing platforms for PA but also mapping surface hydrology and environmental monitoring (Colomina & Molina, 2014; Pajares, 2015; Whitehead & Hugenholtz, 2014; C. Zhang & Kovacs, 2012). These aerial robotic platforms can be deployed and targeted on-demand, and have become an important complement to traditional EO platforms, capable of filling in spatial and temporal gaps in satellite data. UAS have become increasingly stable and reliable in terms of quality and accuracy (Aasen *et al.*, 2015; Gómez-Candón *et al.*, 2014). Most professional grade platforms are capable of 25-45 minute flights and can carry a range of sensors, including RGB cameras, multispectral/hyperspectral sensors, thermal infrared cameras, as well as LiDAR and geophysical sensors. UAS are now deployed across a broad range of agricultural production systems, with applications in crop stress identification (Gago *et al.*, 2015), biomass estimation (von Bueren *et al.*, 2015), yield monitoring (Torres-Sánchez *et al.*, 2014), fertilisation and irrigation scheduling (Bellvert *et al.*, 2014); pest control (Gonzalez-de-Santos *et al.*, 2017) and subsurface drainage identification (Allred *et al.*, 2018). In Ireland, UAS are currently being tested for a wide range of applications in grassland management, for example, in the identification of N loads from livestock urine in grazed pasture fields (Maire *et al.*, 2018). The two UAS platforms used in different aspects of this research are illustrated in Figure 1-13 below.

Figure 1-13 Two UAS used during the project. A DJI Matrice 600 (rear) and a DJI Phantom 4 Pro (foreground). The Matrice 600 is equipped with a Flir Zenmuse XT thermal sensor. The DJI has an integrated RGB camera.

The ability to deploy UAS on demand is especially advantageous in regions such as Ireland, where extensive cloud cover frequently obscures the surface for satellite platforms. Deploying at short notice is well suited to operational monitoring, for example, for mapping different stages of crop development. Flight missions may be programmed to follow predefined routes autonomously. Platform speed and height can be set to produce accurate orthomosaic imagery or to obtain accurate photogrammetric measurements (as demonstrated in Chapter 5). Currently, regulations limit the maximum altitude of UAS flights to ensure physical separation from manned flights in controlled airspace. In most parts of Ireland, this is set at 120 m with additional restrictions surrounding airports and other prohibited airspace (Small

Unmanned Aircraft (Drones) and Rockets Order S.I. 563 of 2015). At this altitude, it is still possible to capture centimetre-accurate images using consumer-grade UAS like the DJI Phantom series. The rapid adoption of UAS for remote monitoring has resulted in recent international efforts to harmonise data collection methods, with a focus on data quality, processing techniques and error propagation in UAS products (Singh & Frazier, 2018). This is the goal behind the current EU COST[6] action named "Harmonious" (CA 16219), which aims to bridge the gap between field observations and traditional remote sensing platforms using UAS (Salvatore Manfreda *et al.*, 2018).

[6] European Cooperation on Science and Technology. www.costharmonious.eu (accessed 18 December 2018).

1.6 Earth Observation for mapping soil moisture

EO is widely used to estimate soil moisture (SM). As SM and soil drainage are inextricably linked, there is a great deal of crossover in terms of the data and techniques used. Before introducing some examples of EO projects looking explicitly at soil drainage (in Chapter 2), the following sections outline the state of the art in optical, thermal infrared and microwave EO techniques to map and monitor SM under different environmental conditions. For each method, the inherent advantages and disadvantages are presented, and their current or potential use in drainage mapping is discussed. An overview of these methods is presented in Figure 1-14 below.

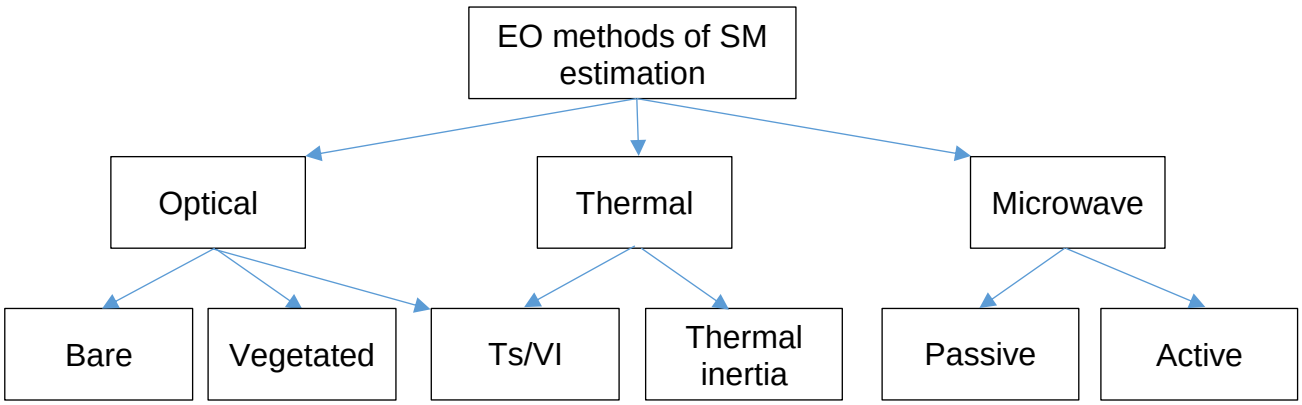

Figure 1-14 Chart of the principal methods of estimating soil moisture using EO satellite platforms.

1.6.1 Soil moisture mapping in the microwave region

Microwave (MW) sensors, commonly known by the acronym RADAR (RAdio Direction And Ranging) measure within the microwave region of the EM spectrum. For SM mapping, MW sensors measure spatial differences in dielectric constant, which quantifies the electric properties of surface materials. The considerable disparity between dielectric constants of natural surface materials (~3-8 in dry conditions) and water (~80) results in significant increases in radar reflectivity from small increases soil moisture content. Three bands in particular are important for SM estimation: X-band (2.4-3.75 cm; 8-12 GHz), C-band (3.75-7.5 cm; 4-8 GHz) and L-band (15-30 cm; 1-2 GHz). RADAR has three important advantages for SM mapping (Kerr *et al.*, 2016): it operates independent of solar radiation, it is largely unaffected by atmospheric attenuation or cloud cover and it can penetrate vegetation (by how much is a function of wavelength, with longer wavelengths penetrating further).

SM can be measured using both passive and active MW sensors. With passive sensors, thermal emission, or brightness temperature, of the land surface is measured, where brightness temperature is inversely related to SM in the top 5 cm (Schmugge *et al.*, 1980). Data from passive RADAR sensors are ill-suited for operational agricultural purposes. Two L-band sensors currently in orbit providing global estimates on near-surface (0-5 cm) SM on a continuous basis are the ESA SMOS (Soil Moisture Ocean Salinity) mission and the NASA SMAP (Soil Moisture Active Passive) missions. Studies have reported high accuracy for both sensors under optimal conditions (flat topography, low vegetation and no radio frequency interference), however with spatial resolution of ~40 km these sensors are best suitable to global/continental-scale SM observations (Figure 1-15). Disaggregation of coarse resolution SM products using 1 km spatial resolution MODIS data can be useful to improve spatial

resolution (Srivastava *et al.*, 2013) but generally SMOS and SMAP are considered unsuitable to operational SM monitoring at PA-scale because of the huge scale discrepancy between RADAR observation scale (several kilometres) and field- or farm scale.

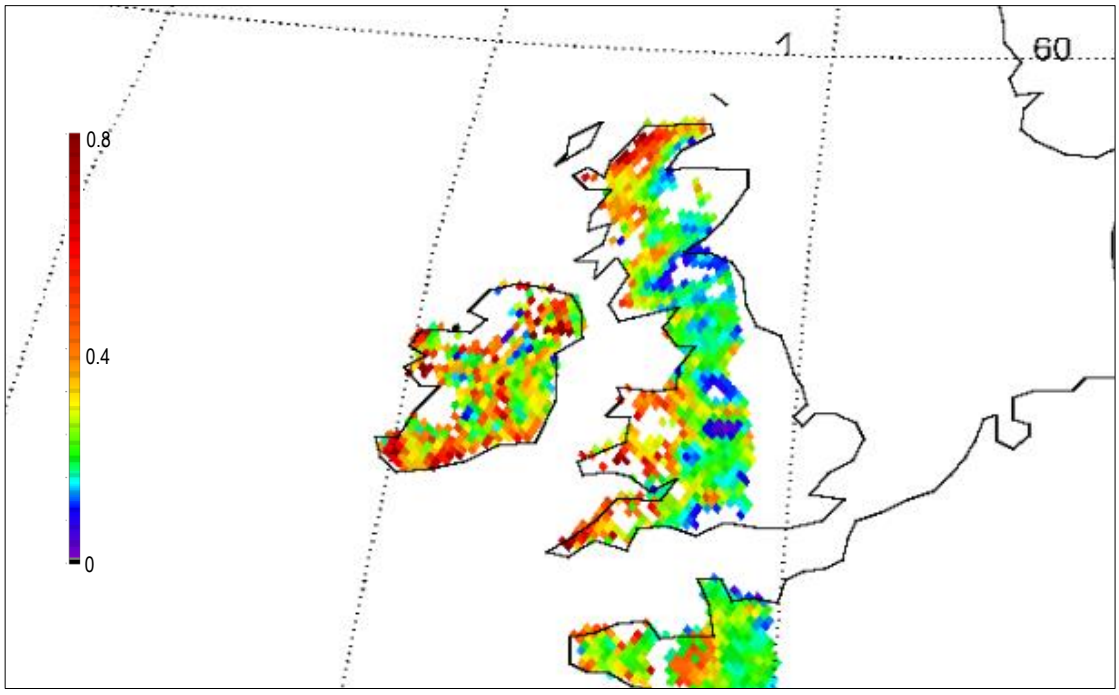

Figure 1-15 Example of the ESA SMOS MIR SMUDP2 Soil Moisture product (26 April 2018). This sensor provides daily volumetric SM estimation $m^3\ m^{-3}$ (cubic metres of water per cubic metre of soil) at very coarse spatial resolution best suited to global SM mapping.

Unlike passive sensors, active MW sensors emit MW pulses and record the intensity of the returned signal (backscatter). High SM will increase backscatter under ideal conditions (flat topography, no vegetation). The higher spatial resolution of active MW sensors makes them better suited to operational SM mapping. However, active MW sensors are equally sensitive to surface roughness and vegetation cover so in densely vegetated areas different contributors to the backscatter signal must be filtered out to provide an estimate of SM

content. These other sources will include volume scattering within overlying canopy, direct ground scattering and double-bounce effects between canopy and ground (Wagner & Pathe, 2005; Walker *et al.*, 2004). Several methods have been developed to account for the effect of vegetation and roughness on SM estimates using empirical, physical, and semi-empirical models. These often require considerable parameterisation, and are only applicable to the specific conditions that are modelled (Barrett *et al*., 2009).

An early study on SM retrieval suggested active RADAR may be applicable where biomass is < 1 t ha^{-1} (Dobson *et al.*, 1992). Applying this approach to SM estimation on intensively managed grasslands, one Irish study ignored the influence of canopy height and assumed backscatter (ENVISAT SAR) was linearly related to SM (Barrett *et al.*, 2012). A significant, positive relationship between backscatter and *in-situ* SM was reported (R^2: 0.67–0.86). Subsequent studies found RADAR SM estimates were less accurate when compared poorly with *in-situ* SM data in very dry and very wet soil conditions (Pratola *et al.*, 2015).

MW data are widely used for soil drainage mapping. The few published instances where C-band SAR was used for soil drainage classification were generally used in combination with multispectral or hyperspectral imagery or other remotely sensed data. For example Liu *et al*. (2008) classified soil drainage at field scale using hyperspectral imagery, soil conductivity and airborne C-band SAR imagery (Liu *et al.*, 2008). The maps produced from SAR images were comparatively noisy (from RADAR speckle) and as a consequence classification accuracy was low (52% compared with 55% for soil conductivity and 68% for hyperspectral data). Niang *et al.* (2012) found evidence for contrasting SAR backscattering coefficients related to

different drainage classes. Extreme drainage classes could be readily distinguished but separating neighbouring drainage classes was more of a challenge, particularly in increasingly wet soil conditions or under increasingly dense vegetation (Niang *et al.*, 2012).

1.6.2 Soil moisture mapping in the visible & near-infrared region

Optical methods of estimating SM are based on the reflectance of EM radiation in the visible and near-infrared (VNIR) region (400-2100 nm). Optical methods are best applied on bare or sparsely vegetated ground where sensors can directly image the surface. However, even where there is vegetation present, SM volumes may be inferred from its impact on canopy growth.

1.6.2.1 Bare soil

The darkening of bare soil as the volume of SM content increases is a familiar phenomenon. Several laboratory-based studies investigated the decrease in soil reflectance as a function of saturation. Lobel and Asner (2002) found a non-linear (exponential) relationship between SM and soil reflectance as a soil moved between wet and dry states. Detection of contrasting SM was enhanced in NIR and SWIR regions compared with visible (RGB) bands (Lobell & Asner, 2002). Subsequently, Kaleita *et al.* (2005) described the relationship between SM and soil reflectance by combining hyperspectral VNIR reflectance with gravimetric (oven-dried soil samples) measurements of SM (Kaleita *et al.*, 2005). The study suggested it was feasible to estimate surface soil moisture in the upper 7 cm from VNIR reflectance, although estimating SM regimes rather than precise SM measurement was more likely. The study also reported

that the accuracy of SM estimation was a function of soil type, with improved accuracy on soils with higher sand content.

For larger scale mapping, Liu *et al.* (2008) used principal component analysis of stacked hyperspectral images, soil electrical conductivity data and C-band RADAR backscatter images to distinguish broad drainage classes (well-, imperfectly- and poorly-drained) over bare fields. The best classification performance was achieved using hyperspectral imagery, where substantial agreement between observed and modelled drainage class was reported imagery (68% compared with and 55% for soil conductivity and 52% for RADAR) (Liu *et al*., 2008). Using a combination of VNIR data at different spatial resolution (Landsat TM images at 30 m spatial resolution, IKONOS satellite imagery at 4 m spatial resolution and aerial RGB orthomosaics at 60 cm spatial resolution), Peng *et al*. (2003) mapped bare soil drainage classes with an overall classification accuracy of 73% when compared to observed validation data (Peng *et al.*, 2003). Merging the high spatial resolution orthomosaics with Landsat TM images and a DEM significantly improved predictive ability over existing, conventionally-produced soil surveys which only achieved 55% accuracy versus validation data. Using RapidEye (6.5m) satellite imagery, Blasch *et al*. (2015) demonstrated the potential of multi-temporal, multispectral soil reflectance over mono-temporal analysis for generating functional soil maps at field scale (Blasch *et al.*, 2015).

1.6.3.2 Vegetated soil

Where vegetation obscures the surface, extreme SM regimes can be inferred detected in multispectral or hyperspectral EO images of the overlying vegetation. Plants respond to environmental stress in a number of ways that can be identified in EO imagery. Physiological responses to stresses may cause a reduction in foliage biomass, photosynthesis and respiration (Barrett-Lennard, 2003; Carter, 1991; Drew, 1983) which can be observed in changes to the reflectance/absorption characteristics of VNIR spectra (400-850 nm). Typically for broadband sensors these changes will occur in a narrow region near 700 nm sensitive to chlorophyll production, and in the SWIR region (1400–2500 nm) where contrasting reflectance values in vegetation can be attributed to changes in plant water content, leaf water potential and stomatal conductance (Carter & Knapp, 2001; Ceccato *et al.*, 2001). Vegetation indices are widely utilised for SM mapping (D. Zhang & Zhou, 2016). For example, 250 m resolution MODIS NDVI images were used in different studies as a proxy for root zone SM (Santos *et al.*, 2014; X. Wang *et al.*, 2007). Several other authors have used Landsat imagery to map soil drainage class (Cialella *et al.*, 1997; Lozano-Garcia *et al.*, 1991). Others have combined moderate- and high-spatial resolution data to map drain function by mapping spatial anomalies in plant vigour related to underlying SM conditions (Cicek *et al.*, 2010; Kross *et al.*, 2015; Khand *et al.*, 2017; Kobryn *et al.*, 2015). Hyperspectral imagery, which can record several hundred continuous, narrow spectral bands are very adept at identifying subtle plant responses to stress. In many cases, the response is species specific reflecting different genetic, biochemical or structural characteristics of the plants involved. In many cases, however, there is a widely observed shift in the position of the red-NIR boundary (the red edge, ~680-730 nm) towards shorter wavelengths (Boochs *et al.*, 1990; Carter, 1991, 1993).

1.6.3 Soil moisture mapping in the thermal infrared region

Thermal infrared radiation (TIR) refers to electromagnetic radiation between 3-14 μm. All bodies with a temperature above absolute zero (0 °K; -273.16 °C) emit radiation as a function of emissivity and temperature as governed by the Stefan-Boltzmann equation (Equation 1.4). This equation states the total radiation emitted from a blackbody is proportional to the fourth power of the absolute temperature of the blackbody (where a blackbody is a hypothetical surface that perfectly absorbs and reemits all energy that is incident upon it (Sabins, 2007)). For grey bodies (i.e. all natural surfaces) an object's emissivity must be accounted for to define accurate temperature readings. Emissivity, a dimensionless value between 0 (perfect reflector) and 1 (perfect emitter), is the ratio of energy from a surface compared to a blackbody at the same wavelength and temperature.

$$E = \varepsilon\sigma T^4 \qquad \text{(Eqn. 1.4)}$$

where $\sigma = 5.67 \times 10^{-8}$ Wm^{-2} K^{-4} (Stefan-Boltzmann constant), T is absolute temperature in degrees Kelvin (K), and ε is surface emissivity.

The relationship between emissivity, radiant- and actual (kinetic) temperature is defined by Equation 1.5 below. Objects and surfaces may have the same kinetic temperature but can differ significantly in the radiation they emit and their radiant temperatures because of different emissivity. Also, where vegetation forms a dense canopy, the emitted thermal signal may have little relationship to underlying soil temperature but instead may reflect stomatal temperature regulation by the canopy (H. G. Jones *et al.*, 2009). Like optical sensors, thermal sensors have limited penetration depth and are susceptible to occlusion by clouds. It also has

coarser spatial resolution, for example, the Landsat 8 thermal bands (which measure thermal radiation in two bands between 10.6-11.19 μm and 11.5-12.51 μm) are captured at 100 m spatial resolution (but provided as resampled 30 m spatial resolution products).

$$T_{rad} = \varepsilon 1/4 T_{kin} \quad \text{(Eqn. 1.5)}$$

where T_{rad} and T_{kin} are radiant temperatures measured by a thermal camera and the kinetic temperature of the surface respectively and ε is emissivity.

1.6.3.1 Thermal inertia

TIR remote sensing is well-established for mapping SM (Idso *et al.*, 1975). A popular TIR technique for mapping spatiotemporal patterns in SM involves identifying differences in diurnal temperature caused by differences in the thermal inertia (TI) of surface materials. TI is a measurement of an object's resistance to ambient temperature change and is strongly dependent on SM. TI is higher on wet soils because water absorbs a greater amount of heat and temperatures change more slowly than for drier soils. In controlled settings, TI can be calculated if several properties are accurately known (Equation 2.7) (Hillel, 1998).

$$TI = \sqrt{kpc} \quad \text{(Eqn. 1.6)}$$

where k is thermal conductivity (the ability of a surface to conduct heat; W m^{-1} K^{-1}), ρ is density (mass per unit volume, kg $m^{-3} \times 10^3$), and c is heat capacity (the product of specific heat and ρ, J m^{-3} $K^{-1} \times 10^6$).

For EO purposes, the thermal conductivity, specific heat capacity and bulk density of specific objects or surfaces are rarely known, so an *apparent* thermal inertia (ATI) is calculated instead (J. Price, 1985; Y. Xue & Cracknell, 1995). There are several ATI functions available for SM monitoring and a number of these have been reviewed in the context of SM monitoring of grassland in New Zealand using MODIS land surface temperature (Sohrabinia *et al.*, 2014). All functions displayed similar correlation values *in-situ* SM measurements but the best performance was during drier, summer months. On bare or sparsely vegetated soils, SM estimates using ATI can be quite precise (Verstraeten *et al.*, 2006). Matsushima et al. (2012) predicted SM on bare or sparsely vegetated surfaces with a precision of 3-4% using an ATI method which allowed classification of mapped soils into broad SM regimes (wet, middle and dry) (Matsushima *et al.*, 2012). ATI can be calculated using albedo and diurnal temperature difference using Equation 1.7.

$$ATI = (1 - A) / \Delta T \qquad \text{(Eqn. 1.7)}$$

where A is albedo (the ratio of reflected and incident radiation) and ΔT is the difference in surface temperature captured by a TIR sensor at daily temperature extrema.

1.6.3.2 Temperature/ vegetation index

When TIR is combined with NDVI, a two-dimensional surface temperature/ vegetation index feature space (Ts/VI) is created that can be of use for SM estimation (Carlson *et al.*, 1994; Gillies & Carlson, 1995; Moran *et al.*, 1994; Sandholt *et al.*, 2002). The Ts/VI technique focuses on the distribution of pixels within the feature space, the location of which can depict gradients of soil moisture and vegetation health. A comprehensive review of the application of Ts/VI can be found in Petropolous *et al.* (Petropoulos *et al.*, 2009). The "universal triangular method", as it has become known, has found broad application at different scales, in different climatic regions and for different land cover (Holzman *et al.*, 2014; Mallick *et al.*, 2009; Sandholt *et al.*, 2002). However, it is reported to be unreliable in regions of complex topography and requires a broad range of temperature and soil moisture values to adequately define the feature space (Rahimzadeh-Bajgiran *et al.*, 2012).

1.7 Earth Observation for mapping floods

Flooding can result from, or result in, saturated soil conditions. The ability to map floods is also applicable for mapping areas of saturated soil. As flood waters recede, the soil matrix will often remain saturated or near saturation for some time after. In agricultural areas this can have a negative impact on crop growth. In Chapter 3, an application is described that combines SAR flood maps from the Sentinel 1 mission with multi-temporal Landsat 8 NDVI imagery to observe the process of recovery for grassland following soil saturation. EO provides a cost-effective and efficient means of producing accurate flood maps in near real-time. The use of both optical and MW sensors for flood mapping is well-established (Joyce *et*

al., 2009; Profeti & Macintosh, 1998; Rango & Salomonson, 1974; Twele *et al.*, 2016). The following section outlines different forms of EO data used to map floods.

1.7.1 Optical sensors

Optical sensors map flood waters using the contrasting reflectance signals of soil/vegetation and water, particularly in the NIR, SWIR and green regions of the electromagnetic spectrum (thermal infrared may also be used) (Du *et al.*, 2016; Ji *et al.*, 2011; Leblanc *et al.*, 2011; Ouma & Tateishi, 2006). Optical imagery is not always suitable for operational flood mapping where cloud cover prevents timely mapping. While this can be partly mitigated by using lower spatial resolution/ higher temporal resolution imagery (for example, Moderate Resolution Imaging Spectroradiometer (MODIS) composite images), which minimises cloud interference but comes at the loss of mapping accuracy (Chen *et al.*, 2013). UAS are now increasingly used for small areas mapping of floods, below cloud cover, with studies describing their use for quantifying buildings at risk or measuring flood depth (Ridolfi & Manciola, 2018). An added benefit of optical sensors is their ability to measure plant stress and thus quantify vegetation recovery following flood events. Several studies have examined the role of EO data for mapping plant recovery following inundation (Džubáková *et al.*, 2015; Pantaleoni *et al.*, 2007) or extreme weather/ natural disasters (Fu *et al.*, 2014; Rodgers *et al.*, 2009).

1.7.2 Microwave sensors

SAR sensors are extremely efficient sensors for operational flood mapping because of their ability to map independent of solar illumination and cloud cover. However, SAR images require additional processing and often expert interpretation of the signal. RADAR sees water

as areas of very low backscatter values, where smooth water surfaces result in the specular reflection of microwave pulses in a single direction away from the sensor. Consequently, waterbodies (including flooded areas) appear very dark in SAR imagery. Conversely, rough land surfaces are diffuse reflectors of SAR signals so a greater portion of energy is reflected towards the sensor and, in contrast to waterbodies, it appears bright in SAR imagery. A surface is considered "rough" when it has dimensions comparable to the incident wavelength (i.e. centimetre variation in the case of C-band sensors) (Campbell, 1996). Different polarisation settings can also affect the strength of the returned signal.

Polarisation refers to the geometric plane an MW pulse propagates along, horizontal (H) or vertical (V). For sensors with dual polarisation capability, four combinations are possible (HH, HV, VH, and VV), and all can potentially be used for flood mapping. The HH (horizontal transmit, horizontal receive) combination often displays the highest contrast between water and land. Sentinel 1 primarily operates in VV and VH mode over land surfaces (Sentinel 1 SAR User Guide[7]). VV (vertical transmit, vertical receive) has previously been viewed as less capable than HH for flood mapping (Bourgeau-Chavez *et al.*, 2001; Gstaiger *et al.*, 2012), although Manjusree demonstrated an ability of the polarisation to identify partially submerged fields (Manjusree *et al.*, 2012). Twele *et al*. reported high classification accuracy (>94%) using VV polarised Sentinel 1 imagery (Twele *et al*., 2016). Clement *et al*. achieved similar accuracy (97%) mapping winter floods in the UK in 2015-16 (Clement *et al.*, 2017).

[7] Available at www.sentinel.esa.int/web/sentinel/user-guides/sentinel-1-sar (accessed 12 December 2018)

1.8 Research questions

This research project investigated a number of application where EO data and geocomputational techniques could be used for better understanding of field drainage on Irish grassland farms, for example through the identification of artificially-drained areas, or in potential pathways for drainage at field level. The key research questions underlying this projects were:

1.8.1 Research Question 1

There is no efficient method of mapping the extent and distribution of artificially drained soils on Irish farms. Using advanced machine learning image classification algorithms (support vector machine and random forest), is it possible to distinguish artificially-drained fields on naturally-poorly drained soils using moderate spatial resolution Landsat 8 imagery? A thematic map of artificially drained soils is presented along with an accuracy assessment using expert interpretation of high resolution orthomosaic RGB imagery, and a legacy dataset of field observations from 2005.

1.8.2 Research Question 2

It has been demonstrated in the introduction that wet soils have a negative impact on spring grass yield. How does this look within visible and NIR EO imagery? Are there contrasting reflectance signals for grass growing under poorly-drained or drained conditions? If there is a measurable difference, what are the important Landsat 8 bands for characterising this difference? The important wavelengths for characterising drained- and poorly-drained conditions are derived from random forest estimates of variable importance.

1.8.3 Research Question 3

After establishing whether there is a difference in reflectance properties for drained and poorly-drained conditions, is it possible to observe improvements over time relating to drainage status? For example, can improvements in grass yields following prolonged saturation (flooding), or following the installation of an artificial drainage system be mapped? Improved drainage status (following flooding or drain installation) is inferred from temporal changes in Landsat 8 NDVI values. At field level, statistical analysis of mean NDVI values before and after drainage is used to illustrate improvement in grass production.

1.8.4 Research Question 4

Previous research questions have focused on satellite EO data at moderate spatial resolution. What role do UAS have in high spatial (and temporal) resolution mapping of surface and subsurface drainage pathways? Specifically, can UAS-derived photogrammetric surface models substitute for LiDAR elevation models when modelling nutrient losses in overland flow in a managed grassland environment? Photogrammetric and LiDAR topographical point clouds and topographic models are statistically compared. Also, can UAS thermal cameras identify heat anomalies at the surface that relate to subsurface drainage systems in a managed grassland environment? Thermometer-measured soil temperatures are compared with thermal camera measurements of canopy temperatures in relation to a buried drainage system.

These research questions are addressed in subsequent chapters and discussed collectively in Chapter 7. The following chapter identifies several studies internationally where EO data has been used explicitly to map drainage status under different environmental and land cover conditions. Other forms of remotely sensed data have been used to map drainage, for example using topographical models or geophysical data. The following chapter outlines these previous projects and discusses which approaches could have a role in mapping artifical drainage under Irish conditions.

Chapter 2 Literature Review

2.1. Mapping drainage class

2.1.1 EO-based methods

Since the 1990's, several studies have demonstrated a general relationship between soil drainage class and satellite-derived VI under different land cover. These studies have, until recently, had limited geographical distribution, largely focused on North America and Canada, where the primary focus was mapping tile-drained cropland to understand surface water pollution. This situation is changing slowly, with an increasing number of studies now emerging from Western Europe.

Using a single AVIRIS NDVI image (20 m resolution) and digital topographical data (elevation, slope, aspect and flow accumulation), Cialella *et al.* (1997) used classification tree analysis to classify soil drainage over a 2400 ha boreal forest. The overall accuracy of 81% was achieved against field verified observations of drainage classes ("very poor", "poor", "moderately well", "well" and "excessive"). High prediction accuracy was found in each drainage class (61%, 91%, 86%, 77%, 100% respectively). Local topographic position had the most substantial influence on drainage class, followed by NDVI (Cialella *et al*., 1997).

Campling *et al.* (2002) used logistic models to predict drainage probability class in a ~ 59,000 ha humid tropical region using a combination of soil samples, DEM and Landsat 5 imagery. Under mixed land cover, six drainage classes were identified between "excessively drained" to "very poorly drained". The results showed that DEM and VI provided complementary

information for developing statistical models to map and predict soil drainage classes. VI were among the most critical variables for classification purposes. The greatest success was for distinguishing extreme classes, for example, wet versus dry soils (99%), with less success in distinguishing neighbouring classes (Campling *et al.*, 2002).

Peng *et al.* (2003) used a combination of aerial photography, moderate- and high-spatial resolution EO satellite imagery (Landsat 7 TM and IKONOS) and a DEM to determine soil drainage classes on bare soils. Overall classification accuracy compared to field-verified samples was 73% (Peng *et al*., 2003). This method outperformed a published soil survey (1:15,840 scale) which had an accuracy of 55% compared with field-verified samples.

Niang *et al.* (2012) used discriminant analysis classification (DAC) and decision tree classifiers (DTC) to map soil drainage at a watershed scale using a fusion of optical (15 m resolution ASTER imagery) and microwave imagery (12.5 m spatial resolution RADARSAT-1 imagery). Accuracy of the models varied by algorithm choice and land use. Best overall accuracy was 40% for DAC and 65% for DTC. Bare or sparsely vegetated soils had the highest classification accuracies. Accuracy was reduced on densely vegetated soils. For pasture, for highest accuracy achieved was 56% was for the well-drained class (Niang *et al*., 2012).

Liu *et al*. (2008) mapped three drainage classes under bare soil conditions based on *in-situ* soil observations, topographic variables, apparent soil electrical conductivity, aerial hyperspectral imagery and airborne C-band SAR imagery. Using stepwise discriminant

analysis, they achieved overall accuracy of 68% using hyperspectral data. There was no improvement to classification accuracy by integrating either the SAR or DEM data (Liu *et al*., 2008).

Kiliç (2009) mapped soil drainage classes in the Amik Plain in Turkey using Landsat 7 ETM imagery, topographical data and VI. A maximum likelihood classification found that 51% of soils in the plain were well- or moderately well-drained, with 49% somewhat-, poorly- or very poorly drained (Kiliç, 2009).

In a German study, Tetzlaff *et al.* (2009) used black & white aerial imagery to identify buried drains under heterogeneous soil-, land cover- and management conditions. Phenological stage of overlying vegetation was an essential variable for drain identification. Spring images, in particular, were optimal for identifying drains in cereals and grassland (Tetzlaff, Kuhr, Vereecken, *et al*., 2009).

Kidd *et al.* (2014) modelled drainage class over a 70,000 ha study area in Tasmania using DEM- and remotely-sensed data to predict soil drainage class using decision tree spatial modelling, regression-tree spatial modelling and random-forest with residual-kriging. The regression tree method performed best, aligning well with normal landscape drainage patterns, known soil profile classes, and visual field indicators (Kidd *et al.*, 2014).

Tlapáková *et al.* (2017) reported spring imagery was important for recognising artifical drainage beneath pasture. They stressed the importance of multitemporal imagery for minimising error accruing from land management (for example, treading or overgrazing by livestock). They also found *a priori* knowledge of antecedent SM condition was helpful (Tlapáková *et al*., 2017).

Gokkaya *et al.* (2017) used DTC and satellite image differencing (Landsat 8 SWIR bands) to determine tile drainage area across an agricultural watershed. They estimated 79% of the cultivated area was tile-drained, with 94% overall classification accuracy (Gökkaya *et al.*, 2017).

Møller *et al.* (2017) employed boosted and bagged DTC to predict drainage class at national scale in Denmark. Decision trees were trained from >1000 field observations of soil drainage classes, with 31 predictor variables, including topographic variables, soil and geological data, land use/ land cover maps and a selection of Landsat 8 VI, including NDVI and NDWI. Both methods performed similarly (81% overall accuracy). In this case, the satellite VI were amongst the least important predictor variables for both models (Beucher *et al*., 2017; Møller *et al*., 2017). Subsequently, Møller *et al*. (2018) used an ensemble of machine learning models to map the extent of artificially drained areas in Denmark based on field observations and 46 covariate layers, including satellite imagery. The most critical covariates for predicting artificially-drained areas were related to soil properties and topography. Artificially-drained areas were identified with an accuracy of 76 % (Møller *et al*., 2018).

Postgraduate research in the Midwest USA has investigated the mapping subsurface drainage systems on farmland using panchromatic and VNIR imagery (B. S. Naz *et al*., 2009; B.S. Naz & Bowling, 2008; Roy, 2013; Thompson, 2010). The technique was established in an earlier NASA technical memorandum (Goettelman *et al.*, 1983) and subsequently developed by Verma and others (B.S. Naz & Bowling, 2008; Verma *et al*., 1996). For a fully saturated bare field, for example, following rainfall or irrigation, strips of dry soil appear first over drainage lines and widen gradually until the entire field surface is dry. Drying patterns are influenced by drain spacing, and whether or not drains are functioning properly. Although a popular method, it has been criticised for poor predictive ability, especially in the presence of crop residues (B. S. Naz *et al*., 2009). Where the surface is obscured by a crop, anomalous drainage patterns may manifest as poor crop growth or high canopy temperatures. The technique have been used to map drain lines in order to parameterise hydrological models to better understand the hydrology of agricultural catchments (Northcott *et al.*, 2000).

2.1.2 Topographic methods

Several studies have classified soil drainage using only topographic, soil- or land cover data without integrating satellite imagery. Bell *et al.* (1994) mapped three drainage classes at a regional scale using soil observations, geological maps and topographic variables. The study achieved an accuracy of 74%, which exceeded the accuracy of a conventional, published soil survey (Bell *et al.*, 1994). Kravchenko *et al.* (2002) distinguished three drainage classes at field-scale based on soil observations; terrain attributes and soil electrical conductivity. Discriminant analysis and co-kriging provided the most accurate results (90%) (Kravchenko *et al.*, 2002). Finally, Zhao *et al.* (2013) developed an artificial neural network (ANN) model for

soil drainage classification using *in-situ* soil profiles and topographic attributes. They found 52% of predicted drainage classes were identical to field observations while 94% of model-predicted drainage classes were within one class (Zhao *et al.*, 2013).

2.1.3 Geophysical methods

Drain installation involves the excavation and mixing of soil strata. These mixed soils have different geophysical properties that then appear anomalous against the natural soil background and may be detectable using geophysical methods of RS. Subsurface drainage systems have been identified using land-based geophysical techniques, in particular, magnetometry and ground penetrating radar (GPR). Magnetometry measures changes in ambient magnetic fields caused by contrasts in the magnetism of soil (Gibson & George, 2004). These changes are a often proportional to iron content, usually in its ferrous form (hematite (Fe^2O^3) or magnetite (Fe^3O^4)). Variation in soil type and management strategies can produce different magnetic signatures. The excavation of soil for a drain has the potential to produce a magnetic anomaly, as will the accumulation of iron in and around a drain pipe (Rogers *et al.*, 2005). Moreover, if ceramic pipes are present, they will have their own magnetic field (a legacy of its firing). Plastic pipes will not have a magnetic field. Magnetometers have been used for drainage mapping, but the practice is still far from standard (Rogers *et al.*, 2006; Rogers *et al*., 2005; Ruedisili & Logan, 1978). Rogers *et al.* (2005) used this technique to identify clay tile drains (22 cm diameter) at a depth of 1 m but reported that variability in soil magnetic properties could limit detection ability.

GPR transmit short pulses of high frequency EM energy (10-2500 MHz) into the ground. As waves encounter an interface between different materials (layers or objects) some transmitted energy is reflected back to the sensor. The propagation speed of the EM wave depends upon dielectric constant of the medium, which as was previously discussed is predominantly influenced by the volume of SM present. GPR data require significant processing and expert interpretation, but it has demonstrated its ability identify buried drainage channels under varying field conditions (Allred, 2013; Allred *et al.*, 2004; Allred & Redman, 2010). These papers reported overall efficiency of 81% in locating both clay and plastic drains up to 1 m deep on different textured soils, and under different SM regimes.

Both magnetometers and GPR have been successfully mounted on UAS for increased mobility over large areas. These pilot schemes have not been widely reported however. There are issues with each method for mapping the shallow subsurface. Both sensors would have to be flown quite close to the surface, increasing flight time. Flying close to the surface would require very accurate terrain models for autonomous flight planning. Also, GPR experiences a strong bounce effect as the pulse enters and leaves the ground, the further the antenna is from the surface, the higher the noise from this double impact is, thereby obscuring or hiding reflected signals from shallow subsurface features. While suitable for deeper investigations, UAV GPR is unsuited to agricultural drainage mapping. This is a dynamic area of research, however, and further developments are likely in the coming years.

2.2 Conclusions

Ireland does not currently account for its drainage infrastructure. There is no archive of the location of “legacy” drain works. Neither is there a requirement to report current drainage works below a certain threshold. There is increasing awareness internationally of the need to locate artificially drained areas to improve our understanding of potential environmental impacts, for example, from nutrient transport to surface- and groundwater, or in tackling GHG emissions. EO-based methods are the only practical way to map soil drainage properties between catchment and national scale. These have reported high overall accuracy using Landsat imagery (~30 m spatial resolution). The review of published literature has highlighted the various pros and cons associated witth EO mapping of drainage status.

The techniques used are well-established, largely borrowed from SM mapping and monitoring. The review identified a number of methods that could potentially be applied to mapping artificial drainage in Ireland. For example, previous projects have used Landsat data extensively. Landsat data is free, can be used to map in-field conditions (compared to MODIS, for example) and has a decades-old archive from which to source suitable data. It was clear from previous projects that mapping at certain times of the season can help identify drainage patterns. Previous research acknowledged an improvement in map classification accuracy by using springtime images, where contrasting drainage class or buried drainage features can be more readily distinguished (Tlapáková *et al*., 2017). Previous studies had made extensive use of topographical data, in some cases separately but frequently in combination with other datasets. Topography is closely related to SM within the study area, with increasing soil wetness a factor of elevation height and slope aspect. The inclusion of such data could be

expected to increase map accuracy. It was also clear how the number of drainage classes that are defined using RS or EO drainage classifications often do not match the number of classes that could be defined from a traditional soil classification. The number of classes for remotely sensed studies were generally lower, and more likely to distinguish extreme classes. Intermediate classes were less likely to be distinguished with any certainty. In several studies, aggregating intermediate classes had a positive effect on overall accuracy. The reasons for this were clear, *in-situ* surveys take into account a number of different factors that are not available to remote sensors (soil profiles and morphological characteristics, for example). A reflectance-only approach, while cost-effective, could not hope to classify soil drainage to the same degree of accuracy as field-based surveys. Nevertheless, several studies described indicated that EO-based surveys were as accurate, or more accurate, than existing published soil surveys in some regions.

2.3 Thesis structure

The results of previous drainage mapping studies have formed the basis for the approach adopted in this thesis and outlined in subsequent chapters. In the following chapters, methodologies, results and discussions are presented for EO mapping drainage status in a predominantly managed grassland environment. The format for the remainder of the thesis is outlined below.

Chapter 3 examines the effect of soil saturation on grassland production following prolonged saturation following extensive winter flooding in 2015-2016. Flood maps are created using a 6 month archive of Sentinel 1 C-band SAR images to map the extent of saturated soils across

the country. Knowing the location of flooded soils, it is possible to observe the recovery of grassland as flood waters recede and soils drain. For the first stime, the long-term impact of floods and prolonged soil saturation is illustrated using EO imagery, showing a persistant impact on grass growth lasting several months.

Chapter 4 descibes the results of a machine-learning image classification of artificial drainage on heavy grassland soils in the BMW region of the Republic of Ireland. This chapter further explores some of the findings from Chapter 3, where the visisble and infrared reflectance signal for prolonged saturation are used to classify naturally poorly-drained soils into “drained” and “undrained” classes. Two machine learning algorithms, Support Vector Machine (SVM) and Random Forest (RF) algorithms are tested. Changes in drainage status over time were identified at one location where following artificial drainage had been installed.

Chapter 5 is the first of two chapters examining potential applications for UAS in mapping drainage pathways on Irish farms. Consumer-grade UAS with built-in RGB cameras are currently extremely popular in research and industrial appications for high spatial resolution 3D surface modelling. This chapter presents a performance assessment of UAS photogrammetry for creating digital surface models (DSM) that might substitute for aerial LiDAR digital elevation models (DEM). Photogrammetric DSM and LiDAR DEM are compared using regression analysis. The spatial resolution at which models are most comparable are identified. Potential sources of error are discussed.

Chapter 6 continues with potential UAS applications on Irish farms. A UAS-mounted thermal infrared (TIR) camera is used to identify subsurface drainage channels or artifically drained locations based on surface temperature anomalies. Two field experiments are outlined. An initial saturation test on a 5 m x 5 m grassed plot investigated how soil temperature (upper 10 cm) and TIR canopy temperature readings responded to increasing soil saturation. A subsequent field test used a UAS-mounted TIR camera to map an artificial drainage system installed on a sports pitch. The accuracy of the method is discussed and future work in this area is proposed.

This page is intentionally blank

Chapter 3 Mapping the extent and duration of soil saturation following winter floods and its effect on grass growth

3.1 Introduction

3.1.1 Background

In winter 2015-2016, a series of devastating storms brought extensive and persistent flooding to many areas of the the British Isles (Figure 3-1). In Ireland, the volume of seasonal rainfall brought Storms Desmond, Eva and Frank during December 2015 was unprecedented. Half of synoptic precipitation stations nationally reported their wettest winter on record, while some stations in the South and Midlands experienced >350% their long-term average precipitation for the season (Met Éireann, 2016). Nearly 50% of river gauges operated by the Office of Public Works (OPW) reported their highest-ever heights (NDFEM, 2016). The heavy rains resulted in extensive pluvial flooding beyond traditional floodplains and saw widespread devastation and prolonged disruption within rural communities. In the context of this reserach, these floods presented an opportunity to observe the impact of prolonged and widespread soil saturation on grass production in the following spring (2016). By first mapping flood extent and duration, it would then be possible to monitor the recovery from saturation on formerly flooded fields.

Figure 3-1 Flooded farmland in County Galway in January 2016. Source: Irish Times. 7 January 2018.

3.1.2 Objectives

The objective of this study was to observe the recovery of grass growth on flooded pasture using multi-temporal Landsat 8 NDVI imagery. To achieve this, Sentinel 1 SAR images were initially required to map flooded areas as well as to identify areas of persistent flooding. Recovery was observed in mean Landsat 8 NDVI images from May, June and July 2016. To assess the accuracy of the SAR flood map an existing flood map from Copernicus EMS map was ussed. Similarity between the produced thematic maps were assessed using an error matrix, following the method outlined in Congalton (1991). Reports of flooded farms from Teagasc advisors were also available. A comparative flood map was also made using Sentinel 2 imagery. There was no data to validate the recovery datam although the findings could be corroborated by findings in previous research which suggested significant reduction

in spring yield following saturatied conditions (Section 1.3). Additional information and discussion on flood depth and flood volume are included in Appendix F.

3.2 Materials and Methods

3.2.1 Data collection

3.2.1.1 Sentinel 1

Floods were mapped using images from Sentinel 1A C-band SAR mission. Thirty-three Sentinel 1A Level-1 Ground Range Detected images were downloaded from Copernicus Open Access Hub (previously known as Sentinels Scientific Data Hub, or SciHub)[8]. A complete list of scenes used are presented in Appendix A. Images were acquired every 12 days from 19 November 2015 until 23 February 2016, and twice after that on 30 March and 11 April. The scenes provided almost nationwide coverage. Two narrow strips of land on the east and west coasts lay outside the image swaths and were omitted to reduce processing time. Images are available for these areas, however, the tract of land excluded was relatively small and predominantly coastal or mountainous in nature (see red areas in Figure 3-2).

[8] https://scihub.copernicus.eu. Accessed 12 December 2018.

3.2.1.2 Sentinel 2

A Sentinel 2A multispectral image from 21 December 2015 (cloud cover <3%) was downloaded as a Level 2A surface reflectance product from Copernicus Open Access Hub. This was used to create a flood map for a region of interest south of Athlone, Co. Westmeath using a normalised difference water index (NDWI) (McFeeters, 1996) (Equation 3.1). This index uses green and NIR bands (unlike the NDWI described in Equation 2.3) to delineate open water features.

$$NDWI = \frac{NIR - Green}{NIR + Green} \quad \text{(Eqn. 3.1)}$$

where Green and NIR are surface reflectance bands measured by a multispectral camera.

The United Nations Space-based Information for Disaster Management and Emergency Response (UN-SPIDER) has also released an NDWI-based methodology for using Sentinel 2 flood mapping that is suitable to regions with low cloud cover[9].

Data specifications for both Sentinel missions are provided in Table 3-1 below.

[9] http://www.un-spider.org/advisory-support/recommended-practices/flood-mapping-and-damage-assessment-using-s2-data/ (accessed 2 December 2018).

Table 3-1 Data specifications for the Sentinel satellites used in the study.

	Sentinel 1A	**Sentinel 2A**
Frequency/ wavelength	C-band (5.4 GHz)	0.443 – 2.150 µm (VIS – SWIR)
Orbit	693 km (sun-synchronous)	786 km (sun-synchronous)
Interval	12 days (6 with full constellation)	10 days (5 with full constellation)
Acquisition dates	19 Nov. 2015 1, 13, 25 Dec. 2015 6, 18, 30 Jan. 2016 11, 23 Feb. 2016 30 Mar. 2016 11 Apr. 2016	21 Dec. 2015
Mode	Interferometric Wide Swath	Multispectral Imager
Swath width	250 km	290 km
Product	Level-1 Ground Range Detected	Level-2A Surface Reflectance
Spatial resolution	10 m	10 - 20 m
Polarisation	VV+VH	n/a
% cloud cover	n/a	3%

3.2.1.3 Landsat 8

Sixteen Landsat 8 scenes were downloaded as Level 1C top-of-atmosphere (TOA) images from the United States Geological Service (USGS) Earth Explorer website[10]. These were converted to surface reflectance using the LEDAPS algorithm (Schmidt *et al.*, 2013) and cloud and cloud shadow masked using the F-mask algorithm (Zhu *et al.*, 2015). Scenes focused on the Midlands and Western region where flooding was widespread, particularly in the Shannon catchment. The mosaic was used to monitor grass recovery on flooded areas during 2016. A second mosaic was created for 2015 (using 19 mosaicked scenes) to allow comparison with a non-flood year. The complete list of Landsat 8 scenes are presented in Appendix D.

[10] https://earthexplorer.usgs.gov. Accessed 12 December 2018.

3.2.1.4 Additional datasets

Several other datasets were necessary to complete this study.

A mask for existing rivers, streams and lakes was created from PRIME 2 data from Ordnance Survey Ireland (OSI). Vector data were rasterised in ArcGIS (v.10.2.2) by first densifying the polyline vertices (Densify function, Editing toolset), then converting points (Feature Vertices to Point function, Feature toolset) and finally rasterised (Point to Raster function, Conversion toolset).

A mask for ~128 turlough areas was created from an existing dataset (Johnston, nd). Turloughs are seasonally flooded wetlands found in regions with limestone geology. Due to their often extensive nature and a lack of agreement on how to define their extent spatially, compiling an accurate mask was a challenge. The existing dataset had sparse spatial data, comprising only of a single point reference. At the time of writing (2018), Geological Survey Ireland (GSI) were engaged in a nationwide mapping project of turloughs using Sentinel 1 images (T. McCormack, 2018, personal communication, 21 November).

Land cover data was taken from 1:100,000 CORINE 2012 Land Cover database (EPA, 2012). CORINE is criticised for its poor ability to accurately map the fragmented landscapes common to Ireland (Cawkwell *et al.*, 2017), but was the only land cover dataset available (Ordnance Survey Ireland (OSI) are currently engaged in a producing a national land cover map; C. Bruton, 2018, personal communication, 21 November 2018). Soil and subsoil information was provided by the 1:50,000 Teagasc Soils and Subsoils map (Fealy *et al.*, 2009).

3.2.2 Sentinel 1A flood mapping procedure

3.2.2.1 Workflow

The SAR flood map was created following a recommended practice published by UN-SPIDER (UN-SPIDER, 2016). The workflow presented by UN-SPIDER was chosen because it would be easily reproducible by researchers. The study did not set out to explore possible improvements on this workflow by varying parameterisation.

The workflow was executed with ESA's Sentinel Application Platform, SNAP (v. 4.0), following a step-by-step procedure of calibration, filtering, masking and rectification. Additional processing and visualisation was carried out in ArcGIS. SAR images were initially calibrated as VV polarised σ° images in decibels (dB). RADAR speckle (inherent random noise caused by different scattering surfaces within a pixel) was removed using a Lee-Sigma filter (Lee, 1983). This smoothing filter assumes noise follows a Gaussian distribution and replaces central pixels within a 7 x 7-pixel moving window with the average of all values within the window that fall within two standard deviations of the mean. A large pixel window was selected to better establish local mean backscatter values. Additonal experimentation with filter type was not explored in this study, but different choices of filter and window size would have had an impact on the threshold values used to determine flooded areas.

Histogram thresholding to determine low backscatter values allowed a binary segmentation of each SAR scene into a "water" class and a complement "non-water" class. Threshold backscatter values can be determined manually or algorithmically (Otsu, 1979; Sahoo *et al*., 1988), for the current study mean threshold values were defined manually for each of the 33

scenes by comnputing a mean backscatter value within a 30 m buffer from centre points in lakes present in each scene. The assumption was these areas would be most representative of a flat water surface, unroughened by waves or emergent vegetation (this approach assumed calm water conditions at the time of capture). The threshold approach is straightforward and simple to implement, but a single backscatter value may not represent a range of backscatter values that characterise flat water within a scene, for example, where water surfaces are slightly roughened by currents, emerging vegetation or wind. Other methods have been proposed that use change detection (Brivio *et al*., 2002; Clement *et al*., 2017; Long *et al*., 2014; Martinis *et al*., 2011; Y. Wang, 2002), clustering (Horritt, 1999; Mason *et al*., 2012) or a combination of these techniques (Martinis *et al*., 2009; Matgen *et al*., 2011). Optimised thresholding methods using artificial neural network or support vector machine algorithms have been proposed (Insom *et al*., 2015; Kussul *et al*., 2008). Further experimentation with thresholding techniques was not explored further in this study, but it is acknowledged that choice of a thresholding technique will have had an impact on the definition of flood and non-flood areas particularly at flood boundaries with land.

The final step was to transform SAR images to a projected coordinate reference system (Irish Transverse Mercator). This was done within SNAP using inherent ground control references and NASA's Shuttle RADAR Topography Mission (SRTM) Global 3 arc-second DEM. Individual scenes were mosaicked into a single image for each acquisition date using the Mosaic to New Raster tool in ArcGIS.

3.2.2.1 Noise removal

Low backscatter values not associated with flooding were a potential source of error. The principal sources of this noise were topographic shadow (low backscatter values caused by terrain sloping in the opposite direction of SAR pulse), estuaries and beaches (which appeared as water or not depending on tidal regime) and flat constructed surfaces (car parks, flat roofs, airport runways etc.). Processing-related anomalies, for example, banding along swath edges and between merged scenes were also removed.

Low backscatter noise was reduced by using a processed SAR image from a summer month (July 2015) to create a mask of normally-occurring low backscatter regions. Additionally, slope rasters created from the DEM to mask out gradients > 5º which may cause shadow effects. Single pixel flood areas (100 m^2, or 0.01 ha) were masked, as were pixels classed as flooded only once. This reduced potential misclassification errors arising from initial processing. Flood area for each acquisition date was calculated as the summed area of remaining pixels. To account for a ~7 m positional inaccuracy (< 1 pixel) in Sentinel 1 registration (Bourbigot *et al.*, 2016), raster flood boundaries were expanded and trimmed by one pixel width (10 m) in ArcGIS (Nibble and Expand functions, Generalisation toolset) to provide an estimate of minimum and maximum flood extent.

3.3 Results

3.3.1 Flood extent

The final flood map is illustrated in Figure 3-2 below[11]. After processing, the maximum area flooded during winter 2015/16 was estimated to be 24,356 ha. This was greater than the combined surface area of two of the largest lakes on the River Shannon, Loughs Ree and Derg (with a combined area of 22,300 ha). The minimum and maximum extents estimated following processing were 16,155 ha and 32,957 ha respectively. Estimates of flood extent for each of the eleven acquisition dates are presented in Table 3-2 below. Persistent flooding was identified on ~ 3000 ha nationally, where floods at a specific pixel location on 8 or more occasions between November 2015 and April 2016. Approximately 70 ha were flooded for the entire period of the study (Table 3-3). Individual flooded regions ranged from a minimum of 0.02 ha to a maximum of 846 ha. The worst affected counties all bordered the River Shannon, with over half the flooded area (~12,500 ha) occurring in Cos. Galway, Mayo and Roscommon. The peak flood event of the season occurred on 13 December with a flood of 19,950 ha, the first acquisition date immediately following Storm Desmond. A second peak event occurred on 11 February following Storm Imogen reached 19,360 ha.

[11] The image has been publicly available to download via the ArcGIS Online portal since 2017 (www.esri.com).

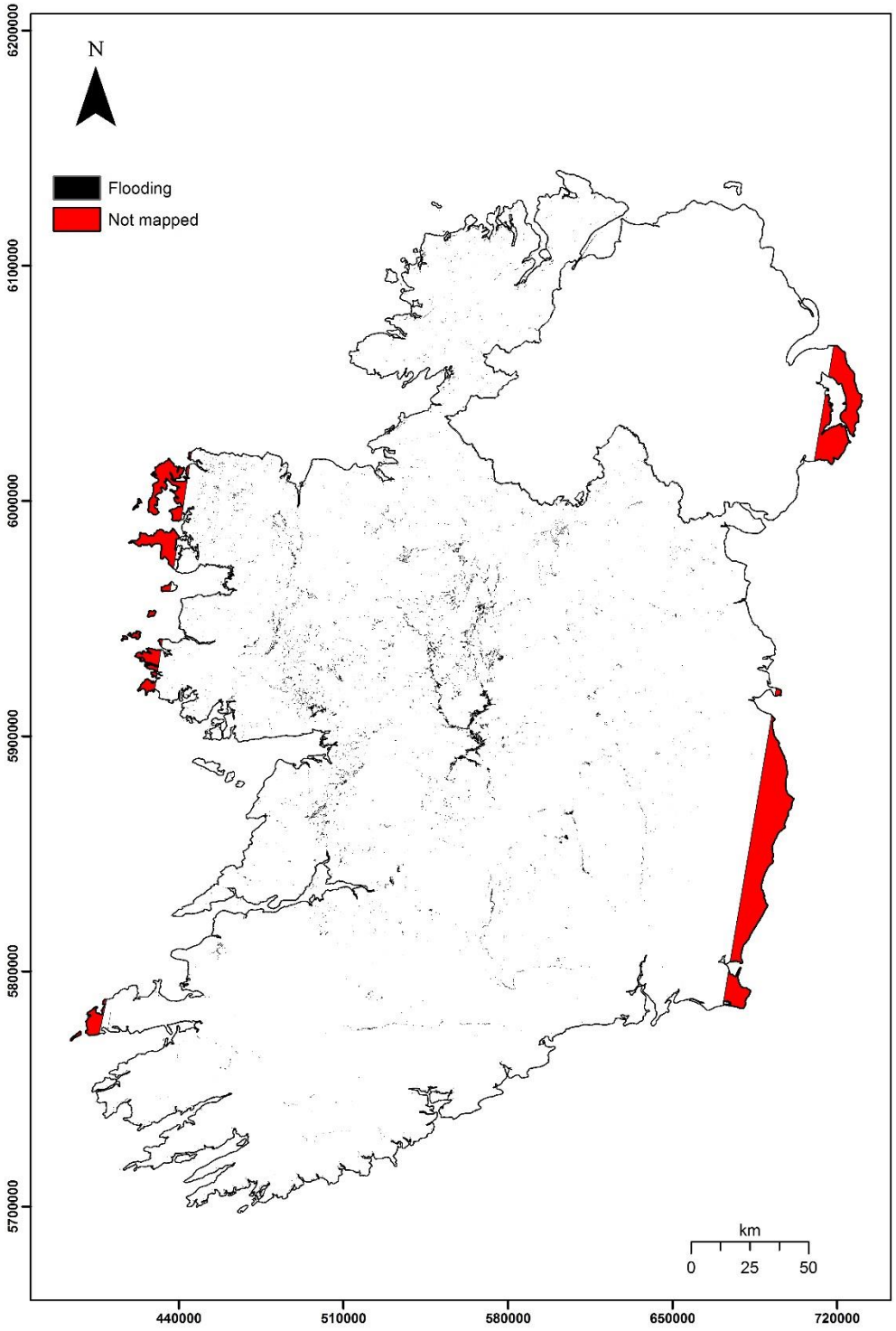

Figure 3-2 Extent of flood waters for the Republic of Ireland based on processed Sentinel 1 SAR imagery acquired between November 2015 and April 2016. (CRS: Irish Transverse Mercator, ESPG: 2157).

Table 3-2 Estimated extent of flooding nationally on each acquisition date between November 2015 and April 2016.

Acquisition date	Area (ha)
19 November 2015	10,380
1 December 2015	10,780
13 December 2015	19,950
25 December 2015	17,720
6 January 2016	9,920
18 January 2016	9,575
30 January 2016	15,880
11 February 2016	19,360
23 February 2016	2,620
30 March 2016	2,500
11 April 2016	7,630

Table 3-3 Number of times a Sentinel 1A pixel was classified as flooded indicating the extent of persistent flooding nationally

No. times classed as flooded	Area (ha)
2	6,840
3	4,470
4	3,350
5	2,750
6	2,520
7	2,035
8	1,340
9	720
10	260
11	70

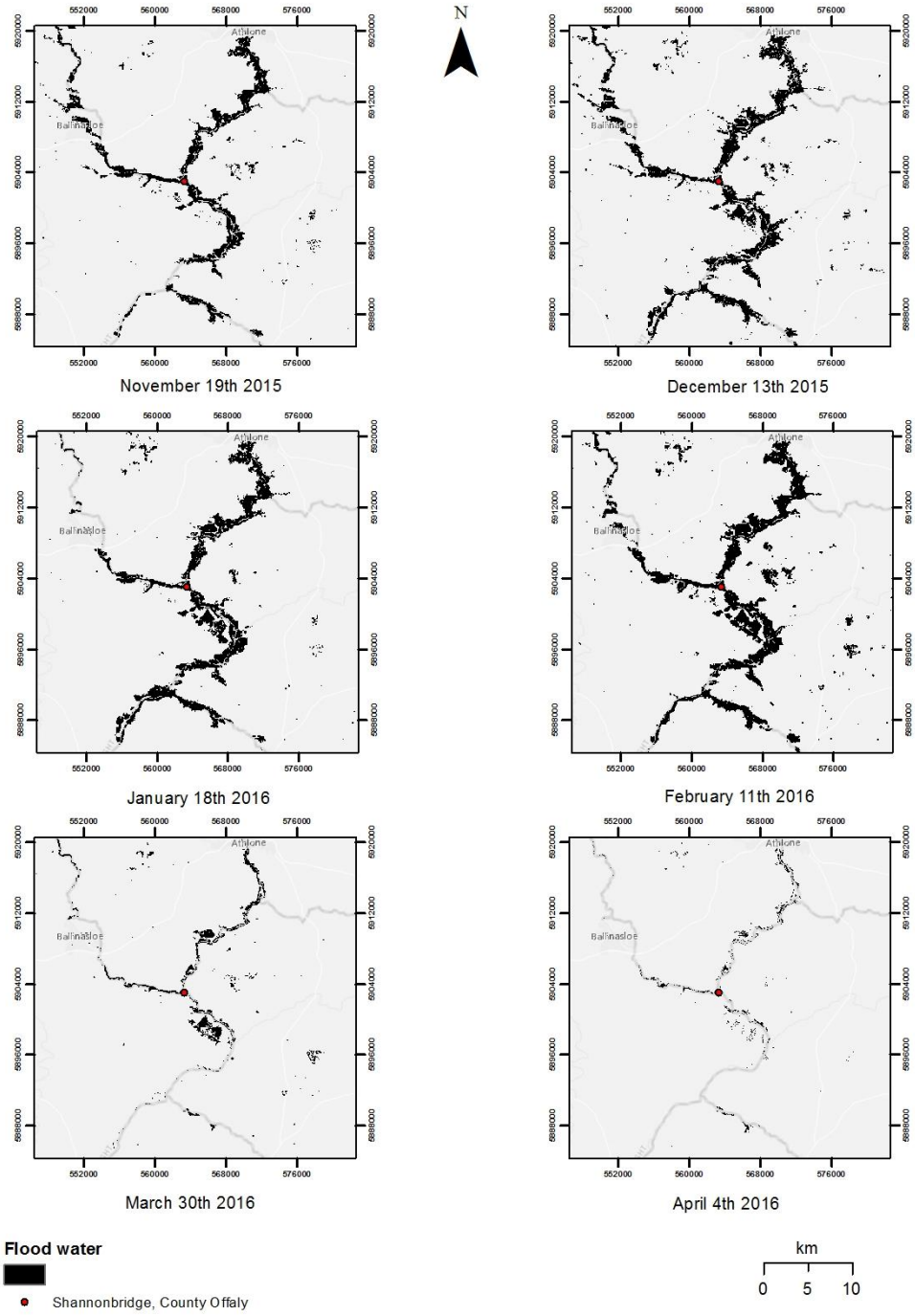

Figure 3-3 Extent of flooding at Shannonbridge, County Offaly. Already extensively flooded before the December storms, flood levels remained mostly unchanged until mid-February 2016 with small areas remaining flooded until April 2016.

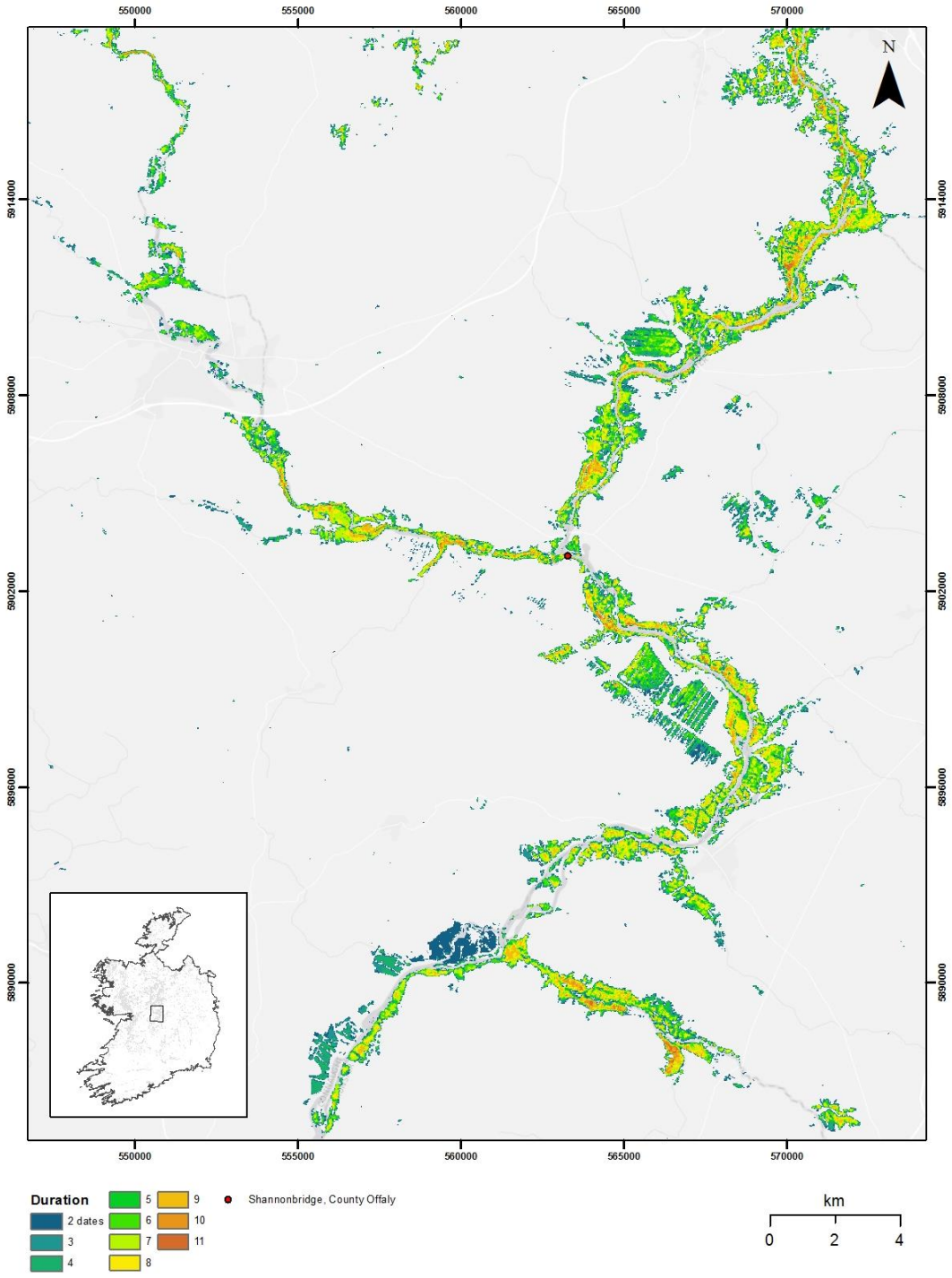

Figure 3-4 Persistence of flooding at Shannonbridge, Co. Offaly. Pixels are colour-coded by flood duration based on the presence of flooding in Sentinel 1A images. Eleven images were taken every 12 days. Classes represent the number of times individual pixels were classed as “water”.

The persistence of flooding over the study period is illustrated in Figure 3-3 for an region of interest around Shannonbridge, Co. Offaly. Located at the confluence of the River Shannon with the River Suck and River Brosna, flood levels in the Shannonbridge area remained largely unchanged from November 2015 until February 2016. Flood persistence is further illustrated in Figure 3-4 on a pixel-by-pixel basis, where pixels are coloured by the number of times it was classed as flooded. Given its location, much of the region depicted in Figure 3-4 was flooded between 6 and 9 times between November 2015 and April 2016. A small number of pixels in the scene were among those flooded for the entire duration of the study.

Flood extent showed a strong, positive correlation with total precipitation depth in the 5 days preceding the Sentinel 1 acquisition data (R^2= 0.51, p= 0.01) (Figure 3-5). This likely reflected the rapid expansion of flood waters on saturated soils or where rainfall fell onto existing flood areas, or through the development of ponding and runoff on saturated soils. An example of this may be seen following intense rain over a 24-hour period on 10-11 April (Met Éireann, 2016) where up to 58 mm was recorded in parts of the southwest, while stations in Dublin reported their wettest day in 50 years. The volume of rainfall resulted in a three-fold increase in flood area from 2,500 ha on 30 March to 7,600 ha flood on 11 April. In another example on the 13 February map, a period of flood contraction during January 2016 was reversed by persistent rain over several days. The result was a ~19,357 ha flood, only marginally smaller than the post-Storm Desmond maximum in mid-December.

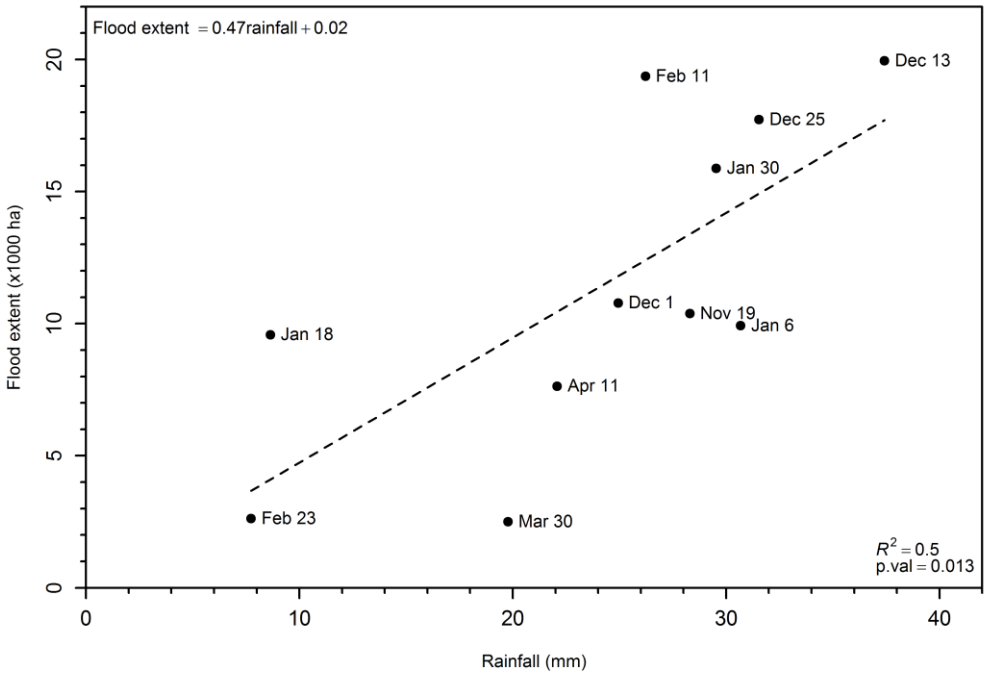

Figure 3-5 Simple linear regression showing the relationship between flood extent and rainfall depth in the previous five days measured for each Sentinel 1A acquisition date.

3.3.2 Validation

The flood map was validated against three independent sources:

- Farm reports of flood damage from individual farmers within the Shannon Catchment
- Sentinel 2 flood map over a specific area (Athlone, County Westmeath)
- Copernicus EMS flood map (EMSR149) over a specific area (Athlone, County Westmeath).

3.3.2.1 Farm reports

Reports of flooded farms to Teagasc advisors provided a direct means of validating the map. The locations of fifty-seven farms which reported flood damage was overlain on the Sentinel 1 map. Forty-nine of these farms (86%) intersected the flood boundary. As only flooded properties were reported it was not possible to measure Type 1 error (false positives), where flooding was predicted but did not occur. The average area flooded on these farms was ~3 ha, although for one farm the flood area was 176 ha. The majority of farms were on the banks of the River Shannon. Flooded farms in the Shannonbridge/Athlone area are illustrated in Figure 3-6.

3.3.2.2 Sentinel 2 flood map

The green shaded area in Figure 3-7 shows the flood extent mapped by Sentinel 2 on 21 December 2015. The blue shaded area is the flood extent mapped by Sentinel 1 four days later (25 December 2015). There was a 58% overlap of flood extent between both maps in this region of interest. The Sentinel 1 map showed a smaller area. The 4-day separation between data capture may explain some disparity in extent from changes in water levels over the period. Waxing and waning of flood waters would be expected at the edges of the floods as waters drain naturally between rain events, but other reasons are also possible. Weather stations during the Sentinel 1 overpass recorded 17 mm rainfall on the 25th December with wind speeds of ~4 ms^{-1} (gusting 11 ms$^{-1)}$. These conditions could have sufficiently roughened water surfaces to increase backscatter above defined threshold values resulting in the smaller flood area. There may also have been some roughening of waters from emergent vegetation near the flood boundaries. It is acknowledged that initial processing of SAR imagery to

remove pixels only flooded once will have reduced the area of the floods in some areas. This could explain the 42% difference in the extent of the SAR and NDWI flood maps on this date.

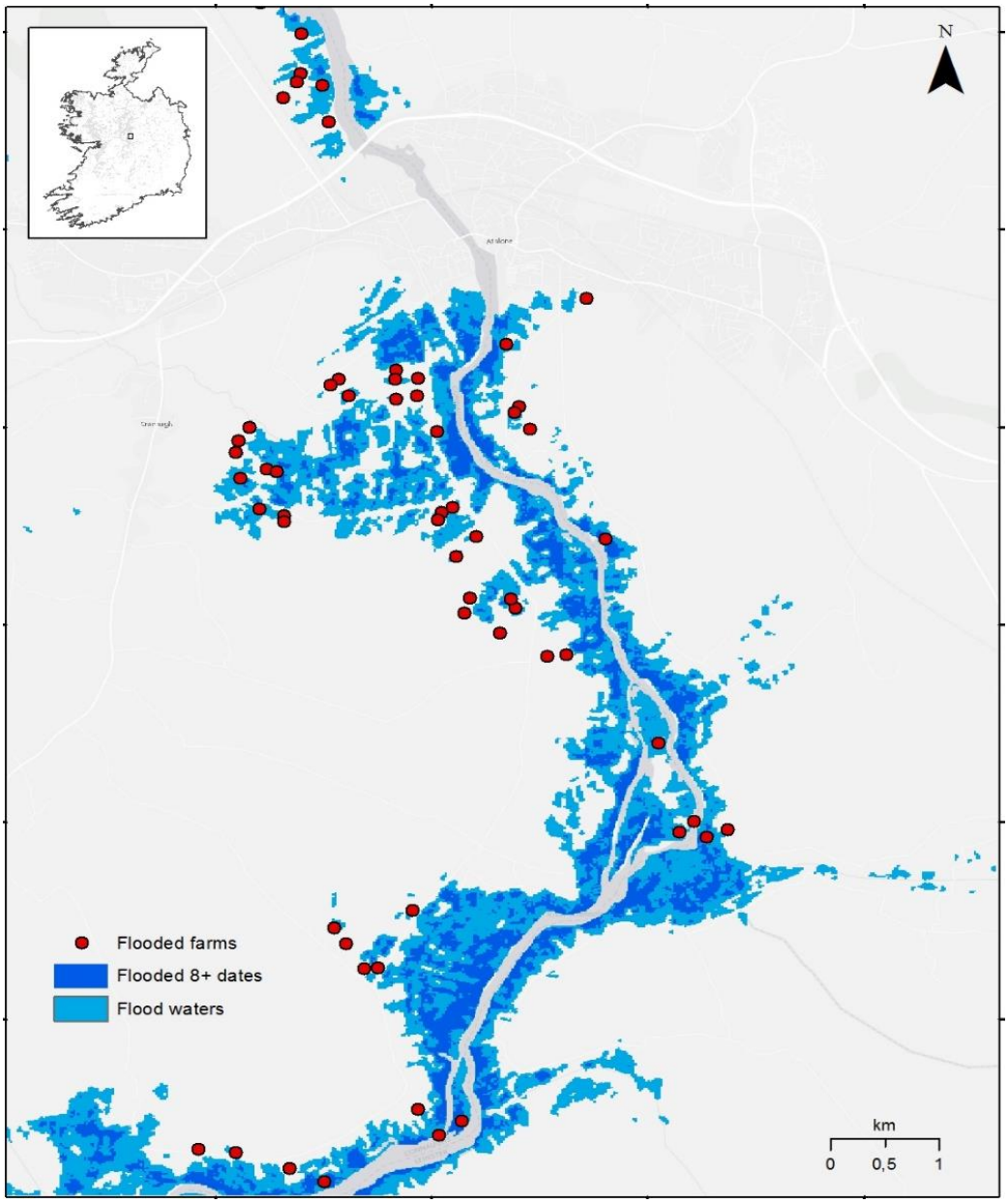

Figure 3-6 Location of farms reporting flood damage in the environs of Athlone, County Westmeath. Areas classed as flooded more than eight dates are coloured dark blue.

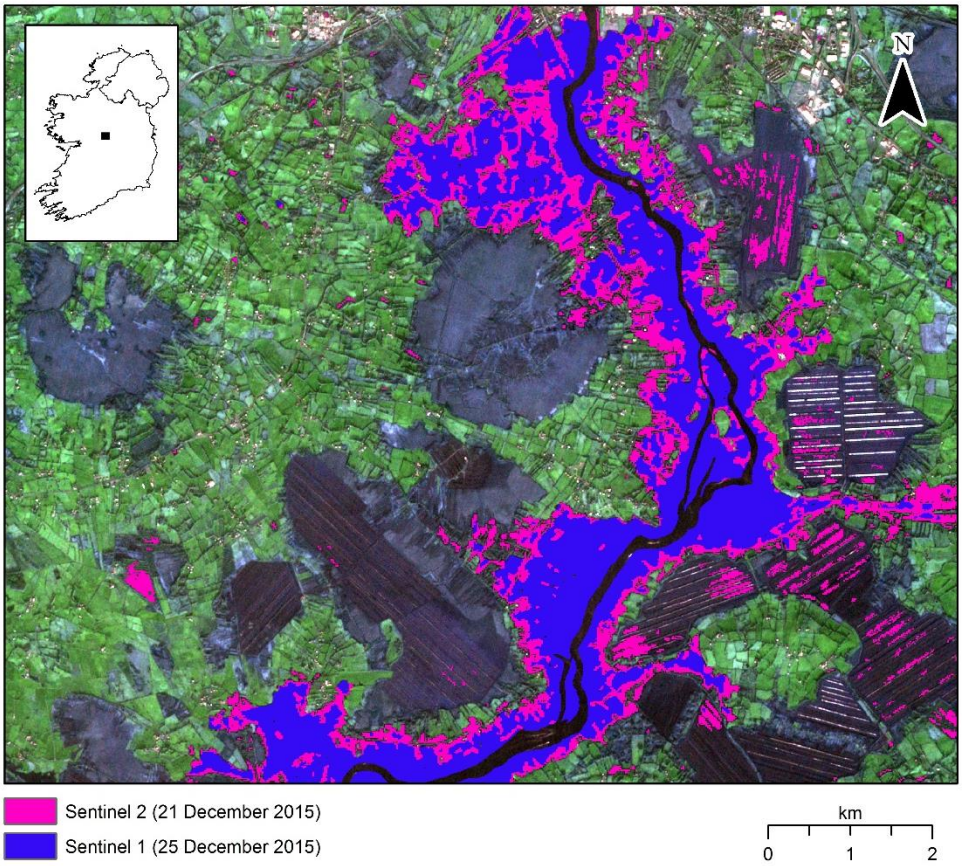

Figure 3-7 Comparison of Sentinel 1 and Sentinel 2 flood extents. Base mapping is Sentinel 2 true colour composite at 10 m spatial resolution.

3.3.2.3 Copernicus EMS map

The accuracy of the SAR flood map was assessed against a Copernicus EMS flood map from 13 December. The Copernicus EMS map was assumed to be the more accurate map as it was compiled from multiple sources with different wavelengths and polarisations. Accuracy assessment was based on 88 randomly sampled points that intersected the flood extent. In error matrices classification errors occurs when a pixel of one class is allocated to another. User accuracy reflects the accuracy of the product from the viewpoint of the user. It is a measure of how reliable the product is, and the likelihood a class will be present on the

ground. Producer accuracy describes how often actual classes are correctly classified. Against Copernicus, Sentinel 1 had producer accuracy of 68.5%, failing to identify flooding at 17 locations where Copernicus EMS had identified flooding. The disparity between the two sensors may be related to the temporal disparity in overpass dates, with actual differences in flood extent captured. It may also be due to the availability of different SAR sensors with differrent polarisations and processing workflows to create the Copernicus EMS map.

Table 3-4 Accuracy assessment of Sentinel 1 flood map versus Copernicus EMS.

	Sentinel 1 flood map				
Copernicus EMS		No Flood	Flood	Total	User Accuracy.
	No Flood	**37**	1	38	97.4%
	Flood	17	**33**	50	66.0%
	Total	54	34	88	
	Producer Accuracy.	68.5%	97.1%		Overall Accuracy 79.5%

From Table 3-4, Sentinel 1 showed good overall agreement to Copernicus (79.5%). Producer accuracy for flooded areas was also very high (97.1%). Lower user accuracy for flooded areas (66%) can perhaps be explained by the poorer ability of Sentinel 1 at resolving surface water where there is overlying canopy. Local meteorological conditions on 13 December were mild (3 mm rainfall, speed 4 ms^{-1} gusting 10 ms^{-1}) so an effect on backscatter coefficients from prevailing weather conditions are unlikely to be the reason for the difference in classification accuracy. Combining Sentinel 1 with Sentinel 2 improved overall classification (91%; Table 3-5).

Table 3-5 Accuracy assessment of combined Sentinel 1 & Sentinel 2 maps versus Copernicus EMS.

	Combined Sentinel 1 & 2 flood maps				
Copernicus EMS		No Flood	Flood	Total	User Accuracy
	No Flood	31	7	38	81.6%
	Flood	1	49	50	98.0%
	Total	32	56	88	
	Producer Accuracy	96.9%	87.5%		Overall Accuracy 91.0%

3.3.3 Impacted soils and land use

The Teagasc/ EPA Soils and Subsoils map was used to determine natural soil type. The majority of inundated soils were determined to be low-lying alluvial or lacustrine soils (8100 ha, or 33% of the total area). This was followed by reclaimed (or cut) organic soils (7000 ha, 28%) and "poorly-drained" mineral soils (1500 ha, 6%). Approximately 3000 ha (13%) of soils flooded were classified as 'well drained'. Using CORINE 2012 data, approximately 61% of the area flooded was deemed to be agricultural land, of which ~50% was pasture, and an additional 11% of areas principally dominated by agriculture but with significant natural vegetation also. Peats and inland marshes made up 23% of the total. The area of arable land and forestry affected was negligible (< 1% in each case). Urban areas (including sports facilities and industrial/transport-related land cover) constituted less than 2% of the inundated area. The remaining ~13% was made up of several categories of land cover, for example, marine and inland waterways, beaches or quarries (Table 3-6). While every effort was made to mask out existing water areas at an earlier stage, approximately 6% of the flooded area were waterbodies of one nature or another. The cause of this is very likely the disparity in spatial resolution between CORINE and the SAR flood map, in particular exact definition of shoreline is not exact. This would be true for each of the land cover classes listed in Table 3-6, where sub-pixel variation is not considered and where boundaries between adjoining

landcover classes are simplified. This could be rectified in future mapping projects by using higher resolution land cover maps currently being produced by OSI.

Table 3-6 Type of cover and area flooded using CORINE land cover Level 3 descriptions

CORINE Level 3 description	Code	Hectares	%
Continuous urban fabric	111	0.46	<0.1%
Discontinuous urban fabric	112	43.47	0.2%
Industrial or commercial units	121	33.1	0.1%
Road and rail networks	122	1	<0.1%
Ports	123	2.11	<0.1%
Airports	124	27.48	0.1%
Mineral extraction sites	131	101.2	0.4%
Dump sites	132	37.45	0.2%
Construction sites	133	0.22	<0.1%
Green urban areas	141	2.72	<0.1%
Sport and leisure facilities	142	329.79	1.4%
Non-irrigated arable land	211	201.39	0.8%
Fruit trees and berry plantations	222	0.27	<0.1%
Pasture	231	11,886.42	49.6%
Complex cultivation patterns	242	47.22	0.2%
Agriculture with areas of natural vegetation	243	2527.27	10.5%
Broad-leaved forests	311	92.36	0.4%
Coniferous forests	312	31.59	0.1%
Mixed forests	313	82.55	0.3%
Natural grasslands	321	271.88	1.1%
Moors and heathland	322	24.13	0.1%
Transitional woodland scrub	324	611.32	2.6%
Beaches, dunes and sands	331	248.89	1.0%
Bare rock	332	81.23	0.3%
Sparsely vegetated areas	333	126.21	0.5%
Inland marshes	411	3327.24	13.9%
Peat bogs	412	2144.14	8.9%
Salt marshes	421	156.37	0.7%
Intertidal flats	423	226.17	0.9%
Watercourses	511	315.79	1.3%
Water bodies	512	784.58	3.3%
Coastal lagoons	521	6.73	<0.1%
Estuaries	522	85.15	0.4%
Sea	523	99.78	0.4%

3.3.4 Physical damage to farms

Physical damage to farms as a result of flooding included loss of winter fodder supplies (hay and silage), drowned animals and damage to buildings and yards. Intersecting the SAR flood map with structural data included in the PRIME 2 dataset, 13 of 24 buildings (54%) identified within the flood extent were visually confirmed to be related to agricultural activities using high-resolution aerial imagery (ArcGIS base mapping). The remaining structures were identified rural domestic properties, river- or lakeside amenities (sheds or boat houses) or structures within sports or industrial facilities.

A lasting impact was the reduction in grass growth cuased by heavy rainfall and saturated soils. This is illustrated in Figure 3-8 below, where mean Landsat 8 NDVI imagery from Spring 2014-2016 were plotted against total spring rainfall for each Met Eireann station in the BMW region. Mean NDVI values were extracted from grassland within a 1 km zone surrounding each station. Using a polynomial regression model, a signifincat negative trend was observed for decreasing NDVI values with higher rainfall (and greater soil saturation). High variance in the model may be partially explained by error in landcover classification caused by the coarse resolution of the CORINE dataset for masking grass areas, as well as some effect from mixed landcover within individual Landsat 8 pixels. The similarity to Figure 1-8 is striking and underlines the correlation between NDVI and measured plant biomass.

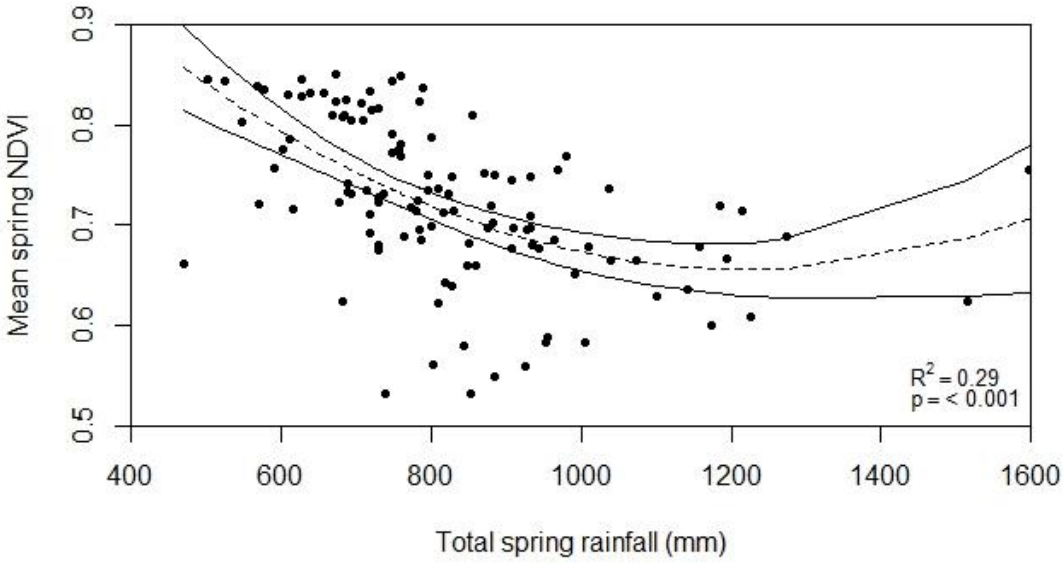

Figure 3-8 The impact of increasing rainfall on grass productivity during spring for heavy soils in the Border, Midlands and Western (BMW) region of Ireland.

The prolonged soil saturation following the 2015-2016 floods was reduced grass production in spring 2016. This was observed in Landsat 8 NDVI imagery, where values for flooded regions in spring 2016 were significantly lower than non-flooded areas. For example, the mean NDVI value for flooded pasture in spring 2016 was 0.70 (± 0.18). The corresponding mean value for flooded grassland in the same period was 0.78 (± 0.11) for heavy soils or 0.80 (± 0.12) for well-drained soils. A non-parametric Kruskal-Wallis rank sum test carried out using the 'stats' package (v.3.4.1), and 'dunn.test' package (v.1.3.4) in R statistical software found a significant effect from flooding on NDVI values (chi-sq. = 585.36, $p < 0.001$, df = 10). The Kruskal-Wallis test is a non-parametric *test* that is used when the normailty assumptions of parametric tests such as ANOVA are not met. Pairwise multiple comparisons showed no evidence for different NDVI values during the first eight acquisition dates. However, there were significant differences after eight events. As illustrated in Figure 3-9, there were only marginal

differences in mean NDVI values during May, June and July as a result of flooding during November and December with NDVI values stable at 0.8 to 0.82. PIxels flooded at the beginning of January (60 days submerged in Figure 3-9) experienced a minor depression in NDVI the following May. This difference was not statistically significant however. Pixels still flooded after February 11 had significantly lower NDVI in May and June. Soil still saturated by early April experienced NDVI in May that were far below expected levels (~0.55 vs ~0.80). Values did not recover to expected levels until the following July meaning grass growth was up to 8 weeks behind expected levels on the ~ 7,000 ha of grassland still flooded in April 2016.

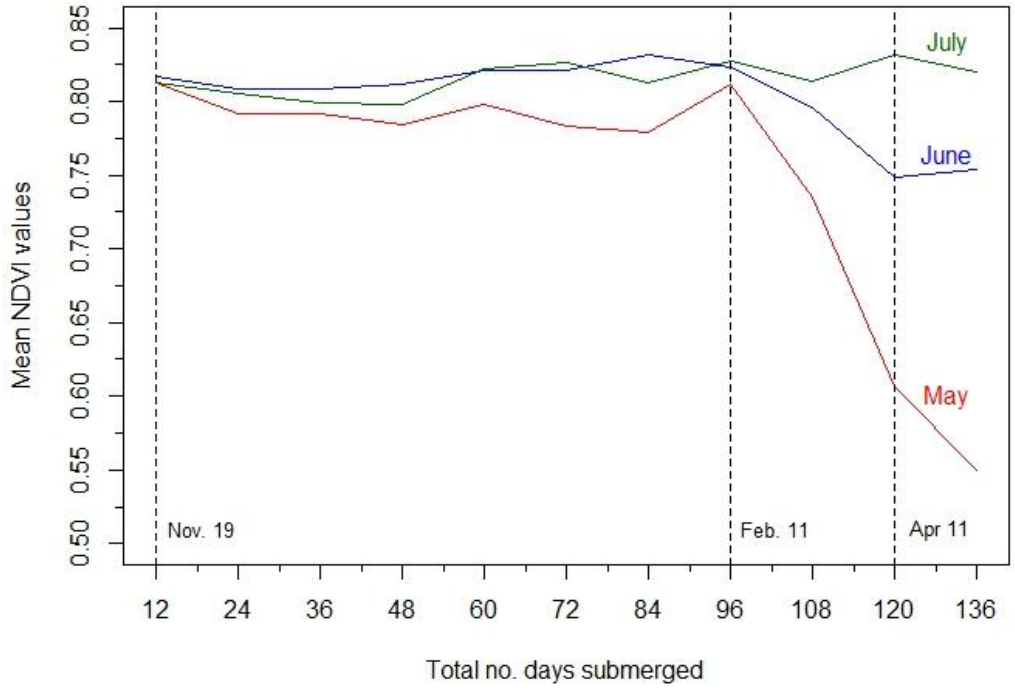

Figure 3-9 The recovery of grassland in the BMW region as a factor of flood duration based on Landsat 8 NDVI values. There was no net effect from flooding during the traditional winter period. However, where floods and soil saturation persisted after the second week in February, there was an increasingly longer recovery period. Fields still saturated by the second week in April took several weeks to recover fully.

3.4 Discussion

3.4.1 Measuring post-flood recovery

Beyond the initial physical damage caused by floods to infrastructure and material goods, the lasting impact to rural communities is the challenge in recovery of grass production and utilisation. These impacts may last for several weeks in some areas. The objective of this study was to identify saturated soils and observe the process of recovery once flood waters receded. This study identified how NDVI values were lower on saturated pastures the following spring compared with areas that were not fooded and not exposed to the same level of saturation. However, NDVI values were only significantly different when the period of submergence exceeded 96 days. After 108 days, a significant decrease in NDVI was recorded compared with the preceding period. This decline in values continued, with NDVI values after 120 days significantly lower again than the preceding observation (see Figure 3-9 above). From these figures, it appeared that flooding during November and December had little impact on grassland NDVI the following spring. However, flooding and saturation in late winter increased the likelihood of depressed NDVI in spring and early summer.

The economic impact on farmers is significant where fodder stores are exhausted and replacement grass cannot be grown or grazed. The erratic weather events over the last four years have exposed the risk to the livestock and dairy industries from any delay in the start of the grass growing season. Section 1.4.2.2 noted the considerable sums of money required to source fodder during previous years. Using EO data, this study has shown how Landsat 8 NDVI images can identify delayed spring growth on saturated soils. This map could support farmers in the worst affected regions claim financial assistance after extreme weather events

where production has been delayed. These maps could also identify areas where persistent saturation issues, following flooding or under normal circumstances, constrain primary production and maybe better suited to other land uses. Flooding of the magnitude of winter 2015/2016 is unusual, however, there is a long-term, upward trend in the annual number of rain days and this increased volume of precipitation will likely result in greater flood risk in the future (Kiely *et al.*, 2009). Future climate scenarios for water supply and flooding suggest a probable increase in the magnitude and frequency of winter floods in the western half of Ireland before the end of this century in response to increased surface runoff on heavy soils (Charlton *et al.*, 2006). This study indicated how the timing of flooding/ saturation had an important impact on grass growth. As illustrated in Figure 3-9, flooding in the traditional winter period had little impact on grass production the following spring. Prolonged saturation lasting into late winter however had a greater impact on the beginning of the grass growing season. This can be seen in the NDVI values illustrated in Figure 3-9 but also in PastureBase grass growth curves for 2016-2018 illustrated in Figure 1.9.

3.4.2 Future directions

The SARn flood map prepared for this study was the first national flood map prepared for Ireland using Sentinel 1 images. In the longer term, detailed flood maps such as this can assist direct Irish government capital spending on future flood prevention. Spending on flood prevention is expected to increase to €100 million by 2021 as flood events increase in frequency and magnitude (NDFEM, 2016). Even a small investment in an EO monitoring method could benefit flood relief measures. Sentinel 1 allows rapid, near-real time identifcation of flooded areas under all atmospheric conditions, day or night every 6 days. It can identify where flood waters persist for several weeks, synoptically mapping locations

where rural or isolated buildings and infrastructure may be at risk. EO maps could confirm damage to properties supporting and or expediting post-flood insurance claims, and also allow insurers to determine the level of risk to rural homes and businesses (Galy & Sanders, 2002). While the Copernicus EMS currently offers an emergency service mapping, the benefit of a dedicated Sentinel 1 SAR flood map has the ability to monitor flooding across the year, not only in an emergency situation. Identifying consistent areas of water ponded on the surface following heavy rainfall could be an efficient way of identifying soil drainage problems. There are also possiblilities for improved soil moisture mapping using Sentinel 1, from the higher spatial resolution and a shorter revisit period using both Sentinel 1 satellites. Sentinel 2 can can be an invaluable resource for monitoring vegetation recovery in the future. Its short revisit time (2-3 days versus 16 days for Landsat 8), higher spatial resolution (10 m versus 30 m) and additional red edge bands can significant improve current means of mapping vegetation stress and recovery (Delegido *et al.*, 2011). At local scales (<0.5 km^2), UAS can provide greater flexibility in monitoring vegetation recovery when optical satellites cannot (Gago *et al.*, 2015).

3.5 Concluding remarks

In this chapter, a combination of SAR and optical EO imagery was used to map the extent of saturated soils and monitor grass recovery after flooding. The long term impact of saturated soils on grass growth in the study area was demonstrated using multi temporal Landsat 8 NDVI imagery. The potential of the ESA Sentinel 2 satellite for flood mapping was also highlighed. The Sentinel 2 mission can also play a role in mapping vegetation recovery. Its improved spatial, spectral and temporal resolution (relative to Landsat 8) should be better able to characterise stress and recovery in future projectcs. In the following chapter, contrasting NDVI values for on wet , saturated grassland will be the focus of separate mapping exercise. Having observed a significant difference in reflectance values between saturated and non-saturated soils after flooding, can this be applied to the classification of soils wet and dry soils (i.e. poorly-drained vs drained), or to identify changes in soil drainage condition over time.

This page is intentionally blank

Chapter 4 Machine learning methods for identifying artificially drained pasture fields using multispectral Earth Observation imagery

4.1 Introduction

An efficient and accurate method to map artificially-drained soils would be an invaluable asset to help farmers, catchment managers and policymakers understand and quantify the agronomic benefits and environmental impacts associated with artificially draining heavy soils (Armstrong & Garwood, 2006; Fitzgerald *et al*., 2008; Schulte *et al*., 2012; Shalloo *et al*., 2004; Sharma *et al*., 2018; Skaggs *et al*., 1994; Wingler & Hennessy, 2016). Accurate soil drainage maps that characterise drainage at field scale, including artificially-drained areas, could improve modelling of grass production (Fitzgerald *et al*., 2008), and models of soil hydrology (Schulte *et al*., 2005; Schulte *et al*., 2015). Studies suggest it could improve on-farm decision-making regarding slurry applications (Kerebel & Holden, 2016), or facilitating targeted implementation of best management practices to reduce diffuse nutrient losses (Schulte *et al*., 2006; Skaggs *et al*., 1994). Accurate soil drainage maps might also help refine coarse scale estimates of carbon sequestration rates (Soussana *et al*., 2007) or other greenhouse gas (GHG) emissions from agricultural sources (Clagnan *et al*., 2018; Oertel *et al*., 2016; Paul *et al*., 2018).

The conventional treatment for heavy soils to make them agriculturally productive and profitable is to install artificial drainage. Detailed data on the distribution of artificially-drained

soils is rare however, both in Ireland and internationally. Available soil data are generally inadequate for supporting day-to-day operations or PA because they overlook the huge spatial variability that occurs within typical mapping units.

As established in Chapters 1 and 2, mapping soil drainage using EO data is well-established. Previous studies have demonstrated how satellite imagery can accurately and robustly map drainage conditions across diverse environments (Beucher *et al*., 2017; Campling *et al*., 2002; Cialella *et al*., 1997; Møller *et al*., 2018; Møller *et al*., 2017; Zhao *et al*., 2013). In Ireland, the contrast in grass growth as a factor of local soil drainage conditions is well established (see Section 1.3.1). The following chapter describes a novel approach to mapping artificial drainage on heavy, grassland soils in the Border, Midlands and Western region or Ireland using machine learning algorithms, EO multispectral imagery and DEM data. This is the first study of its kind in Ireland to look explicitly for artificially-drained areas using EO observations of contrasting growth patterns. Previous *ad-hoc* attempts to quantify soil drainage have been carried out in the past under the remit of *An Foras Taluntais*, a precursor to Teagasc. These records were never fully completed at national level and were never carried out in a harmonised way. They also did not try to identify drainage at the field level. The method described herein uses an extensive and free archive of multispectral imagery from the USGS Landsat 8 program and ESA Sentinel 2 mission. It avails of powerful, machine learning algorithms, Support Vector Machine and Random Forest, to process and analyse the imagery. These algorithms are widely recognised as more accurate than traditional classification algorithms for general land cover mapping (Huang *et al*., 2002; Mountrakis *et al*., 2011; Pal, 2005; Pal & Mather, 2005). Based on published accounts (see Chapter 2 above), these

algorithms have not been used previously for soil- or field drainage mapping explicitly, but have typically performed better than 90% in overall accuracy for general land cover mapping. The main objectives of this chapter were to:

- Create a map of artificially-drained heavy soils at a regional level in the Republic of Ireland based on contrasting canopy reflectance signals.
- Assess the accuracy of the map against high-resolution imagery and field observations.
- Investigate whether improved grass growth can be identified following drain installation using this method.

4.2 Materials and Methods

4.2.1 Study area

The study area for this chapter was heavy grassland soils in the Border, Midlands and Western (BMW) region of the Republic of Ireland, an area of ~808,494 ha (Figure 4-1). Soil drainage estimates were based on the 1:50,000 Teagasc/ EPA Soils and Subsoil Mapping Project (Fealy *et al*., 2009), which estimated ~ 51% of mineral soils within the study area were poorly-drained (these were largely groundwater and surfacewater gleys and alluvial soils). High rainfall values result in a shorter growing/grazing season compared to other regions, with less grass produced and livestock required to be housed for longer periods during inclement weather. Beef and sheep are the principal agricultural industries but profitability is generally lower than other regions of Ireland (Patton *et al*., 2017). The percentage of lands artificially drained across the region is unknown. A report by the Economic and Social Research Institute (ESRI) in the early 1980s attempted to estimate artificially drained soils based on grant allocations for land drainage projects over several preceding decades. This included the Western Drainage Scheme, which ostensibly allowed for the drainage of ~182,500 ha in the

region between 1979-1986 (Bruton & Convery, 1982) (Table 4-1). As noted in Section 1.2.2 above, it was not always apparent that field drainage works followed the allocation of grant aid. Privately-funded drainage works continue to be carried out.

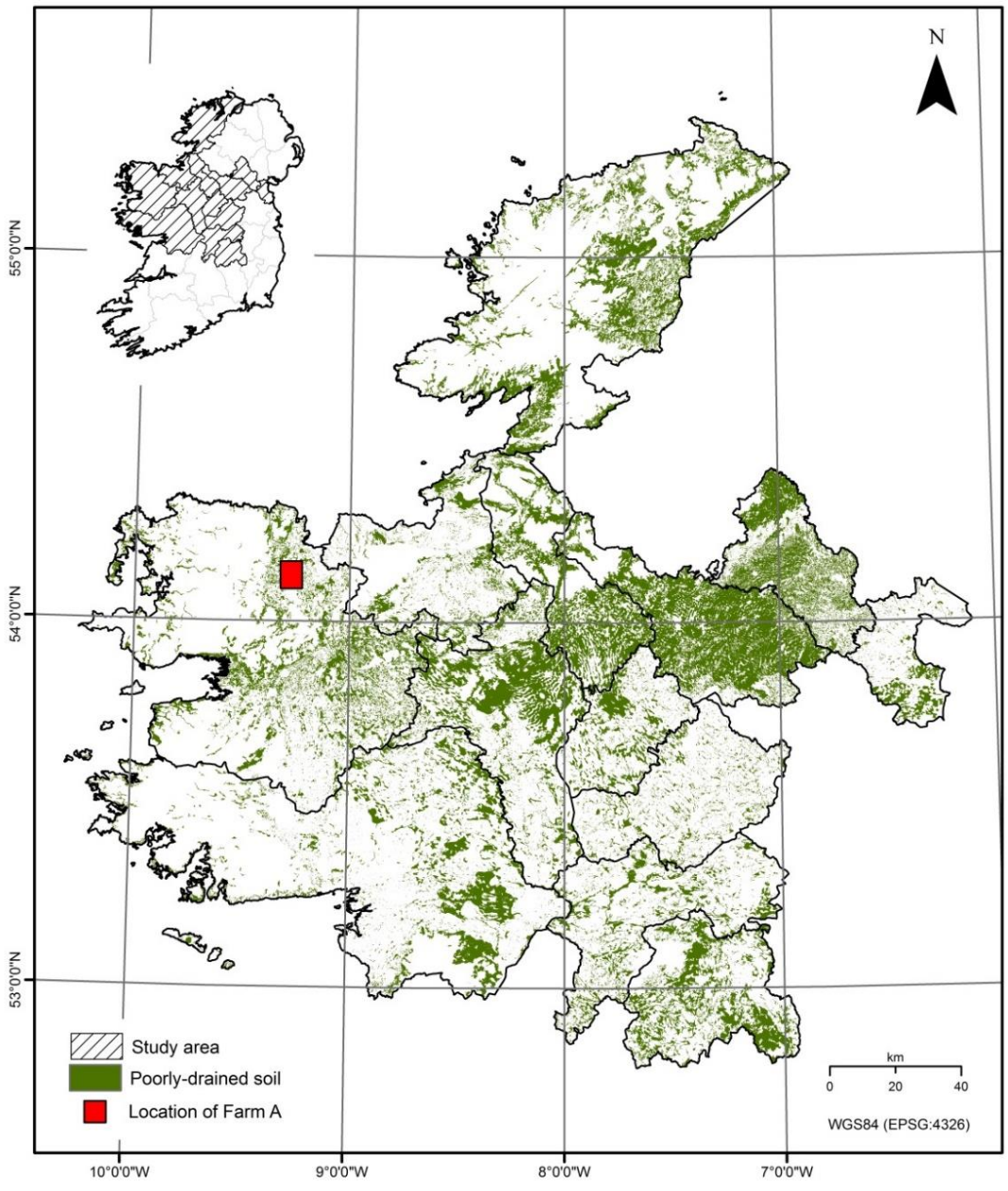

Figure 4-1 Border, Midlands and Western region of the Republic of Ireland showing the extent of heavy grassland soils and the location of Farm A. Soil data based Teagasc/ EPA Soils and Subsoil map. Land cover based on CORINE 2012.

Table 4-1 Estimates of the percentage of land drained in the BMW region (Bruton and Convery 1982). Estimates were based on grant-allocations within the period 1949-86. They do not account for non-grant aid works and assume all actions were subsequently undertaken.

County	% farmland artificially drained
Cavan	25-30%
Donegal	20-25%
Galway	20-25%
Laois	>30%
Leitrim	10-15%
Longford	15-20%
Louth	15-20%
Mayo	20-25%
Monaghan	25-30%
Offaly	>30%
Roscommon	15-20%
Sligo	10-15%
Westmeath	>30%

4.2.2 Datasets

Forty-nine Landsat 8 scenes (path 206–209, rows 21–23) covering the period April/ May 2014-2016 were downloaded from the USGS EarthExplorer portal (see Appendix D). These images captured grass growth during a phenological peak (see Figure 1-9). Scenes were downloaded as radiometrically calibrated and terrain corrected Level 1TP images, atmospherically corrected to surface reflectance using LEDAPS (Masek *et al.*, 2013) and cloud/cloud-shadow masked using F-mask (Zhu *et al.*, 2015). Processed multi-temporal scenes were mosaicked into a single, mean surface reflectance image using the Mosaic to New Raster function (Data Management toolbox in ArcGIS v.10.2.2). There was no single image of the study area as cloud cover obscured different areas of each scene on any given acquisition date. It was possible to use coarser spatial resolution imagery, for example 250 m resolution MODIS data using composite images taken over several days. This was not ideal for the current study as the large pixels would have resulted in higher instances of mixed land

cover. The approach adopted combined all available Landsat 8 scenes by month using data from each of the three years of the study. NDVI and NDWI images were used as a proxy for plant biomass and health (Gao, 1996; Rouse *et al*., 1974) (see Section 1.5.2 above). The mosaic was then masked to "poorly-drained" soils using the Teagasc/ EPA Soils and Subsoil map and "dry grassland" using CORINE 2012. Buildings were masked using OSI PRIME 2 vector data and parcels of forest were masked using the 2012 Forestry Inventory Parcel System (DAFM, 2013a). To allow a comparison between Landsat 8 and Sentinel 2 data for drainage mapping, a Sentinel 2A from May 2017 was downloaded as a Level 2A surface reflectance product from the Copernicus Open Access Hub. This was cloud masked using cloud masks supplied with the image data and masked for soil type and land cover as previously described.

4.2.3 Training data

Training data were for "poorly-drained" and "drained" class labels were determined by visual inspection of high spatial resolution imagery (Digital Globe/ ArcGIS base mapping). The ArcGIS base map is compiled from several years of data, from different sources. This was an issue when trying to ensure consistency in training data across the region, for example, ensuring conditions identified in high resolution mapping were still representative of the conditions recorded in EO images. Areas showing extensive growth of water-tolerant vegetation (reeds and rushes) were labelled "poorly-drained". Training class was defined by 60, 200 or 500 pixels per class to investigate whether classification accuracy was linked to number of training samples. Each training set was independently compiled from random sample of points generated across the study area. Drainage status was based on expert interpretation of drainage status with a 30 m diameter area (corresponding to the size of a 30

m x 30 m Landsat 8 pixel. Only points located within homogenous areas of land cover were selected to avoid class mixing. An equal numbers of samples from each class were recorded for each training set. Training data was finally extracted for each of the multispectral bands, topographical data and spectral indices (see Table 4-2).

Table 4-2 Variables used in each model over different level of training (60, 200, and 500 samples per class).

Model	Variables*
1	Landsat bands 2:7, NDVI, NDWI, Slope, HAND, distance to drainage, TWI
2	Landsat bands 2:7
3	Landsat bands 2:7, NDVI
4	Landsat bands 2:7, NDWI
5	Landsat bands 2:7, NDVI, NDWI
6	NDVI, NDWI, Slope, HAND, distance to drainage, TWI
7	Landsat bands 2:7, Slope, HAND, distance to drainage, TWI
8	NDVI, Slope, HAND, distance to drainage, TWI
9	NDWI, Slope, HAND, distance to drainage, TWI
10	Slope, HAND, distance to drainage, TWI

*NDVI = normalised difference vegetation index; NDWI = normalised difference water index, slope = topographic slope (gradient), HAND = height above nearest drainage, TWI = topographic wetness index. See Section 4.2.5 for further explanations of these terms.

In selecting training data, no assumption was made on whether there was artificial drainage present. only that based on visual inspection of the high-resolution image, a 30 m diameter area surrounding the sample point met, or did not meet, the criteria for poorly drained conditions. Using the training set for 500 pixels, a line graph depicting drained and poorly drained classes indicated that the “poorly drained” class could be distinguished from “drained” class by greater reflectance of red (0.64- 0.67 μm) and shortwave infrared (SWIR) (1.5- 2.3 μm) wavelengths, with lower reflectance at near-infrared (NIR) wavelengths (0.85- 0.88 μm)

(Figure 4-2). Graphs for 60 and 200 training classes (not illustrated) showed the same trends. Healthy grass canopy absorbs greater amounts of red light to fuel photosynthesis and produce chlorophyll. Healthy grass, with more chlorophyll being produced, will reflect a greater amount of NIR energy than unhealthy grass. These wavelengths, therefore, can provide important information about grass health and yield in the study area.

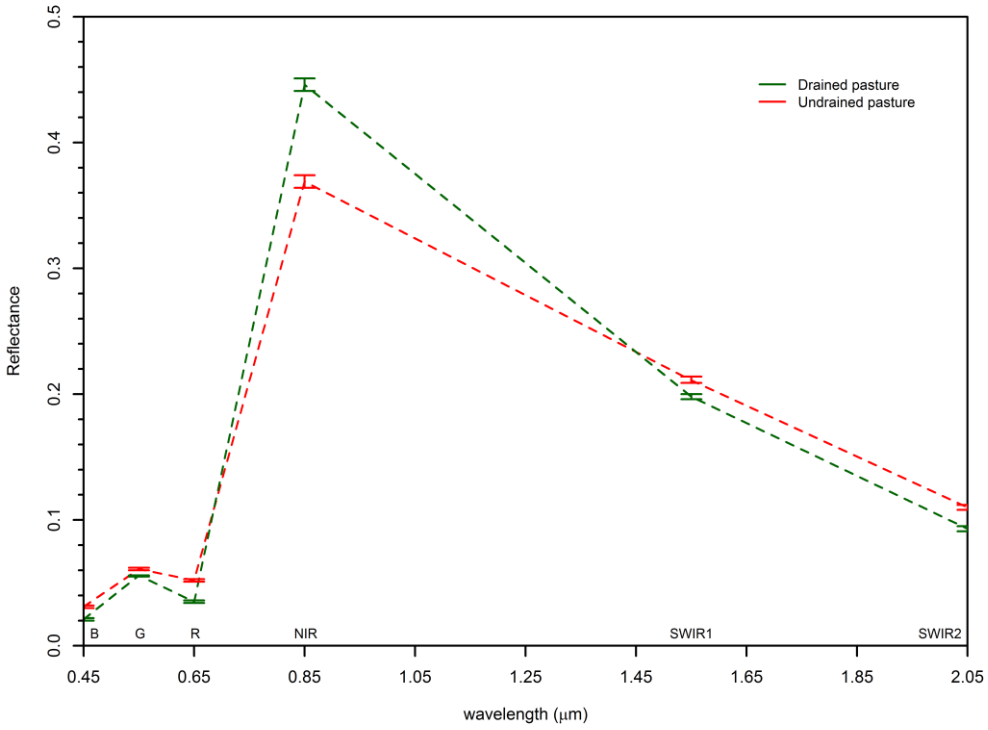

Figure 4-2 Contrasting reflectance values (Landsat 8 bands 2-7) for “drained” and “poorly drained” class labels. Mean values derived from 500 training samples used to train the classification. Arrows indicate 95% confidence intervals at each band.

Figure 4-3 below shows further contrast between both class labels for month-on-month difference NDVI imagery. This graph was compiled from random samples of pixel data extracted from monthly NDVI composites for the years 2014-2016. The graph shows mean NDVI values drained and poorly-drained class labels for grassland in the region between February and November (2014-2016). Insufficient images were available in January and December due to cloud cover. An apparent surge in NDVI values in April/May over the preceding months matches the peak phenological stage in grass growth noted in Figure 1-9 above. “Drained” and “poorly drained” conditions can be distinguished at this stage quite clearly, with NDVI values for stronger and earlier growth for drained conditions during spring relative to poorly-drained conditions. There was also a clear separation in difference NDVI values during July. It is important to restate that this graph shows month-on month differences in NDVI values for the two drainage types, indicating change in values between the current- and previous month. The depression of poorly drained NDVI values here indicate no change, or very little change, in July NDVI compared to June. There is a positive increase for drained grassland between the two months, although the magnitude of this increase is not comparable to the change between March/April and April/May. The dichotomy illustrates the difference in potential grass yield between the two drainage classes.

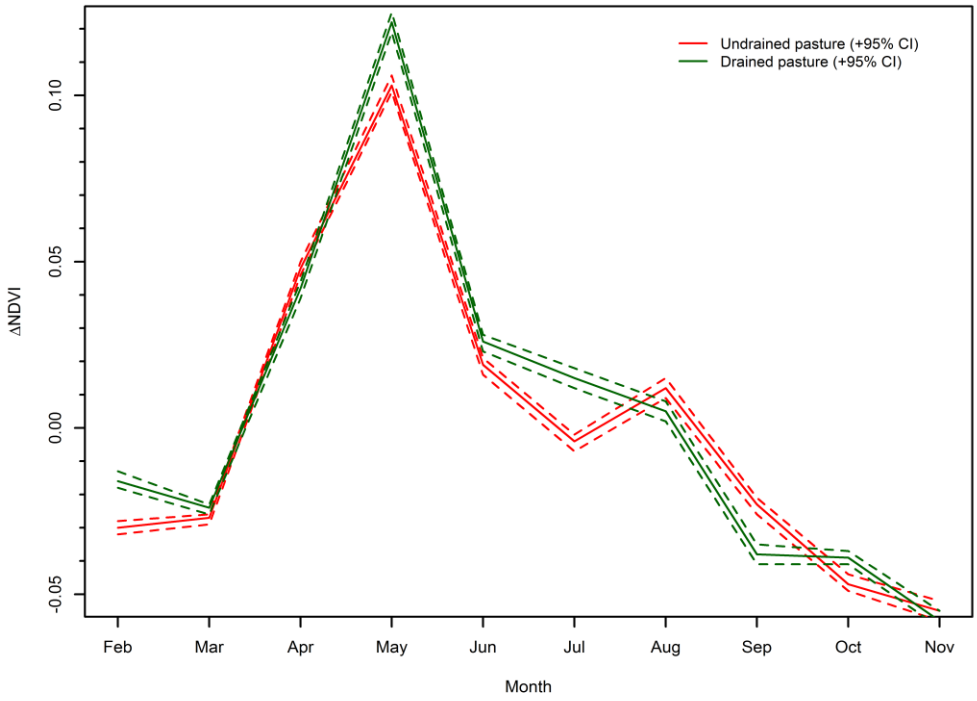

Figure 4-3 Month-on-month changes for mean NDVI values across the study area over three years (2014-2016) based on Landsat 8 NDVI images. The magnitude of increase is highest between March and May in both drainage classes, but higher for drained soils.

4.2.4 Accuracy assessment

4.2.4.1 Validation

Two forms of validation were used in the study: visual interpretation of recent high-resolution imagery (Digital Globe/ ArcGIS base mapping), and ground-truth data collected for the Teagasc/ EPA Soils and Subsoil project in 2005. The use of Digital Globe imagery, through Google Earth or GIS base mapping, is a well-established method for validating remote sensing land cover classifications (Knorn *et al.*, 2009; Lillesand *et al.*, 2015). Drainage condition was inferred from an interpretation of surface conditions in a 30 m radius around 920 randomly selected points (see Figure 4-4). To reduce potential contamination from boundarys (shadow, buildings and mixed land cover), a minimum distance of 30 m between assessment points and adjacent boundaries/ structures was enforced. The ground-truth data collected in 2005 comprised of 230 GNSS-located field observations of drainage status, based on soil type, surface drainage, landscape position and land cover. Reference points were filtered by textural classes ("clayey", "loamy", "peaty") and land cover ("improved grassland" and "wet grassland") to meet the criteria for the current drainage classification within the study area.

In each case, an error matrix was used to assess accuracy. This is the standard tool for quantifying overall accuracy in land cover classification, as well as errors of commission- and omission (Congalton, 1991). Kappa statistics, which compares observed accuracy with an expected accuracy due to random chance, are also reported. Relative accuracy between models was calculated based on a procedure to calculate Z statistics and p-values as outlined by Rossiter (Rossiter, 2014).

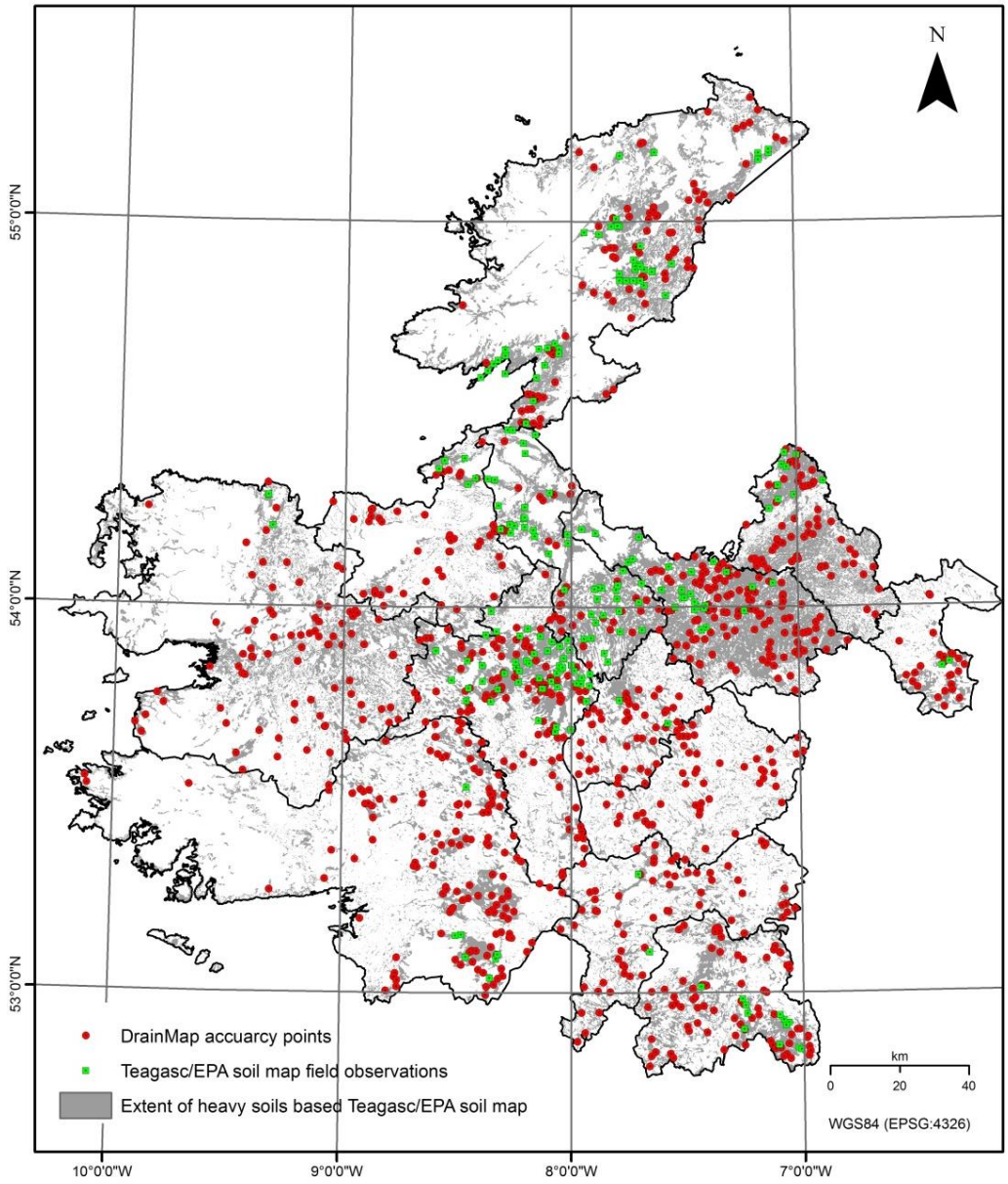

Figure 4-4 Location and distribution of validation points used in the study. Includes visual assessment points based on interpretation of high-resolution satellite imagery (red) and field observations of drainage status based on the Teagasc/ EPA Soils and Subsoil Map recorded in 2005.

Error matrices are the most common way of expressing the accuracy of remote sensing land cover classifications. There may be distinct patterns to the spatial distribution of classification errors in thematic maps. Error matrices are criticised for not providing an indication of the

spatial distribution of errors, or spatial variation in classification uncertainty. Foody (2002) outlines various approaches to provide such information, for example, geostatistical modelling approaches or visualising classification uncertainty. Comber et al. (2012) suggested a geographically-weighted approach to report land cover accuracy in a more informative way.

4.2.4.2 Farm A

Additional validation was available from a livestock farm within the study area (Farm A in Figure 4-1). A groundwater drainage system was installed here in 2014 as part of the Heavy Soils Programme (HSP). This programme was established to improve the profitability of grassland farms on heavy soils through the adoption of key technologies including appropriate drainage solutions (Teagasc, 2018). The 3 ha field had no previous drainage in place and rushes were present within the sward before drainage. This location presented an opportunity to determine whether temporal changes in canopy reflectance could be identified that corresponded to improvements in field drainage regime. No satellite data was available in 2014 as a result of extensive cloud cover over the region at the time of acquisition. Surface reflectance Images from Landsat 5 Thematic Mapper (2010) and Landsat 7 Enhanced Thematic Mapper (2013) were required for years where Landsat 8 imagery was unavailable.

4.2.5 Terrain data

A hydrologically-corrected, 20 m DEM (vertical accuracy +/- 2.5m) was used to model terrain attributes that influence water movement on or below the surface. These include distance to drainage (Euclidean distance and along slope), slope aspect (Zevenbergen & Thorne, 1987) and height above nearest drainage (Rennó *et al.*, 2008). Height above nearest drainage and

distances to drainage were derived in combination with PRIME 2 vector stream data, which included both surface drainage and open ditches. A topographic wetness index (TWI) was also modelled. TWI, a function of local slope and specific contributing area (Seibert & McGlynn, 2007), is used to quantify topographical controls on hydrological processes (Beven & Kirkby, 1979). Topographic data were created in ArcGIS and SAGA GIS (v.4.1.0).

4.2.6 Algorithm selection and parameterisation

The drainage classification was scripted in R statistical software using "e1071" (v.1.6-8) and "randomForest" (v.4.6-12) packages for SVM and RF respectively (see Appendix E). Model inputs were training data and the ten mosaic combinations presented in Table 4-2 above. Both algorithms allowed for internal fine-tuning to further parameterise the classifiers. The output in each case was a binary segmentation of the mosaic images into "drained" or "poorly-drained" classes.

4.2.6.1 Support Vector Machine

The SVM algorithm was initially conceived for two-class segmentation problems, although it can be adopted for multi-class problems where a series of binary separations are computed (Cortes & Vapnik 1995). Unlike conventional parametric methods, for example, maximum likelihood or K-means classifiers, that cluster pixels based on common centroids (Gibson, 2000), SVM identifies decision boundaries between linearly separable classes by defining the broadest possible margin between classes (known as the optimal hyperplane). For linearly *inseparable* data, a kernel function γ initially transforms the data, while a penalisation term C defines a tolerance threshold for overlapping classes (Cortes & Vapnik 1995). A radial basis

function (RBF) kernel was used in this study as it provided marginally higher accuracy during initial tests (see Table 4-3). The strong performance of RBF has been reported elsewhere compared with other kernel types (Huang *et al*., 2002). Values for γ and C were fine-tuned for each model.

Table 4-3 Error matrices for SVM models created using different kernel types. Based on 920 reference points (60 training samples per class). OA= overall accuracy (%), K= kappa statistic, PA= producer accuracy (%), UA= User accuracy (%). Highest OA underlined in **bold**.

n= 929		SVM					
				DRAINED		UNDRAINED	
		OA	K	PA	UA	PA	UA
Kernel	RBF	**83.75**	0.65	67.39	89.29	94.62	81.36
	Linear	82.56	0.62	65.85	87.10	93.57	80.62
	Polynomial	83.64	0.64	67.12	89.25	94.62	81.23
	Sigmoid	83.64	0.64	67.12	89.25	94.62	81.23

4.2.6.2 Random Forest

The RF alorithm is an ensemble clasification method that determines class labels based on the pooled results of multiple randomly-created decision tree classifiers. The algorithm uses bootstrapped training data to develop each tree independantly, while each node split is based on a randomly selected set of predictor variables (Breiman, 2001). A majority vote usually determines the final classification label. Random subsetting reduces the overall importance of any one individual tree or set of variables. It also reduces the correlation between individual trees. The RF algorithm can also provide a measure of variable importance by measuring the decrease in accuracy as different variables are omitted. This mean decrease accuracy (MDA)

is a direct measure of the impact of each variable on overall accuracy. It measures differences in out-of-the-bag (OOB) error resulting from differences between an original data set and data with randomly permutated variables. Permutation should have little effect on model accuracy if the variable is unimportant, but removing important variables should significantly decrease accuracy. A second mechanism, mean decrease gini (MDG) measured node purity at each split, or the likelihood of obtaining identical (pure) or different (impure) outputs. Gini importance indicates how often a particular feature was selected for a split, and how large its overall value was in discriminating classes (Breiman, 2001).

4.3 Results

4.3.1 Model performance

Accuracy assessments based on error matrices are presented in Tables 4.4 and 4.5 for each model at each training level. The result of the best performing model is illustrated in Figure 4.5 below.

4.3.1.1 Image-based validation

Using high-resolution image validation, the best overall performing model was an RF algorithm (using 60 training samples) for Model 5 (Landsat bands, NDVI and NDWI). Overall accuracy was 91.4% (95% CI [89.6%, 93.2%]) (Figure 4-5). At 200 training samples, the best performing model was an RF algorithm applied to Model 1 (Landsat bands, both VI and DEM variables), with an overall accuracy of 91.1% (95% CI [89.2%, 92.9%]). At 500 training samples, the best performing model was again an RF algorithm applied to Model 3 (Landsat bands, NDVI), which had an overall accuracy of 89.0% (95% CI [87.0%, 91.0%]). The reason

for the reduction in accuracy with higher training samples was not clearly understood. The likely reason was an unidentified fault in the training data, for example, where conditions observed in high resolution base mapping did not reflect the conditions on the ground at the time of acquisition. The most likely candidate for this was landcover change that confused the algorithms. While RF was best across all categories, SVM also performed strongly, with overall accuracies of 86.9% [84.7%, 89.1%], 89.6% [87.7%, 91.6%] and 87.3% [85.1%, 89.4%] at each respective training level. A two-tailed binomial Z-score comparison found a significant difference in accuracy between RF and SVM outputs (z= 3.08, p= 0.002) at the lowest training level but not at higher levels of training (z= 1.03, p= 0.3; z= 1.15, p= 0.2 respectively).

4.3.1.2 Field-based validation

Conversely, using field observed validation, the best overall performing models were derived from the SVM algorithm. At 60 Model 3 (Landsat bands and NDVI), with an overall accuracy of 68.7% (95% CI [62.7%, 74.7%]). At 200 Model 3 had an overall accuracy of 67.4% (95% CI [61.6%, 73.4%]). At 500 training samples, Model 1 (all variables) was the best with an overall accuracy of 66.96% (95% CI [61.0%, 73.0%]). A two-tailed binomial Z-score comparison found no significant difference between algorithms at each level of training (z= 0.20, p= 0.84; z= 0.50, p=0.61 and z= 0.09, p= 0.93 respectively). Although marginal reductions in overall accuracy were noted as the level of training increased using both sets of validation data, the difference between results at each level were not statistically significant.

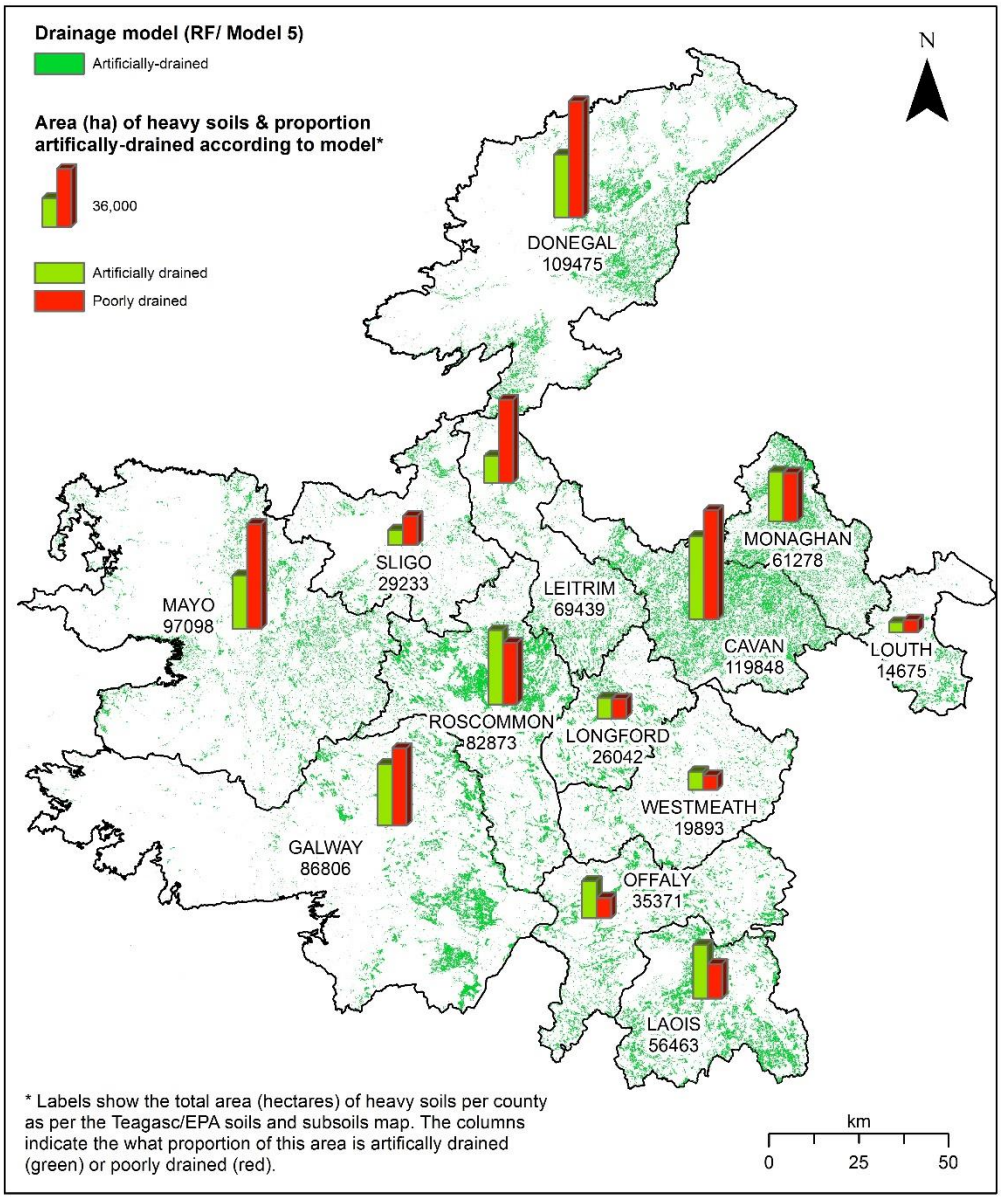

Figure 4-5 Extent and distribution of artificially drained soils in the study area. County labels indicate the total areas of heavy soils per county based on the Teagasc/ EPA Soils and Subsoil Map. The accompanying bar charts indicate the proportion of artificially-drained/ poorly drained soils according to the best performing model.

Table 4-4: Error matrices for each model (SVM and RF) at each level of training (60, 200 and 500 training samples) based on high resolution images. OA= overall accuracy (%), K= kappa statistic, PA= producer accuracy (%), UA= User accuracy (%). Highest OA underlined in **bold**.

60 training samples		SVM						RF					
		OA	K	DRAINED		UNDRAINED		OA	K	DRAINED		UNDRAINED	
				PA	UA	PA	UA			PA	UA	PA	UA
Model	1	83.37	0.64	95.3	80.55	65.49	90.26	90.76	0.78	94.1	92.8	82.97	85.77
	2	85.65	0.68	95.62	83.61	69.34	90.64	88.04	0.72	94	88.82	75.91	86.14
	3	**86.96**	0.71	95.87	85.3	71.68	91.01	91.3	0.79	94.14	93.57	84.5	85.77
	4	86.1	0.69	95.81	84.07	70.03	91.01	89.13	0.75	94.38	90.05	78.11	86.89
	5	86.63	0.7	96.01	84.69	70.93	91.39	**91.41**	0.79	94.15	93.72	84.81	85.77
	6	80.54	0.59	95.75	75.96	60.95	91.76	88.91	0.74	93.11	91.12	79.36	83.52
	7	75.65	0.5	95.54	68.91	54.79	92.13	88.15	0.73	94.74	88.21	75.32	88.01
	8	78.59	0.54	94.19	74.43	58.66	88.76	88.15	0.72	93.56	89.43	76.69	85.02
	9	75.65	0.5	94.97	69.37	54.85	91.01	82.72	0.61	92.88	81.93	65.7	84.64
	10	52.11	0.12	79.34	44.1	34.47	71.91	50.98	0.06	74.88	46..55	32.1	61.8
200 training samples		SVM						RF					
		OA	K	DRAINED		UNDRAINED		OA	K	DRAINED		UNDRAINED	
				PA	UA	PA	UA			PA	UA	PA	UA
Model	1	85.54	0.67	95.14	83.92	69.48	89.51	**91.2**	0.79	93.87	93.72	84.7	85.02
	2	88.91	0.72	91.93	92.5	81.37	80.15	90.54	0.77	93.4	93.26	83.58	83.9
	3	**89.67**	0.75	92.79	92.65	82.09	82.4	90.98	0.78	93.85	93.42	84.07	85.02
	4	88.26	0.72	92.12	91.21	79.12	80.9	89.78	0.75	93.47	92.04	81.23	84.27
	5	89.13	0.74	93.68	90.81	79.09	85.02	91.09	0.78	93.86	93.57	84.39	85.02
	6	82.83	0.62	93.19	81.78	65.71	85.39	88.37	0.73	91.17	89..13	76.43	86.52
	7	85.76	0.67	93.79	85.6	70.93	86.14	88.37	0.73	94.17	89.13	76.49	86.52
	8	82.5	0.61	92.41	82.08	65.59	83.52	88.26	0.72	94.45	88.67	75.9	87.27
	9	79.35	0.55	92.01	77.64	60.43	83.52	85.43	0.67	93.18	85.76	70.85	84.64
	10	53.48	0.06	73.68	53.6	31.91	53.18	57.93	0.08	74.18	62.48	33.78	46.82
500 training samples		SVM						RF					
		OA	K	DRAINED		UNDRAINED		OA	K	DRAINED		UNDRAINED	
				PA	UA	PA	UA			PA	UA	PA	UA
Model	1	83.37	0.64	95.29	80.55	65.49	90.26	88.15	0.73	94.74	88.21	75.32	88.01
	2	86.3	0.69	94.53	85.6	71.43	88.01	88.04	0.72	92.76	90.2	77.54	82.77
	3	87.07	0.71	95.25	86.06	72.42	89.51	**89.02**	0.74	94.52	89.74	77.67	87.27
	4	**87.28**	0.71	95.27	86.37	72.87	89.51	86.2	0.68	93.26	86.83	72.44	84.64
	5	87.17	0.71	95.57	85.91	72.31	90.26	88.7	0.74	94.78	88.91	76.55	88.01
	6	85	0.67	95.1	83.15	68.48	89.51	87.72	0.72	94.55	87.75	74.52	87.64
	7	83.48	0.64	95.14	80.86	65.75	89.89	87.28	0.7	92.81	88.91	75.51	83.15
	8	84.35	0.65	93.5	83.77	68.36	85.77	87.5	0.71	94.24	87.75	74.36	86.89
	9	81.09	0.58	92.84	79.48	62.88	85.02	82.39	0.61	93.61	80.7	64.71	86.52
	10	49.24	0.03	72.91	45.33	30.54	58.8	50.87	0.05	73.54	48.09	31.24	57.68

Table 4-5 Error matrices for each model (SVM and RF) at each level of training (60, 200 and 500 training samples) based on the Teagasc/EPA field observations. OA= overall accuracy (%), K= kappa statistic, PA= producer accuracy (%), UA= User accuracy (%). Highest OA underlined in **bold**.

60 training samples		SVM						RF					
		OA	K	DRAINED		UNDRAINED		OA	K	DRAINED		UNDRAINED	
				PA	UA	PA	UA			PA	UA	PA	UA
Model	1	66.96	0.27	44.32	59.09	80.99	70.12	66.09	0.25	43.33	59.09	80.71	68.90
	2	64.78	0.15	39.13	40.91	75.78	74.39	**67.83**	0.27	45.24	57.58	80.82	71.95
	3	**68.70**	0.28	46.25	56.06	80.67	73.78	65.22	0.23	42.05	56.06	79.58	68.90
	4	65.22	0.17	40.00	42.42	76.25	74.39	66.09	0.23	42.86	54.55	79.45	70.73
	5	65.22	0.17	40.00	42.42	76.25	74.39	66.52	0.27	43.96	60.61	81.29	68.90
	6	61.74	0.07	33.33	33.33	73.17	73.17	61.30	0.17	38.14	56.06	78.02	63.41
	7	65.22	0.13	38.33	34.85	74.71	77.44	65.22	0.21	41.67	53.03	78.77	70.12
	8	62.61	0.08	34.38	33.33	73.49	74.39	63.91	0.20	40.45	54.55	78.72	67.68
	9	63.48	0.10	35.94	34.85	74.10	75.00	63.91	0.20	40.45	54.55	78.72	67.68
	10	46.09	0.00	21.00	31.82	51.83	65.38	46.52	0.00	28.89	59.09	71.58	41.46
200 training samples		SVM						RF					
		OA	K	DRAINED		UNDRAINED		OA	K	DRAINED		UNDRAINED	
				PA	UA	PA	UA			PA	UA	PA	UA
Model	1	65.37	0.17	39.43	32.90	76.73	74.18	65.27	0.26	42.10	55.84	64.11	59.35
	2	63.30	0.15	37.30	26.98	74.06	73.36	63.32	0.25	40.85	55.33	62.54	59.28
	3	**67.37**	0.19	41.49	39.84	79.31	74.98	67.15	0.26	43.32	56.43	65.63	59.41
	4	61.28	0.12	35.22	22.44	71.46	72.56	61.42	0.22	39.62	54.95	61.00	59.21
	5	64.07	0.15	38.09	29.03	75.06	73.67	**65.99**	0.26	42.57	56.05	64.69	59.37
	6	66.14	0.18	40.22	35.43	77.72	74.49	64.05	0.25	41.31	55.51	63.13	59.30
	7	61.70	0.13	35.65	23.29	72.00	72.72	61.82	0.23	39.87	55.02	61.32	59.22
	8	63.30	0.15	37.30	26.98	74.06	73.36	63.32	0.25	40.85	55.33	62.54	59.28
	9	64.09	0.15	38.11	29.09	75.08	73.67	64.06	0.25	41.32	55.51	63.14	59.30
	10	42.24	0.00	15.61	39.81	46.92	65.00	43.53	0.01	28.05	56.42	46.52	58.57
500 training samples		SVM						RF					
		OA	K	DRAINED		UNDRAINED		OA	K	DRAINED		UNDRAINED	
				PA	UA	PA	UA			PA	UA	PA	UA
Model	1	**66.96**	0.27	44.32	59.09	80.99	70.12	65.22	0.21	41.67	53.03	78.77	70.12
	2	60.43	0.14	36.56	51.52	76.64	64.02	63.04	0.18	39.33	53.03	78.01	67.07
	3	63.48	0.18	39.53	51.52	77.78	68.29	64.78	0.19	40.74	50.00	77.85	70.73
	4	62.17	0.15	37.65	48.48	76.55	67.68	61.74	0.19	39.00	59.09	79.23	62.80
	5	63.48	0.18	39.53	51.52	77.78	68.29	**67.35**	0.18	40.00	48.48	77.33	70.73
	6	60.87	0.09	34.62	40.91	74.34	68.90	66.09	0.23	42.86	54.55	79.45	70.73
	7	61.74	0.09	34.72	37.88	74.05	71.34	61.74	0.16	38.04	53.03	77.54	65.24
	8	61.74	0.12	36.25	43.94	75.33	68.90	63.91	0.19	40.23	53.03	78.32	68.29
	9	60.43	0.09	34.18	40.91	74.17	68.29	63.91	0.17	39.51	48.48	77.18	70.12
	10	40.43	0.00	19.47	32.35	60.68	43.83	42.17	0.00	23.62	45.45	65.05	40.85

4.3.2 Temporal changes in modelled drainage status

At Farm A, increases in mean and maximum NDVI values were observed in spring NDVI images following drainage works in 2014 compared with NDVI images from pre-drainage years (see Table 4-6; Figure 4-6). The change in NDVI values was concomitant with an increase in the area of the field classed as "drained" by the RF model. For example, in 2010, the proportion of the 3-ha field classed as drained was 0.72 ha (25% of the area). This increased to 1.8 ha (58%) in 2015 and 2.1 ha in 2016 (68%). No other treatments which may have had an effect on NDVI occurred in the same period.

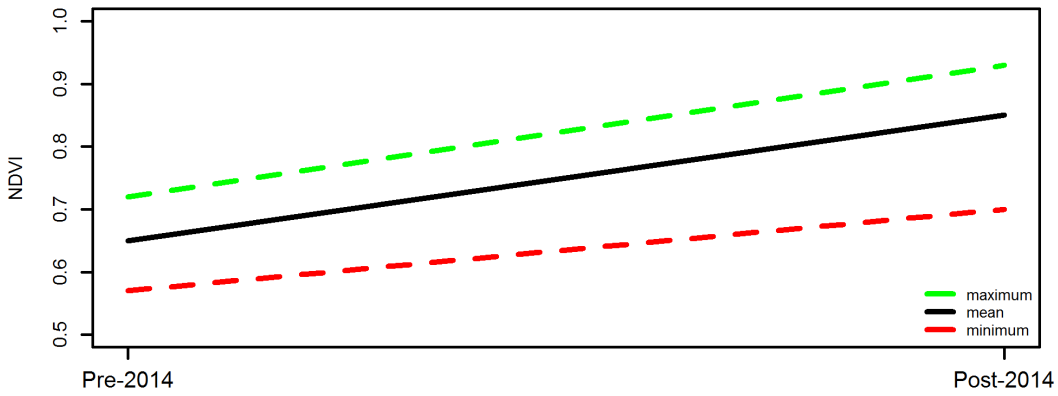

Figure 4-6 Visual representation of the general increases in minimum, mean and maximum NDVI values at Farm A following the installation of field drainage. The graph shows selected summary statistics for years before 2014 and after 2014.

Table 4-6 Descriptive statistics for observed NDVI values in April/May before and after installation of a groundwater drainage system at Farm A

Farm A				
Year	Min	Max	Mean	St.dev.
2010	0.65	0.82	0.73	0.04
2013	0.71	0.87	0.80	0.04
2014	Imagery unavailable. Drainage installed July/August			
2015	0.68	0.91	0.85	0.06
2016	0.76	0.94	0.86	0.05

4.3.3 Comparison with Sentinel 2

The best performing model for Landsat 8 (RF Model 5) was subsequently applied to the Sentinel 2A images to determine whether the improved spatial- and spectral resolution had any impact on classification accuracy. The Sentinel 2 imagery was not acquired contemporaneously to the Landsat 8 data and did not cover the same footprint. This initial assessment recorded good overall accuracy (71.8%; 95% CI [65.5%, 74.7%]). This was less accurate than the model using Landsat 8 data. Reasons for this are discussed in Section 4 below.

4.4 Discussion

4.4.1 Extent and distribution

The study area (heavy grassland soils) was initially estimated to be ~808,494 ha based on the intersection of coarse-scale soil and land cover maps. This study assumed the soil drainage designations of the Teagasc/EPA map were broadly accurate and that wherever drained conditions were identified for heavy soils, it was as a result of artificial drainage. Similarly, poorly-drained areas were assumed to represent areas where there was no artificial drainage in place, or where existing drainage may have been defunct or no longer functioned correctly.

The study suggested the area of poorly drained soils in the region were considerably overestimated by the Teagasc/EPA soil map (see Table 4-7). The best performing model suggested ~345,000 ha of soils previously classed as “poorly-drained” showed no indication of a persistent saturation problem. This means that as much as 44% of heavy soils in the study area were potentially misclassed. Without more extensive validation work, it was not possible to say with greater certainty whether the “drained” conditions identified by the classification were the result of artificial-drainage and not, for example, discrete areas of naturally, well-drained soils within larger poorly drained soil units. In Figure 4-5, it was clear that there was considerable county-by-county variation in modelled estimates of artifically drained lands. In most case, the modelled estimates exceeded those proposed by Bruton and Convery, but do exhibit some consistency in that the counties with the highest (Laois, Offaly and Westmeath), and lowest (Sligo and Leitrim) proportions of drained land correspond to those identified in the earlier assessment by Bruton and Convery.

Table 4-7 County-by-county improvements in the area of drained lands from Teagasc/ EPA Soils and Subsoil Map.

	Poorly drained Teagasc/EPA (ha)	DrainMap		% heavy soils that are drained according to the current study
		Drained (ha)	Poorly drained (ha)	
Cavan	119,848	51,813	67,965	43%
Donegal	109,475	39,206	72,066	36%
Galway	86,806	38,459	48,300	44%
Laois	56,463	33,445	21,679	59%
Leitrim	69,439	16,552	51,678	24%
Longford	26,042	12,700	12,162	49%
Louth	14,675	6,455	7,987	44%
Mayo	97,098	33,228	65,230	34%
Monaghan	61,278	31,022	30,363	51%
Offaly	35,371	23,117	12,527	65%
Roscommon	82,873	46,134	38,265	56%
Sligo	29,233	9,611	18,137	33%
Westmeath	19,893	11,388	9,005	57%
BMW Region	808,494	353,130	455,364	44%

4.4.2 Model performance

Both algorithms performed strongly, with RF having the highest accuracy using image-based validation data and SVM performing better with field-based validation data. Neither dataset used in the validation was without potential sources of uncertainty or bias. While the use of high-resolution imagery to validate thematic maps is widely practised, interpretation of such data can be highly subjective, as it depends on the experience of the observer to correctly distinguish land cover classes (Foody, 2002). For example, the legacy field observations used for this study where potentially no longer representative of current field conditions, as they were from a reference dataset collected in 2005.

Using the field observations, best overall accuracy was reduced from 91.4% to 68.7%. Lower accuracy from these validation points was expected. The records were created several years earlier and, in some cases, might not accurately reflect current conditions on site, for example where there was a subsequent installation of drains or where existing drains became blocked etc. Also, as point descriptions of field drainage, they were not necessarily an appropriate scale for validation of this EO-based project. The drainage assessment at the particular point of record may not be representative of the wider surroundings. This discrepancy between the observation scales, for example between point- and pixel-based estimates of surface phenomena, can result in different estimates of surface properties (Goodchild, 2001). Thus, observed drainage status for a given location may not reflect the drainage properties of the surrounding 900 m^2 (the footprint of a Landsat 8 pixel). Any future expansion of this study should prioritise the collection of current, appropriate ground-truth to validate these model outputs.

Using MDA, the most valuable Landsat 8 band for separating drainage classes was NIR. NDVI and NDWI were also important (Figure 4-7). NDVI was alsio important in previous drainage mapping projects (Cialella *et al*., 1997; Levine *et al*., 1994), while NDWI was the highest-ranking spectral dataset in a recent Danish drainage mapping study (Møller *et al*., 2018). NIR was integral to both these indices, however individually, both Landsat SWIR bands ranked low in overall importance suggesting NIR was the key band. Terrain attributes had only a minor impact on overall model accuracy, but elevation, aspect and distance to drainage were consistently among the highest-ranking terrain attributes where included. Both elevation and aspect have a direct influence on precipitation volume and insolation, and both are known

to negatively impact vegetation growth through their impact on soil temperature, soil moisture content and the number of degree days (Keane & Sheridan, 2001). Elevation was identified as an important predictor of soil drainage class in previous studies (Campling *et al*., 2002; Cialella *et al*., 1997).

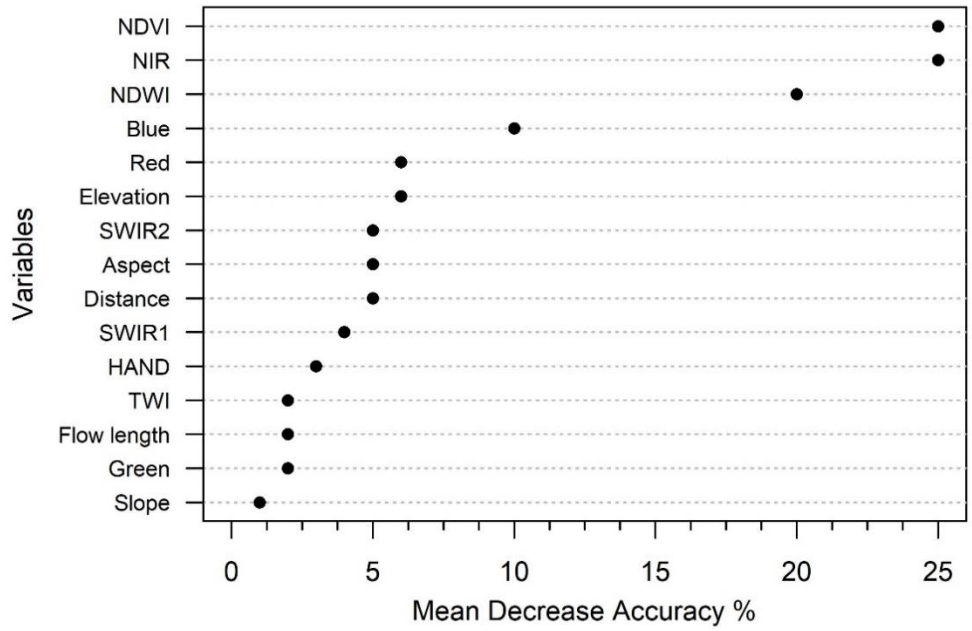

Figure 4-7 Variable importance for Landsat 8 bands and topographical data (based on the mean decrease accuracy tool supplied by the RF algorithm).

Binary segmentation of grassland into “drained” and “poorly-drained” classes was chosen for this study as the review of previous projects had indicated that enforcement of conventional soil drainage classes onto EO-based estimations of soil drainage was inappropriate and resulted in lower overall accuracy (Levine *et al*., 1994; Niang *et al*., 2012). Zhao *et al*. demonstrated how reducing the number of classes by aggregating neighbouring drainage classes increased overall accuracy from 52% to 94% (Zhao *et al*., 2013). More accurate

definition of intermediate drainage classes might be possible with improved spectral resolution. The MDA assessment of the critical Sentinel 2 bands (Figure 4-8) found red-edge bands (~0.68-0.74 µm), which are closely correlated with canopy chlorophyll content (Delegido *et al*., 2011; Pinar & Curran, 1996), were more important than the NIR band as indicators of vegetation health/stress. Future hyperspectral missions such as the EnMAP mission (Guanter *et al*., 2015) may also play a role in future development of this project. EnMAP will capture 230 spectral bands between 0.42 - 2.45 µm at 30 m spatial resolution that will be capable of identifying small differences in chlorophyll concentrations due to underlying stresses. Hyperspectral imagery has been used previously for identifying saturated conditions beneath the surface (Emengini *et al*., 2013) and has been used to good effect for drainage classification (Liu *et al*., 2008).

The lower classification accuracy of the Sentinel 2 classification can be explained by the insufficient archive of images available at the time of the study to identify persistent drainage problems required for this study. As a single image rather than a multi-temporal mosaic, the Sentinel 2 reflectance values were more likely influenced by meteorological conditions immediately prior to the acquisition. The weeks preceding image capture in May 2017 were drier and warmer than long-term averages. This would have had a positive impact on soil condition and vegetation growth on heavy soils in the region. This is likely the explanation for an increase in errors of commission in the accuracy assessment where poorly-drained pixels were misclassified as drained.

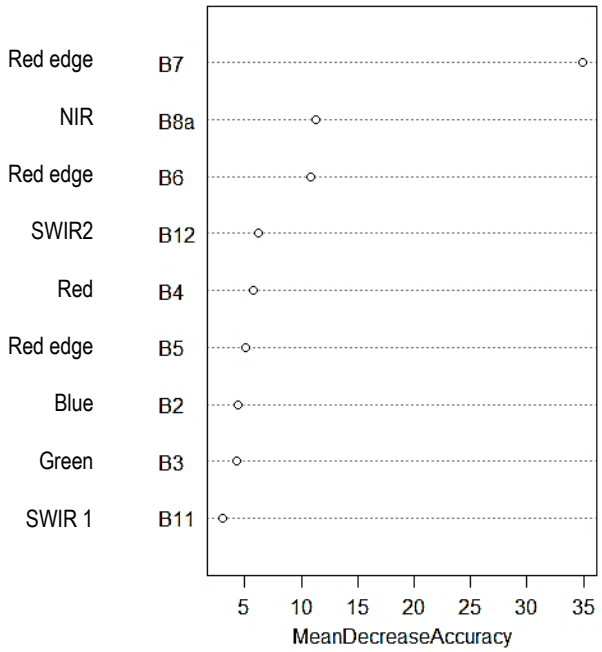

Figure 4-8 Variable importance for Sentinel 2A bands (based on the mean decrease in classification accuracy determined by the Random Forest algorithm)

4.4.3 Temporal improvements

An important result was the identification of temporal changes in spring NDVI values at Farm A in the years following drainage works. The gains in 2016 were notable considering the severe winter storms in 2015-2016 and prolonged soil saturation that persisted into spring 2016. The increase in mean, minimum and maximum NDVI was consistent with improved soil environment following drainage resulting in better grass growth. Kobryn *et al*. identified a similar pattern with temporal improvement in NDVI values after drainage installation that were consistent with measured changes in groundwater levels (Kobryn *et al*., 2015). These results suggest this EO method could serve as a quick and straightforward assessment of drain function, identifying long-term changes in drainage status on farms and as a way of assessing the suitability or functionality of installed drainage works.

There are some caveats to this however. It was not possible to assess NDVI data for surrounding fields to see how they compared to the newly drainage status in Farm A. This was due largely to cloud cover obscuring the surrounding area in one or more years. Use of coarser spatial resolution data (MODIS, for example) to complete the temporal sequence was not an option as the larger pixel size would negate any in-field assessment of drainage improvement. Secondly, different Landsat missions were necessary to complete the temporal series. These satellites have marginally different sensor configurations and band widths, were taken on different dates, from different orbits and viewing angles etc. There is the possiblility that some of the observed increase in NDVI was a product of different sensor specification. Furthermore, these were single date acquisitions. The point has already been raised in Section 4.3.3 that single date images (rather than mosaics) are susceptible to antecedent meteorological conditions, potentially lowering NDVI values. Again, with the relatively small size (3 ha) of the target field, it was fortunate to get a useable image for each of the years (albeit from different sensors). It was not feasible to produce a mosaic of images with mean NDVI values at the required spatial resolution.

4.4.4 Misclassification error

The contributing images to the mosaic had uneven spatial distribution as a result of cloud cover. A consequence of this was areas of the mosaic had less data available to calculate mean values per pixel. The number of contributing images to the mosaic ranged from one to eighteen images. Where there were higher number of contributing images, lower misclassification errors were reported (Figure 4-9). A longer temporal series of images, using both Landsat 8 and Sentinel 2 imagery would allow the study area to be imaged

approximately every three days (Li & Roy, 2017). This would require only minor corrections to compensate for small but consistent differences in reflectance values due to different sensor configurations between the two platforms (Flood, 2017), and the short revisit period could significantly mitigate the loss of data due to cloud occlusion.

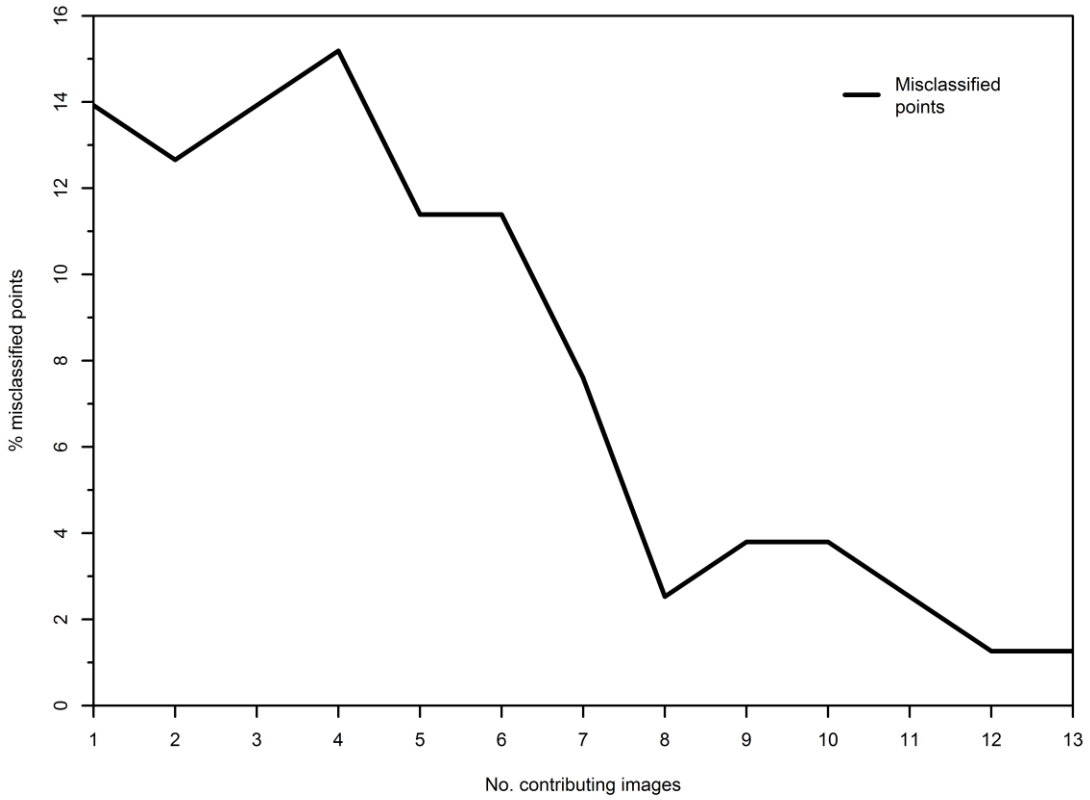

Figure 4-9 Misclassification errors for the best-performing model as a factor of number of contributing images. As the number of contributing images increases the misclassification rate is reduced.

.4.5 Applications and future developments

Precise spatial data on the distribution of artifically drained soils has many applications for agricultural and environmental management. As demonstrated for Farm A, a remote sensing technique to assess field drainage at field-scale could enable better management of farm drainage networks, identifying where drainage infrastructure may require maintenance or replacement or quantifying whether specific drainage treatments have corrected the underlying saturation problem. As discussed previously, one important benefit of a field drainage map could be a better understanding of pathways for diffuse nutrient loss from fields. A clearer demarcation of drainage status on heavy soils could enhance the identification of hydrologically sensitive areas (HSA), discrete regions of farms prone to generating surface runoff and a high risk for diffuse nutrient loss to surface water. Thomas *et al*. demonstrated how a better understanding of hydrological connectivity between HSA and surface drainage networks could help target mitigation measures to reduce such losses from intensively manged farmland (I. Thomas, Jordan, *et al*., 2016; I. Thomas, Mellander, *et al*., 2016). Improved mapping of the discrete locations where saturation may occur, or where infiltration may be impeded, or where these issues have been improved, could help achieve the objectives of the EU Water Framework Directive, to achieve 'good' ecological status in rivers, lakes, estuaries and coastal waters by 2027. Additional EO and RS methods of monitoring or mapping potential pathways for nutrient losses are presented in subsequent chapters. A further potential application is in the administration of farm payments. Functioning field drainage is a diagnostic sign of intensive agricultural activity, therefore any method that can identify artifically drained fields on naturally marginal soils would be a valuable asset in the validation of area-based payments as required under the EU Common Agricultural Policy (CAP). This is particularly important in light of proposed changes to the CAP, announced in

2018, where farmers will be allowed to validate payments using EO or UAS data (EC, 2018). Distinguishing productive grassland from degraded or marginal areas also has a role in more accurate quantification of carbon sequestration potential of Irish farmland (Cawkwell *et al*., 2017).

4.5 Conclusions

Accurate mapping of field drainage is essential to inform specific farm management decisions. It is also critical at a national level to fully understand the broader environmental impacts of agriculture, for example, nutrient enrichment of surface water, GHG emission and carbon sequestration. Existing soil drainage maps are too coarse, or too generalised, to represent accurately the actual soil conditions at a specific location. In this chapter, a new machine learning approach to mapping artifically-drained heavy, grassland soils was assessed using multitemporal, multispectral imagery in combination with topographical data. The method proposed here found the “drained” and “poorly-drained” estimates of soil drainage using the Teagasc/EPA map were incorrect, with an over-estimation of poorly-drained conditions across the region. If correct, this finding could have considerable implications for understanding the potential environmental impacts associated with soil drainage. Future expansion of this study would benefit from the higher spatial, spectral and temporal resolution imagery provided by the Sentinel 2 mission. Additional validation data, based on recent field-observation would give a better assessment of model accuracy. The method also detected temporal changes in drainage status within a specific field following drainage works. The ability of a NDVI time-series to monitor temporal improvements or deterioration in drainage status could be a useful tool for monitoring drainage regime and drainage function at a regional level.

Chapter 5 Performance assessment of UAS photogrammetry and aerial LiDAR for modelling overland flow in intensively managed grassland

5.1 Introduction

Surface runoff from agricultural fields is a leading source of phosphorus (P) in surface water (Schoumans *et al.*, 2014). When P becomes dissolved in water (dissolved reactive phosphorous; DRP) and transported via overland flow to surface waters it can have a detrimental impact on aquatic habitats. In previous chapters, the propensity for runoff to develop on poorly drained soils has been outlined. In the Republic of Ireland, total mean emissions of P to surface water is estimated to be >2700 t yr^{-1} predominantly from heavy grassland soils (Mockler *et al.*, 2017). The precise delineation of source areas and pathways for nutrient loss via overland flow, known as hydrologically sensitive areas (HSA), can permit targeted implementation of best management practices regarding P loss. This may include for example, the implementation of buffer strips or riparian zones or the use of variable application rates for fertilisers. This is a benefit to farmers, as more precisely targeted measures are less costly and disruptive than a broad-scale implementation of remedial measures (Haygarth *et al.*, 2009).

Previous research has shown how high spatial resolution DEM can improve the spatial definition of HSA in agricultural catchments (Agnew *et al.*, 2006; Walter *et al.*, 2000). In most cases, the source of the high-resolution DEM was laser scanning (LiDAR), which is able to accurately resolve fine-scale topographic variation even under dense canopy (Bailly *et al.*, 2008; Brubaker *et al.*, 2013). Thomas *et al.* recently demonstrated the effectiveness of LiDAR for defining HSA in complex agricultural landscapes, where accurate delineation of microtopographic features (gullies, ditches, depressions etc.) had an important influence on understanding nutrient pathways at plot level (I. Thomas, Jordan, *et al*., 2016; I. Thomas, Mellander, *et al*., 2016; I. A. Thomas *et al*., 2017). These papers demonstrated how aerial LiDAR effectively mapped pathways for nutrient loss, delivery points (where pathways intersected surface drains or streams) and breakthroughs (where pathways crossed field- or road boundaries). The identification of delivery points allows mitigation measures to be considered at critical locations of nutrient transfer, which could significantly improve cost-effectiveness (Doody *et al.*, 2012). The high cost of acquiring aerial LiDAR data has largely curtailed its wider adoption within precision agriculture (Xiaoye, 2008). Typically, only areas >500 ha are mapped with manned aerial sensors, with mapping costs in Ireland currently (2018) around €8 ha^{-1}. LiDAR surveys over smaller areas (fields or farms) are typically carried out using a fixed terrestrial scanner that is moved between locations until a full scan of an area is complete. A 25 acre field could, depending on topography and cover, take up 2 days with costs in the region of ~€1000 day^{-1}. Consequenty the costs incolved in surveying small areas may also be prohibitive.

Photogrammetry is a well-established alternative method of topographic modelling which creates 3D geometry from overlapping stereoscopic images (Linders, 2016). Structure-from-motion (SfM) photogrammetry is a relatively new form of photogrammetry that differs from traditional photogrammetric approaches by automatically determining camera position and orientation without the requirement for predefined ground control at known positions (Westoby *et al.*, 2012). Taking advantage of software developments for scene reconstruction (Snavely *et al.*, 2008), automatic feature detection (Lowe, 1999; J. Wu *et al.*, 2013) and dense image matching algorithms (Remondino *et al.*, 2014), SfM photogrammetry has become an affordable alternative to LiDAR and traditional photogrammetry for the creation of dense point clouds for topographic modelling. In addition to advances in image processing software, unmanned aerial systems (UAS) or -vehicles (UAV) have become popular platforms for capturing overlapping image sets suitable for SfM photogrammetric modelling. Consequently, UAS photogrammetry is now widely used for mapping landforms and microtopography (Nouwakpo *et al.*, 2016; Westoby *et al.*, 2012), and is increasingly used for hydrological and environmental modelling and precision agriculture (Grenzdörffer *et al.*, 2008; Salvatore Manfreda *et al*., 2018). An additional benefit of using SfM is that where multispectral imagery is used, additional data for precision agriculture purposes can be collected, for example, creating VI to quantify biomass and canopy health.

A fundamental difference between the two techniques is that LiDAR can reconstruct two forms of topographical model, digital elevation models (DEM) and digital surface models (DSM). A DEM is a model of the bare surface with no intermediate objects present, for example, buildings or vegetation canopy. A DSM is a model of the uppermost surface only, which may

include structures and canopy. Photogrammetry can only produce a DSM, so the characteristics of overlying vegetation have a significant impact on the accuracy of modelled surface elevations. A recent study, focusing specifically on topographical accuracy of a UAS-derived DSM, found DSM can accurately model terrain attributes in grassland environments, and that DSM models of grassed surfaces were suitable for modelling hillslope processes and identifying microtopographic features (Florinsky *et al.*, 2017). This suggested UAS photogrammetry could accurately model runoff processes at field scale on intensively managed grassland.

Users of SfM photogrammetry must be aware of important sources error that can be introduced to models from inappropriate flight altitude and pattern, poor scene contrast or image quality, insufficient overlap, unsuitable sensor type or viewing angle (Carravick *et al.*, 2016; S. Manfreda *et al.*, 2018). However, where potential error sources are managed correctly, users can produce centimetre accurate topographical models comparable to LiDAR (Fonstad *et al.*, 2013; Harwin & Lucieer, 2012; Nouwakpo *et al.*, 2016). Measured ground control points (GCP) evenly distributed over a study area are crucial for mitigating positional errors that are introduced by the reconstruction process and are recommended for creating accurate models (Küng *et al.*, 2011). Advances in low cost (< €5000) post process kinematic (PPK) UAS systems have reduced the need for independent GCP to some degree. PPK corrects UAS location after images have been captured reducing the time required on-site for placing and recording suitable ground control and providing models with ~3 cm positional accuracy.

Currently, the cost of a suitable UAS capable of conducting photogrammetric surveys is <€1000. Suitable processing software is available, but licence costs can be prohibitive. Cloud-based commercial licences can be as low as ~€200 per month, however. Open-source software options are also available (for example visualSFM, MICMAC or Open Drone Map) but may not be intuitive to non-professional users. Inspite of these costs, photogrammetric models for delineation of HSA is still a significantly cheaper option for farmers than either aerial or terretsrial LiDAR. The question posed in this chapter is how photogrammetric models compare with LiDAR models for estimating nutrient losses in overland flow.

This project aimed to compare surface models created by aerial LiDAR and structure-from-motion (SfM) photogrammetry for modelling surface runoff from intensively managed grassland. The objectives of the study were to:

- Establish the accuracy of photogrammetric DSM and LiDAR DEM against GNSS-measured elevations.
- Compare derivative products (slope and topographic wetness) and overland flow/ P-loss estimates generated by each method.
- Investigate the relationship between vertical error in modelled photogrammetric elevation and sward height and topographic gradients.
- Identify the grid resolution at which SfM and LiDAR models of overland flow and P-loss are most similar for this study area.

5.2 Materials & Methods

5.2.1 Study Area

The study was conducted within a mixed agricultural catchment in the Republic of Ireland (53°49'33'' N, 6°26'28'' W; Figure 5-1). It was located within the extent of a previous Teagasc research project, the Agricultural Catchments Programme (ACP), which was established in 2008 to provide a comprehensive evaluation of the effectiveness of the Nitrates Directive NAP and Good Agricultural Practices measures in Ireland at the farm and catchment scales. LiDAR data had been previously collected over the catchment for research on modelling HSA (I. Thomas, Jordan, *et al*., 2016; I. Thomas, Mellander, *et al*., 2016; I. A. Thomas *et al*., 2017). In previous studies, this catchment was designated "Arable B" and this nomenclature is retained here.

The specific area of interest was a nine-hectare pasture field subdivided into seven paddocks under grazing rotation. Topographically, the site was characterised by a steady elevational gradient from the NE to SW (60-77 m above sea level). A prominent scarp ~3 m high along the northern boundary began at the western edge and extended eastwards for approximately 300 m Using the Irish Soil Information System, soils in the study area were classified as moderately-drained clay loam Luvisols (Clongeel series), with an estimated soil depth of 1.38 m (Creamer *et al*., 2014). The underlying geology was calcareous greywacke & banded mudstone (Salterstown Formation) (GSI Geological Map Series 100k scale).

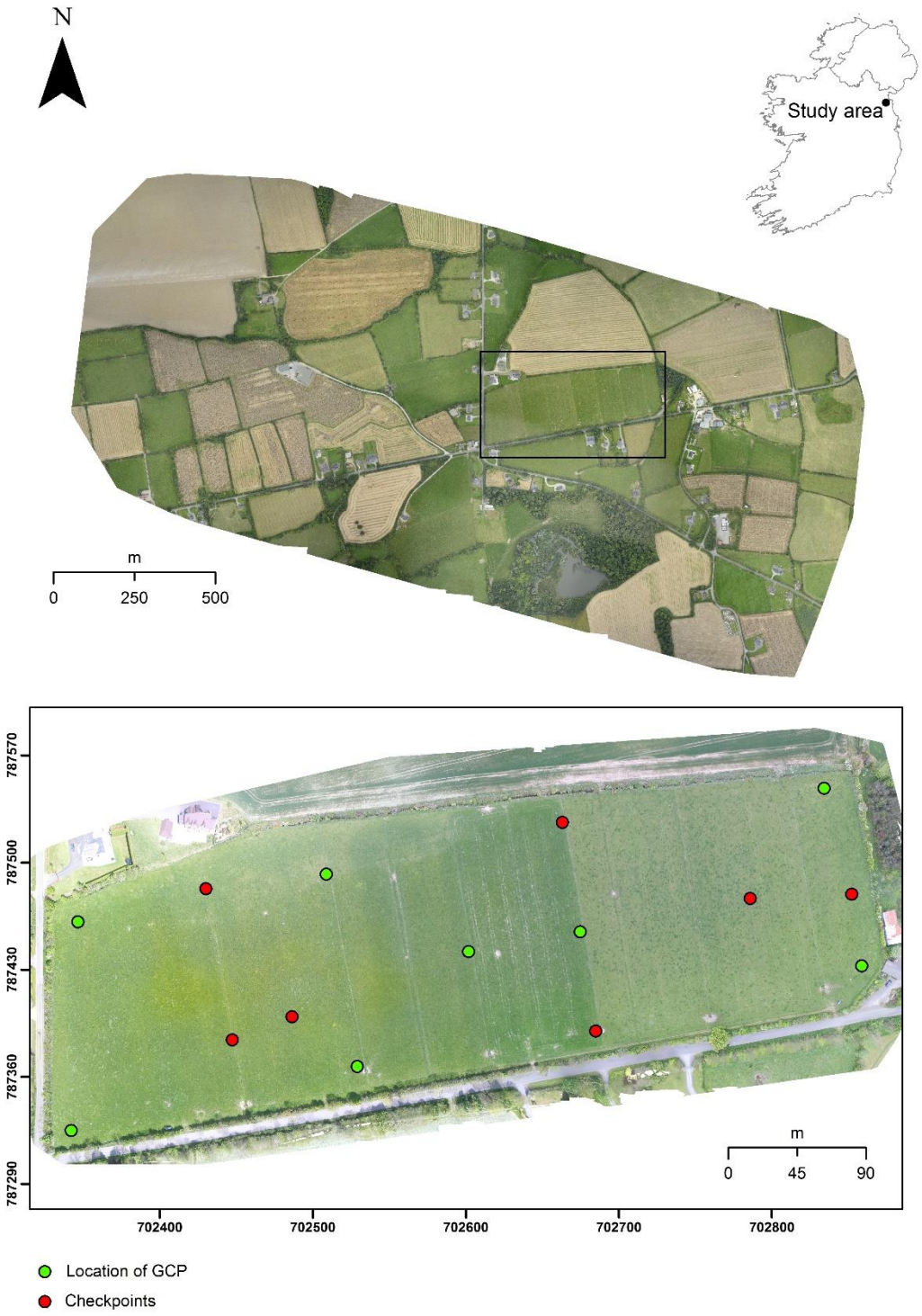

Figure 5-1 Location of study area (inset). (top) Imagery acquired during the manned flight (Sept. 2015). (bottom) Imagery acquired during UAS survey (May 2017) (CRS: Irish Transverse Mercator; EPSG 2157).

There were differences in sward height between paddocks due to the practice of rotational grazing. Mean grass canopy height across all paddocks was 0.16 m (+/- 0.09 m). At the time of the UAS flight, the easternmost paddocks had been recently grazed and had less cover than the westernmost paddocks. In other areas, small areas of the canopy had been removed due to poaching (grass cover removed) around water- or feeding troughs. Elsewhere, canopy height was observed to be higher due to the presence of weeds clusters within the sward. Sward height was measured using two steel tapes. One was held vertically perpendicular to the ground surface, while the other was run along it until it rested on the sward. The location of each measurement was recorded using a Trimble R8 5800 GNSS RTK unit (+/- 0.02 m positional accuracy).

5.2.2 Data Collection

Three separate periods of data collection contributed to this study:

An airborne (helicopter) LiDAR survey was conducted over the catchment in December 2011 as part of the Agricultural Catchments Programme. LiDAR data was collected at an altitude of 275 m above ground level. Point density was ~40 points/m^2. Mean vertical accuracy for the survey was reported to be 0.03 m (+/- 0.014 m) based on ground control points (GCP) established across the entire catchment.

Aerial imagery was acquired from a manned flight in September 2015. A Cessna C-172 carried a suite of sensors which included RGB images from a Nikon D800E 36 MP SLR (Cahalane *et al.*, 2017).

Low-altitude imagery was acquired in May 2017 using a 12 MP, gimbal-mounted RGB camera on a DJI Phantom 3 Advanced quadcopter. The UAS missions were flown semi-autonomously using Pix4D Capture mission control software.

Flight specifications for each flight are presented in Table 5-1. GCP and independent checkpoints were located within the footprints of each flight and recorded using a Trimble R8 5800 GNSS RTK unit (+/- 0.02 m positional accuracy).

Table 5-1 Specifications for the manned and unmanned flights

	Aerial	**UAS**
Altitude (m)	~500	70
Survey area (ha)	261	9
Along-track overlap	60%	90%
GSD (cm/pixel)	6	3
Camera angle	90°	80°
Footprint (m)	300 x 200	120 x 90
Sensor width (mm)	35.9	6.17
Focal length (mm)	50	3.61
No. images	108	659
Flight time (mins)	~11	~30

5.2.3 Point cloud creation

Photogrammetric software has made the processing chain from 2D images to 3D geometric model relatively straightforward with minimal requirement for user intervention. Agisoft and Pix4D are popular, commercial desktop- or cloud-based packages that provide end-to-end processing chains for point cloud, mesh and orthomosaic production (AgiSoft, 2016; Pix4D, 2017). These follow similar processes of feature extraction and matching, bundle block adjustment and point cloud densification. However, detailed information on the algorithms used are commercially sensitive and not publicly available. Open-source software options are available but are often not appealing to non-professional or non-research users. One example is VisualSFM is a free, GUI-based software which uses a suite of open-source algorithms for feature detection, feature matching and sparse cloud reconstruction. It also integrates an external patch-based multi-view stereo algorithm for dense point matching (Furukawa & Ponce, 2010; C. Wu). As these software utilise different algorithms within their workflow, the point clouds produced by each method are different. The point cloud generated by Pix4D had the lowest positional RMSE against GCP and independent checkpoints and was used exclusively in subsequent analysis (see Table 5-2). A mimimum of 3 GCP are typically the required to geolocate (scale, orient, position) a project. Eight ground control points were used to georeference this project. Checkpoints are not used in geolocating the project, but are used to assess the absolute accuracy of the model. Seven check points were used in this project. The same GCP and checkpoints were used for each of the three software. The same GCP and checkpoints were used for each of the three software.

Table 5-2 Quality assessment of the photogrammetric point clouds versus GCP and independent checkpoints.

	UAS			**Aerial**
	Pix4D	Agisoft	VisualSFM	Pix4D
Mean points per image	41,593	40,000	11,329	69,237
Mean matched points per image	14,872	4,000	--	32,159
Total no. points (x 10^6)	66.46	56.93	22.54	51.11
Mean no. points (per m^2)	485	285	221	21
RMSE / ground control (m)	0.02	0.035	0.42	0.05
RMSE / checkpoints (m)	0.03	0.05	--	0.16

5.2.4 Gridded raster data

To compare LiDAR and photogrammetric topographic models, gridded raster data were created for terrain attributes that influence the magnitude and direction of movement of surface water. Raster data were generated at four spatial resolutions (0.5 m, 1 m, 2 m and 5 m) from raw point clouds using the LAS to DEM tool (ArcGIS 10.5, Conversion toolbox). Terrain attributes were created using open source GIS software (Geographic Resources Analysis Support System (GRASS, v. 7.4) and System for Automated Geoscientific Analyses (SAGA, v.6.2.0.). Elevation data were initially hydrologically corrected to ensure fully connected flow paths using SAGA GIS (L. Wang & Liu, 2006).

Variables included:

Slope. Slope characterises the magnitude and direction of surface runoff. A choice of several algorithms was available.Comparative studies indicated different algorithms perform identically in most cases (Hodgson, 1998). The 9-parameter 2nd order polynomial algorithm used in this study is a popular choice in slope modelling (Zevenbergen & Thorne, 1987).

Topographic wetness index (TWI). TWI is also widely used to measure general landscape wetness or as an indicator of the propensity of an area to generate overland flow (Beven & Kirkby, 1979). It is defined by Equation 5.1. Specific upslope area indicates the volume of water flowing towards a particular position of landscape location while local slope angle is assumed to reflect subsurface lateral transmissivity (Grabs *et al.*, 2009; Sørensen & Seibert, 2007). TWI can be derived in several ways based on the how flow movement is modelled. Two TWI were produced using single- and multiple flow-routing algorithms, D8 (O'Callaghan & Mark, 1984) and MD∞ (Seibert & McGlynn, 2007), to explore whether more complex flow routing algorithms used to define upslope contributing area produced different results.

$$TWI = \ln(a/\tan \beta) \qquad \text{(Eqn. 5.1)}$$

where a is the specific upslope area (i.e. the upslope area per unit contour length) and tan β is the local surface slope.

An additional method of delineating potential pathways for P loss was an implementation of the Simulated Water Erosion model (SIMWE) developed for the Water Erosion Prediction Project (WEPP). Implemented through a GRASS GIS module (r.sim.water), this tool was designed to replicate high resolution (≥ 1 m) surface flow in small catchments with variable topography, soil type and land cover (Mitas & Mitasova, 1998; Mitasova *et al.*, 2004). The inputs are an elevation model (DEM or DSM), first-order partial derivatives of elevation (dX and dY), rainfall and soil infiltration rates and surface roughness (Manning's *n* coefficient). Simulations here assumed a very heavy storm event (20 mm/h) on a low infiltration soil (5 mm/h) to ensure sufficient flow paths were initiated. The Manning's coefficient for surface

roughness (*n*= 0.15) was based on published estimates of flow through short grass/pasture (Engman, 1986). Within SIMWE, flow is modelled as a kinematic wave with a diffusion term to enable flow to overcome minor depressions or obstacles when encountered (Hofierka & Knutová, 2015). The algorithm has recently been applied to urban overland flow mapping using UAS-derived elevation models (Jeziorska *et al.*, 2016). Overland flow estimates generated by SIMWE were subsequently used to model potential P loss by applying a DRP concentration of 0.03 mg/l to modelled overland flow rates (m^3/s) to give estimated losses of P (kg yr^{-1}).

5.2.5 Statistical analysis

Statistical analysis was undertaken with R statistical software (v. 3.4.4). Where bootstrapping occurred for correlation coefficients and R^2 values, the study used 10,000 replications of 138 data points using bias-corrected 95% confidence intervals. Simple linear regression determined how much variability in LiDAR-derived products could be explained by photogrammetric methods and identified the grid size at which the methods were most similar. Welch two-sample t-tests were used to test the hypothesis that both models had equal means. The Welch t-test was favoured because it is robust against non-normal distributions when the sample size is ≥ 15 per group and doesn't assume equal variance.

5.3 Results

5.3.1 Modelled elevations versus GNSS-measured points

When compared against GNSS-measured spot heights within the study area, both photogrammetric and LiDAR methods displayed strong, positive correlation with surveyed elevations ($R^2 \geq 0.99$, $p < 0.001$) (Table 5-3). These statistics are an effective way of determining global values over the map. It is acknowleged that descriptive statistics such as these cannot adequately capture the heterogeneity in the distribution of spatial error across the study area. Readers are referred to Section 5.3.5 for further discussion on the spatial distribution of error at this site as a function of sward height. Extracted spot heights from each of the model types indicated that both LiDAR and photogrammetry consistently overestimated measured elevations. Absolute mean and median vertical error (i.e. abs(measured height – modelled height)) for both models was in the range 0.12-0.15 m. Maximum vertical error was greatest for SfM DSM. The lowest RMSE (0.15 m) was achieved by LiDAR (50 cm, 1 m and 2 m resolution). RMSE for SfM-derived models was constant across resolutions (~0.17 m), and was highest for model created from the manned flight (0.21-0.24 m). Difference raster (DEM minus DSM) at each resolution illustrated the spatial distribution of vertical error between the two methods. Mean error was typically between 0 and +/- 0.2 m. In Figure 5-2, red/blue areas indicate where the DSM elevations were lower/higher than the LiDAR DEM. The cause of this distinct spatial pattern could be related to observed changes in sward height between paddocks. The area was under rotational grazing, where the westernmost paddocks had not been grazed for several days. These had greater sward cover than the eastern paddocks which had been recently grazed. At each resolution (50 cm, 1 m, 2 m and 5 m) mean error (+/- std. dev.) between the corresponding elevation rasters was 0.002 m (+/- 0.1 m), 0.003 m (+/- 0.1 m), 0.03 m (+/- 0.1m) and 0.06 m (+/- 0.11 m) respectively.

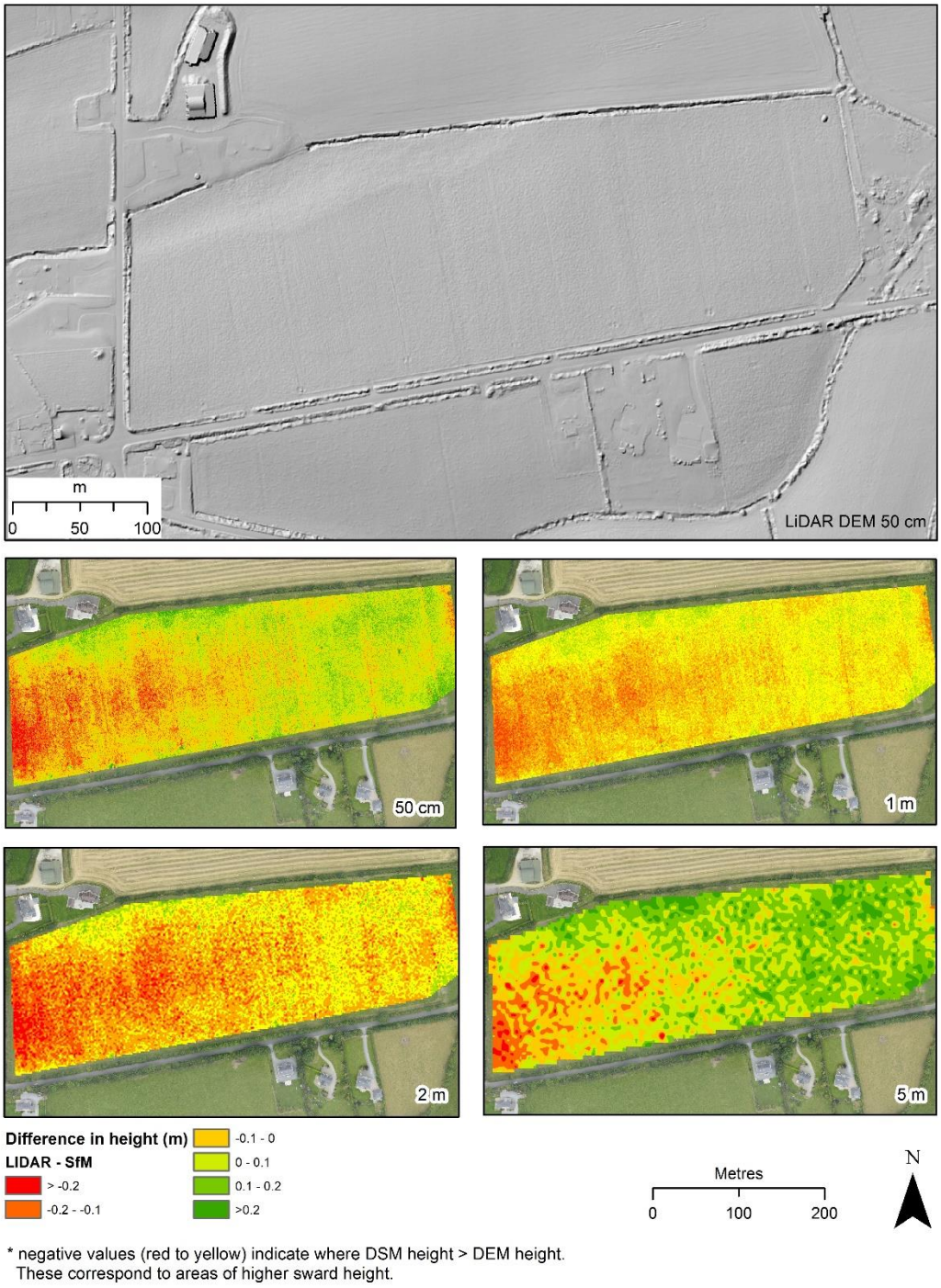

Figure 5-2 Difference of models at varying resolutions for photogrammetry vs LiDAR elevations. Areas in red indicate locations where photogrammetry heights were lower than LiDAR. Blue indicates areas where photogrammetry heights were greater than LiDAR. These height differences correspond to different sward height across the paddocks.

Table 5-3 Summary statistics for vertical error, slope, TWI and surface discharge created by LiDAR and photogrammetry (UAS and aerial)

		UAS				Aerial				LiDAR			
		0.5 m	1 m	2 m	5 m	0.5 m	1 m	2 m	5 m	0.5 m	1 m	2 m	5 m
vertical error (m) vs GNSS	RMSE	0.18	0.18	0.17	0.17	0.21	0.21	0.21	0.24	0.15	0.15	0.15	0.18
	Mean	-0.14	-0.14	-0.12	-0.12	-0.14	-0.14	-0.12	-0.14	-0.14	-0.14	-0.14	-0.15
	Median	-0.14	-0.13	-0.12	-0.11	-0.13	-0.13	-0.12	-0.12	-0.14	-0.14	-0.14	-0.16
	St. dev.	0.12	0.11	0.12	0.11	0.16	0.16	0.16	0.19	0.05	0.05	0.05	0.09
	Minimum	-0.41	-0.39	-0.44	-0.41	-0.15	-0.17	-0.25	-0.3	-0.25	-0.25	0.005	-0.41
	Maximum	0.17	0.13	0.20	0.17	0.48	0.48	0.49	0.57	-0.03	-0.03	0.005	0.11
Slope °	Mean	4.8	3.1	3.2	3.1	4.2	3.3	3.3	3.2	3.9	3.3	3.1	3.1
	Median	4.4	2.9	3	2.9	3.7	2.8	3.3	3.2	3.4	3.2	3.1	3
	St. dev.	2.6	1.5	1.4	1.3	2.5	1.7	1.4	1.2	1.9	1.4	1.3	1.2
	Minimum	0.53	0.2	0.28	0.36	0.55	1.1	0.61	0.39	0.13	0.4	0.41	0.49
	Maximum	14.6	9.3	8.4	8.5	13.2	9.1	8.5	8.5	10.1	10.3	9.7	8.1
TWI	Mean	2.7	4.1	5.1	6.3	3.5	4.9	6.1	6.7	3	4.1	5.3	6.2
	Median	2.2	3.3	4.3	6	3.1	4.7	6.2	6.7	2.6	3.5	4.9	6
	St. dev.	1.3	1.7	1.8	1.5	1.6	1.4	1.5	1.2	1.4	1.7	1.8	1.3
	Minimum	0.82	2	2.8	4	1.2	2.2	2.9	4.2	1.2	2.2	2.9	4.2
	Maximum	7.3	8.3	10.2	11.6	7.7	8.7	10.2	11.4	9.8	10.7	11.7	9.1
Overland flow (l/s)	Mean	n/a	0.4	0. 8	2	n/a	0.3	0.8	2	n/a	0.4	0.8	2
	Median		0.3	0. 7	2		0.2	0.5	2		0.3	0.7	2
	St. dev.		0.4	0.6	1		0.4	0.9	2		0.3	0.6	1
	Minimum		0.01	0.02	0.06		0	0	0. 03		0.02	0.02	0.09
	Maximum		3	3	6		2	4	8		2	4	6

5.3.2 Comparison of slope and Topographic Wetness Index values

The boxplots in Figure 5-3 illustrate the distributions of attribute values for each model/resolution. In each case, there was a low range of values due to relatively homogenous terrain within the study area. Median slope values and their interquartile ranges displayed exhibited greater correspondence as spatial resolution became coarser. TWI distributions displayed greater variability. Scale-related trends were observed whereby slope values decreased, and TWI values increased as spatial resolution increased.

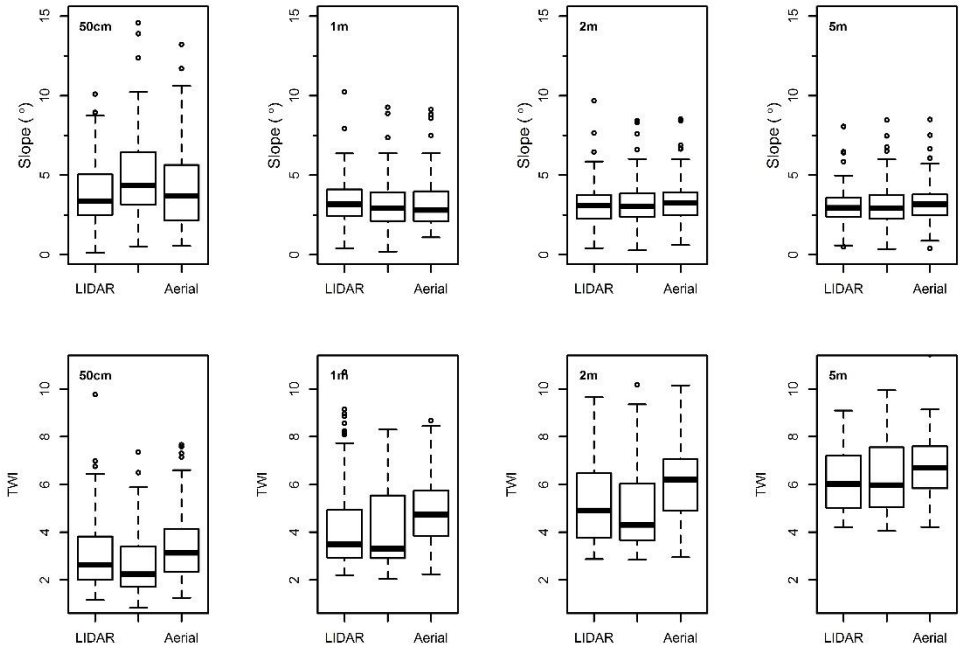

Figure 5-3 Distribution of slope and TWI values derived from LiDAR DEM and SfM DSM

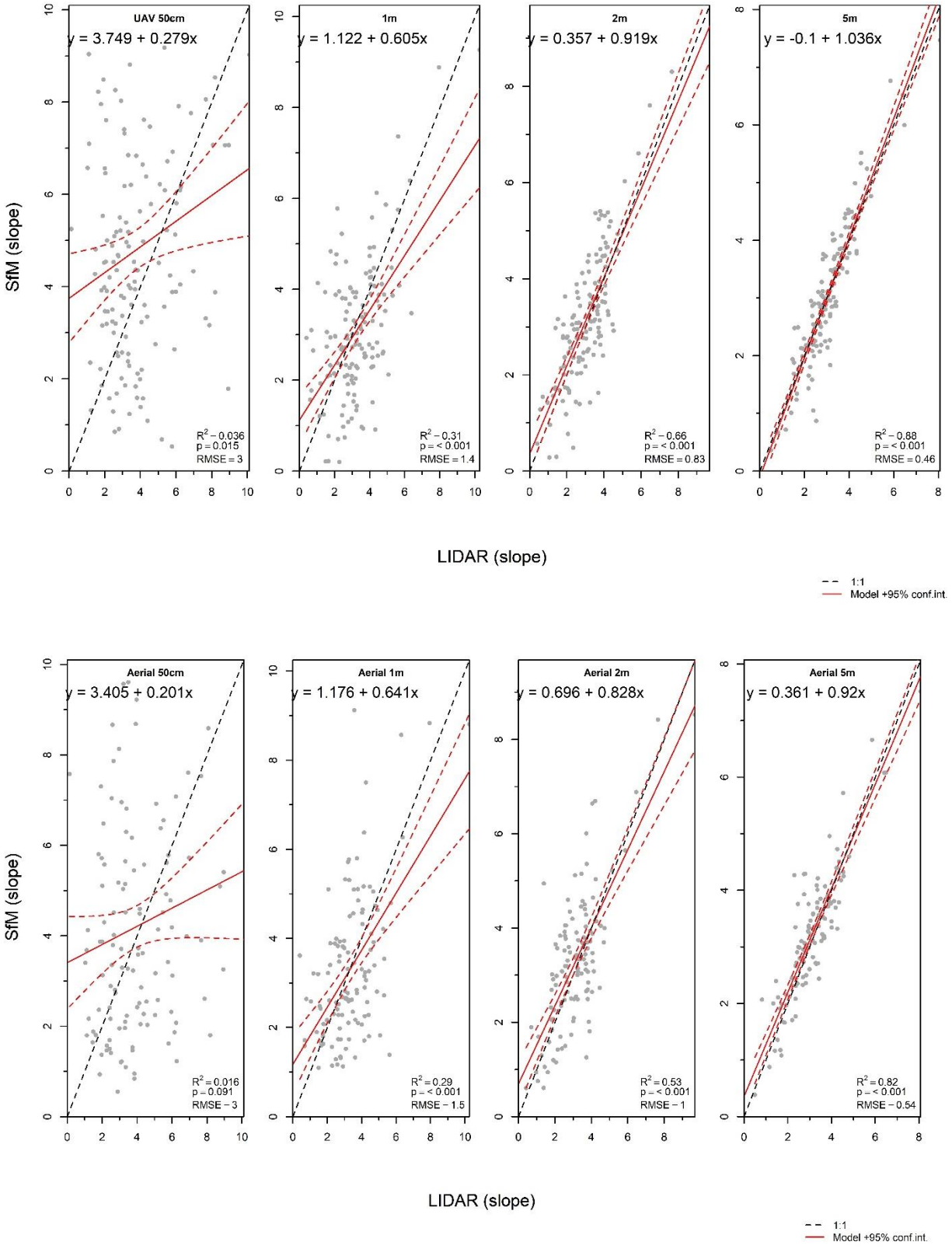

Figure 5-4 Linear regression of LiDAR-derived slope versus SfM-derived slope (a) UAS (top) and (b) aerial (bottom).

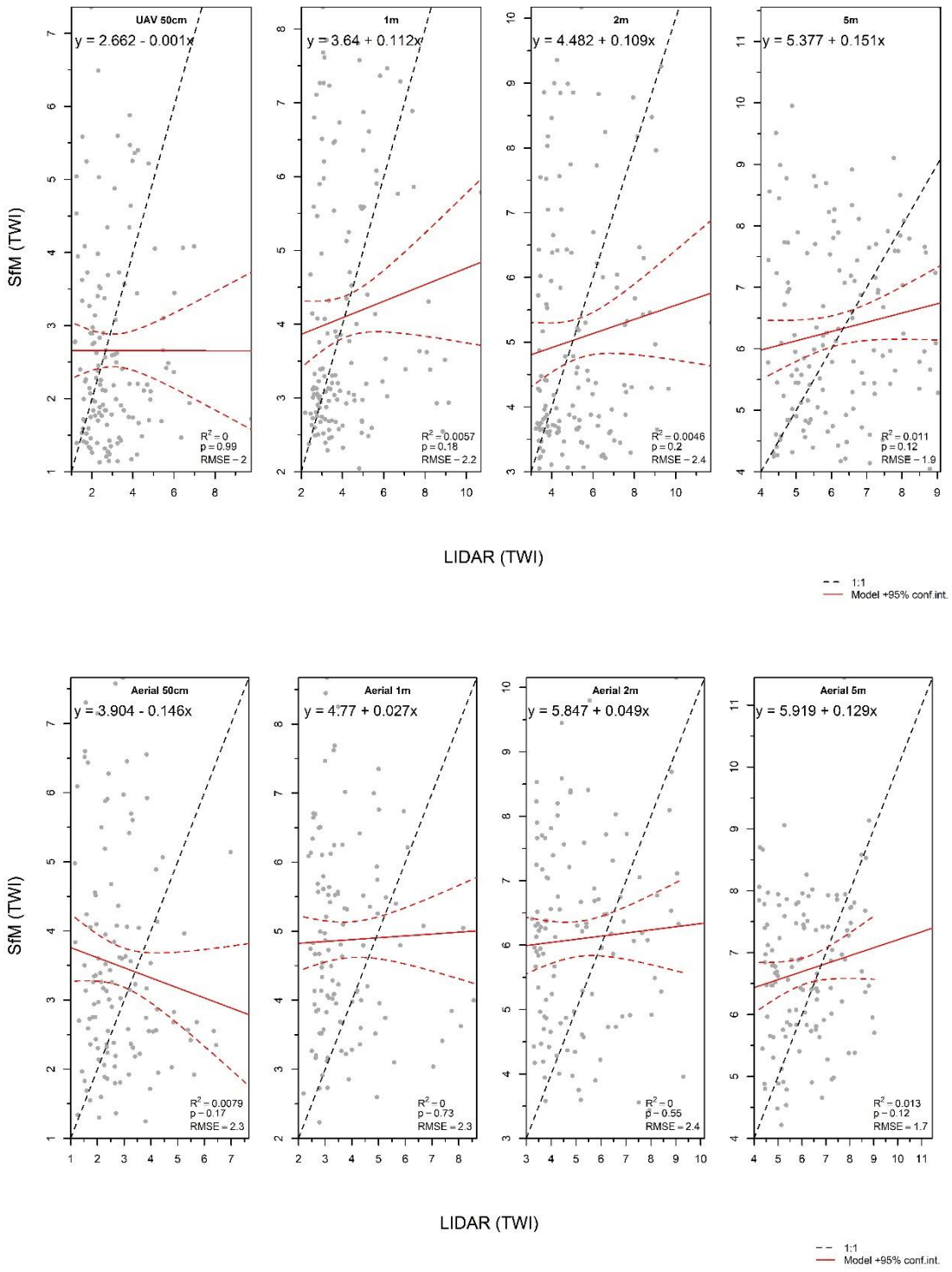

Figure 5-5 Linear regression of LiDAR-derived TWI versus SfM-derived TWI (a) UAS (top) and (b) aerial (bottom).

For slope, weak correlation between methods was observed at 50 cm resolution (0.20, 95% CI [0.05, 0.34]). However correlation coefficients increased linearly at 1 m (0.57, 95% CI [0.41, 0.72]), 2 m (0.81, 95% CI [0.72, 0.87]) and 5 m (0.83, 95% CI [0.69, 0.91]). All regressions were significant ($p< 0.05$) with a steady reduction in RMSE as ground sampling distance increased (3°, 1.4°, 0.83° and 0.46° respectively). Slopes derived from the manned flight performed similarly (R^2= 0.01 at 50 cm (95% CI [0, 0.08])), increasing linearly at 1 m (0.29, 95% CI [0.12, 0.50]), 2 m (0.53, 95% CI [0.34, 0.70]) and 5 m (0.82, 95% CI [0.70, 0.89]) (Figure 5-4).

TWI created from the DEM and DSM demonstrated weak correlation at all resolutions. It was assumed that irregular sward height resulted in top of canopy slopes that were uncorrelated with the terrain slope of the underlying surface. Slope rasters had far greater correlation, which increased as resolution became coarser. The issue must therefore be in other data contributing to the TWI, the upslope contributing area, which measures the number of pixels draining into a given pixel. It was also unusual that correlation did not improve at coarser resolutions. Linear regression between the DSM TWI and DEM TWI had very high variability with R^2 at or near zero in each case (Figure 5-5). At 50 cm resolution, no clear trend was observed ($p=0.88$), but significant trends were observed at 1 m, 2m and 5 m despite low R^2 values ($p= 0.03$, 0.01 and 0.05 respectively). This was also found for TWI derived from the manned flight (R^2 ~0; $p >0.05$). A series of low pass filters were applied to the TWI images reduced local variation between surrounding cells, improving the R^2 values between DEM and DSM, particularly at 2m and 5m where filtered $R^2 = 0.60$ and $R^2 = 0.70$ respectively.

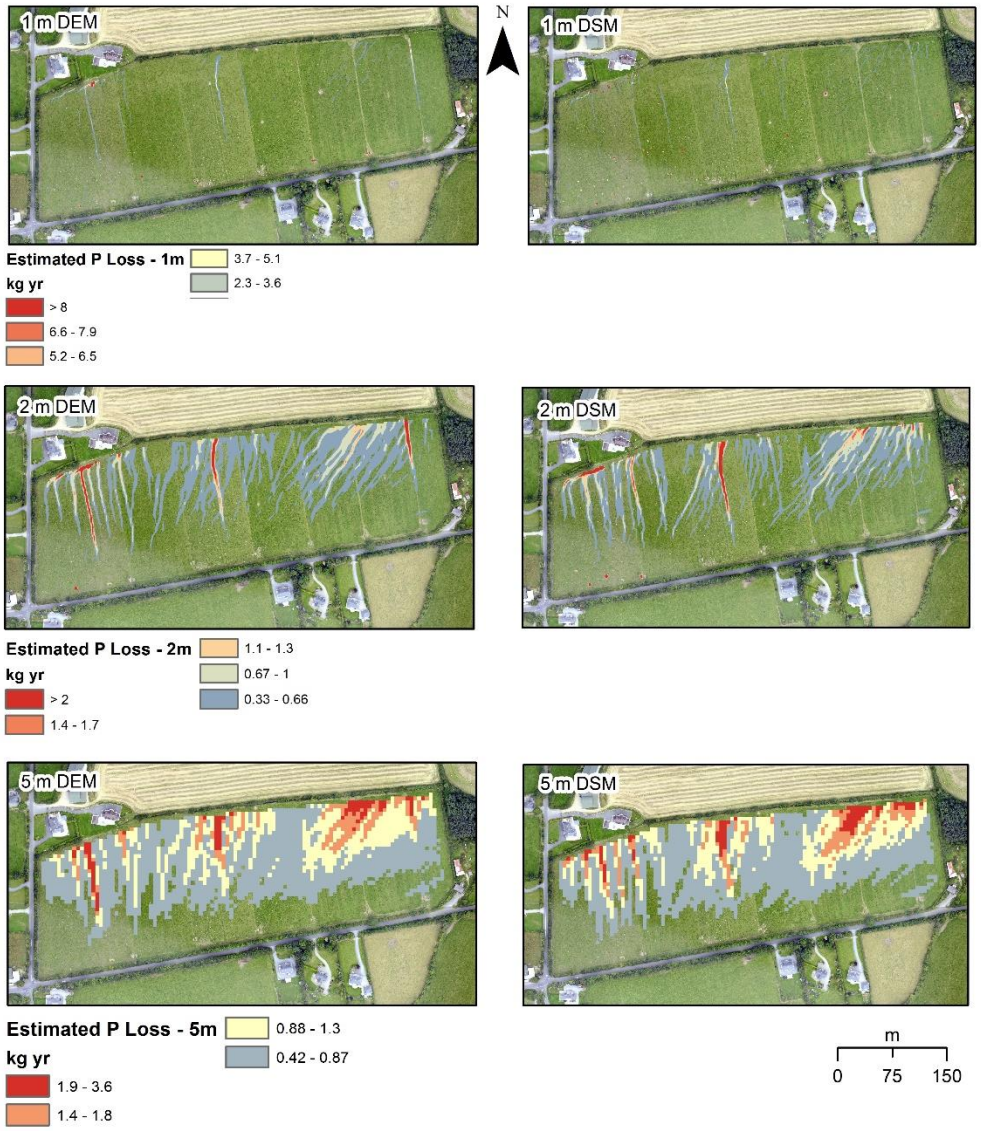

Figure 5-6 Modelled P-loss (kg yr^{-1}) using overland flow rates (m^3/s) estimated by SIMWE models developed from LiDAR DEM and UAV DSM at 1 m, 2 m and 5 m resolution. P concentrations of 0.03 mg/l were assumed.

5.3.3 Overland flow

5.3.3.1 Definition of pathways

Using SIMWE, both LiDAR and SfM models delineated pathways for overland flow (see Figure 5-6). The required raster were inputted into the model (see Section 5.2.4 for implementation). At 1 m resolution, LiDAR identified three main pathways running N-S through the site, running into an E-W running ditch along the northern boundary. Other pathways running SW-NE were identifiable in the NE of the study area. If LiDAR is assumed to represent ground conditions, the equivalent SfM DSM at this resolution over-predicted the number of potential pathways running into the E-W ditch along the northern boundary. At 2 m, each method highlighted coterminous problem areas, even where individual flow paths within these areas diverged somewhat. SfM DSM still over-predicted the number of potential pathways. At 5 m pathways defined by the models were largely indistinguishable, with comparable areal extent and flow rates (m^3/s) recorded.

5.3.3.2 Estimated flow and P loss

Modelled discharge rates (litres per second) via overland flow using each method are presented in Table 5-4. Bootstrapped Pearson's correlation coefficients between DSM and DEM overland flow volumes exhibited moderate correlation at 1 m (0.49, 95% CI [0.24, 0.63]), increasing at 2 m (0.79, 95% CI [0.69, 0.85]) and 5 m (0.96, 95% CI [0.95, 0.98]). Regression analysis was significant at each grid resolution ($p< 0.001$). R^2 values also increased from 1 m (0.24, 95% CI [0.05, 0.40]), 2 m (0.62, 95% CI [0.47, 0.72]) to 5 m (0.93, 95% CI [0.90, 0.96]). Applying a low-pass filter to the 1 m model improved R^2 values to 0.43 (95% CI [0.22, 0.67]), 0.72 (95% CI [0.59, 0.84]) and 0.88 (95% CI [0.77, 0.94]) using 3 x 3, 5 x 5 and 7 x 7

neighbourhoods. Discharge estimates based on the aerial survey were also significant (p= 0.01, p< 0.001 and p< 0.001) but displayed greater variability (1 m: R^2= 0.05, 95% CI [0.002, 0.11]; 2 m: R^2= 0.25, 95% CI [0.14, 0.44]; 5 m: R^2= 0.33, 95% CI [0.18, 0.46]).

Table 5-4 Summary statistics for water discharged (l s^{-1}) per model/ resolution

	1 m		2 m		5 m	
	DSM	DEM	DSM	DEM	DSM	DEM
Min	0.01	0.02	0.02	0.02	0.06	0.09
Mean	0.36	0.37	0.77	0.75	1.91	1.92
Median	0.27	0.27	0.66	0.66	1.73	1.80
SD	0.34	0.30	0.55	0.52	1.21	1.19
Max	2.74	1.96	2.82	3.40	5.53	5.36

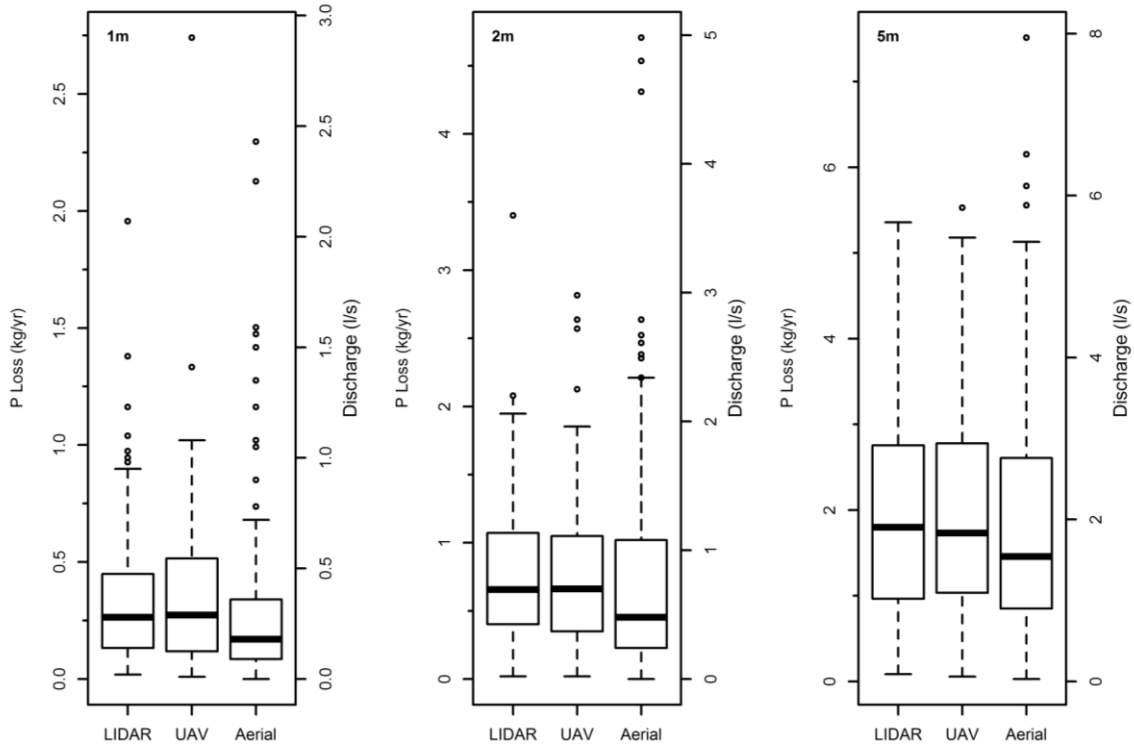

Figure 5-7 Distribution of modelled surface discharge (l/s) and estimated P loss (kg/yr^{-1}) per model/ resolution

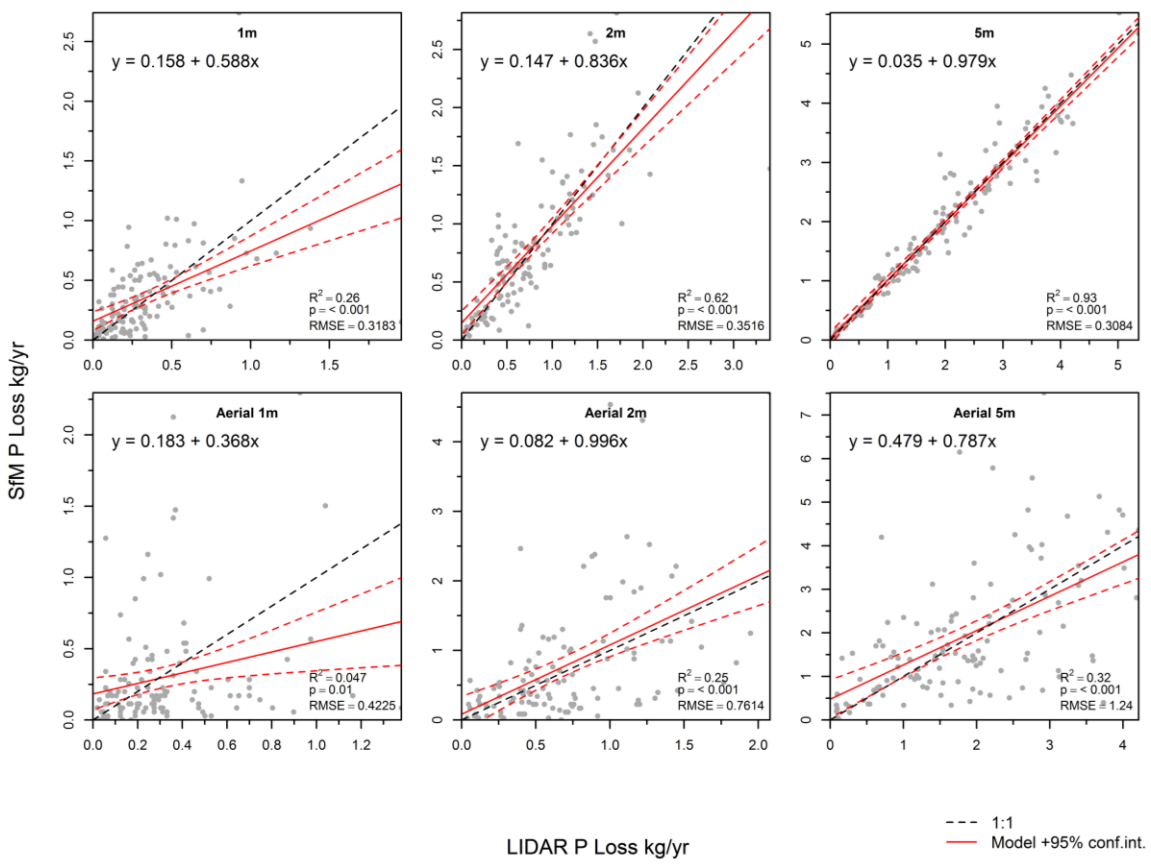

Figure 5-8 Regression of P loss (kg yr^{-1}) by model/ resolution (UAS (top) and aerial (bottom)).

By applying a DRP concentration (0.03 mg/l) to the flow rates (m^3/s) outlined above, it was possible to estimate P loss (kg yr^{-1}) for each method/resolution (Figure 5-7). Regression analysis was significant at each resolution for LiDAR versus UAS DSM ($p< 0.001$) with R^2 values increasing as grid size increased (R^2=0.26 (95% CI [0.07, 0.42]), 0.62 (95% CI [0.47, 0.72]) and 0.93 (95% CI [0.90, 0.96]).respectively) (Figure 5-8).

5.3.3.3 Identifying breakthroughs

A disadvantage of the SfM method the inability to measure beneath the canopy, which an issue for identifying breakthrough points along hedgerows. Depending on local hedge condition, breakthrough points may be wholly-occluded by overhanging canopy. There be occasions where field-to-field or field-to-road transfers can be resolved. During the manned flight, which had a wider footprint than the UAS survey, several breakthrough points at 2 m resolution that corresponded to breakthroughs the LiDAR DEM (Figure 5-9). SfM was not consistent; howeverA further challenge is inability to identify surface drainage beneath vegetation. If the locations known, they could be accounted for during model processing by modifying the DEM (Callow *et al.*, 2007). If the objective is to characterise hydrology within a single field, then such corrections may not be necessary. Single-field surveys are more suited to small UAS operating on a single battery as most non-expert users are likely have. This would also allow for greater control over ground conditions at the time of the survey, for example, post-grazing or post-harvest surveys will ensure low grass cover.

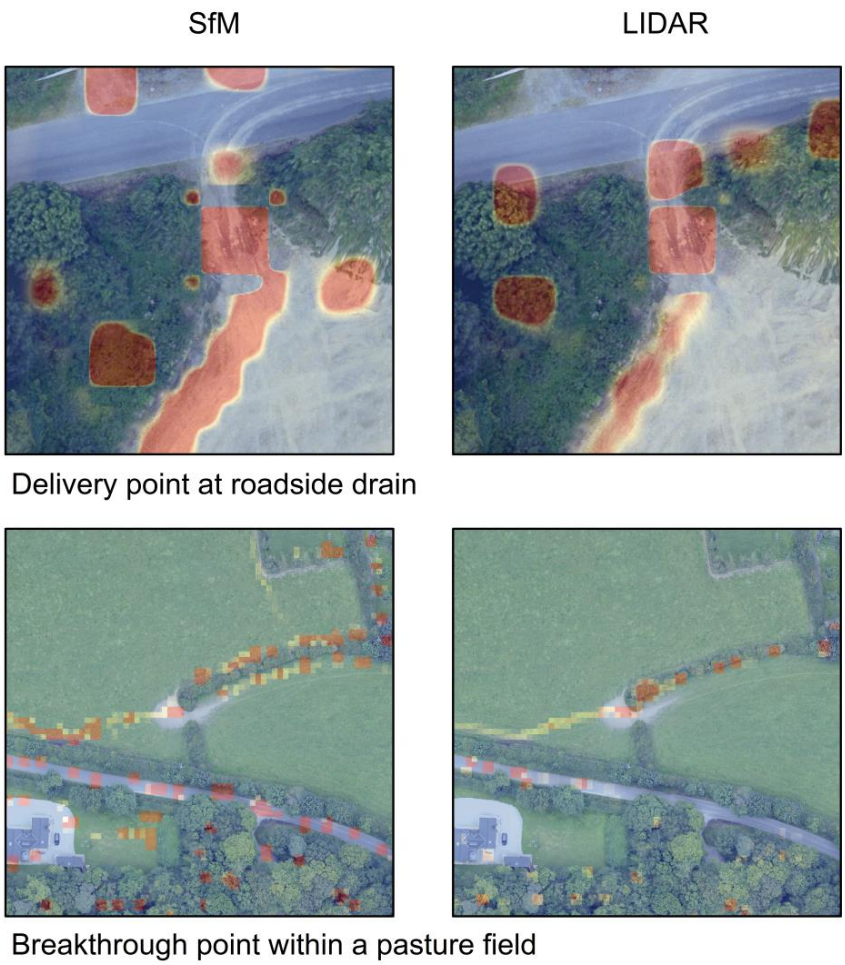

Figure 5-9 Identification of breakthrough points through boundaries on 2 m resolution topographical models.

5.3.4 Statistical tests

Welch's t-tests for unequal variances were conducted on slope, TWI and P loss/overland flow raster values to determine whether there were statistical differences between models. For each test, the null hypothesis was that mean attribute values were equal. The alternative hypothesis was that they were not equal ($\alpha = 0.05$). At 50 cm resolution for slope and TWI, the null hypothesis was rejected ($p < 0.001$ and $p = 0.01$ respectively), and it was concluded models derived from each technique were statistically different. At 1 m and above, the null

hypothesis could not be rejected with no evidence the models were different. For overland flow and P-loss estimates at all resolutions, the null hypothesis could not be rejected with no indication the models were different ($p > 0.05$ at 1 m, 2 m and 5 m resolution (Table 5-5). This indicated that when using the SIMWE model to calculate overland flow and associated P loss on managed grassland, there was no statistical difference to the final outputs whether a LiDAR DEM or a photogrammetric DSM were used to create the contributing topographical layers.

Table 5-5 Welch's t-tests for differences between model type/ resolution for slope, TWI and P loss via overland flow

Slope	t-test	
	t (df)	p
50 cm	3.50 (276)	<0.001
1 m	-0.92 (292)	0.36
2 m	0.91 (290)	0.36
5 m	0.39 (292)	0.70
TWI	t-test	
	t (df)	p
50 cm	-2.52 (292)	0.01
1 m	0.23 (296)	0.82
2 m	-1.43 (295)	0.15
5 m	0.49 (291)	0.62
Overland flow/ P-loss	t-test	
	t (df)	p
1 m	0.68 (254)	0.49
2 m	0.41 (259)	0.68
5 m	-0.03 (260)	0.98

5.3.5 Quantification of vertical error

Error in DEM/DSM can be considered the disparity in elevation values modelled by a DEM/DSM and a reference for the 'real' surface. Errors may derive from a variety of sources, for example, sampling, measurement and interpolation (Fisher & Tate, 2006). Three common sources of uncertainty were assessed for this study:

- Canopy height.
- Distance to a GCP.
- Slope.

Sward height demonstrated moderate to strong, positive correlation with measured vertical error at 50 cm resolution (0.62, 95% CI [0.52, 0.71]). Linear regression suggested grass height explained 38% of variability in measured error (RMSE= 0.08m; R^2= 0.38, p< 0.001). As the resolution coarsened, the relationship between canopy height and vertical error became progressively weaker (1 m: RMSE= 0.09 m; R^2= 0.24, p< 0.001; 2 m: RMSE= 0.11 m; R^2=0.1, p< 0.001) until no significant relationship was observed at 5 m resolution (RMSE= 0.13 m; R^2 = 0, p= 0.31) (Figure 5-10). The results indicated that at 5 m spatial resolution there was no relationship between measured error and grass height (at least where canopy was <= 0.4 m).

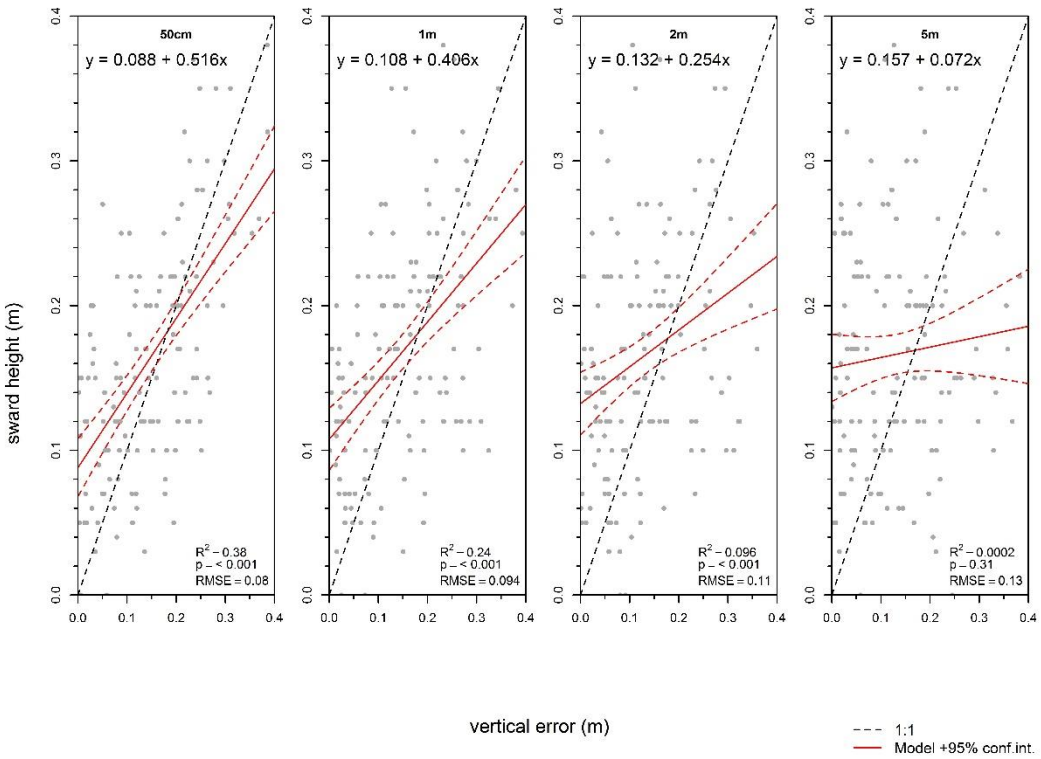

Figure 5-10 Linear regression of vertical error (m) versus measured sward height (m) at 132 randomly selected locations. A moderate positive correlation was observed between sward height and error at 50 cm resolution but decreased as the grid size became larger. There was no relationship between vertical error and sward height at 5 m.

Establishing GCP is a prerequisite for georeferencing photogrammetric models. GCP should be evenly distributed across a subject site without large spacing and taking into consideration elevation changes. To assess whether the location of the GCP had any effect on measured error, a Euclidean distance surface was created within the site at each resolution, and error measured as a function of distance to the nearest GCP. The results are illustrated in Figure 5-11 below. At each resolution in the SfM DSM, there was no effect from distance of a GCP. This was expected. The surveyed area was just 9 ha and had no significant change elevation

within the site. In all cases there was no significant effect from distance to GCP on DSM error (p>0.05; RMSE=~59 m).

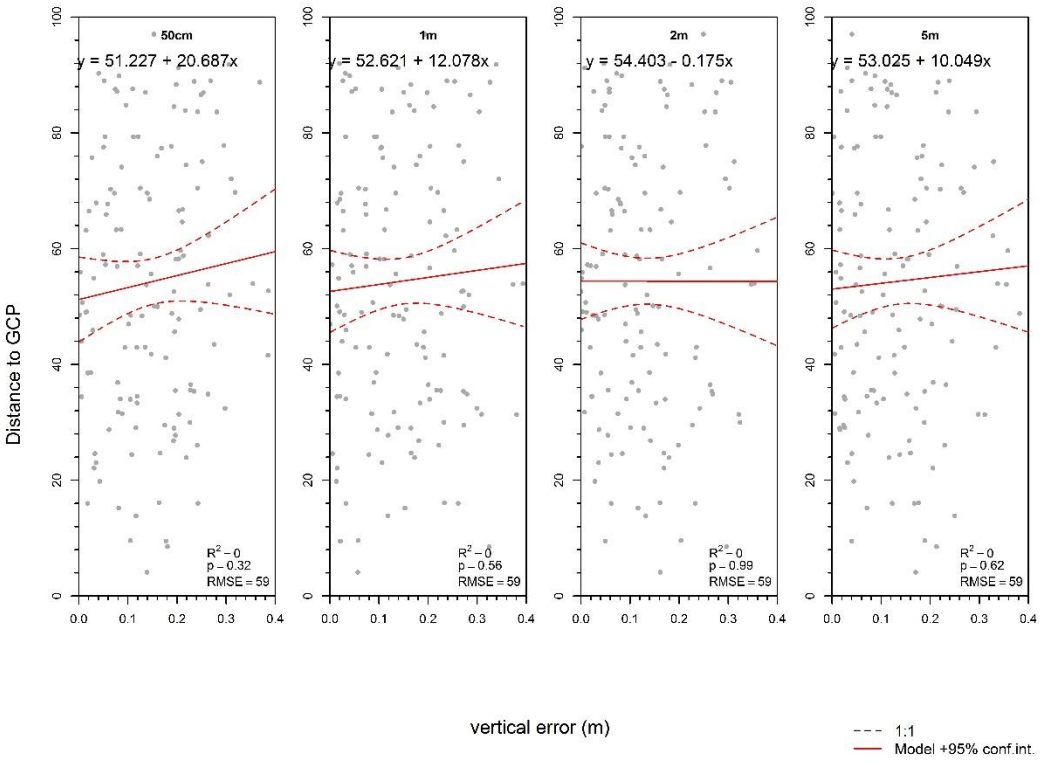

Figure 5-11 Linear regression of vertical error (m) versus distance to GCP at 132 randomly selected locations. There was no relationship at any of the modelled resolutions.

The final potential effect on model accuracy was slope. Changes in elevation over an area may influence the interpolation procedures, and a positive correlation between error and slope has been noted in previous. The results are illustrated in Figure 5-12 below. At each resolution in the SfM DSM, there was no effect from lope. Slope was calculated from the LiDAR DEM.(p>0.05; RMSE=5.3 ° at 50 cm, to 3.3° at 1 m, 3.4° at 2 m and 3.2° at 5 m). This was expected given the low range of slopes within the site (between 0 and 10 degrees).

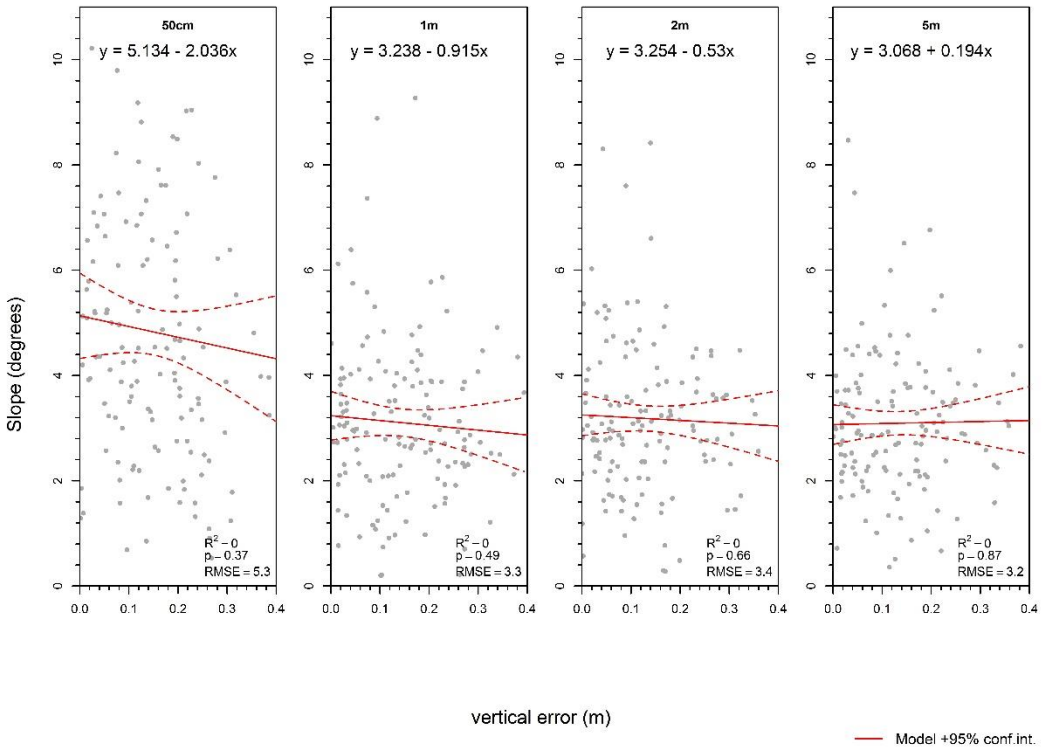

Figure 5-12 Linear regression of vertical error (m) versus slope at 132 randomly selected locations. There was no relationship between error and slope at any of the modelled resolutions.

5.4 Discussion

Previous work by Thomas *et al*. in the vicinity of the study area had demonstrated how aerial LiDAR could identify HSA and define microtopographic features that acted as conduits or barriers for the diffuse P loss (I. Thomas, Jordan, *et al*., 2016; I. Thomas, Mellander, *et al*., 2016; I. A. Thomas *et al*., 2017). The ability for UAS DSM to deliver accurate overland flow models in densely vegetated areas has been called into question (Jeziorska *et al*., 2016). In this chapter, therefore, the accuracy of UAS DSM were compared with LiDAR DEM to see

how they modelled overland flow (and associated P loss) within intensively managed grasslands.

The accuracy assessment of the original LiDAR data suggested a vertical RMSE of 0.03 m (± 0.014 m) over the catchment. Within the study area, it was found to be 0.15 m (± 0.05 m). This was only marginally less than the RMSE for the best performing UAS photogrammetric point clouds (at 0.18 m ± 0.11 m). Commercial photogrammetric software (Agisoft and Pix4D) produced SfM point clouds with the lowest RMSE versus independently measured ground control. Higher rmse in point cloud created from the manned flight imagery was possibly due to differences in survey altitude (Rock *et al.*, 2011). However, there was a reduction in image overlap across the study area when the flight had to fly low to avoid cloud at ~500 m. Reduction of overlap and the concomitant loss of reduundancy across multiple images is known to reduce accuracy for SfM point clouds (Küng *et al.*, 2011).

Global measures of accuracy such as RMSE used in the regression analysis of this study, are relatively quick to calculate, easy to report and interpret and is recognised internationally. However, they imply that error is uniform across the DEM. As noted in earlier chapters, a single metric may not accurately account for spatial variability or high autocorrelation within a map or elevation model. As acknowledged by Darnell et al. (2008), the lack of a robust and easily implemented replacement for analysing uncertainty in maps and models remains to be an issue for spatial analysts. However the consequences of error can be severe as they propagate into derived products. Three common sources of error were analysed in the chapter. Of these, only grass height had an observed effect under the study conditions, amd

only below 5 m grid resolution. There were several other potential sources of error that were not analysed (for exampe include camera internal parameters, or other settings (for example, image overlap). The objective of this chapter was to demonstrate the usability of UAS photogrammetry for afrm-based topographic modelling. For end-user on the farm, changing Internal ccamera parameters would not be a pressing concern. They could, however, make allowences to mitigate errors accruing from canopy height and GCP placement, for example. Of the three potential sources investigated in this study, grass height had the greatest impact on error. This can be seen in the difference DEM (Figure 5-2), where the spatial patterns of height difference corresponded to observed differences in grass heights between paddocks. These anomalies were consistent across each of the grid resolutions. An intersting result from the current study was that at 5 m resolution, there was no longer an effect from sub-pixel grass height. Further studies would be needed to see if this result was broadly applicable across all intensively managed grassland farms.

VisualSFM had considerably higher RMSE (0.42m), which was due to doming deformation of the point-cloud. Doming can occur in photogrammetric point clouds where image acquisition is along parallel viewing directions or where insufficient GCP has been established (James & Robson, 2014; Ouédraogo *et al.*, 2014). As neither of these applied to the current study, the doming was likely the result of inaccurate calibration of image radial distortion (Rosnell & Honkavaara, 2012). The effect was partially corrected using MATLAB's Image Processing Toolbox (v. 9.0) but could not be eliminated, even where additional GCP were used for rectification. Further issues with the VisualSFM cloud included a highly irregular distribution of densified points where large patches were left unfilled. This is a reported issue with the patch-

based MVS algorithm used by VisualSFM, where densification often fails to complete in areas of poor surface texture (Carravick *et al*., 2016).

SfM produced models of overland flow and P loss that was statistically identical to aerial LiDAR models. The closest association was at 5 m resolution (R^2 = 0.93). Models at 2 m resolution were statistically similar but had higher variability (R^2 = 0.62). SfM over-estimated some pathways at 1 m and 2 m resolution, but at 5 m-resolution the extent of defined pathways and delivery points using each model were spatially coterminous. Below 1 m resolution, both LiDAR and SfM models produced unrealistic flow paths in the TWI and SIMWE models. This effect was previously observed (Gyasi-Agyei *et al*., 2006), where the authors concluded that the spatial resolution of a model must be higher than the ratio of mean elevation change per pixel to vertical resolution to successfully extract hydrological pathways from surface models. Although the results of t-tests suggested no significant difference between TWI with resolutions greater than 50 cm resolution, very weak correlations and highly variable relationships were observed between methods. The increased uncertainty in the TWI models is more likely to come from flow routing calculations, as slope showed strong predictive ability, particularly as resolution increased. Applying low-pass filters to TWI reduced variability in each raster and improved correlations between models. However, filtering is a blunt instrument that removes systematic errors but also changes correct observations (O'Callaghan & Mark, 1984). Excessive filtering blurred boundaries and spread extended potential source areas over a wider area which was unsuitable to defining spatially discrete HSA zones for cost-effective management solutions. Earlier work within the catchment (I. A. Thomas *et al*., 2017) concluded high spatial resolution raster grids (< 1 m) confounded flow

accumulation and flow direction algorithms, and that 1 m and 2 m raster grids were optimal for identifying HSA within agricultural catchments. At this resolution, microtopography, delivery points and breakthroughs, could be adequately resolved, while still being spatially representative of broader topographical gradients for modelling hillslope processes (Heathwaite *et al*., 2005).

A 5 m resolution SfM DSM could be considered a "high-resolution" product in comparison to the coarser topographical models commonly used in hydrological modelling. Optimal DEM resolutions are site- and subject-specific.For example, coarse resolution models may be appropriate in locations where microtopography is not dominant (Cavazzi *et al.*, 2013; Murphy *et al.*, 2009). Comparison of LiDAR and SfM found each method identified the same delivery point locations at 5 m resolution; however the spatial extent of the delivery points were quite broad. Nevertheless, the similar performance between LiDAR and SfM suggested SfM DSM could substitute for LiDAR DEM in intensively managed grasslands without significant difference in estimates of overland flow/ P loss. Additional studies would be necessary to determine whether other landcover targets performed similarly. Targeted remedial measures can reduce the cost of implementing broad remedial measures to lower the volume of P entering surface water. Thomas *et al*. reported that where aerial LiDAR was used to define HSA, the implementation costs of riparian buffer strips was reduced by 66% and 90% over 1 and 5 years, respectively, due to an average decrease in the length of riparian buffer strips of 97% (I. Thomas, Jordan, *et al*., 2016). The potential saving using UAS SfM could be higher, given the lower costs involved in acquiring and processing photogrammetric models. A specific cost-benefit analysis was not undertaken on this occasion.

5.5 Conclusions

This study concludes that UAS-derived DSM can substitute for aerial LiDAR data when estimating overland flow and P loss on intensively managed grasslands at 5 m resolution. For maximum accuracy, models should be acquired when grass cover is low (post-grazing/ mowing). An accurate method of defining pathways and delivery points for nutrient loss from farmland can represent a considerable cost saving to farmers where targeted mitigation measures can be put in place. The use of UAS photogrammetry in topographical modelling as a substitute for LiDAR is increasingly common. Although UAS DSM come with reduced positional accuracy, they represent an enormous cost-saving over aerial (or terrestrial) LiDAR. Using UAS allows users to produce topographical models on-demand, so any changes in field topography can be captured immediately and their effect on overland water flow quantified. The next generation of UAS with PPK ability is improving the positional accuracy of outputs without a requirement for GCP. This is making the collection of accurate models less time-consuming. Using UAS has additional benefits, for example, whsubsurface prospect (see Chapter 6) or mapping stressed vegetation in relation ot underlying drainage conditions (Chapter 4).

This study was carried out within a “typical”, intensively manged pasture field. The field was spilt into approximately equal sized paddocks and was under a rotational grazing system. There was noting in the topography of the field that suggested the technique developed here would not be reproducible in similar fields, once sward height was low. The results of this study reveal that photgrammetric DSM can substitute for LiDAR DEM. Modelled elevations are in close agreement at all resolution. Derived slope data has its closest agreement at 2-5

m. Topographic wetness models were considerably different and required significant filtering to make them similar. The loss in spatial accuracy required to achive this would not be acceptable on a precision agriculture farm. Further research would be required to see if this is observation is repeated in other study areas. When overalnd flow (and associated P loss) were modelled using SIMWE, the results indicated that estimates of P loss at field/paddock scale were identical for LiDAR DEM and from UAS DSM. This finding has important consequences for accurately and affordably predicting surface pathways and delivery points in intensively managed grassland in the context of reducing agricultural pollution of surface water.

This page is intentionally blank

Chapter 6 A thermal inertia approach for mapping artificial drainage systems using a UAS thermal infrared sensor

6.1 Introduction

Accurate information on the location and layout of drainage systems is invaluable for reducing the risk of environmental pollution in agricultural catchments. At present in Ireland, there is no national information system for subsurface drainage, no requirement for documenting new drain installations and no efficient means of detecting existing drains systems. This is not unique to Ireland, an international study in 2005 found just 11 of 161 countries (7%) had sub-national data for artificially-drained areas (Feick *et al*., 2005). Moreover, farmers may not be fully aware of the complete drain infrastructure beneath their fields, for example, where systems were installed decades previously, or where locational records were lost or never kept.

The traditional method of prospecting for drainage channels is to probe the ground looking for a drain pipe. This is effective and inexpensive, but very time-consuming. The use of mechanical excavators to locate pipes brings a risk of additional damage to soil structure or to the surface. For these reasons, several non-invasive techniques have been developed which allow for rapid investigation over broad areas with no physical impact. These have been previously described in Section 2.4 above, but the salient points are restated here.

- Geophysical techniques including magnetometry and GPR have been tested (Allred *et al*., 2004; Rogers *et al*., 2005) and are quite successful under test conditions.
- Satellite remote sensing is well-established for delineating drainage class for both bare and vegetated soils (Cialella *et al*., 1997; Gökkaya *et al*., 2017; Møller *et al*., 2018). Individual drainage lines have been successfully mapped using visible and NIR aerial photography. For these methods, drain lines are most easily identified on bare soils, where differential drying patterns on the soil surface several days following precipitation/irrigation indicate drain lines (Verma *et al*., 1996). The method has been criticised for poor predictive ability, especially in the presence of crops or crop residue (B. S. Naz *et al*., 2009), although canopy reflectance can also be used to delineate drain-related soil moisture patterns.

Thermal infrared (TIR) cameras have been used for decades to detect heat anomalies at the surface relating to subsurface moisture patterns. Abdel-Hady and colleagues used airborne TIR sensors to identify contrasting heat signatures associated with buried pipes and natural drainage channels (Abdel-Hady *et al*., 1970). Vlcek and King identified artificial and natural drainage patterns below immature forest canopy using TIR imagery (Vlcek & King, 1983). Until quite recently, however, the expense of acquiring high spatial- and temporal resolution TIR imagery curtailed its use outside of research. However, the improved miniaturisation of sensors and their integration onto UAS has seen increased use of TIR for precision agriculture and ecosystem monitoring (C. Zhang & Kovacs, 2012). In recent research, Allred and colleagues accurately mapped 60% of a known subsurface drainage system using a UAS TIR system. Their study was carried out using a thermal orthomosaic acquired during a single

flight. Buried drains were detectable even where the surface was occluded by crop residue and partial canopy (Allred *et al*., 2018).

Identifying differential rates of cooling/warming between diurnal temperature extrema is a well-established method of thermal remote sensing (Section 1.6.3). Thermal inertia (TI) (Equation 6.1) describes the speed at which an object approaches the temperature of its surroundings. For It is not possible to calculate TI using remotely-sensed data as it is not possible to accurately calculate values for bulk density, thermal conductivity and specific heat capacity for all objects within an image footprint. Instead, apparent thermal inertia (ATI), the difference in temperature between temperature extremes, is used as a proxy for TI. The effect of ATI is usually stronger on bare ground because the added impact of evapotranspiration from vegetation can reduce the amplitude of heat fluxes from soil (Price, 1985). Sohrabinia *et al*. provide a recent assessment of the different ATI methods for soil moisture mapping in managed grassland (Sohrabinia *et al*., 2014).

$$TI = \sqrt{k\rho c} \qquad \text{(Eqn. 6.1)}$$

where TI ($J \cdot m^2 \cdot K^{-1} \cdot sec^{-1/2}$) is thermal inertia, k ($W \cdot m^{-1} \cdot K^{-1}$) is thermal conductivity, ρ ($kg \cdot m^{-3}$) is bulk density, and c ($J \cdot kg^{-1} \cdot K^{-1}$) is soil heat capacity.

This chapter describes an ATI method to identify drainage systems in managed grassland using UAS TIR images captured during morning and afternoon flights. It is based on the assumption that subsurface drains have contrasting thermal properties to the surrounding soil matrix that can create measurable temperature anomalies at the surface. Under this assumption, wetter (i.e. poorly-drained) soils emit less heat compared to dry (or drained) soils

due to the greater volume (and higher specific heat capacity) of soil water. Specific heat capacity is the amount of heat that must be added to raise the temperature by 1°C. For a given soil, its heat capacity is the summed total of all its phases. Soil minerals typically have similar heat capacity values (~2.0 × 10^6 J m^{-3} K), but water is nearly twice as high (~4.2 × 10^6 J m^{-3} K). It is influenced primarily by soil moisture content.

Consequently, the radiant temperature of wet soils changes more slowly (i.e. they display higher ATI). In contrast, dry soils heat up more quickly (i.e. they display lower ATI). In this study, ATI is defined as the difference between morning and afternoon daytime radiant temperatures as estimated by a UAS TIR sensor (allowing for emissivity) (Equation 6.2).

$$ATI = \varepsilon TIR_{am} - \varepsilon TIR_{pm} \quad \text{(Eqn. 6.2)}$$

Where TIR_{am} and TIR_{pm} are surface temperature observations captured by the TIR camera in the morning and afternoon respectively and ε is as estimation of surface emissivity.

The objectives of this chapter were to identify whether the presence of artificial subsurface drainage created differences in surface temperatures that could be detected using UAS TIR. Specifically, it was tested whether surface temperatures over grass-covered soils provided an estimate of ATI that was proportional to thermal fluxes of the underlying soil (Soliman *et al.*, 2013). This method was tested under controlled field conditions where a subsurface drainage system had been installed.

6.2 Methods & Materials

6.2.1 Study site

The study area was a sports facility at Rathcoffey, Co. Kildare, Republic of Ireland (53°20'0''N, 6°41'20''W; Figure 6-1). The site was previously agricultural land that had recently been landscaped for use as playing pitches. Rush-infestation and surface water observed in nearby fields at the time of the study (April 2018) indicated considerable soil drainage problems in the wider surroundings. Poor drainage on site resulted from its low-lying landscape position and low permeability of underlying subsoils[12]. A subsurface drainage system, consisting of interconnected plastic pipes at ~10 m intervals, was installed in October 2017 to reduce waterlogging at the site which restricted access to the fields during winter months or following heavy rainfall at any time during the year. Intersecting these channels was a dense network of coarse sand-filled mole channels at ~1 m spacing. Ditches associated with the earlier field boundaries had been piped and backfilled and integrated into the recently installed drainage system. The pitches were not in use at the time of the survey. Grass height was maintained by mowing and was uniform at the time of the study (~4.5 cm).

.

[12]. Underlying subsoils were poorly drained calcareous groundwater gleys of the Mylerstown soil series. Irish Soil Information System Soil Association 650a (R. J. Jones *et al.*, 2014).

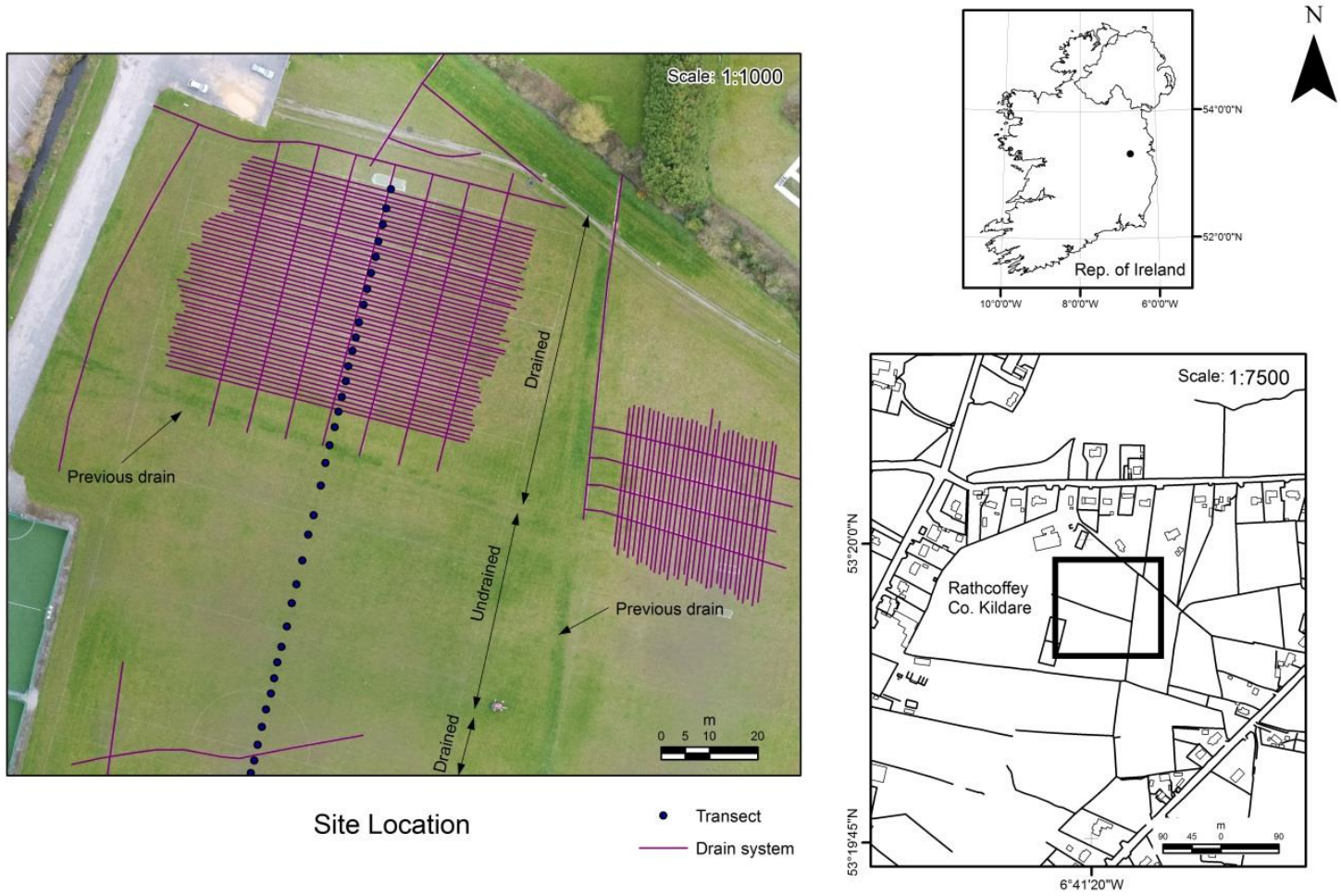

Figure 6-1 Site location showing the extent of the subsurface drainage system and the soil temperature transect (overlain on the orthomosaic).

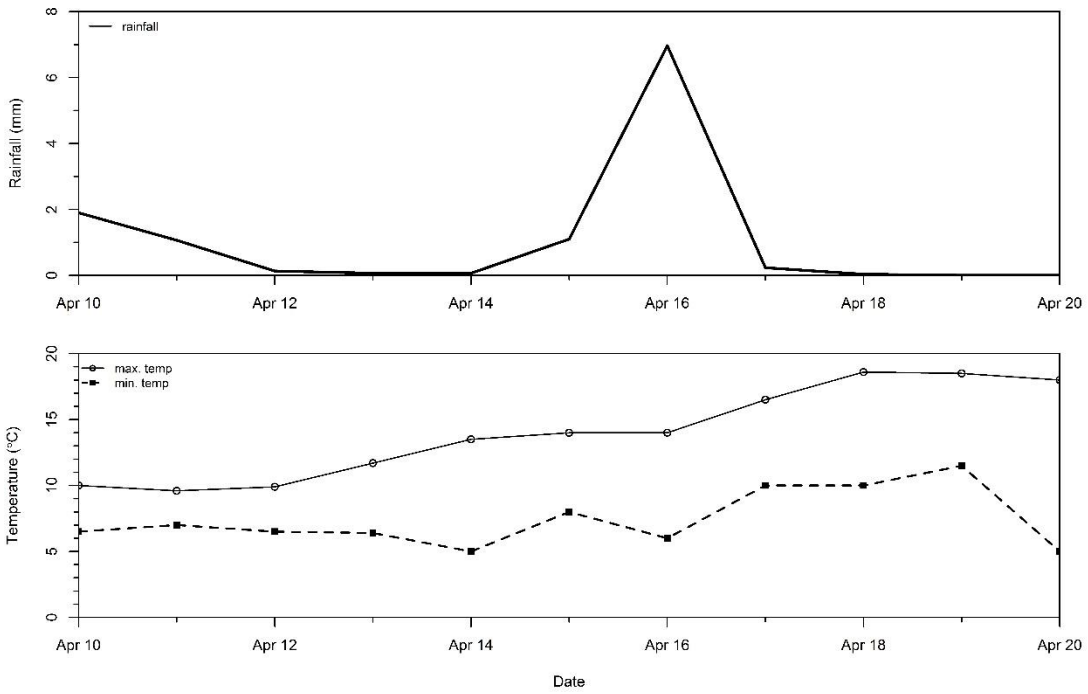

Figure 6-2 Local meteorological conditions (air temperature and precipitation) preceding the UAS TIR survey (April 20th, 2018)

Mean precipitation and temperature readings were acquired from local meteorological stations within 10 km of the study area. In the ten days preceding the flight, 11.5 mm of rainfall was recorded by local precipitation stations (Figure 6-2), with 6.5 mm recorded four days before the survey. Wind speeds on the day were steady at 9 knots (or 4.5 ms^{-1}) from the southwest. Maximum daily temperatures over the same period rose steadily from a low of 10°C to a high of 18°C. Conditions on the day were dry and warm with a minimum of 5°C (6 am) and a maximum of 18°C (2 pm). Relative humidity (RH) at 6 am on the day was 94%, decreasing to ~60% by noon, and ~50% by 2 pm. Local climatic conditions will change from survey to survey and this will have an effect on ground conditions. Sunlight/shadow, relative humidity and wind speed can all effect soil/ canopy temperatures.In previous studies (e.g. Naz and

Bowling, 2008) rain had fallen in the recent past, so soil was in the process of drying out. This allowed temperature gradients to be observed.

6.2.2 Methodology

For the UAS survey, 8-bit radiometric images (R-JPEG; 640 x 512 pixels) were captured by a DJI FLIR Zenmuse XT 9 mm thermal camera (7.5 - 13.5 µm) mounted on a DJI Matrice 600 UAS. The camera specification indicated the sensor can detect temperature differences of ~0.05° C (DJI, 2018). Thermal images were obtained at 120 m altitude at 9 am, 1030 am, 12 pm and 2 pm. At this altitude, the image footprint was approximately 167 m x 134 m, with a ground sampling distance of ~0.25 m. Further acquisitions were planned on the day at different altitudes, but a battery failure on the UAS required the survey to be concluded prematurely. The low dynamic range of pixel values in each TIR image was substantially increased by using polished aluminium bowls (~30 cm diameter) as ground targets. Prior to each flight, a number of bowls were filled with boiling water to increase the range of temperature values (hot targets). When left empty the very low emissivity of the polished aluminium surface (ε = ~0.04) functioned as cold targets (see Figure 6-3). Emissivity (ε), a dimensionless value between 0 (perfect reflector) and 1 (ideal emitter), is the ratio of energy from a surface compared to a blackbody at the same wavelength and temperature. A blackbody is a hypothetical surface that perfectly absorbs and reemits all energy that is incident upon it. The relationship between emissivity, radiant- and actual (kinetic) temperature is defined by Equation 6.3. The emissivity of the grass surface was assumed to be constant (ε = ~0.98) across the area for the duration of the study.

$$T_{rad} = \varepsilon^{1/4} T_{kin} \quad \text{(Eqn. 6.3)}$$

where T_{rad} and T_{kin} are radiant temperatures measured by a thermal camera and the kinetic temperatur of the surface respectively, and ε is emissivity.

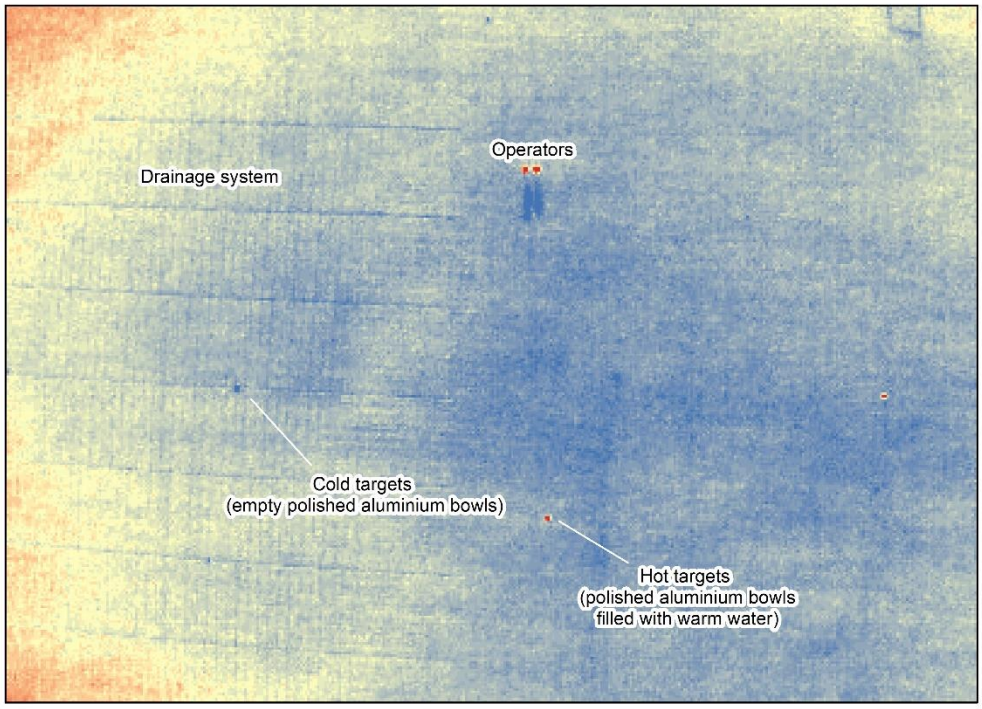

Figure 6-3 Hot (red) and cold (blue) ground targets (polished aluminium bowls) used during the UAS survey to assist in rectification and increase dynamic range within the scene. The heat and shadow created by the operators is also noted.

Before the UAS survey was conducted, a diurnal experiment assessed whether soil temperature and TIR pixel intensity were different for dry and saturated conditions. The test was carried out on a 5 m x 5 m grassed area on consecutive days in May 2017. Grass was cut on the day before the survey and maintained at a uniform height of ~4.5 cm over the two

days of the experiment. On Day 1, there had been no rain and no irrigation of the plots in the preceding 10 days. Before Day 2, the 5 m x 5 m area was vigorously irrigated until water began to pool on the soil surface. This was allowed to infiltrate/ evaporate before study continued and no surface ponding remained during the experiment on the second day.

TIR images were captured at nadir using a FLIR Tau 640 from a fixed, stationary platform ~10 m above ground level. This was not the same sensor used in the UAS experiment, but had been used previously for both aerial and ground-based TIR surface mapping (Cahalane *et al*., 2017). Soil- and ambient air temperatures were logged every hour between 4 am and 2 pm. Soil temperatures were mean soil temperatures measured in the upper 10 cm using a Digitron 2046T thermometer.

For the UAS survey, intensity values (radiant heat) were recorded as 8-bit digital numbers (DN) between 0 and 255 with the internal radiometric data extracted using the FLIR Tools software (www.flir.com/products/flir-tools). Radiometric dData were exported from FLIR Tools as .csv files and converted to raster (.tiff) using the "rgdal" package in R statistical software (v.3.3.1). Radiant temperatures were converted to kinetic temperatures using Equation 6.1. Due to the limited extent of the study area, a single image covered the entire area without a need to generate an thermal mosaic. Individual images were georeferenced and cor-registered using a 3rd order polynomial transformation in ArcGIS (v. 10.5). A 3 cm resolution true colour orthomosaic was used as the reference image. The orthomosaic was created before the TIR flight from UAS RGB imagery (Phantom 4 Pro) and generated using Pix4D photogrammetric software (www.pix4d.com). Before each flight, mean soil temperature in the

upper 10 cm was recorded every 3-5 m along a ~140 m transect using a Digitron 2046T thermometer. The transect crossed both drained and un-drained areas of the site (see Figure 6-1). It took ~15 minutes to walk the transect. The survey started immediately after the soil temperatures were record. Any increase in soil temperature from the time the first temperature was recorded to the time the UAS was airborne was assumeed to be minimal. To determine the overall accuracy of the method for identifying buried drain lines, the length of the observed drains were measured within ArcGIS and compared against the observed drain lengths.

6.3 Results

6.3.1 Initial saturation test

Measured soil- and air temperatures displayed a strong, positive correlation for saturated (ρ=0.85, p= 0.0002) and dry soil conditions (ρ=0.83, p=0.0005). Dry soils were typically >1°C warmer throughout the day but displayed greater variability than saturated soils as indicated by lower R^2 values (0.70 vs 0.87) for saturated conditions, and lower RMSE (see Figure 6-4 top). Air temperatures on each day were similar, but differences in cloud cover will have affected the amount of solar radiation reaching the surface. Statistical tests (paired t-tests) compared mean soil temperatures for each soil moisture state. A significant difference was recorded for dry (mean= 14.2°C ±1.4°C) and saturated (mean= 12.8°C ±1.3°C) conditions ($t_{(12)}$ =-4.5, p= 0.0007).

Pixel intensity values were higher for surface temperatures under dry conditions (Figure 6-4 bottom). Peaks in intensity values on each day largely corresponded to periods of clear skies, when the test area received direct insolation. Paired t-tests indicated a significant difference

between pixel intensity values for dry (mean= 155 ±19 DN) and saturated (mean= 117 ±13 DN) conditions ($t_{(12)}$=24.8, $p < 0.0001$). The result suggested underlying saturation had a negative effect on surface TIR pixel intensity relative to dry conditions under grass canopy.

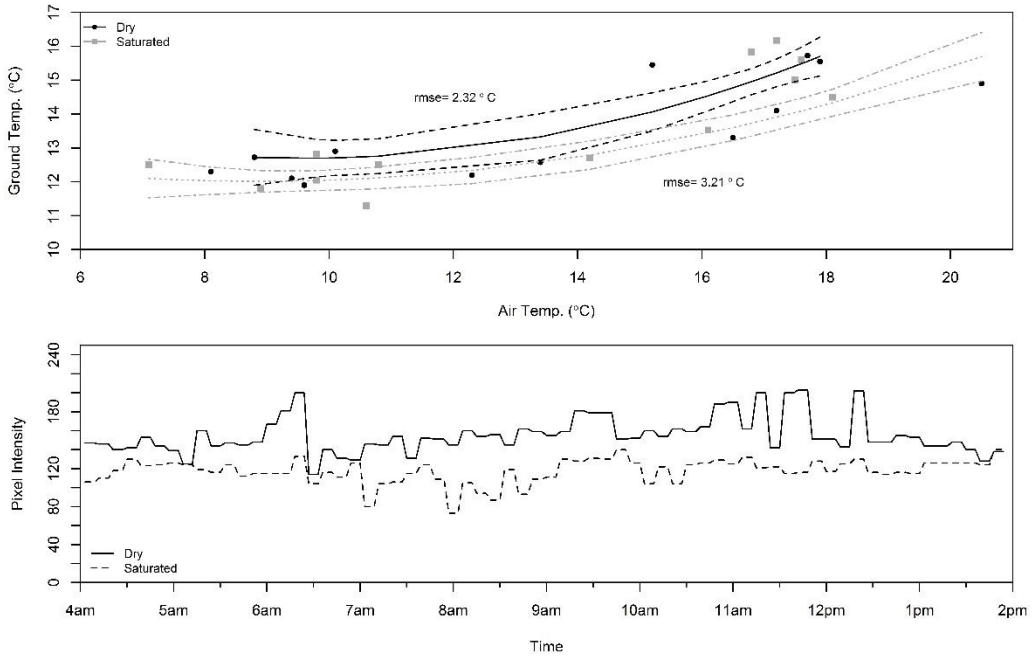

Figure 6-4 (top) Relationship between ambient air and soil temperatures under dry and saturated conditions; (bottom) Contrasting pixel intensity for identical grass plots under dry and saturated conditions.

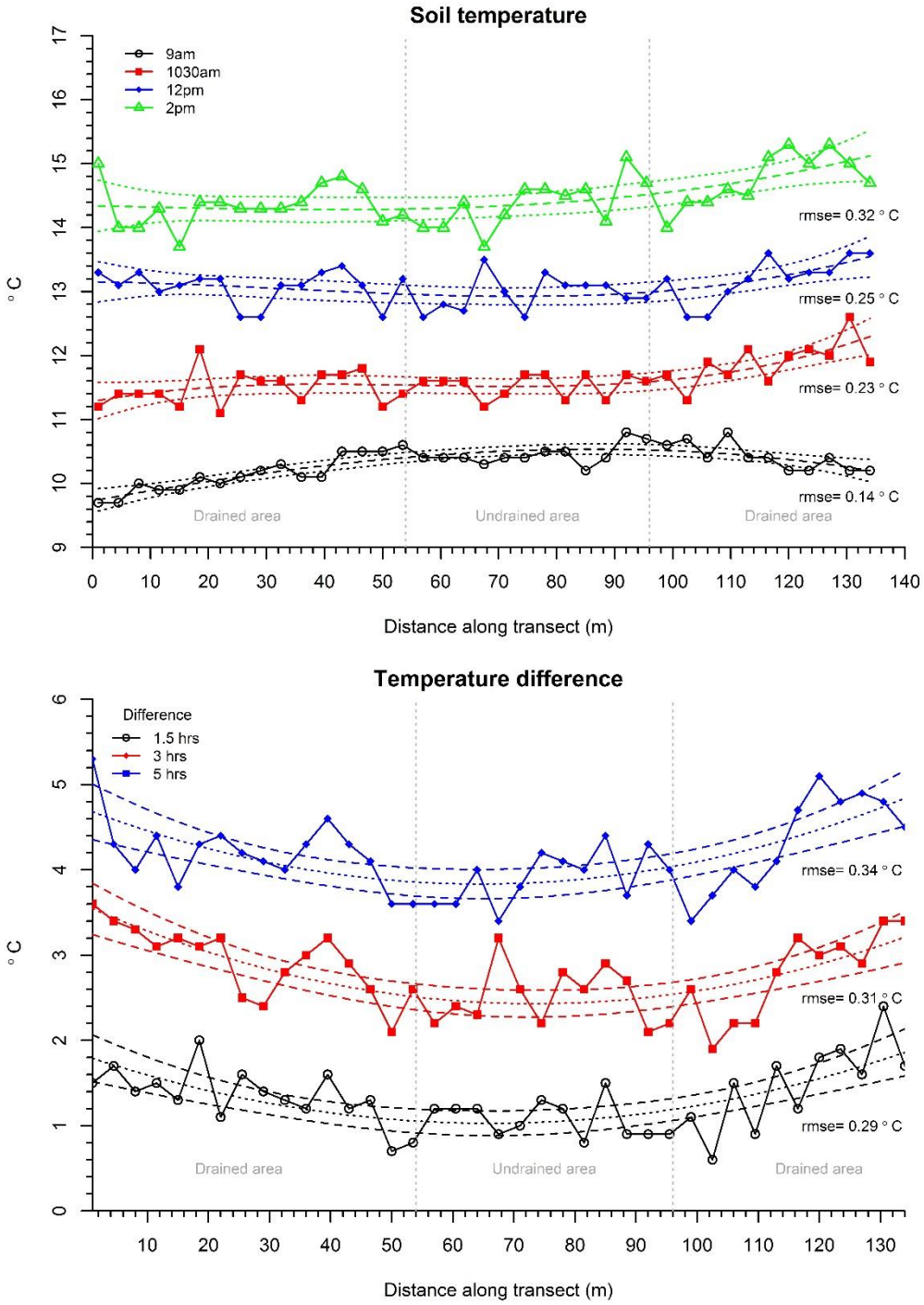

Figure 6-5 (top) Soil temperature readings (upper 10 cm) during the UAS flight; (bottom) Temperature differences between drained and undrained portions of the site with reference to the morning (9 am) temperature profile (+1.5 hour, +3 hour and +5 hour intervals).

6.3.2 Soil temperature observations

On the day of the UAS flight, soil temperatures were observed to increase slowly as ambient temperatures rose. At 9 am, soil temperatures were still quite cold (9.7–10.8°C) but increased steadily by approximately 1.3-1.4°C at each subsequent interval (10.30 am: 11.1–12.6°C; 12 pm: 12.6–13.6°C; 2 pm: 13.7–15.3°C) (Figure 6-5 top). Differences in temperature were plotted for different interval periods to track changes in ATI over the day. Three intervals were possible: 1.5 hrs (T_{9am} minus T_{1030am}), 3 hrs (T_{9am} minus T_{12pm}) and 5 hrs (T_{9am} minus T_{2pm}). A consistent pattern emerged where drained areas were approximately 0.5–1°C warmer than undrained portions.

Undrained areas had lower temperature increases suggesting a higher ATI than drained soils (Figure 6-5 bottom). T-tests found a significant difference in temperature differences between drained (mean= 2.89°C ± 0.43°C) and undrained (mean= 2.50°C ± 0.36°C) areas ($t_{(26)=}$ 2.44, p= 0.02), suggesting the presence of artificial drainage had an effect on the rate of temperature change for drained soils.

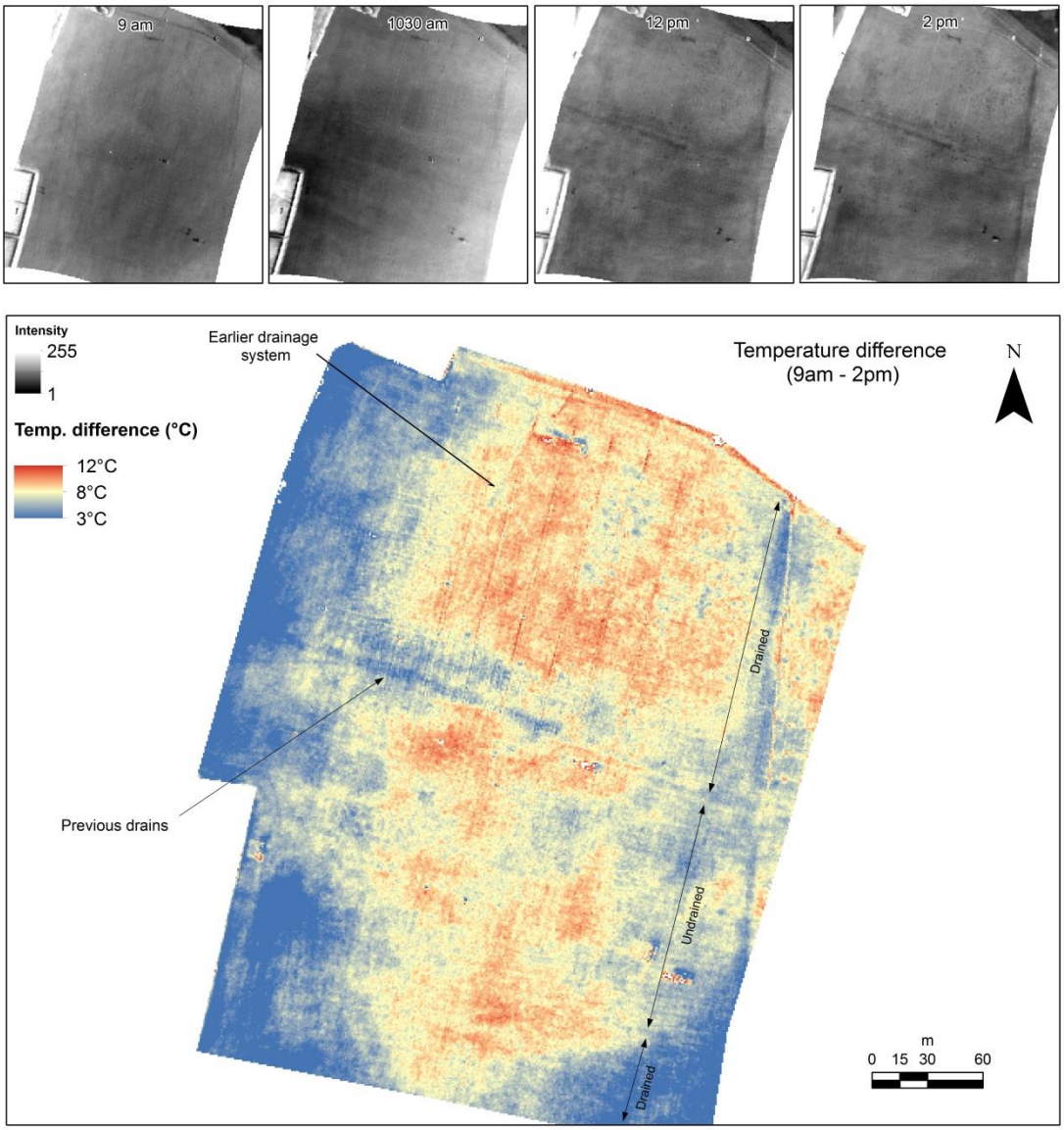

Figure 6-6 Individual TIR images at each time interval with a 5-hr temperature difference image showing differential rates of heating between drained and undrained portions of the site. Individual drain lines are visible, as well as portions of an earlier drainage system.

6.3.3 UAS survey: TIR observations

Surface temperatures were recorded by radiometric images at 9 am, 1030 am, 12 pm and 2 pm (Figure 6-6). At the beginning of the survey (9 am), mean temperatures across the study area was estimated to be 10.3°C ± 0.27°C. Mean temperatures increased in each subsequent image (1030 am: 11.6°C ± 0.32°C; 12 pm: 13.1°C ± 0.30°C; 2 pm: 14.5°C ± 0.40°C). Canopy temperatures were initially colder than measured soil temperatures (5.5-7.5°C vs. 9-11°C) but increased rapidly as ambient temperatures increased. Initially, a moderate, negative correlation was observed between soil- and surface temperatures (ρ= -0.65), but this was reduced in subsequent intervals very weak correlations were observed (ρ= -0.06, -0.15 and 0.01 at 1030 am, 12 pm and 2 pm respectively). Welch two-sample t-tests revealed a significant difference in mean surface ATI between drained (mean= 10.35°C ± 0.74°C) and undrained (mean= 9.68°C ± 0.37°C) areas of the field after 5 hours ($t_{(24)=}$ 3.19, p= 0.004). This difference in mean ATI between known areas of contrasting drainage properties suggested artificially-drained areas are detectable using UAS-TIR based on differential rates of temperature increase at the surface.

Surface temperatures recorded by the TIR sensor were higher in drained areas relative to undrained areas by approximately 1-1.5°C (Figure 6-7 top). A 5-hour difference image produced using Equation 6.2 (T_{9am} minus T_{2pm}) indicated temperature anomalies corresponding to drained and undrained locations. Drained areas displayed higher temperatures (i.e. lower ATI) relative to undrained areas (Figure 6-7 bottom).

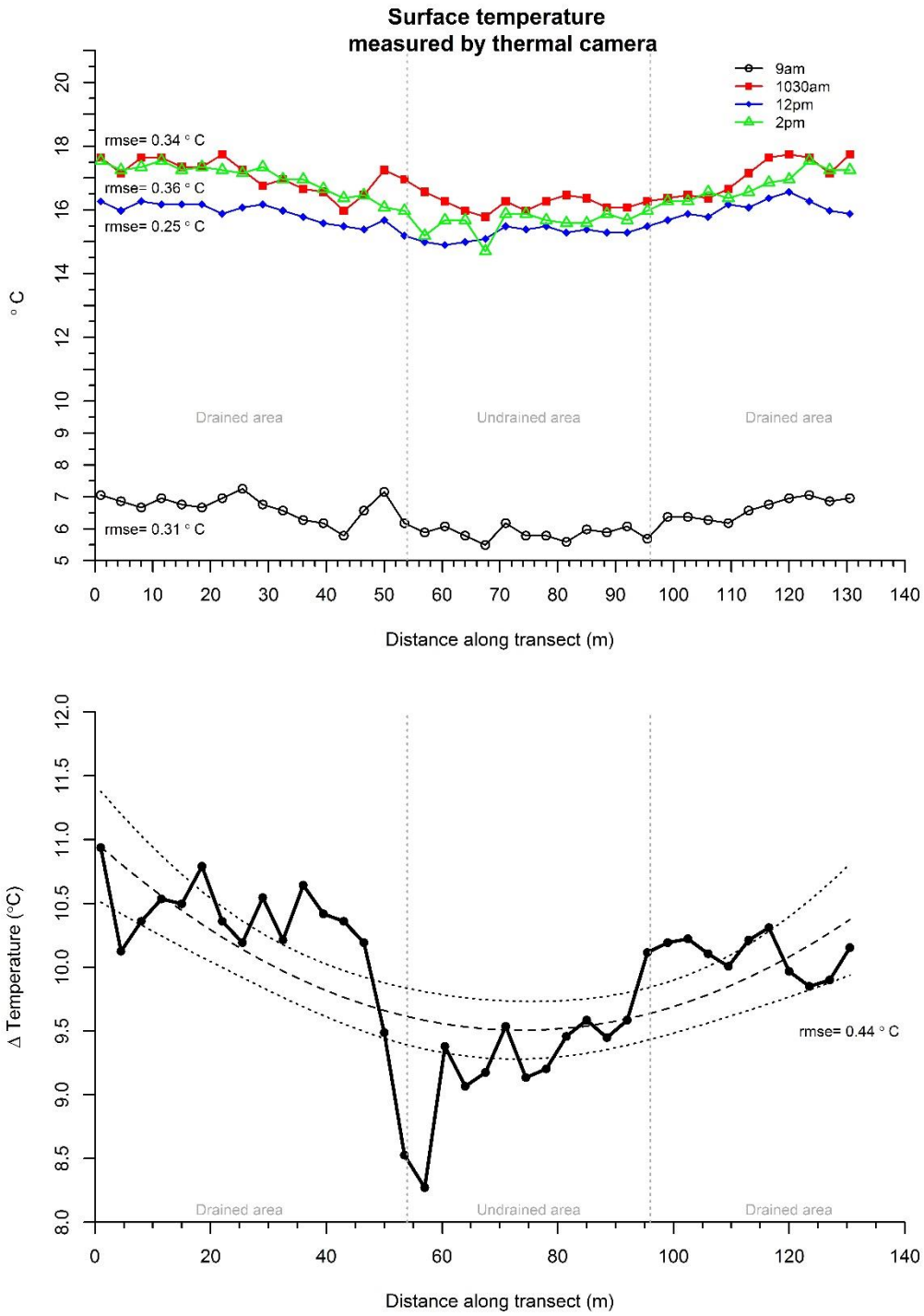

Figure 6-7 (top) Surface temperature readings measured by the TIR camera; (bottom) Difference in surface temperatures between drained and undrained portions of the site (5-hr difference 9 am – 2 pm)

Increasing Pearson correlation coefficients were recorded between soil- and surface ATI as the period between morning and afternoon acquisitions increased.It was highest after five hours (1.5-hr: ρ= 0.07; 3-hr: ρ= 0.32; 5-hr: ρ= 0.52). Further acquisitions were planned over the day. However, an equipment failure forced the termination of the study. Simple linear regression indicated a moderate, positive relationship between thermometer-measured soil ATI and the ATI estimated by the TIR sensor (Figure 6-8). As surface temperatures were consistently warmer than soil temperatures, the range of thermal inertia was higher for the surface. The relationship beween soil- and surface ATI became stronger the greater the time period between measurements. With a diffference of 1.5 hours, for example, the rmse between soil and surface ATI was 8°C (R^2=0, p=0.38). By increasing time between measurements, the rmse value decreased while R^2 values increased. Variance remained high, the highest R^2 value at 5 hours difference was 0.24, however the relationship between soil- and surface ATI at 5 hours was significant (p=0.001) suggesting soil – and surface ATI were propotional across this site.

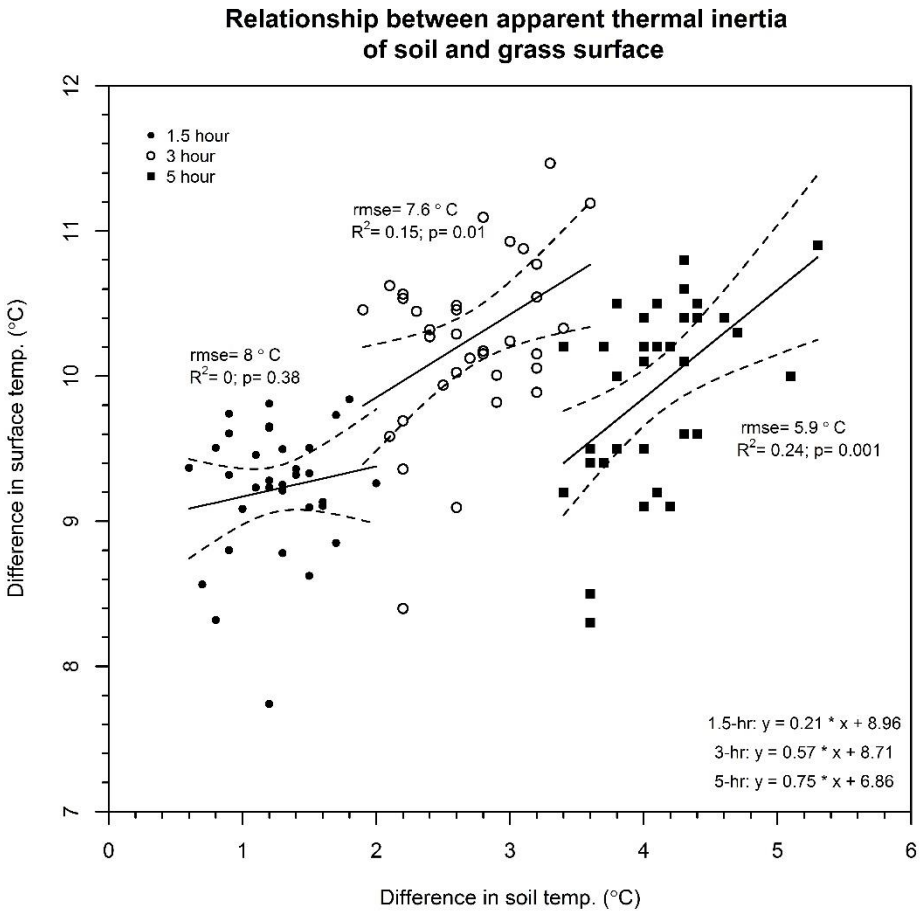

Figure 6-8 Relationship between soil- and canopy ATI at 1.5-hr, 3-hr and 5-hr difference.

6.3.4 UAS survey: Subsurface drainage

Three types of drainage channel were known to be present within the study area at the time of the UAS flight:

- Existing drains associated with former field boundaries.
- PVC tile drains installed as part of the new drainage system.
- Sand-filled mole channels installed as part of the new drainage system.

Figure 6-9 Detected drains using UAV TIR method.

The two associated with earlier agricultural boundaries became increasingly evident in TIR images after 1030 am. In the TIR images they appeared as cooler, darker linear anomalies at the centre and east of the area (see Figure 6-6). These former ditches had an overall length of 236 m within the study area The ATI image detected there length for approximately 152 m (or 64%) (Figure 6-9). The reason why ~84 m of these drains were undetected by the TIR sensor is unclear. It was not possible to investigate the area further. Perhaps drains were not located where they had been reported. This is not unusual, previous studies have been consistent in the identification of drains with 60-65% accuracy. The absence of an efficient method of drain

mapping was one of the primary reasons for the study (Section 1.2). Each of seven NS-running tile drains at the northern end of the study area was identifiable in the 5-hr difference image. Each of these drains was approximately 60 m long (420 m in total) (see layout on Figure 6-1). The UAS TIR method identified 250 m (~59%) of these drains. The reason for undetected drains in this area would appear to be related to the density of the mole drainage system in this area (visible as dark red linear anomalies in Figure 6-6), as well as the existence of an earlier, unknown herringbone-layout drainage system was also delineated. The existence of this system was not known at the time of the survey. Only partial traces of this system was identified in the difference image, but traces of this system were also visible in the original 12 pm and 2 pm images.

6.4 Discussion

6.4.1 Mapping artificial drainage

The results of the saturation test and UAS survey indicated that, under the specific conditions of the experiments, artificially-drained areas could be distinguished beneath a dense grass canopy. Using UAS TIR imagery, surface ATI was found to be approximately proportional to the ATI of the underlying soil. This was demonstrated in the similar temperature responses to drained and undrained conditions using soil temperature and the TIR camera, and by the moderate correlation between soil and surface ATI after 5 hours. A temperature difference of ~0.5–1.5°C recorded by the TIR camera between drained and undrained areas was consistent with the findings of the initial saturation experiment, even though there was generally poor correlation between soil- and surface temperatures over the investigation. An earlier study into soil temperature differences concerning mole-pipe subsurface drainage

found a 0.2°C difference between drained and undrained plots (Scotter & Horne, 1985). Despite differences in groundwater levels and soil moisture content, the authors reported the measured difference in temperature was within the range observed by replicate thermometers during the study. Consequently, they proposed that the mole drainage had no observable effect on soil temperature.

The present study suggests that differences can be observed in both thermometer and TIR measurements. Low agreement between point-based soil temperature measurements and coarser resolution raster data was expected and had been previously reported (Soliman *et al*., 2013). A more accurate understanding of the relationship between soil- and surface temperatures would likely require temperature measurements at a shallower depth than those collected in this study. Soil temperatures become cooler, have narrower diurnal range and experience increasing lag behind surface temperatures with increasing depth (Hillel, 1998). The reason for the moderate negative relationship between soil- and surface temperatures at 9 am was not immediately clear (see Figure 6-7). It likely represented a cumulative effect of different environmental parameters, including a possible lag effect of cool night-time temperatures or perhaps contrasting rates of photosynthesis and transpiration (Woledge & Parsons, 1986). Other effects cannot be ruled out., particularly the high relative humidity on the morning of the survey which .may have influenced the surface temperature measurements to some degree.

TIR images identified portions of individual tile drains, but the densely grouped mole drains were more difficult to distinguish individually. A possible reason for this was the different thermal properties of sand-mole channels compared with air-filled collector pipes (0.026 W/mK at 20°C, versus ~0.2 to 3 W/mK for wet/dry sand respectively) (Farouki, 1981). The thermal conductivity of the sand-filled channels is dependant on temperature and moisture gradients, which will impact on the amount of radiant heat measured by the sensor. The UAS ATI method delineated approximately 59% of tile drains and 64% of the now piped (or partially-piped) drain associated with the earlier field boundary system. These findings are consistent with the results of Allred who used a single TIR image to identify ~60% of the overall length of tile drains on a bare field (Allred *et al*., 2018). The Allred approach identified spatial anomalies in moisture content in a method that that conceptually was quite close to the NIR approach of used by Verma, Naz etc. (B. S. Naz *et al*., 2009; Verma *et al*., 1996). Previous studies have occurred on bare soils. The ATI method tested here was carried out in under densely vegetated conditions. Spatial- and temporal- anomalies in surface temperature were recorded. The ATI approach mitigates the potential that a single thermal image may not have sufficient thermal contrast to identify drain lines at a given time.

The existing (infilled) boundary ditches were identified as cooler anomalies, in contrast to the warmer, newer subsurface drainage system. In the case of the east-west ditch crossing the centre of the study area, this received water from the new subsurface drainage system and therefore was likely to have a higher volume of waterpresent, resulting in lower surface temperatures from the effect of evaporative cooling. The 5-hour temperature difference image identified regions of high ATI which did not correspond to known drainage features. These

could reflect further unknown drains, or perhaps variability in soil texture or structure that could impact thermal properties

6.4.2 Future improvements

This study used a single longwave thermal infrared sensor to identify spatial anomalies in surface temperature. Future work in this area could focus on the integration of TIR data with optical imagery (RGB or multispectral). Some commercial companies currently provide dual sensors, for example, the FLIR Duo Pro, or MicaSense Altum that would allow complementary and simultaneous mapping of surface emittance and reflectance properties. The fusion of thermal and VNIR data could enhance identification of subsurface drains in grassland, where there may also be contrasting reflectance associated with sward over or adjacent to drain tiles. For example, VNIR reflectance from EO satellites has identified mproved vegetation growth in response to drainage installations (Kobryn *et al*., 2015). Similarly, shortwave infrared bands (SWIR, 1.4 to 3 μm) sensitive to moisture content could have an important role in identifying vegetation stresses (Gao, 1996; Yao *et al.*, 2018). The spectral characteristics of "drained" and "undrained" sward (albeit at a coarser spatial resolution) are discussed and illustrated in Chapter 3.

A constraint on automated drain detction will always be the problems caused by heterogeneity in soil physical properties (texture and structure) over small distances. Sudden changes in soil texture and structure will be a source of potential uncertainty in mapping using UAS TIR. Better knowledge of the the spatial extent of these soil properties at field scale is necessary. TIR remote sensing can play a role here. Soil texture maps have been developed using

remotely sensed TIR time series measurements (ASTER) (Muller, 2016), where temporal thermal patterns were extracted from a time series principal components analysis and input into a multiple linear regression model to estimate soil texture fractions. The development of TIR drainage mapping as a commercial service would need to al;oow for or account for natural cahnges in soil moisture as a result of soil type.

An improvement to this method would be automate the process. Previous studies, such as Naz & Bowling (2008) used a stepwise approach that first identified potentially drained areas using a decision tree classification, followed by directional edge enhancement filtering, density slice classification, Hough transformation, and automatic vectorization. The Hough transformation provided the best results in producing a map without discontinuity between lines. Connolly and Holden (2017) mapped peatland drains using object-based image analysis (OBIA) on a very high spatial resolution Geoeye-1 imagery. OBIA may be less accurate on a single channel thermal image than RGB or multispectral imagery. Combined thermal and optical data could give better results. There are iterative GIS procedures that could be scripted to automate detection, for example skeletonisation or raster thinning[13]. Automating the process would need to address gap filling in detected lines. None of the RS methods currently available for drain mapping can extract drain network perfectly. Compensating for these gaps was not the focus of this study, but would make an interesting avenue of future work. Gap filling using fuzzy inference has been used in previous road extraction projects that could be suited to the problem of drain gap filling (Hashemi *et al*., 2011). This approach used correlation between extracted segments to deteermine whether there is sufficient agreement.

[13] Hasthorpe, J. & Mount, N. 2007. The generation of river channel skeletons from binary images using raster thinning algorithms. Paper submitted to GISRUK 2007. Available online at https://www.geos.ed.ac.uk/~gisteac/proceedingsonline/GISRUK2007/PDF/P7.pdf

Mahktan *et al*. (2012) used a Radon transformation for gap filling whereby linear features are thinned and endpoints are detected. Endpoints are the connected using a spline interpolation. This method had a good performance on straight vectors, but failed at intersections.

6.4.3 Extending the ATI method to agricultural mapping

Grass height as a potential source of error was minimised by ensuring the grass cover was mown and maintained at ~4.5 cm to replicate post-grazing sward height for intensively managed grassland. These results suggest the ATI method proposed here could be undertaken for livestock farms immediately following grazing or cutting. The impact of increased sward height was not explicitly measured in this study, but increasing canopy height could be expected to have a dampening effect on heat flux from the soil surface thereby masking surface ATI. Topography over the study area was flat, with slope and aspect unlikely to have influenced incoming solar radiation to any significant degree. Neither was the playing surface obscured by shadow from adjacent hedges or buildings. Irregular topography and microtopography and field boundaries might have a greater impact on insolation in agricultural settings. Nonetheless, the results presented herein suggest the UAS ATI approach has considerable promise in mapping artificial drainage systems and for identifying artificially-drained areas on intensively managed grassland. UAS are constrained by regulations setting maximum flying altitude, and also by battery power, which limits the area they can expect to map in a day. For wider catchment mapping, there are potential applications for manned flights using a combination of TIR sensors integrated with multi- or hyperspectral sensors, as currently exists in the form of Sensorpod (Cahalane *et al*., 2017).

6.4.4 Potential applications

The development of an effective method for mapping subsurface drains could permit mapping of drainage infrastructure and bring considerable environmental benefits. Currently, in Ireland there is no effective means of locating buried drains over broad areas. Knowledge of drain location can improve understanding of hydrological processes at field level, and the impact this can have generally on surface runoff, streamflow, sedimentation and soil erosion at broader scales (Armstrong & Garwood, 2006; Gramlich *et al.*, 2018). Mapping subsurface drainage can improve modelling of greenhouse gases (GHG), for example, by providing a greater understanding of the spatial extent of potentail areas of denitrification (on wet soils)or carbon losses (on drained organic soils) (Clagnan *et al.*, 2018; Paul *et al*., 2018). Identifying drained lands and mapping drain locations is an important step in facilitating the rewetting or restoration of wetlands to recreate carbon sinks to offset carbon dioxide emissions. Rewetting of peatlands is considered an important climate change mitigation tool to reduce emissions and create suitable conditions for carbon sequestration. Paul et al. (2018) estimated that rewetting histic soils and restoring natural water table conditions could result in annual savings of 3.2 million tons CO^2 equivilant. This would obviously have knock-on impacts on farm operations and income in some instances, while presenting opportunities in terms of biodiversity and landscape conservation. A clearer understanding of drain location and drain spacing can help mitigate the excessive loss of nitrates in drain flow, a leading contributor to water quality reduction and loss of aquatic habitat and biodiversity (Blann *et al*., 2009; Kladivko *et al.*, 2004; Skaggs *et al*., 1994). Identifying buried drain locations as a means of mitigating nitrate losses before they reach waterbodies would be a considerable move towards implementing the objectives of the European Union Water Framework Directive (2000/60/EC), which sets out to achieve "good quantitative status" and "good chemical status"

of surface water quality by 2027 at the latest. A 2018 report from the Environmental Protection Agency (EPA) warned of deteriorating water quality in Ireland's rivers as a result of nitrogen and phosphorus, with a 3% net decrease in water quality between 2015 and 2017 (EPA, 2018).

6.5 Conclusions

There is widespread interest in developing reliable and effective methods of mapping artificially-drained areas and subsurface drainage systems. The proliferation of UAS and affordable optical sensors within precision agriculture has provided new opportunities for novel approaches to identify subsurface drains. The ability to effectively and cheaply detect the locations of subsurface drainage would be a major step towards mitigating nitrate losses from farmland and improve water quality status. This study assessed whether UAS-derived TIR imagery could locate artificially drained areas or individual drainage lines using a thermal inertia method with images taken during the morning and afternoon. Significant differences in surface- and soil temperatures were observed between drained and undrained locations of the site. The results of the experiments indicated that UAS TIR images could provide an estimate of surface TI that is proportional to the TI of the underlying soil. The study demonstrated that, under the conditions of the survey, TI could distinguish artificially drained areas from undrained areas within a field using a UAS TIR. The identification of individual pipes was achievable, although it was not always possible to detect the entire length of a drain. This is not uncommon. Other optical/ thermal methods have fallen short here too. The drains associated with previously boundaries were detectable. The thermal signals of the

mole drains were less clearly defined, however, this may have been due to the overall effect on thermal properties in the broader soil profile created by the dense network of mole drains.

These results presented here show potential for UAS-based thermal remote sensing for identifying drainage systems on grassland. Future research would need to evaluate the effect of prevailing weather conditions, variable soil/ topography and canopy height. As UAS play an increasing role in precision agriculture, this method has the potential to be an affordable and efficient means of identifying subsurface drainage for intensively managed grasslands. It also has potential applications in other disciplines, for example, pipeline leak monitoring or archaeological prospection.

This page is intentionally blank

Chapter 7 Conclusions

The impact of poor soil drainage and excess soil saturation on agricultural production was outlined in Chapter 1. It was shown how many Irish farms, through a combination of heavy soils and high rainfall, experience reduced profit and pose a greater risk for environmental damage than comparable farms in drier areas. Underlying this work is the poor understanding of soil drainage regimes at farm level in Ireland. At the coarse scale of soil maps such as the Irish Soil Information System (1:250,000) local variations are over simplified or overlooked and cannot accurately describe farm or field soil properties. Additionally, these maps do not account for subsurface drainage. Once drained, artifically-drained soils no longer respond to saturation in the same way. These changes must be accounted for when developing agronomic or environmental models that rely on accurate characterisation of soil drainage. The reaserch outlined in the preceding chapters has identified several novels ways in which EO data can be used to map drainage at farm level using satelitte- and UAS-based sensors and a variety of state-of-the-art methods, including machine learning image classification, thermal remote sensing and structure from motion photogrammtery.

7.1 Research questions

This section discusses the key research findings from Chapters 3-6 with respect to the principal research questions proposed in Chapter 1 (Section 1.8).

7.1.1 Research Question 1

There is no efficient method of mapping the extent and distribution of artificially drained soils on Irish farms. Using advanced machine learning image classification algorithms (support vector machine and random forest), is it possible to distinguish artificially-drained fields on naturally-poorly drained soils using moderate spatial resolution Landsat 8 imagery?

The results from Chapters 3 and 4 strongly support the conclusion that moderate resolution EO imagery from the Landsat 8 mission can accurately detect artificially-drained fields on heavy grassland soils. Freely available data from the Landsat 8 mission has the neccesary radiometric-, spectral- and spatial resolution to classify drainage properties on intensively managed grassland at field-level. Landsat 8 NDVI images in Chapter 3 demonstrated their ability to monitor the medium-term recovery from saturated soils following flooding. Such information could benefit farming communities in persistently flooded areas by mapping the persistent impact of wet soils on grass production. The maps and graphs in Chapter 3 could provide an on-going assessment of the rate of recovery on farmland worst affected by extreme weather, identifying locations or individual farms where support efforts or relief funds could be best directed to. In Chapter 4, VI, individual spectral bands and topographic data were combined to map areas of persistent saturation across a large area. These were not explicitly in flooded areas, but rather on heavy soils which were more likely to have impeded drainage and were susceptible to extended periods of saturation. The BMW area was chosen as it had a high percentage of poorly drained soils, and experienced high annual volumes of rainfall. The combination of poor soil drainage and heavy rain is a recognised constraint on farm productivity in the region. Drainage works are known to have been carried out here over several decades, but it was not known where the drained soils were. The novel approach outlined in Chapter 4 classified soil drainage conditions by mapping contrasting reflectance

over known heavy soils. The different signals for drained and poorly drained classes related to contrasting plant health. The study assumed that the underlying soil map was correct in its classification of soil type and natural drainage class. According to Chpater 4, 44% of heavy soils in the region had been artificially drained. It also found a broad agreement between previous assessments of drained areas based on grant allocations during the twentieth century and percentage of soils classed as artifically drained by the current study.

The improved spatial, spectral and temporal resolution of Sentinel 2 is better suited to classification by reducing the impact of mixed pixels at field boundaries. Very high spatial resolution is available with commercial EO satellites but the cost of using such data is prohibitive over large study areas. The Landsat and Senitinel missions provide their data free of charge. The accuracy assessment of the drainage classification model in Chapter 4 demonstrated how model accuracy was influenced by the number of satellite scenes available for analysis. The number of available scenes depended on the percentage of cloud cover within a scene at the time of acquisition. Unfortunately, cloud and cloud shadow are insurmountable constraints on the use of optical satellite data in Ireland. As discussed in Chapter 4, the Landsat 8 scenes making up the mosaic ranged in number from 1 to 18 images over a three year period of the study. Higher misclassification rates occurred where the number of contributing images was low.

The current Sentinel 2 mission, with its improved spatial, spectral and temporal resolution is a marked improvement on the Landsat 8 mission. Sufficient data was not available when this project began to justify using Sentinel 2 data. Had the project started now, it would certainly

have been used. One can only speculate as to how the resulting maps would have been improved, but better definition of drained areas within fields woul dcertainly be possible, while the addition of red edge bands not available to Landsat may have had an effect on the classification algorithms. The improved temporal resolution of Sentinel 2, with a return period of 2-3 days over Ireland should, theoretically, produce a greater volume of cloud free images. Ten-day, monthly and seasonal composites of Sentinel 2 data have already been created for some areas of mainland Europe (Griffiths *et al.*, 2019). However, as Figure 7-1 illustrates, even with high temporal resolution optical data cloud cover will still be a signifincat challenge. When sufficient Sentinel 2 data is available to create high-resolution temporal composites, there will be an opportunity to enhance identification of field drainage condition on Irish farms. There is also the possibility of combining data from the two platforms, or the possibility of data fusion with coarser resolution sensors, for example using MODIS (250 m) or Sentinel 3 (300 m) images. The reduction in spatial resolution may be offset by the increased spectral resolution, but may not suit the small field sizes and fragmented nature of the Irish landscape in most of the study area. The integration of data from planned hypersectral missions, for example EnMAP or PRISMA, could also facilitate a more robust characterisation of vegetation stress relating to drainage condition. .

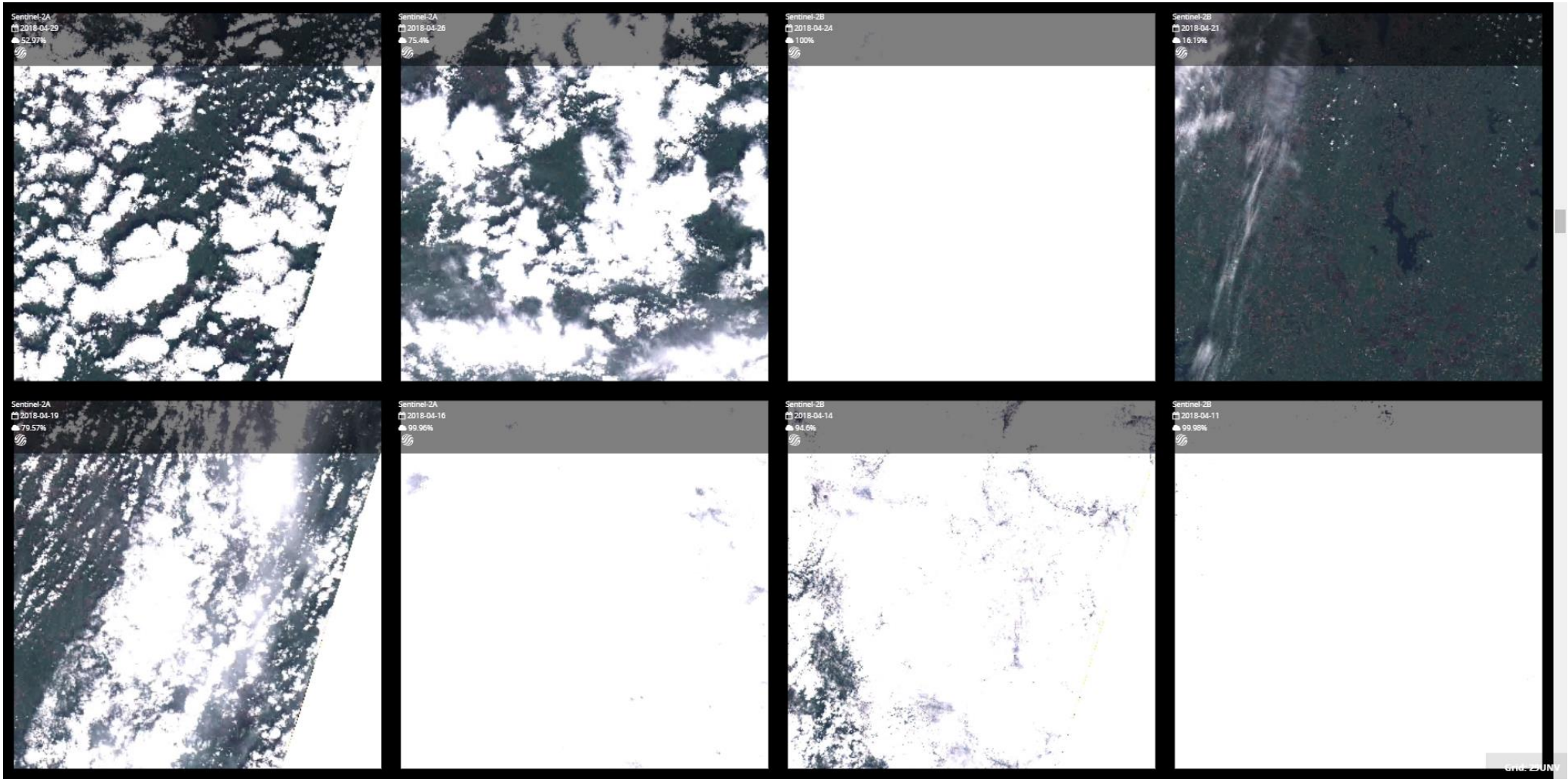

Figure 7-1 Cloud cover over the Midlands for Sentinel 2A and Sentinel 2B (tile 29 UNV) for 8 dates between 11-29 April 2018 (Source: Remote Pixel web viewer).

The need for accurate ground-truth was acknowledged in Chapter 4 where there was a clear disparity in map accuracy based on whether image- and field-based methods of validation were used. Field based accuracy assessments were the less accurate of the two methods The disparity underlines the requirement for up-to-date, accurate validation data when mapping such a highly spatially variable property as field drainage. The available field-based validation data was collected over a decade before the current project, with no guarantee the observations reflected current drainage conditions. Changes in land cover were likely responsible for this. But it should also be acknowledged that programmes such as the Heavy Frams Programme have been on-going in these areas for several years, providing a knowledge base for farmers on methods to improve farm production on heavy soils. Some of the improvements in drainage status since 2005 may be as a result of initiatives such as this. The collection of ground-truth reference data over large areas is time-consuming and expensive but is an essential element of land cover mapping. Collection of validation data is an area where proximal sensors could be employed to great effect. These are sensors placed into or above that ground that measure, directly or indirectly, soil properties, for example, soil moisture and soil temperature. Proximal sensors are currently available to Irish farmers currently, but there is no data on how extensive there use is. One commercial company (Grasstec, in partnership with Remote Signals) produce soil temperature monitors that record soil- (10 cm depth) and ground (canopy) temperature every 3 hours and make the data available through a mobie phone app. As established in Chapter 6, diurnal soil temperature data can be used to distinguish drained and undrained soils. Use of single sensor data as ground-truth would be complicated due to the spatial disparity in scale between point- and aggregated gridded-data. These scale issue could be partially mitigated by using distributed sensors linked wirelessly to provide more spatially representative field data (Bogena *et al.*,

2010). The fragmented nature of Irish farms could likely be an issue for establishing networked sensors for synoptic monitoring purposes.

There were some restrictions on the classification approach taken in Chapter 4 that should be noted. The model was trained on two classes, drained and undrained which best suited the support vector machine algorithm that was used for the classification. The high accuracy attained by the model likely reflects this binary division. In reality, there is a spectrum of drainage states between these two extremes. In the field, these differences are determined by observations of the whole soil profile, taking into account features associated with saturation (for example, gleying and mottling). However, identifying intermediate classes solely using multispectral imagery is more difficult to achieve, where saturation is determined by vegetation stresses. In this regard, it is less clear cut at what stage This was identified as an issue during the literature review, where higher success rates were achived when fewer classes were considered. The greater spectral resolution of narrow band hyperspectral sensors could improve the classification of intermediate classes, where differences in vegetative stress may be more readily observable. Hwoever, the identification of intermediate classes would require more detailed field observations of drainage status. Secondly, the model assumed the soil and land cover data that were used to mask the EO data were accurate. Given the ~25 ha minimum mapping units for each of these datasets, discrepancies between predicted and actual conditions at field and point-scale are expected due to the high heterogeneous nature of land cover and soil type across small distances. In some cases, the drained conditions recognised by the model in Chapter 4 could in fact be pockets of naturally well-drained soil, for example. Similarly, the model cannot account for differences between

farms that may effect the phenological stages of grass growth, for example local weather, or different management strategies, for example grazing intensity and nutrient input.

7.1.2 Research Question 2

Are there contrasting signals for grass growing under poorly-drained and drained conditions? Furthermore, if there is a measurable difference, what are the important Landsat 8 wavelengths for characterising this difference?

The spectral characteristics for “drained” and “poorly-drained”classes specific to Landsat 8 were defined in Chapter 4 (see Figure 4-2). Spectral characteristics were slightly different for Sentinel 2 (Figure 4-7) and would be different for all any other sensor, as a result of different sensor specification, oribital path and height, viewing angle etc. For Landsat 8 imagery, pixels that were assigned the class label “poorly drained” were distinguished from the “drained” class by greater reflectance of red (0.64- 0.67 µm) and shortwave infrared (SWIR) (1.5- 2.3 µm) wavelengths, and by lower reflectance in near-infrared (NIR) wavelengths (0.85- 0.88 µm). This would be the typical spectral response for stressed vegetation, where less red light is absorbed for photosynthesis and less NIR light is being reflected due to lower chlorophyll production. The remaining *visible* bands were not as efficient at identyfing poor drainage. This was not surprising, poor drainage may be difficult to see unless a significant saturation issue has developed. EO data has long been used to observe subtle changes in plant health before they are visible to the naked eye.

The variable importance measured through the the Random Forest algorithm found the Landsat 8 NIR band and VI based on it (in this case NDVI and NDWI) had the greatest

predictive value of all variables used (spectral and topographical). For Sentinel 2, red edge and NIR bands were critical. Red edge bands are located in region of the EM spectrum where reflectance values of green vegetation rapidly increase between red and NIR regions. These are not available on Landsat 8, but have been shown to be important for mapping chlorophyll content vegetation biomass. The shortwave infrared bands (SWIR2) was the more important of the two SWIR bands, with its sensitivity to soil and vegetation moisture content.. Thermal infrared bands (not used in this study due to a malfunction with the Landsat 8 TIR band during the period of study) measure land surface temperature from emitted thermal radiation. The Sentinel 2 mission does not have a thermal band, which is an advantage for Landsat 8 over the Sentinel 2 satellites. The Landsat thermal bands are at a coarser spatial resolution (120 m resampled to 60 m), however, resulting in a greater likelihood of mixed pixels.

As illustrated in Figure 4-3, the timing of image acquisition to correspond with the peak phenological stage for grass growth was important. This was also noted by Tetzlaff *et al.* (2009) and Tlapáková *et al.* (2017) in the review of similar projects in Chapter 2 (Section 2.1.1). Drainage class in the BMW area could be best distinguished using springtime images (April and May). The drained class, spring images had a higher monthly rate of change for NDVI values relative to the undrained class. Classes coulud also be distinguished in late summer where the opposite effect was observed. In this period, a moisture deficit on well drained soils created drought conditions which depressed NDVI. Conversely, the undrained class had higher NDVI as it had access to a greater volume of soil moisture. This was recenty illustrated in a map produced by Teagasc's Spatial Analysis Unit, where 10-day composite MODIS NDVI imagery mapped seasonal grass growth in 2018 compared with a 10 year

average (2002-2012) (Figure 7-2). Due to a sustained heat wave in summer with low precipitation rate, the soils in the southern and eastern region experienced a drought and were less productive. These areas produced an estimated 5-10% less grass than normal. The poorly drained soils in the BMW regionwere less impacted, or in some areas produced more biomass than usual. This was because the heavy soils in this region were less constrained by the moisture deficit experienced elsewhere, while they benefitted from higher temperatures and greater sunlight.

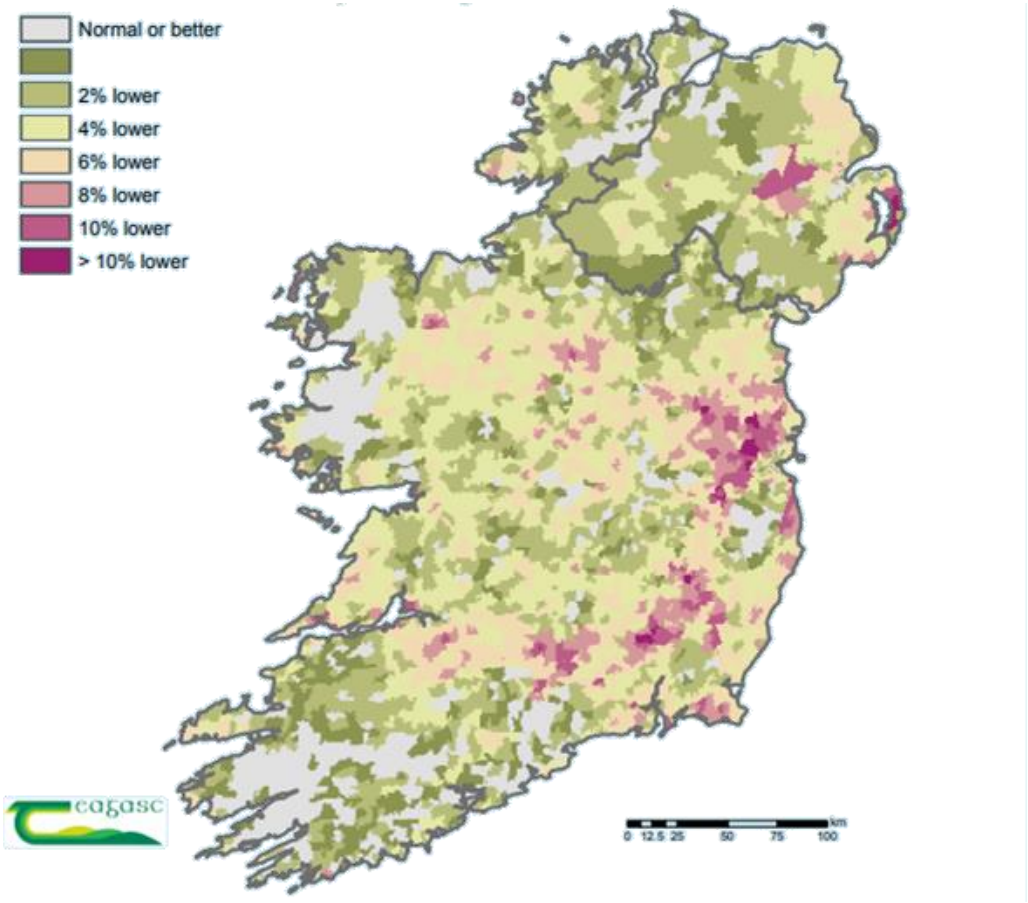

Figure 7-2 Fodder production in 2018 (percentage difference from 10-year average based on 10-day composite MODIS NDVI images) (Stuart Green, Teagasc).

7.1.3 Research Question 3

Using Landsat 8 NDVI images, is it possible to observe improvements in drainage status over time? For example, can improvements in grass yields be mapped following prolonged saturation (flooding), or following the installation of an artificial drainage system?

In Chapter 3 and Chapter 4 it was demonstrated how multispectral imagery, and particularly vegetation indices such as the NDVI, can monitor spatial patterns in canopy reflectance that relate to contrasting levels of soil saturation. For example, in Chapter 3 Landsat 8 NDVI imagery was used as a proxy for biomass and potential yield to observe the improvement in grassland production following prolonged saturation. Reduced growth and an inability to utilise the grass that is grown is a massive economic ocnstraint in rural communities following floods. This was neatly illustrated in Chapter 3 (Figure 3-9), where mean Landsat 8 NDVI values were expressed as a factor of flood duration. When floods and associated soil saturation persisted into early spring (when grass was actively growing), the recovery period back to expected levels took increasingly longer. It was illustrated how NDVI values for pixels still saturated in mid-April had lower than normal values than non-flooded areas and did not fully recover to expected levels of production for at least two months. The economic impact of this reduced production is considerable, particularly where fodder supplies have been consumed or destroyed and where there is no additional capacity to grow or harvest grass locally for several weeks. Monitoring vegetation condition against some benchmark (local average NDVI, for example) makes it possible to record grassland recovery and generate maps of the temporal and spatial distribution of saturated soils. It may not be possible to achieve this using moderate resolution EO data, but would be possible using coarser

resolution data, for example MODIS or Sentinel 3. There would be an associated lack of spatial accuracy however, as due to mixed pixels. UAS-based systems would be to monitor recovery over smaller areas is also an option.

It was subsequently demonstrated in Chapter 4 how the installation of a groundwater drainage system at Farm A in the BMW region resulted in increases to minimum, mean and maximum NDVI values over a periof of several years. These increases were consistent with an improved (drier, aerated) soil environment. This observation corresponds to several previously reported studies outlined in Section 1.3.1, where a link was made between grassland productivity and depth to watertable (for example, Brereton & Hope-Cawdery, 1988). At Farm A, a wet, poorly drained field experienced year-on-year increases in NDVI values (once again used as a proxy for biomass and yield) following the installation of a groundwater drainage system in 2014. The increases in spring 2016 were remarkable considering the extent of saturated soils in western counties following several successive, winter storms between November 2015 and April 2016 (as discussed in Chapter 3).

The time-series of NDVI, although incomplete and derived from different Landsat sensors, suggested an improvement in growth following drainage. With continued observations, it could be possible to identify the deterioration in growth (a reduction in NDVI) associated with declining drain function, for example, where maintenance (cleaning) or replacement (of mole drains, for example) is necessary. As this method used only NDVI to identify improvement, NDVI mosaics created from UAS imagery could substitute for satellite imagery. This would mitigate the the loss of data that occurs where extensive there is cloud cover. The use of UAS

would allow for more systematic monitoring of drain function. The very high spatial resolution provided by UAS might also identify growth anomalies related to contrasting drainage properties, which could potentially be used to identify subsurface drainage lines.

7.1.4 Research Question 4

What role do UAS have in high spatial (and temporal) resolution mapping of surface and subsurface drainage pathways? Specifically, can UAS-derived photogrammetric surface models substitute for LiDAR elevation models when modelling nutrient losses in overland flow in a managed grassland environment? Photogrammetric and LiDAR topographical point clouds and topographic models are statistically compared. Also, can UAS thermal cameras identify heat anomalies at the surface that relate to subsurface drainage systems in a managed grassland environment?

UAS were used to great effect in this research for high spatial and temporal resolution mapping. UAS are an important complement to satellite data, capable of acquiring data on demand when satellites cannot and at a spatial resolution that is unmatched by any operational EO satellite currently in orbit. The versatility of UAS, in conjunction with photogrammetric software, for accurately modelling field topography was demonstrated in Chapter 5. A ~9 ha field was surveyed in ~30 minutes using a widely available out-of-the-box drone system. Processed in ease-to-use (commercial) software, high resolution surface models and RGB orthomosaics can be produced in a matter of hours. The DSM produced in Chapter 5 were not statistically different to DEM created using 40 ppm LiDAR data, especially at 2 m and 5 m spatial resolution. Slope and overland flow rasters created using LiDAR and

photogrammetry were not statistically significant For the study area, grass height was a source of error but its effect was no longer at 5 m spatial resolution. This finding represents a huge cost saving for individuals who require high resolution topographic data of intensively managed grassland but who are unable to afford the very high cost of laser scanning. The use of thermal remote sensing for mapping subsurface drainage was demonstrated against a known drainage system. The identification of ~60% of the system is consistent with recent studies in the USA using NIR and TIR.

7.2 Benefits of EO for drainage mapping

While there have been several studies identifying the contrasting economic fortunes of farms under contrasting drainage regimes, the impact of wet soils on farm management and environmental quality (refer to Section 1.3), there has never been a concerted attempt to map soil drainage properties on Irish farms in any consistent or harmonised way. There were practical reasons for this:

Soil is a complex, 3-phase medium which is spatially and temporally heterogeneous. Mapping soil properties using conventional survey methods is expensive and labour-intensive.

Conventional survey methods do not accurately reflect broader conditions at field scale and can have little relevance beyond the immediate sample location.

Improved drainage is a temporary adjustment. Drains require regular maintenance or replacement to keep them operating at expected capacity. Mole drains for example, may need replacement every other year in some locations to remain operational.

EO/RS offers several advantages over conventional mapping for improved characterisation of soil drainage properties:

- It offers unparalled geographical coverage.
- It allows for repeated measurements, in particular since UAS permit data capture on-demand.
- It provides a greater context to drainage conditions by capturing a wider view of an area than traditional point-based sampling.
- It can be conveniently combined with other raster data, for example, topographical data, and quickly imported and processed by GIS or image processing software.

7.2.1 Cost benefit

The greatest advantage of using EO data is the low cost of acquiring the data relative to conventional surveys. There is an unprecedented volume of moderate resolution EO data now freely available through different USGS/NASA and ESA missions. The Landsat mission has a legacy archive stretching back over 40 years. The current Landsat 7 and Landsat 8 platforms will continue to provide multispectral data at 30 m spatial resolution (and thermal infrared data at 120 m) for a nmber of years, with another mission, Landsat 9, planned for launch in 2020. The Sentinel 2 mission is in operation since 2014 and fully operational since 2017. Two further satellites, Sentinel 2C and Sentinel 2D, are expected to launch from 2021 onwards.

The time and effort required to process and analyse RS data is also being reduced. Increasingly, EO data is being made available to end users as analysis-ready, surface reflectance products (Level 2A) with associated pixel quality assurance (QA) layers for cloud masking. The easy availability of imagery, processed in a consistent way is a huge benefit to

land cover mapping or projects using multi-temporal data. Computation and production time can be reduced by using surface reflectance products as long as due care and attention is given to the quality assurance. An important step that is often necessary is reprojection of data into regional or national coordinate reference systems optimised for localised use (Serbin & Green, 2018).

7.2.2 Data processing

Coupled with the free availability of high quality image data is an increasing number of free or open-source software to analyse the data. Free GIS software, for example, QGIS, ORFEO, GRASS and SAGA are all capable of image processing, classification and visualisation. QGIS in particular is an extremely successfult substitute to commercial software such as ArcGIS or ERDAS. The Sentinel toolbox (SNAP), used extensively in processing SAR data in Chapter 3, can also be used to process optical images from a range of sensors. Increasingly, scripting languages, for example, Python or R, are providing access to advanced machine learning and data analytics. Machine learning has been used to great effect in previous land cover mapping in Ireland (Barrett *et al.*, 2014; Cawkwell *et al.*, 2017). The accuracy achieved using SVM and RF in Chapter 4 are very promising. Highest overall accuracy for high spatial resolution image-based validation was 91.4%. Using field observations, the highest overall accuracy was 68.7% (see Table 4-3 & Table 4-4). RF preformed better using image-based validation data, while SVM performed better with field-based validation data. The differences in accuracy between each algorithm were not statistically significant however.

7.2.3 Timeliness

The research presented above is timely. There is a growing need for up-to-date soil data, including a better awareness of the spatial distribution of artifically-drained fields. The installation of drainage on farms can have unintended or unpredictable consequences that may cause environmental damage, for example, nutrient loss to waterbodies, increased streamflow and flooding, increased soil erosion and loss of habitat and biodiversity (Section 1.3). A recent EPA report indicated how Irish surface- and coastal waters are experiencing increased eutrophication (EPA, 2018) with a modest reduction in water quality since 2015. Knowing locations of increased likelihood for nutrient loss, either as overland flow or in drain flow, would allow targetted remediation measures to be put in place that allow improved mitigation of potential impacts. Another reason for accurate landcover data is the need to quantify greenhouse gas (GHG) emissions and determine carbon budgets from changing levels of management intensity. There is also an increasing awareness of the need to improve grass growth and utilisation following several fodder shortages in recent years. Land drainage is widely seen in the agri-food industry as a vital component in achieving the ambitious production intensification goals of Food Harvest 2020 and Food Wise 2025. Prior to this research, there were no data indicating current drainage status on Irish farmland, for example where might benefit from improved drainage, in order to increase production and utilisation, and to reduce the risk of poaching-and structural damage. A clearer understanding of the potential impacts on agricultural production is critical in light of increasing climate uncertainty and the possible effect extreme or unpredictable weather might have over the coming decades. The expectation nationally is for wetter winters resulting in greater soil saturation with drier summers resulting in increased drought (Holden & Brereton, 2002). A long-term, upward trend in the annual number of rain days and the volume of precipitation will likely

result in higher soil saturation/ flooding in the future, especially in the western half of the country (Charlton *et al*., 2006; Kiely *et al*., 2009).

7.3 Future work

A key aspect of this study was the use of very high spatial and temporal resolution UAS data to detect surface and sub-surface drainage properties at field level. Drone capability will continue to develop in the coming years and their potential applications for precision agriculture will continue to expand. Potential follow on studys for expanding the research described above would be to develop the two field-based studies to examine their efficiency at scaling up research to farm- to catchment scale. There are important benefits to such an exercise. The ability to map at high resolution drainage pathways at the surface or in subsurface at field level can have considerable impacts for catchment water quality management. Accurate accounting of drainage pathways has implications for understanding sources of water quality degradation within a watershed. Representing complex spatial patterns over large areas is difficult and hydrological models are frequently hampered by poor reproducibility of experiments at plot and catchment level (Zehe & Blöschl 2004). It would therefore be desirable that the novel EO approaches discussed in preceding chapters are supported by additional validated experiments at wider levels to address whether catchment scale photogrammetry and detection of drained areas using thermal or multispectral data can accurately parameterise hydrological models and estimates of runoff and nutrient enrichment. Aurousseau *et al*. (2009) modelled drainage flow over a catchment and were able to indicate which areas in the catchment contibuted most runoff and had the greatest impact on water

pollution. Mapping drainage over a catchment can also allow better estimation of drainage capacity and discharge (Yang *et al.*, 2000).

There are problems with upscaling the use of UAS photogrammetry to farm or catchment level. This was already addressed to some degree already in Chapter 5. The pressing issue is to adequately map breakthroughs and delivery points beneath hedges and obscuring canopy. Passive sensors cannot penetrate vegetation and will never be able to map hidden drains. Integrating drainage information to DEM or DSM, for example from vector mapping, requires additional processing and a greater scrutiny of surface drain topology. Taking on larger surveys at a field-by-field will have additional concerns where procedures and methods between areas may effect results. In reality, the key to the widespread adoption of high resolution topographic modelling is to make existing high resolution datasets freely available to the public. High-resolution topographic data is essential to quantify flood depths and volumes accurately. The national mapping agency (OSI) has recently engaged airborne laser scanning of 185,000 ha nationally at high point density[14] which will be of benefit to future mapping projects. Many European countries have taken steps to high-resolution elevation data freely available (for example, Denmark[15], Spain[16] and the Netherlands[17]). The UK provides free LiDAR-derived raster datasets at 0.25 m to 2 m spatial resolution with a vertical accuracy of ~5 cm[18]. A recently launched initiative in Ireland (Open Topographic Data Viewer)

[14] www.osi.ie/products/bluesky-aerial-imagery-lidar/bluesky-ireland. Accessed 12 December 2018.
[15] https://download.kortforsyningen.dk/content/dhmpunktsky. Accessed 12 December 2018.
[16] http://centrodedescargas.cnig.es/CentroDescargas/buscadorCatalogo.do?codFamilia=LIDAR. Accessed 12 December 2018
[17] http://www.ahn.nl/common-nlm/open-data.html. Accessed 12 December 2018.
[18] https://data.gov.uk/dataset/lidar-composite-dsm-1m1. Accessed 12 December 2018.

has put some publically-held high resolution data freely available at 1 m[19]. The current archive is very limited however and is nowhere near national coverage. At smaller scales, high-resolution elevation data can be captured using UAS imagery to build photogrammetric DSM. UAS DSM can produce high-resolution elevation data comparable to LiDAR under certain circumstances (see Chapter 4 below). UAV DSM have been successfully applied to high-resolution flood modelling and prediction (Coveney & Roberts, 2017; Şerban *et al.*, 2016).

One need only look at the upsurge of remote sensing applications that followed the release of Landsat data in 2008 to see the potential to different sectors that free topographical data may provide. following sections look at potential future research directions based the on the research described in this thesis

7.3.1 Climate change

Land–use change is an important driving force affecting ecosystem processes and services, and can have wide-ranging and longterm environmental consequences. Further development of this research can support and inform climate change mitigations by improving national greenhouse gas (GHG) inventories where management intensity on grassland increases or decreases. As pasture-based agricultural practices intensify, more detailed and precise inventories of Irish grassland is necessary to achieve sustainable grassland management. Reducing GHG emission on Irish grasslands is a pressing challenge for the agri-food sector to meet. Under proposed EU legislative changes (due to come into effect in 2021), member states will be required to account for GHG emissions and removal from managed cropland and grassland. Improved drainage management, including rewetting of drained soils, is a

[19] www.gsi.ie/en-ie/events-and-news/news/Pages/Open-Topographic-Data-Viewer0424-6054.aspx. Accessed 12 December 2018.

cost-effective method for increasing carbon sequestration on managed grassland. Therefore expansion of the drainage classification to cover all soils (organic and mineral) nationally and its integration with existing soil maps, should be a priority for future research. The results presented herein demonstrate how EO data can provide a performance assessment of drainage condition, something that is not currently provided for within existing maps. Providing on-going assessments of current drainage performance should be a key part of future development of the project.

7.3.2 Soil moisture deficits

Additional modelling of soil drainage to identify an intermediate stage between "drained" and "undrained" states would be useful. From an EO perspective, this might require greater spectral resolution, for example, by incorporating data from upcoming hyperspectral missions, or making greater use of proximal data on soil moisture and soil temperatures. The fusion of remote and proximal data and techniques can enhance the capability to measure soil properties. Proximal sensors have benefitted from advances in distributed wireless sensor networks, increasing the spatial coverage of these probes. They are gaining popularity in agricultural applications for irrigation scheduling and acquiring local agrometeorological data. There are also exciting new techniques for field-scale soil moisture measurements that are very accurate compared to in-situ soil moisture measurements. Cosmic ray neutrons probes and GNSS L-band reflectometry both show promise for SM measurements over intermediate scales between point based sampling and satellite ground sampling distances (~300m2). From a training and validation perspective, additional fieldwork would be necessary to accurately match spectral characteristics and soil moisture content with actual soil drainage

classes. Linking modelled drainage classes to soil moisture deficit (SMD) calculations currently provided by Met Eireann would provide field-level assessments of SMD. The integration of an EO-based drainage classification would be an improvment on existing model and a potentially powerful tool in precision grassland management, with greater predictive ability for the development of saturation or drought conditions or a better understanding of the risks of sol compaction or plulvial floodiing risk.

7.3.3 Precision agriculture

EO and RS technologies as a practical tool for PA is still very much in a developmental stage in Ireland. As demonstrated in this thesis, UAS have huge potential on Irish farms, for high resolution mapping and monitoring of farm performance. UAS have untapped potential in Irish farming, for example in weed or pest detection, monitoring nutrient deficiency, and for biomass and yield prediction. Some of these ares are being actively researched at the moment but further investment is needed to transfer research knowledge into a practical workflow for farms. Additional UAS-based techniques will continue to be developed that maximise the complementay ability of thermal and hyper/multispectral sensors to identify crop or environmental stresses at unprecedented spectral, spatial, and temporal resolution. The flexibility and affordability of UAS will likely see there use on Irish farms increase in the coming years, whether by farmers themselves or through dedicated service providers. There are several regulatory issues for thew ider use of UAS, and technical issues regarding data acquisition and processing that must be fully addressed before this can happen. The increasing availability of image processing, image mosaicing and image classification software will assist in overcoming many of the technical obstacles to using EO and RS data.

Farmers need to be informed and educated on the potential uses of UAS and EO data, and the potenatial cost-savings and advantages of investing in EO and UAS technology.

This page is intentionally blank

References

Aasen, H., Burkart, A., Bolten, A., & Bareth, G. (2015). Generating 3D hyperspectral information with lightweight UAV snapshot cameras for vegetation monitoring: From camera calibration to quality assurance. *ISPRS Journal of Photogrammetry and Remote Sensing, 108*, 245-259. doi:10.1016/j.isprsjprs.2015.08.002

Abdel-Hady, M., Abdel-Hafezl, M., & Karbs, H. (1970). Subsurface drainage mapping by airborne infrared imagery techniques. *Proceedings of the Oklahoma Acadamy of Science, 50*, 10-18.

AgiSoft. (2016). PhotoScan Professional (Version 1.2.6). Retrieved from www.agisoft.com

Agnew, L. J., Lyon, S., Gérard-Marchant, P., Collins, V. B., Lembo, A. J., Steenhuis, T. S., & Walter, M. T. (2006). Identifying hydrologically sensitive areas: Bridging the gap between science and application. *Journal of Environmental Management, 78*(1), 63-76. doi:https://doi.org/10.1016/j.jenvman.2005.04.021

Ali, I., Greifeneder, F., Stamenkovic, J., Neumann, M., & Notarnicola, C. (2015). Review of Machine Learning Approaches for Biomass and Soil Moisture Retrievals from Remote Sensing Data. *Remote Sensing, 7*(12), 23. doi:10.3390/rs71215841

Allred, B. (2013). A GPR Agricultural Drainage Pipe Detection Case Study: Effects of Antenna Orientation Relative to Drainage Pipe Directional Trend. *Journal of Environmental and Engineering Geophysics, 18*(1), 55-69. doi:10.2113/JEEG18.1.55

Allred, B., Eash, N., Freeland, R., Martinez, L., & Wishart, D. (2018). Effective and efficient agricultural drainage pipe mapping with UAS thermal infrared imagery: A case study. *Agricultural Water Management, 197*, 132-137. doi:10.1016/j.agwat.2017.11.011

Allred, B., Fausey, N., Peters, L., Chen, C., Daniels, J., & Youn, H. (2004). Detection of buried agricultural drainage pipes with geophysical methods. *Applied Engineering in Agriculture, 20*(3), 307. doi:10.13031/2013.16067

Allred, B., & Redman, D. (2010). Location of agricultural drainage pipes and assessment of agricultural drainage pipe conditions using ground penetrating RADAR. *Journal of Environmental and Engineering Geophysics, 15*(3), 119-134.

Anderson, M. G., & Burt, T. P. (1978). The role of topography in controlling throughflow generation. *Earth Surface Processes, 3*(4), 331-344. doi:10.1002/esp.3290030402

Armstrong, A., & Garwood, E. (2006). Hydrological consequences of artificial drainage of grassland. *Hydrological Processes, 5*(2), 157-174. doi:10.1002/hyp.3360050204

Arnesen, A. S., Silva, T. S. F., Hess, L. L., Novo, E. M. L. M., Rudorff, C. M., Chapman, B. D., & McDonald, K. C. (2013). Monitoring flood extent in the lower Amazon River floodplain using ALOS/PALSAR ScanSAR images. *Remote Sensing of Environment, 130*, 51-61. doi:10.1016/j.rse.2012.10.035

Atzberger, C. (2013). Advances in remote sensing of agriculture: context description, existing operational monitoring systems and major information needs. *Remote Sensing, 5*(2). doi:10.3390/rs5020949

Aurousseau, P., Gascuel-Odoux, C., Squividant, H., Trepos, R., Tortrat, F. & Cordier, M.O. (2009) A plot drainage network as a conceptual tool for the spatial representation of surface flow pathways in agricultural catchments. *Computers & Geosciences*, 35, 276–288.

Ayars, J. E., & Evans, R. G. (2015). Subsurface drainage—What's next? *Irrigation and Drainage, 64*(3), 378-392. doi:10.1002/ird.1893

Bailly, J. S., Lagacherie, P., Millier, C., Puech, C., & Kosuth, P. (2008). Agrarian landscapes linear features detection from LiDAR: application to artificial drainage networks. *International Journal of Remote Sensing, 29*(12), 3489-3508. doi:10.1080/01431160701469057

Barrett-Lennard, E. G. (2003). The interaction between waterlogging and salinity in higher plants: causes, consequences and implications. *Plant and Soil, 253*(1), 35-54. doi:10.1023/A:1024574622669

Barrett, B., Dwyer, E., & Whelan, P. (2009). Review Soil Moisture Retrieval from Active Spaceborne Microwave Observations: An Evaluation of Current Techniques. *Remote Sensing*, 2009, 1, 210-242; doi:10.3390/rs1030210.

Barrett, B., Dwyer, E., & Whelan, P. (2012). Sensitivity of spaceborne radar to near-surface soil moisture in grasslands across southern Ireland. *Irish Geography, 45*(2), 131-149. doi:10.2014/igj.v45i2.15.

Barrett, B., Nitze, I., Green, S., & Cawkwell, F. (2014). Assessment of multi-temporal, multi-sensor radar and ancillary spatial data for grasslands monitoring in Ireland using machine learning approaches. *Remote Sensing of Environment, 152*(Supplement C), 109-124. doi:10.1016/j.rse.2014.05.018

Barros, N., Gomez-Orellana, I., Feijóo, S., & Balsa, R. (1995). The effect of soil moisture on soil microbial activity studied by microcalorimetry. *Thermochimica Acta, 249*(Supplement C), 161-168. doi:10.1016/0040-6031(95)90686-X

Batey, T. (2009). Soil compaction and soil management – a review. *Soil Use and Management, 25*(4), 335-345. doi:10.1111/j.1475-2743.2009.00236.x

Behmann, J., Mahlein, A.-K., Rumpf, T., Römer, C., & Plümer, L. (2015). A review of advanced machine learning methods for the detection of biotic stress in precision crop protection. *Precision Agriculture, 16*(3), 239-260. doi:10.1007/s11119-014-9372-7

Belgiu, M., & Drăguţ, L. (2016). Random forest in remote sensing: A review of applications and future directions. *ISPRS Journal of Photogrammetry and Remote Sensing, 114*, 24-31. doi:10.1016/j.isprsjprs.2016.01.011

Bell, J. C., Cunningham, R. L., & Havens, M. W. (1994). Soil drainage class probability mapping using a soil-landscape model. *Soil Science Society of America Journal, 58*, 464-470. doi:10.2136/sssaj1994.03615995005800020031x

Bellvert, J., Zarco-Tejada, P. J., Girona, J., & Fereres, E. (2014). Mapping crop water stress index in a 'Pinot-noir' vineyard: comparing ground measurements with thermal remote sensing imagery from an unmanned aerial vehicle. *Precision Agriculture, 15*(4), 361-376. doi:10.1007/s11119-013-9334-5

Beucher, A., Møller, A. B., & Greve, M. H. (2017). Artificial neural networks and decision tree classification for predicting soil drainage classes in Denmark. *Geoderma*. doi:10.1016/j.geoderma.2017.11.004

Beven, K. J., & Kirkby, M. J. (1979). A physically based, variable contributing area model of basin hydrology / Un modèle à base physique de zone d'appel variable de l'hydrologie du bassin versant. *Hydrological Sciences Bulletin, 24*(1), 43-69. doi:10.1080/02626667909491834

Bilotta, G. S., Brazier, R. E., & Haygarth, P. M. (2007). The impacts of grazing animals on the quality of soils, vegetation and surface waters in intensively managed grasslands. In D. L. Sparks (Ed.), *Advances in Agronomy* (Vol. 94, pp. 237-280): Academic Press.

Blann, K. L., Anderson, J. L., Sands, G. R., & Vondracek, B. (2009). Effects of agricultural drainage on aquatic ecosystems: a review. *Critical Reviews in Environmental Science and Technology, 39*(11), 909-1001. doi:10.1080/10643380801977966

Blasch, G., Spengler, D., Hohmann, C., Neumann, C., Itzerott, S., & Kaufmann, H. (2015). Multitemporal soil pattern analysis with multispectral remote sensing data at the field-scale. *Computers and Electronics in Agriculture, 113*(Supplement C), 1-13. doi:https://doi.org/10.1016/j.compag.2015.01.012

Bodoque, M. J., Guardiola-Albert, C., Aroca-Jiménez, E., Eguibar, Á. M., & Martínez-Chenoll, L. M. (2016). Flood damage analysis: first floor elevation uncertainty resulting from LiDAR-derived digital surface models. *Remote Sensing, 8*(7). doi:10.3390/rs8070604

Bogena, H., Herbst, M., Huisman, J., Rosenbaum, U., Weuthen, A., & Vereecken, H. (2010). Potential of Wireless Sensor Networks for Measuring Soil Water Content Variability All rights reserved. No part of this periodical may be reproduced or transmitted in any form or by any means, electronic or mechanical, including photocopying, recording, or any information storage and retrieval system, without permission in writing from the publisher. *Vadose Zone Journal, 9*(4), 1002-1013. doi:10.2136/vzj2009.0173

Bolanos, S., Stiff, D., Brisco, B., & Pietroniro, A. (2016). Operational surface water detection and monitoring using RADARSAT 2. *Remote Sensing, 8*(4). doi:10.3390/rs8040285

Bontemps, S., Arias, M., Cara, C., Dedieu, G., Guzzonato, E., Hagolle, O., Inglada, J., Matton, N., Morin, D., Popescu, R., Rabaute, T., Savinaud, M., Sepulcre, G., Valero, S., Ahmad, I., Bégué, A., Wu, B., de Abelleyra, D., Diarra, A., Dupuy, S., French, A., ul Hassan Akhtar, I., Kussul, N., Lebourgeois, V., Le Page, M., Newby, T., Savin, I., Verón, R. S., Koetz, B., & Defourny, P. (2015). Building a data set over 12 globally distributed sites to support the development of agriculture monitoring applications with Sentinel-2. *Remote Sensing, 7*(12). doi:10.3390/rs71215815

Boochs, F., Kupfer, G., Dockter, K., & KÜHbauch, W. (1990). Shape of the red edge as vitality indicator for plants. *International Journal of Remote Sensing, 11*(10), 1741-1753. doi:10.1080/01431169008955127

Bourbigot, M., Johnsen, H., & Piantanida, R. (2016). *Sentinel 1 Product Definition*. Retrieved from https://sentinel.esa.int/documents/247904/1877131/Sentinel-1-Product-Definition

Bourgeau-Chavez, L. L., Kasischke, E. S., Brunzell, S. M., Mudd, J. P., Smith, K. B., & Frick, A. L. (2001). Analysis of space-borne SAR data for wetland mapping in Virginia riparian ecosystems. *International Journal of Remote Sensing, 22*(18), 3665-3687. doi:10.1080/01431160010029174

Breiman, L. (2001). Random Forests. *Machine Learning, 45*(1), 5-32. doi:10.1023/A:1010933404324

Brivio, P. A., Colombo, R., Maggi, M., & Tomasoni, R. (2002). Integration of remote sensing data and GIS for accurate mapping of flooded areas. *International Journal of Remote Sensing, 23*(3), 429-441. doi:10.1080/01431160010014729

Brown, K. M., Hambidge, C. H., & Brownett, J. M. (2016). Progress in operational flood mapping using satellite synthetic aperture radar (SAR) and airborne light detection and ranging (LiDAR) data. *Progress in Physical Geography: Earth and Environment, 40*(2), 196-214. doi:10.1177/0309133316633570

Brubaker, K. M., Myers, W. L., Drohan, P. J., Miller, D. A., & Boyer, E. W. (2013). The use of LiDAR terrain data in characterizing surface roughness and microtopography. *Applied and Environmental Soil Science, 2013*, 13. doi:10.1155/2013/891534

Bruton, R., & Convery, F. (1982). *Land drainage policy in Ireland*. Retrieved from Dublin: https://www.esri.ie/pubs/PRS4.pdfhttps://www.esri.ie/pubs/PRS4.pdf

Burdon, D. J. (1986). Hydrogeological aspects of agricultural drainage in Ireland. *Environmental Geology, 9*(1), 41-65. doi:10.1007/BF02439885

Cahalane, C., Walsh, D., Magee, A., Mannion, S., Lewis, P., & McCarthy, T. (2017). Sensor Pods: multi-resolution surveys from a light aircraft. *Inventions, 2*(1). doi:10.3390/inventions2010002

Callow, J. N., Van Niel, K. P., & Boggs, G. S. (2007). How does modifying a DEM to reflect known hydrology affect subsequent terrain analysis? *Journal of Hydrology, 332*(1), 30-39. doi:10.1016/j.jhydrol.2006.06.020

Campbell, J. (1996). *Introduction to Remote Sensing* Guilford Press.

Campling, P., Gobin, A., & Feyen, J. (2002). Logistic Modeling to Spatially Predict the Probability of Soil Drainage Classes. *Soil Science Society of America Journal, 66*(4), 1390-1401. doi:10.2136/sssaj2002.1390

Carlson, T. N., Gillies, R. R., & Perry, E. M. (1994). A method to make use of thermal infrared temperature and NDVI measurements to infer surface soil water content and fractional vegetation cover. *Remote Sensing Reviews, 9*(1-2), 161-173. doi:10.1080/02757259409532220

Carpenter, S. R., Caraco, N. F., Correll, D. L., Howarth, R. W., Sharpley, A. N., & Smith, V. H. (1998). Nonpoint pollution of surface waters with phosphorus and nitrogen. *Ecological Applications, 8*(3), 559-568. doi:10.1890/1051-0761(1998)008[0559:NPOSWW]2.0.CO;2

Carravick, J. L., Smith, M. W., & Quincey, D. J. (2016). *Structure from Motion in the Geosciences*: Wiley-Blackwell.

Carter, G. (1991). Primary and secondary effects of water content on the spectral reflectance of leaves. *American Journal of Botany, 78*(7), 916-924. doi:10.2307/2445170

Carter, G. (1993). Responses of leaf spectral reflectance to plant stress. *American Journal of Botany, 80*(3), 239-243. doi:10.2307/2445346

Carter, G., & Knapp, A. (2001). Leaf optical properties in higher plants: linking spectral characteristics to stress and chlorophyll concentration. *American Journal of Botany, 88*(4), 677-684.

Cavazzi, S., Corstanje, R., Mayr, T., Hannam, J., & Fealy, R. (2013). Are fine resolution digital elevation models always the best choice in digital soil mapping? *Geoderma, 195-196*, 111-121. doi:10.1016/j.geoderma.2012.11.020

Cawkwell, F., Barrett, B., Nitze, I., Green, S., Black, K., & Hallahan, P. (2017). *The Irish Land Mapping Observatory: mapping and monitoring land cover, use and change* (2011-CCRP-MS1.4). Retrieved from

Cazorzi, F., Fontana, G. D., Luca, A. D., Sofia, G., & Tarolli, P. (2012). Drainage network detection and assessment of network storage capacity in agrarian landscape. *Hydrological Processes, 27*(4), 541-553. doi:10.1002/hyp.9224

Ceccato, P., Flasse, S., Tarantola, S., Jacquemoud, S., & Grégoire, J.-M. (2001). Detecting vegetation leaf water content using reflectance in the optical domain. *Remote Sensing of Environment, 77*(1), 22-33. doi:10.1016/S0034-4257(01)00191-2

Chaouch, N., Temimi, M., Hagen, S., Weishampel, J., Medeiros, S., & Khanbilvardi, R. (2011). A synergetic use of satellite imagery from SAR and optical sensors to improve coastal flood mapping in the Gulf of Mexico. *Hydrological Processes, 26*(11), 1617-1628. doi:10.1002/hyp.8268

Charlton, R., Fealy, R., Moore, S., Sweeney, J., & Murphy, C. (2006). Assessing the impact of climate change on water supply and flood hazard in Ireland using statistical downscaling and hydrological modelling techniques. *Climatic Change, 74*(4), 475-491. doi:10.1007/s10584-006-0472-x

Chen, Y., Huang, C., Ticehurst, C., Merrin, L., & Thew, P. (2013). An evaluation of MODIS daily and 8-day composite products for floodplain and wetland inundation mapping. *Wetlands, 33*(5), 823-835. doi:10.1007/s13157-013-0439-4

Cialella, A. T., Dubayah, R., Lawrence, W., & Levine, E. (1997). Predicting Soil Drainage Class Using Remotely Sensed and Digital Elevation Data. *Photogrammetric Engineering & Remote Sensing, 63*(2), 7.

Cicek, H., Sunohara, M., Wilkes, G., McNairn, H., Pick, F., Topp, E., & Lapen, D. R. (2010). Using vegetation indices from satellite remote sensing to assess corn and soybean response to controlled tile drainage. *Agricultural Water Management, 98*(2), 261-270. doi:10.1016/j.agwat.2010.08.019

Clagnan, E., Thornton, S. F., Rolfe, S. A., Tuohy, P., Peyton, D., Wells, N. S., & Fenton, O. (2018). Influence of artificial drainage system design on the nitrogen attenuation potential of gley soils: Evidence from hydrochemical and isotope studies under field-scale conditions. *Journal of Environmental Management, 206*, 1028-1038. doi:10.1016/j.jenvman.2017.11.069

Clark, M., & Tilman, D. (2017). Comparative analysis of environmental impacts of agricultural production systems, agricultural input efficiency, and food choice. *Environmental Research Letters, 12*(6), 064016.

Clement, M. A., Kilsby, C. G., & Moore, P. (2017). Multi-temporal synthetic aperture radar flood mapping using change detection. *Journal of Flood Risk Management, 11*(2), 152-168. doi:10.1111/jfr3.12303

Colomina, I., & Molina, P. (2014). Unmanned aerial systems for photogrammetry and remote sensing: A review. *ISPRS Journal of Photogrammetry and Remote Sensing, 92*(Supplement C), 79-97. doi:https://doi.org/10.1016/j.isprsjprs.2014.02.013

Congalton, R. G. (1991). A review of assessing the accuracy of classifications of remotely sensed data. *Remote Sensing of Environment, 37*(1), 35-46. doi:10.1016/0034-4257(91)90048-B

Cortes, C., & Vapnik , V. (1995). Support-Vector Networks. *Machine Learning, 20*(3), 24. doi:10.1023/A:1022627411411

Coveney, S., & Roberts, K. (2017). Lightweight UAV digital elevation models and orthoimagery for environmental applications: data accuracy evaluation and potential for

river flood risk modelling. *International Journal of Remote Sensing, 38*(8-10), 3159-3180. doi:10.1080/01431161.2017.1292074

Coyle, C., Creamer, R., Schulte, R., O'Sullivan, L., & Jordan, P. (2016). A Functional Land Management conceptual framework under soil drainage and land use scenarios. *Environmental Science & Policy, 56*, 39-48. doi:10.1016/j.envsci.2015.10.012

Creamer, R., Simo, I., O'Sullivan, L., Reidy, B., Schulte, R. P. O., & Fealy, R. M. (2016). *Soil Property Maps*. Retrieved from Ireland: https://www.epa.ie/pubs/reports/research/land/EPA%20RR%20204%20final%20web.pdf

Creamer, R., Simo, I., Reidy, B., Carvalho, J., Fealy, R., Hallett, S., Jones, R., Holden, A., Holden, N., Hannam, J., Massey, P., Mayr, T., McDonald, E., O'Rourke, S., Sills, P., Truckell, I., Zawadzka, J., & Schulte, R. (2014). *Irish Soil Information System Synthesis Report*. Retrieved from Johnstown Castle, Ireland

Creighton, P., Kennedy, E., Shalloo, L., Boland, T. M., & O' Donovan, M. (2011). A survey analysis of grassland dairy farming in Ireland, investigating grassland management, technology adoption and sward renewal. *Grass and Forage Science, 66*(2), 251-264. doi:10.1111/j.1365-2494.2011.00784.x

CSO. (2016). Farm Structure Survey 2016. Retrieved from https://www.cso.ie/en/releasesandpublications/ep/p-fss/farmstructuresurvey2016/da/

D' Addabbo, A., Refice, A., Pasquariello, G., Lovergine, F. P., Capolongo, D., & Manfreda, S. (2016). A Bayesian network for flood detection combining SAR imagery and ancillary data. *IEEE Transactions on Geoscience and Remote Sensing, 54*(6), 3612-3625. doi:10.1109/TGRS.2016.2520487

DAFF. (2011). *Food Harvest 2020. A vision for Irish agri-food and fisheries*. Dublin Retrieved from https://www.agriculture.gov.ie/media/migration/foodindustrydevelopmenttrademarkets/agri-foodandtheeconomy/foodharvest2020/2020FoodHarvestEng240810.pdf

DAFM. (2013a). *The second national forest inventory Republic of Ireland: main findings* (978-1-4064-2806-3). Retrieved from Johnstown Castle: https://www.agriculture.gov.ie/media/migration/forestry/nationalforestinventory/2012/Forest%20Inventory%20Main%20Findings.pdf

DAFM. (2013b). Stautuatory obligations when draining land. In M. Moore (Ed.), *Teagasc manual on drainage and soil management* (pp. 4). Dublin: Teagasc.

DAFM. (2015). *Food Wise 2025. A 10-year vision for the Irish agri-food industry*. Dublin Retrieved from https://www.agriculture.gov.ie/media/migration/foodindustrydevelopmenttrademarkets/agri-foodandtheeconomy/foodwise2025/report/FoodWise2025.pdf

DAFM. (2018). *Annual Report 2017*. Retrieved from https://www.agriculture.gov.ie/media/migration/publications/2018/DAFM2017AnnualReport010818.pdf

Daly, K., Mills, P., Coulter, B., & McGarrigle, M. (2002). *Modeling phosphorus concentrations in Irish rivers using land use, soil type and soil phosphorus data* (Vol. 31).

Davie, T. (2008). *Fundamentals of Hydrology*. New York: Routledge.

de Moel, H., van Alphen, J., & Aerts, J. C. J. H. (2009). Flood maps in Europe – methods, availability and use. *Natural Hazards and Earth System Sciences, 9*, 289-301.

Delegido, J., Verrelst, J., Alonso, L., & Moreno, J. (2011). Evaluation of Sentinel-2 red-edge bands for empirical estimation of green LAI and chlorophyll content. *Sensors, 11*(7), 7063-7081. doi:10.3390/s110707063

DHPLG. (2018). River Basin Management Plan for Ireland 2018 - 2021. In (pp. 184): Department of Housing, Planning and Local Government.

Di Baldassarre, G., Schumann, G., Brandimarte, L., & Bates, P. (2011). Timely low resolution SAR imagery to support floodplain modelling: a case study review. *Surveys in Geophysics, 32*(3), 255-269. doi:10.1007/s10712-011-9111-9

Diamond, J., & Shanley, T. (2003). Infiltration rate assessment of some major soils. *Irish Geography, 36*(1), 32-46. doi:10.1080/00750770309555810

Dillon, E., Moran, B., & Donnellan, T. (2017). Teagasc National Farm Survey 2016 Results. In (pp. 99): Teagasc.

DJI. (2018). Zenmuse XT. Retrieved from https://www.dji.com/zenmuse-xt/info#specs

Dobson, M. C., Pierce, L., Sarabandi, K., Ulaby, F. T., & Sharik, T. (1992). Preliminary analysis of ERS-1 SAR for forest ecosystem studies. *IEEE Transactions on Geoscience and Remote Sensing, 30*(2), 203-211. doi:10.1109/36.134071

Domeneghetti, A., Vorogushyn, S., Castellarin, A., Merz, B., & Brath, A. (2013). Probabilistic flood hazard mapping: effects of uncertain boundary conditions. *Hydrology and Earth System Sciences, 17*, 3127-3140. doi:10.5194/hess-17-3127-2013

Doody, D. G., Archbold, M., Foy, R. H., & Flynn, R. (2012). Approaches to the implementation of the Water Framework Directive: Targeting mitigation measures at critical source areas of diffuse phosphorus in Irish catchments. *Journal of Environmental Management, 93*(1), 225-234. doi:10.1016/j.jenvman.2011.09.002

Doody, D. G., Higgins, A., Matthews, D., Foy, R. H., Pilatova, K., Duffy, O., & Watson, C. J. (2010). Overland flow initiation from a drumlin grassland hillslope. *Soil Use and Management, 26*(3), 286-298. doi:10.1111/j.1475-2743.2010.00279.x

Drew, M. C. (1983). Plant injury and adaptation to oxygen deficiency in the root environment: a review. *Plant and Soil, 75*(2), 179-199. doi:10.1007/BF02375564

Du, Y., Zhang, Y., Ling, F., Wang, Q., Li, W., & Li, X. (2016). Water bodies' mapping from Sentinel-2 imagery with modified normalized difference water index at 10-m spatial resolution produced by sharpening the SWIR band. *Remote Sensing, 8*(4). doi:10.3390/rs8040354

Duffy, P. (2007). *Exploring the history and heritage of Irish landscapes*: Four Courts Press.

Dunne, T., & Black, R. (1970). Partial area contributions to storm runoff in a small New England watershed. *Water Resources Research, 6*(5), 1296-1311. doi:10.1029/WR006i005p01296

Džubáková, K., Molnar, P., Schindler, K., & Trizna, M. (2015). Monitoring of riparian vegetation response to flood disturbances using terrestrial photography *Hydrology and Earth System Sciences, 19*(1), 195-208.

Earl, R. (1997). Prediction of trafficability and workability from soil moisture deficit. *Soil and Tillage Research, 40*(3), 155-168. doi:10.1016/S0167-1987(96)01072-0

EC. (2018). Modernising the CAP: satellite data authorised to replace on-farm checks. Retrieved from https://ec.europa.eu/info/news/modernising-cap-satellite-data-authorised-replace-farm-checks-2018-may-25_en

Emengini, E. J., Blackburn, G. A., & Theobald, J. C. (2013). Discrimination of plant stress caused by oil pollution and waterlogging using hyperspectral and thermal remote sensing *Journal of Applied Remote Sensing, 7*(1). doi:10.1117/1.JRS.7.073476

Engman, E. (1986). Roughness coefficients for routing surface runoff. *Journal of Irrigation and Drainage Engineering, 112*(1), 39-53. doi:10.1061/(ASCE)0733-9437(1986)112:1(39)

EPA. (2012). Corine Land Cover 2012. from Environmental Protection Agency http://www.epa.ie/soilandbiodiversity/soils/land/corine/tech/

EPA. (2018). *Water Quality in 2017: An Indicators Report*. Retrieved from Johnstown Castle http://www.epa.ie/pubs/reports/water/waterqua/Water%20Quality%20in%202017%20-%20an%20indicators%20report.pdf

Farouki, O. T. (1981). *Thermal properties of soils*. Retrieved from Hanover, New Hampshire: https://apps.dtic.mil/dtic/tr/fulltext/u2/a111734.pdf

Farrelly, P., Crosse, S., O'Donoghue, P., Whyte, S., Farrelly, P. B., Burns, T., Byrne, D., Holmes, O., Maklin, R., J., M., & Salley, F. (2014). *Environmental analysis of scenarios related to the implementation of recommendations in Food Harvest 2020*. Retrieved from

Fealy, R., Green, S., Loftus, M., Meehan, R., Radford, T., Cronin, C., & Bulfin, M. (2009). *Teagasc EPA Soil and Subsoils Mapping Project*. Retrieved from http://hdl.handle.net/11019/361

Feick, S., Siebert, S., & Döll, P. (2005). *A digital global map of artificially drained agricultural areas*. Retrieved from Frankfurt am Main, Germany: https://d-nb.info/1054768153/34

Fischer, G., Nachtergaele, F., Prieler, S., van Velthuizen, H., Verelst, L., & Wiberg, D. (2008). *Global agro-ecological zones assessment for agriculture*. Retrieved from Rome:

Fitzgerald, J. B., Brereton, A. J., & Holden, N. M. (2008). Simulation of the influence of poor soil drainage on grass-based dairy production systems in Ireland. *Grass and Forage Science, 63*(3), 380-389. doi:10.1111/j.1365-2494.2008.00637.x

Flood, N. (2017). Comparing Sentinel-2A and Landsat 7 and 8 using surface reflectance over Australia. *Remote Sensing, 9*(7). doi:10.3390/rs9070659

Florinsky, I., V., Kurkov, V., M., & Bliakharskii, D., P. (2017). Geomorphometry from unmanned aerial surveys. *Transactions in GIS, 22*(1), 58-81. doi:10.1111/tgis.12296

Fonstad, M. A., Dietrich, J. T., Courville, B. C., Jensen, J. L., & Carbonneau, P. E. (2013). Topographic structure from motion: a new development in photogrammetric measurement. *Earth Surface Processes and Landforms, 38*(4), 421-430. doi:10.1002/esp.3366

Foody, G. M. (2002). Status of land cover classification accuracy assessment. *Remote Sensing of Environment, 80*(1), 185-201. doi:10.1016/S0034-4257(01)00295-4

Freibauer, A., Rounsevell, M., Smith, P., & Verhagen, J. (2004). Carbon sequestration in the agricultural soils of Europe. *Geoderma, 122*(1), 1-23. doi:10.1016/j.geoderma.2004.01.021

Fu, Y. H., Piao, S., Zhao, H., Jeong, S.-J., Wang, X., Vitasse, Y., Ciais, P., & Janssens, I. A. (2014). Unexpected role of winter precipitation in determining heat requirement for spring

vegetation green-up at northern middle and high latitudes. *Global Change Biology, 20*(12), 3743-3755. doi:10.1111/gcb.12610

Furukawa, Y., & Ponce, J. (2010). Accurate, dense and robust multiview stereopsis. *IEEE Transactions on Pattern Analysis and Machine Intelligence, 32*(8), 1362-1376. doi:10.1109/TPAMI.2009.161

Gago, J., Douthe, C., Coopman, R. E., Gallego, P. P., Ribas-Carbo, M., Flexas, J., Escalona, J., & Medrano, H. (2015). UAVs challenge to assess water stress for sustainable agriculture. *Agricultural Water Management, 153*(Supplement C), 9-19. doi:https://doi.org/10.1016/j.agwat.2015.01.020

Galvin, L. F. (1983). The drainage of impermeable soils in high rainfall areas. *Irish Journal of Agricultural Research, 22*(2/3), 161-187.

Galy, H., & Sanders, R. A. (2002). Using synthetic aperture RADAR imagery for flood modelling. *Transactions in GIS, 6*(1), 31-42. doi:10.1111/1467-9671.00093

Gao, B. (1996). NDWI—A normalized difference water index for remote sensing of vegetation liquid water from space. *Remote Sensing of Environment, 58*(3), 257-266. doi:10.1016/S0034-4257(96)00067-3

Gebbers, R., & Adamchuk, V. I. (2010). Precision Agriculture and Food Security. *Science, 327*(5967), 828.

Gibson, P. (2000). *Introductory remote sensing: principles and concepts*. London: Routledge.

Gibson, P., & George, D. M. (2004). *Environmental Applications of Geophysical Surveying Techniques*: Nova Science Publishers.

Gillies, R. R., & Carlson, T. N. (1995). Thermal remote sensing of surface soil water content with partial vegetation cover for incorporation into climate models. *Journal of Applied Meteorology, 34*(4), 745-756. doi:10.1175/1520-0450(1995)034<0745:TRSOSS>2.0.CO;2

Gislason, P. O., Benediktsson, J. A., & Sveinsson, J. R. (2006). Random Forests for land cover classification. *Pattern Recognition Letters, 27*(4), 294-300. doi:10.1016/j.patrec.2005.08.011

Goettelman, R., Grass, L., Millard, J., & Nixon, P. (1983). *Comparison of multispectral remote-sensing techniques for monitoring subsurface drain conditions*. Retrieved from Ames Research Center: https://ntrs.nasa.gov/archive/nasa/casi.ntrs.nasa.gov/19830016732.pdf

Gökkaya, K., Budhathoki, M., Christopher, S. F., Hanrahan, B. R., & Tank, J. L. (2017). Subsurface tile drained area detection using GIS and remote sensing in an agricultural watershed. *Ecological Engineering*. doi:https://doi.org/10.1016/j.ecoleng.2017.06.048

Gómez-Candón, D., De Castro, A. I., & López-Granados, F. (2014). Assessing the accuracy of mosaics from unmanned aerial vehicle (UAV) imagery for precision agriculture purposes in wheat. *Precision Agriculture, 15*(1), 44-56. doi:10.1007/s11119-013-9335-4

Gonzalez-de-Santos, P., Ribeiro, A., Fernandez-Quintanilla, C., Lopez-Granados, F., Brandstoetter, M., Tomic, S., Pedrazzi, S., Peruzzi, A., Pajares, G., Kaplanis, G., Perez-Ruiz, M., Valero, C., del Cerro, J., Vieri, M., Rabatel, G., & Debilde, B. (2017). Fleets of robots for environmentally-safe pest control in agriculture. *Precision Agriculture, 18*(4), 574-614. doi:10.1007/s11119-016-9476-3

Goodchild, M. F. (2001). Metrics of scale in remote sensing and GIS. *International Journal of Applied Earth Observation and Geoinformation, 3*(2), 114-120. doi:10.1016/S0303-2434(01)85002-9

Grabs, T., Seibert, J., Bishop, K., & Laudon, H. (2009). Modeling spatial patterns of saturated areas: A comparison of the topographic wetness index and a dynamic distributed model. *Journal of Hydrology, 373*(1), 15-23. doi:https://doi.org/10.1016/j.jhydrol.2009.03.031

Gramlich, A., Stoll, S., Stamm, C., Walter, T., & Prasuhn, V. (2018). Effects of artificial land drainage on hydrology, nutrient and pesticide fluxes from agricultural fields – A review. *Agriculture, Ecosystems & Environment, 266*, 84-99. doi:10.1016/j.agee.2018.04.005

Grenzdörffer, G., Engel, A., & Teichert, B. (2008). The photogrammetric potential of low-cost UAVs in forestry and agriculture. *The International Archives of the Photogrammetry, Remote Sensing and Spatial Information Sciences, XXXVII*, 8. doi:10.1.1.151.649

Griffiths, P., Nendel, C., & Hostert, P. (2019). Intra-annual reflectance composites from Sentinel-2 and Landsat for national-scale crop and land cover mapping. *Remote Sensing of Environment, 220*, 135-151. doi:10.1016/j.rse.2018.10.031

Gstaiger, V., Huth, J., Gebhardt, S., Wehrmann, T., & Kuenzer, C. (2012). Multi-sensoral and automated derivation of inundated areas using TerraSAR-X and ENVISAT ASAR data. *International Journal of Remote Sensing, 33*(22), 7291-7304. doi:10.1080/01431161.2012.700421

Guanter, L., Kaufmann, H., Segl, K., Foerster, S., Rogass, C., Chabrillat, S., Kuester, T., Hollstein, A., Rossner, G., Chlebek, C., Straif, C., Fischer, S., Schrader, S., Storch, T.,

Heiden, U., Mueller, A., Bachmann, M., Mühle, H., Müller, R., Habermeyer, M., Ohndorf, A., Hill, J., Buddenbaum, H., Hostert, P., van der Linden, S., Leitão, J. P., Rabe, A., Doerffer, R., Krasemann, H., Xi, H., Mauser, W., Hank, T., Locherer, M., Rast, M., Staenz, K., & Sang, B. (2015). The EnMAP spaceborne imaging spectroscopy mission for Earth observation. *Remote Sensing, 7*(7). doi:10.3390/rs70708830

Gyasi-Agyei, Y., Willgoose, G., & De Troch Francois, P. (2006). Effects of vertical resolution and map scale of digital elevation models on geomorphological parameters used in hydrology. *Hydrological Processes, 9*(3-4), 363-382. doi:10.1002/hyp.3360090310

Hanrahan, L., McHugh, N., Hennessy, T., Moran, B., Kearney, R., Wallace, M., & Shalloo, L. (2018). Factors associated with profitability in pasture-based systems of milk production. *Journal of Dairy Science, 101*(6), 5474-5485. doi:10.3168/jds.2017-13223

Harrigan, S., Murphy, C., Hall, J., Wilby, R. L., & Sweeney, J. (2014). Attribution of detected changes in streamflow using multiple working hypotheses. *Hydrology and Earth System Sciences, 18*, 1935-1952. doi:10.5194/hess-18-1935-2014

Harwin, S., & Lucieer, A. (2012). Assessing the Accuracy of Georeferenced Point Clouds Produced via Multi-View Stereopsis from Unmanned Aerial Vehicle (UAV) Imagery. *Remote Sensing, 4*(6), 26. doi:10.3390/rs4061573.

Hashemi, S.,Valadan Zoej, M. J., Mokhtarzadeh, M., 2011. Automatic road gap detection using fuzzy inference system. ISPRS Hannover Workshop 2011, Commission IV, WG IV/2.

Haygarth, P. M., Apsimon, H., Betson, M., Harris, D., Hodgkinson, R., & Withers, P. J. (2009). Mitigating diffuse phosphorus transfer from agriculture according to cost and efficiency. *J Environ Qual, 38*(5), 2012-2022. doi:10.2134/jeq2008.0102

Heathwaite, A. L., Quinn, P. F., & Hewett, C. J. M. (2005). Modelling and managing critical source areas of diffuse pollution from agricultural land using flow connectivity simulation. *Journal of Hydrology, 304*(1), 446-461. doi:https://doi.org/10.1016/j.jhydrol.2004.07.043

Heuvelink, G. B. M., Burrough, P. A., & Stein, A. (1989). Propagation of errors in spatial modelling with GIS. *International Journal of Geographical Information Systems, 3*(4), 303-322. doi:10.1080/02693798908941518

Hillel, D. (1998). *Environmental Soil Physics*. San Diego: Academic Press.

Hodgson, M. E. (1998). Comparison of angles from surface slope/aspect algorithms. *Cartography and Geographic Information Systems, 25*(3), 173-185. doi:10.1559/152304098782383106

Hofierka, J., & Knutová, M. (2015). Simulating spatial aspects of a flash flood using the Monte Carlo method and GRASS GIS: a case study of the Malá Svinka Basin (Slovakia). *Open Geosciences, 7*(1). doi:10.1515/geo-2015-0013

Holden, N. M., & Brereton, A. J. (2002). An assessment of the potential impact of climate change on grass yield in Ireland over the next 100 years. *Irish Journal of Agricultural and Food Research, 41*(2), 213-226.

Holzman, M. E., Rivas, R., & Piccolo, M. C. (2014). Estimating soil moisture and the relationship with crop yield using surface temperature and vegetation index. *International Journal of Applied Earth Observation and Geoinformation, 28*(Supplement C), 181-192. doi:https://doi.org/10.1016/j.jag.2013.12.006

Horritt, M. S. (1999). A statistical active contour model for SAR image segmentation. *Image and Vision Computing, 17*(3), 213-224. doi:10.1016/S0262-8856(98)00101-2

Huang, C., Davis, L. S., & Townshend, J. R. G. (2002). An assessment of support vector machines for land cover classification. *International Journal of Remote Sensing, 23*(4), 725-749. doi:10.1080/01431160110040323

Hughes, K. J., Magette, W. L., & Kurz, I. (2005). Identifying critical source areas for phosphorus loss in Ireland using field and catchment scale ranking schemes. *Journal of Hydrology, 304*(1), 430-445. doi:10.1016/j.jhydrol.2004.07.042

Humphreys, J., Touhy, P., Phelan, P., & Fenton, O. (2012). *Strong association between soil wetness and profitability at Solohead Research Farm*. Moorepark Dairy Levy Research Update Teagasc. Moorepark. Retrieved from https://www.teagasc.ie/media/website/animals/dairy/Solohead_Open_Day_2012.pdf

Ibrahim, T. G., Fenton, O., Richards, K. G., Fealy, R. M., & Healy, M. G. (2013). Spatial and temporal variations of nutrient loads in overland flow and subsurface drainage from a marginal land site in southeast Ireland *Biology and Environment: Proceedings of the Royal Irish Academy, 113B*(2), 169-186.

Idso, S. B., Schmugge, T. J., Jackson, R. D., & Reginato, R. J. (1975). The utility of surface temperature measurements for the remote sensing of surface soil water status. *Journal of Geophysical Research, 80*(21), 3044-3049. doi:10.1029/JC080i021p03044

Insom, P., Cao, C., Boonsrimuang, P., Liu, D., Saokarn, A., Yomwan, P., & Xu, Y. (2015). A Support Vector Machine-based particle filter method for improved flooding classification. *IEEE Geoscience and Remote Sensing Letters, 12*(9), 1943-1947. doi:10.1109/LGRS.2015.2439575

Jackson, R. D., & Huete, A. R. (1991). Interpreting vegetation indices. *Preventive Veterinary Medicine, 11*(3), 185-200. doi:10.1016/S0167-5877(05)80004-2

James, M. R., & Robson, S. (2014). Mitigating systematic error in topographic models derived from UAV and ground-based image networks. *Earth Surface Processes and Landforms, 39*(10), 1413-1420. doi:10.1002/esp.3609

Jeziorska, J., Mitasova, H., Petrasova, A., Petras, V., Divakaran, D., & Zajkowskic, T. (2016, July 2016). *Overland flow analysis using time series of SUAS-derived elevation models.* Paper presented at the ISPRS Annals of the Photogrammetry, Remote Sensing and Spatial Information Sciences, Prague.

Ji, L., Zhang, L., Wylie, B. K., & Rover, J. (2011). On the terminology of the spectral vegetation index (NIR − SWIR)/(NIR + SWIR). *International Journal of Remote Sensing, 32*(21), 6901-6909. doi:10.1080/01431161.2010.510811

Johnston, P. (nd). *Turlough Database*. Retrieved from: http://erc.epa.ie/safer/resource?id=61afb7df-3fa8-102a-b1da-b128b41032cc

Jones, H. G., Serraj, R., Loveys, B. R., Xiong, L., Wheaton, A., & Price, A. H. (2009). Thermal infrared imaging of crop canopies for the remote diagnosis and quantification of plant responses to water stress in the field. *Functional Plant Biology, 36*(11), 978-989.

Jones, H. G., & Vaughan, R. (2010). *Remote Sensing of Vegetation: principles, techniques and applications*. Oxford: Oxford University Press.

Jones, R. J., Hannam, J. A., Palmer, R. C., Truckell, I. G., Creamer, R. E., & McDonald, E. (2014). *Irish SIS Final Technical Report 2: Interim classification and rationalisation of soil series in Ireland*. Retrieved from Johnstown Castle: http://erc.epa.ie/safer/resource?id=7ed91e36-3abc-11e4-b233-005056ae0019

Joyce, K. E., Belliss, S. E., Samsonov, S. V., McNeill, S. J., & Glassey, P. J. (2009). A review of the status of satellite remote sensing and image processing techniques for mapping natural hazards and disasters. *Progress in Physical Geography: Earth and Environment, 33*(2), 183-207. doi:10.1177/0309133309339563

Kaleita, L. A., Tian, F. L., & Hirschi, C. M. (2005). Relationship between soil moisture content and soil surface reflectance *Transactions of the ASAE, 48*(5), 1979. doi:10.13031/2013.19990

Keane, T., & Sheridan, T. (2001). Climate of Ireland In T. Keane & J. Collins (Eds.), *Climate, Weather and Irish Agriculture* (pp. 36). Dublin: Joint Working Group on Applied Agricultural Meteorology (AGMET).

Kerebel, A., Cassidy, R., Jordan, P., & Holden, N. M. (2013a). Farmer perception of suitable conditions for slurry application compared with decision support system recommendations. *Agricultural Systems, 120*(Supplement C), 49-60. doi:10.1016/j.agsy.2013.05.007

Kerebel, A., Cassidy, R., Jordan, P., & Holden, N. M. (2013b). Soil Moisture Deficit as a predictor of the trend in soil water status of grass fields. *Soil Use and Management, 29*(3), 419-431. doi:10.1111/sum.12054

Kerebel, A., & Holden, N. M. (2016). The relationship between farmer opinion of suitable conditions for nutrient application, soil moisture deficit and weather. *Soil Use and Management, 32*(4), 613-622. doi:10.1111/sum.12298

Kerr, Y. H., Wigneron, J. P., Al Bitar, A., Mialon, A., & Srivastava, P. K. (2016). Chapter 1 - Soil Moisture from Space: Techniques and Limitations. In *Satellite Soil Moisture Retrieval* (pp. 3-27): Elsevier.

Khand, K., Kjaersgaard, J., Hay, C., & Jia, X. (2017). Estimating impacts of agricultural subsurface drainage on evapotranspiration using the Landsat imagery-based METRIC model. *Hydrology, 4*(4). doi:10.3390/hydrology4040049

Kidd, D. B., Malone, B. P., McBratney, A. B., Minasny, B., & Webb, M. A. (2014). Digital mapping of a soil drainage index for irrigated enterprise suitability in Tasmania, Australia. *Soil Research, 52*(2), 107-119.

Kiely, G., Leahy, P., Lewis, C., Xu, X., & Sottocornola, M. (2017). *SoilC - Feasibility of grassland soil carbon survey*. Retrieved from http://www.epa.ie/pubs/reports/research/land/EPA%20RR225_web.pdf

Kiely, G., Leahy, P., Ludlow, F., Stefanini, B., Reilly, E., Monk, M., Harris, J., & 2017]., A. A. (2009). *Extreme weather, climate and natural disasters in Ireland*. Retrieved from https://www.epa.ie/pubs/reports/research/climate/CCRP_5_Kiely_ExtremeWeather_syn_web.pdf.pdf

Kiliç, S. (2009). Mapping soil drainage classes of Amik Plain using Landsat images. *African Journal of Agricultural Research, 4*(9), 4.

Kladivko, E. J., Frankenberger, J. R., Jaynes, D. B., Meek, D. W., Jenkinson, B. J., & Fausey, N. R. (2004). Nitrate leaching to subsurface drains as affected by drain spacing and changes in crop production system. *J Environ Qual, 33*(5), 1803-1813.

Knorn, J., Rabe, A., Radeloff, V. C., Kuemmerle, T., Kozak, J., & Hostert, P. (2009). Land cover mapping of large areas using chain classification of neighboring Landsat satellite images. *Remote Sensing of Environment, 113*(5), 957-964. doi:10.1016/j.rse.2009.01.010

Kobryn, H. T., Lantzke, R., Bell, R., & Admiraal, R. (2015). Remote sensing for assessing the zone of benefit where deep drains improve productivity of land affected by shallow saline groundwater. *Journal of Environmental Management, 150*, 138-148. doi:10.1016/j.jenvman.2014.11.017

Kravchenko, A. N., Bollero, G. A., Omonode, R. A., & Bullock, D. G. (2002). Quantitative mapping of soil drainage classes using topographical data and soil electrical conductivity. *Soil Science Society of America Journal, 66*, 235-243. doi:10.2136/sssaj2002.2350

Kross, A., Lapen, D. R., McNairn, H., Sunohara, M., Champagne, C., & Wilkes, G. (2015). Satellite and in situ derived corn and soybean biomass and leaf area index: Response to controlled tile drainage under varying weather conditions. *Agricultural Water Management, 160*(Supplement C), 118-131. doi:https://doi.org/10.1016/j.agwat.2015.06.007

Küng, O., Strecha, C., Beyeler, A., Zufferey, J.-C., Floreano, D., Fua, P., & Gervaix, F. (2011). *The Accuracy of Automatic Photogrammetric Techniques on Ultra-light UAV Imagery.* Paper presented at the UAV-g 2011 Unmanned Aerial Vehicle in Geomatics, Zurich, Switzerland.

Kussul, N., Shelestov, A., & Skakun, S. (2008). Grid system for flood extent extraction from satellite images. *Earth Science Informatics, 1*(3), 105. doi:10.1007/s12145-008-0014-3

Laidlaw, A. S. (2009). The effect of ssoil moisture content on leaf extension rate and yield of perennial ryegrass. *Irish Journal of Agricultural and Food Research, 48*(1), 1-20.

Lal, R. (2004). Soil carbon sequestration to mitigate climate change. *Geoderma, 123*(1), 1-22. doi:10.1016/j.geoderma.2004.01.032

Lary, D. J., Alavi, A. H., Gandomi, A. H., & Walker, A. L. (2016). Machine learning in geosciences and remote sensing. *Geoscience Frontiers, 7*(1), 3-10. doi:10.1016/j.gsf.2015.07.003

Leblanc, M., Lemoalle, J., Bader, J. C., Tweed, S., & Mofor, L. (2011). Thermal remote sensing of water under flooded vegetation: New observations of inundation patterns for the 'Small' Lake Chad. *Journal of Hydrology, 404*(1), 87-98. doi:10.1016/j.jhydrol.2011.04.023

Lee, J. (1983). A simple speckle smoothing algorithm for synthetic aperture radar images. *IEEE Transactions on Systems, Man, and Cybernetics, SMC-13*(1), 85-89. doi:10.1109/TSMC.1983.6313036

Leon, J. X., Heuvelink, G. B. M., & Phinn, S. R. (2014). Incorporating DEM uncertainty in coastal inundation mapping. *PLoS ONE, 9*(9), e108727. doi:10.1371/journal.pone.0108727

Levine, E. R., Knox, R. G., & Lawrence, W. T. (1994). Relationships between soil properties and vegetation at the Northern Experimental Forest, Howland, Maine. *Remote Sensing of Environment, 47*(2), 231-241. doi:https://doi.org/10.1016/0034-4257(94)90158-9

Li, J., & Roy, P. (2017). A global analysis of Sentinel-2A, Sentinel-2B and Landsat-8 data revisit intervals and implications for terrestrial monitoring. *Remote Sensing, 9*(9). doi:10.3390/rs9090902

Lillesand, T., Kiefer, R. W., & Chipman, J. (2015). *Remote Sensing and Image Interpretation* (7th ed.).

Linders, W. (2016). *Digital Photogrammetry. Theory and Applications*. New York: Springer.

Liu, J., Pattey, E., Nolin, M. C., Miller, J. R., & Ka, O. (2008). Mapping within-field soil drainage using remote sensing, DEM and apparent soil electrical conductivity. *Geoderma, 143*(3), 261-272. doi:https://doi.org/10.1016/j.geoderma.2007.11.011

Lobell, D. B., & Asner, G. P. (2002). Moisture effects on soil reflectance. *Soil Science Society of America Journal, 66*, 722-727. doi:10.2136/sssaj2002.7220

Long, S., Fatoyinbo, T. E., & Policelli, F. (2014). Flood extent mapping for Namibia using change detection and thresholding with SAR. *Environmental Research Letters, 9*(3), 035002.

Lowe, D. G. (1999, 1999). *Object recognition from local scale-invariant features.* Paper presented at the Proceedings of the Seventh IEEE International Conference on Computer Vision.

Lozano-Garcia, D. F., Fernandez, R. N., & Johannsen, C. J. (1991). Assessment of regional biomass-soil relationships using vegetation indexes. *IEEE Transactions on Geoscience and Remote Sensing, 29*(2), 331-339. doi:10.1109/36.73676

Maire, J., Gibson-Poole, S., Cowan, N., Reay, D. S., Richards, K. G., Skiba, U., Rees, R. M., & Lanigan, G. J. (2018). Identifying urine patches on intensively managed grassland using aerial imagery captured from remotely piloted aircraft systems. *Frontiers in Sustainable Food Systems, 2*, 10.

Mallick, K., Bhattacharya, B. K., & Patel, N. K. (2009). Estimating volumetric surface moisture content for cropped soils using a soil wetness index based on surface temperature and NDVI. *Agricultural and Forest Meteorology, 149*(8), 1327-1342. doi:10.1016/j.agrformet.2009.03.004

Mandanici, E., & Bitelli, G. (2016). Preliminary comparison of Sentinel-2 and Landsat 8 imagery for a combined Use. *Remote Sensing, 8*(12). doi:10.3390/rs8121014

Manfreda, S., Dvorak, P., Mullerova, J., Herban, S., Vuono, P., Arranz Justel, J. J., & Perks, M. (2018). Accuracy assessment on unmanned aerial system derived digital surface models. *Preprints, 2018090579*. doi:10.20944/preprints201809.0579.v1

Manfreda, S., McCabe, M., Miller, P., Lucas, R., Pajuelo Madrigal, V., Mallinis, G., Ben Dor, E., Helman, D., Estes, L., Ciraolo, G., Müllerová, J., Tauro, F., de Lima, M., de Lima, J., Maltese, A., Frances, F., Caylor, K., Kohv, M., Perks, M., Ruiz-Pérez, G., Su, Z., Vico, G., & Toth, B. (2018). On the use of unmanned aerial systems for environmental monitoring. *Remote Sensing, 10*(4). doi:10.3390/rs10040641

Manjusree, P., Prasanna Kumar, L., Bhatt, C. M., Rao, G. S., & Bhanumurthy, V. (2012). Optimization of threshold ranges for rapid flood inundation mapping by evaluating backscatter profiles of high incidence angle SAR images. *International Journal of Disaster Risk Science, 3*(2), 113-122. doi:10.1007/s13753-012-0011-5

Martinis, S., Twele, A., & Voigt, S. (2009). Towards operational near real-time flood detection using a split-based automatic thresholding procedure on high resolution TerraSAR-X data. *Natural Hazards and Earth System Sciences, 9*, 303-314. doi:10.5194/nhess-9-303-2009

Martinis, S., Twele, A., & Voigt, S. (2011). Unsupervised extraction of flood-induced backscatter changes in SAR data using Markov image modeling on irregular graphs. *IEEE Transactions on Geoscience and Remote Sensing, 49*(1), 251-263. doi:10.1109/TGRS.2010.2052816

Masek, J. G., Vermote, E. F., Saleous, N., Wolfe, R., Hall, F. G., Huemmrich, H., Gao, F., Kutler, J., & Lim, T. K. (2013). LEDAPS Landsat calibration, reflectance, atmospheric

correction preprocessing code (Version 2): Oak Ridge National Laboratory Distributed Active Archive Center Retrieved from https://daac.ornl.gov/MODELS/guides/LEDAPS.html

Mason, D. C., Schumann, G. J. P., Neal, J. C., Garcia-Pintado, J., & Bates, P. D. (2012). Automatic near real-time selection of flood water levels from high resolution Synthetic Aperture Radar images for assimilation into hydraulic models: A case study. *Remote Sensing of Environment, 124*, 705-716. doi:10.1016/j.rse.2012.06.017

Matgen, P., Hostache, R., Schumann, G., Pfister, L., Hoffmann, L., & Savenije, H. H. G. (2011). Towards an automated SAR-based flood monitoring system: Lessons learned from two case studies. *Physics and Chemistry of the Earth, Parts A/B/C, 36*(7), 241-252. doi:10.1016/j.pce.2010.12.009

Matkan, A., Hajeb, M., Eslami, M., Pourali, S & Sadeghian, S. (2012). Gap filling in road extraction using radon transformation. ISPRS Annals of Photogrammetry, Remote Sensing and Spatial Information Sciences. I-4. 47-52. 10.5194/isprsannals-I-4-47-2012.

Matsushima, D., Kimura, R., & Shinoda, M. (2012). Soil moisture estimation using thermal inertia: potential and sensitivity to data conditions. *Journal of Hydrometeorology, 13*(2), 638-648. doi:10.1175/jhm-d-10-05024.1

McBratney, A. B., Mendonça Santos, M. L., & Minasny, B. (2003). On digital soil mapping. *Geoderma, 117*(1), 3-52. doi:https://doi.org/10.1016/S0016-7061(03)00223-4

McEniry, J., Korres, N. E., & O'Keily, P. (2013). Grass and Grass Silage. In N. Korres, P. O'Kiely, J. Benzie, & J. West (Eds.), *Bioenergy Production by Anaerobic Digestion* (pp. 472). New York: Routledge.

McFarlane, N. M., Ciavarella, T. A., & Smith, K. F. (2004). The effects of waterlogging on growth, photosynthesis and biomass allocation in perennial ryegrass (Lolium perenne L.) genotypes with contrasting root development. *The Journal of Agricultural Science, 141*(2), 241-248. doi:10.1017/S0021859603003502

MetÉireann. (2016). *Spring 2016*. Retrieved from https://www.met.ie/climate/MonthlyWeather/clim-2016-spr.pdf

Minacapilli, M., Cammalleri, C., Ciraolo, G., D'Asaro, F., Iovino, M., & Maltese, A. (2012). Thermal inertia modeling for soil surface water content estimation: a laboratory experiment. *Soil Science Society of America Journal, 76*, 92-100. doi:10.2136/sssaj2011.0122

Mitas, L., & Mitasova, H. (1998, July 1998). *Multi-scale Green's function Monte Carlo approach to erosion modelling and its application to land use optimisation* Paper presented at the Modelling Soil Erosion, Sediment Transport and Closely Related Hydrological Properties Vienna.

Mitasova, H., Thaxton, C., Hofierka, J., McLaughlin, R., Moore, A., & Mitas, L. (2004). Path sampling method for modeling overland water flow, sediment transport, and short term terrain evolution in Open Source GIS. In C. T. Miller & G. F. Pinder (Eds.), *Developments in Water Science* (Vol. 55, pp. 1479-1490): Elsevier.

Mockler, E., Deakin, J., Archbold, M., Daly, D., & Bruen, M. (2017, 23-28 April 2017). *Sources of nitrogen and phosphorus emissions to Irish rivers: estimates from the Source Load Apportionment Model (SLAM).* Paper presented at the 19th EGU General Assembly, Vienna.

Møller, A. B., Beucher, A., Iversen, B. V., & Greve, M. H. (2018). Predicting artificially drained areas by means of a selective model ensemble. *Geoderma, 320*, 30-42. doi:10.1016/j.geoderma.2018.01.018

Møller, A. B., Iversen, B. V., Beucher, A., & Greve, M. H. (2017). Prediction of soil drainage classes in Denmark by means of decision tree classification. *Geoderma, in press*. doi:10.1016/j.geoderma.2017.10.015

Moore, I. D., Gessler, P. E., Nielsen, G. A., & Peterson, G. A. (1993). Soil Attribute Prediction Using Terrain Analysis. *Soil Science Society of America Journal, 57*(2), 443-452. doi:10.2136/sssaj1993.03615995005700020026x

Moran, M. S., Clarke, T. R., Inoue, Y., & Vidal, A. (1994). Estimating crop water deficit using the relation between surface-air temperature and spectral vegetation index. *Remote Sensing of Environment, 49*(3), 246-263. doi:10.1016/0034-4257(94)90020-5

Moran, M. S., Inoue, Y., & Barnes, E. M. (1997). Opportunities and limitations for image-based remote sensing in precision crop management. *Remote Sensing of Environment, 61*(3), 319-346. doi:10.1016/S0034-4257(97)00045-X

Mountrakis, G., Im, J., & Ogole, C. (2011). Support vector machines in remote sensing: A review. *ISPRS Journal of Photogrammetry and Remote Sensing, 66*(3), 247-259. doi:10.1016/j.isprsjprs.2010.11.001

Mulder, V. L., de Bruin, S., Schaepman, M., & Mayr, T. R. (2011). *The use of remote sensing in soil and terrain mapping - A review* (Vol. 162).

Mulla, D. J. (2013). Twenty five years of remote sensing in precision agriculture: Key advances and remaining knowledge gaps. *Biosystems Engineering, 114*(4), 358-371. doi:10.1016/j.biosystemseng.2012.08.009

Müller, B., Bernhardt, M., Jackisch, C. & Schulz, K. (2016). Estimating spatially distributed soil texture using time series of thermal remote sensing – a case study in central Europe. Hydrology Earth System Science, 20, 3765–3775. doi:10.5194/hess-20-3765-2016

Murphy, P., Ogilvie, J., & Arp, P. (2009). Topographic modelling of soil moisture conditions: a comparison and verification of two models. *European Journal of Soil Science, 60*(1), 94-109. doi:10.1111/j.1365-2389.2008.01094.x

Naz, B. S., Ale, S., & Bowling, L. C. (2009). Detecting subsurface drainage systems and estimating drain spacing in intensively managed agricultural landscapes. *Agricultural Water Management, 96*(4), 627-637. doi:https://doi.org/10.1016/j.agwat.2008.10.002

Naz, B. S., & Bowling, L. C. (2008). Automated identification of tile lines from remotely sensed data. *Transactions of the American Society of Agricultural and Biological Engineers, 51*(6), 13.

NDFEM. (2016). *Report on Flooding. December 4 2015 – January 13 2016*. Retrieved from https://www.housing.gov.ie/sites/default/files/publications/files/report_on_winter_2015-16_flooding.pdf

Niang, M. A., Nolin, M., Bernier, M., & Perron, I. (2012). Digital Mapping of Soil Drainage Classes Using Multitemporal RADARSAT-1 and ASTER Images and Soil Survey Data. *Applied and Environmental Soil Science, 2012*, 17. doi:10.1155/2012/430347

Northcott, W. J., Verma, A. K., & Cooke, R. A. (2000). *Mapping Subsurface Drainage Systems using Remote Sensing and GIS* Paper presented at the ASAE Annual International Meeting, Milwaukee, Wisconsin

Nouwakpo, S. K., Weltz, M. A., & McGwire, K. (2016). Assessing the performance of structure-from-motion photogrammetry and terrestrial LiDAR for reconstructing soil surface microtopography of naturally vegetated plots. *Earth Surface Processes and Landforms, 41*(3), 308-322. doi:10.1002/esp.3787

O'Callaghan, J. F., & Mark, D. M. (1984). The extraction of drainage networks from digital elevation data. *Computer Vision, Graphics, and Image Processing, 28*(3), 323-344. doi:10.1016/S0734-189X(84)80011-0

O'Sullivan, L., Creamer, R., Fealy, R., Lanigan, G., Simo, I., Fenton, O., Carfrae, J., & Schulte, R. (2015). Functional Land Management for managing soil functions: A case-study of the trade-off between primary productivity and carbon storage in response to the intervention of drainage systems in Ireland. *Land Use Policy, 47*, 42-54. doi:10.1016/j.landusepol.2015.03.007

Oertel, C., Matschullat, J., Zurba, K., Zimmermann, F., & Erasmi, S. (2016). Greenhouse gas emissions from soils—A review. *Chemie der Erde - Geochemistry, 76*(3), 327-352. doi:10.1016/j.chemer.2016.04.002

Otsu, N. (1979). A threshold selection method from gray-level histograms. *IEEE Transactions on Systems, Man, and Cybernetics, 9*(1), 62-66. doi:10.1109/TSMC.1979.4310076

Ouédraogo, M. M., Degré, A., Debouche, C., & Lisein, J. (2014). The evaluation of unmanned aerial system-based photogrammetry and terrestrial laser scanning to generate DEMs of agricultural watersheds. *Geomorphology, 214*(Supplement C), 339-355. doi:https://doi.org/10.1016/j.geomorph.2014.02.016

Ouma, Y. O., & Tateishi, R. (2006). A water index for rapid mapping of shoreline changes of five East African Rift Valley lakes: an empirical analysis using Landsat TM and ETM+ data. *International Journal of Remote Sensing, 27*(15), 3153-3181. doi:10.1080/01431160500309934

Pajares, G. (2015). Overview and Current Status of Remote Sensing Applications Based on Unmanned Aerial Vehicles (UAVs). *Photogrammetric Engineering & Remote Sensing, 81*(4), 281-329. doi:https://doi.org/10.14358/PERS.81.4.281

Pal, M. (2005). Random forest classifier for remote sensing classification. *International Journal of Remote Sensing, 26*(1), 217-222. doi:10.1080/01431160412331269698

Pal, M., & Mather, P. M. (2005). Support vector machines for classification in remote sensing. *International Journal of Remote Sensing, 26*(5), 1007-1011. doi:10.1080/01431160512331314083

Pantaleoni, E., Engel, B. A., & Johannsen, C. J. (2007). Identifying agricultural flood damage using Landsat imagery. *Precision Agriculture, 8*(1), 27-36. doi:10.1007/s11119-006-9026-5

Patton, D., Shalloo, L., & Horan, B. (2017, August 2017). Dairy farming in the BMW region. *TResearch 12,* 2.

Paul, C., Fealy, R., Fenton, O., Lanigan, G., O'Sullivan, L., & Schulte, R. P. O. (2018). Assessing the role of artificially drained agricultural land for climate change mitigation in Ireland. *Environmental Science & Policy, 80*, 95-104. doi:10.1016/j.envsci.2017.11.004

Peng, W., Wheeler, D. B., Bell, J. C., & Krusemark, M. G. (2003). Delineating patterns of soil drainage class on bare soils using remote sensing analyses. *Geoderma, 115*(3), 261-279. doi:https://doi.org/10.1016/S0016-7061(03)00066-1

Petropoulos, G., Carlson, T. N., Wooster, M. J., & Islam, S. (2009). A review of Ts/VI remote sensing based methods for the retrieval of land surface energy fluxes and soil surface moisture. *Progress in Physical Geography, 33*(2), 224-250. doi:10.1177/0309133309338997

Pinar, A., & Curran, P. J. (1996). Grass chlorophyll and the reflectance red edge. *International Journal of Remote Sensing, 17*(2), 351-357. doi:10.1080/01431169608949010

Pix4D. (2017). Pix4Dmapper Pro Retrieved from www.pix4d.com

Pohl, C., & Van Genderen, J. L. (1998). Multisensor image fusion in remote sensing: concepts, methods and applications. *International Journal of Remote Sensing, 19*(5), 823-854. doi:10.1080/014311698215748

Porporato, A., D'Odorico, P., Laio, F., & Rodriguez-Iturbe, I. (2003). Hydrologic controls on soil carbon and nitrogen cycles. I. Modeling scheme. *Advances in Water Resources, 26*(1), 45-58. doi:10.1016/S0309-1708(02)00094-5

Potter, K. (1991). Hydrological impacts of changing land management practices in a moderate-sized agricultural catchment. *Water Resources Research, 27*(5), 845-855. doi:10.1029/91WR00076

Pratola, C., Barrett, B., Gruber, A., & Dwyer, E. (2015). Quality Assessment of the CCI ECV Soil Moisture Product Using ENVISAT ASAR Wide Swath Data over Spain, Ireland and Finland. *Remote Sensing, 7*(11). doi:10.3390/rs71115388

Price, J. (1985). On the analysis of thermal infrared imagery: the limited utility of apparent thermal inertia. *Remote Sensing of Environment, 18*(1), 59-73. doi:10.1016/0034-4257(85)90038-0

Price, K. (2011). Effects of watershed topography, soils, land use, and climate on baseflow hydrology in humid regions: A review. *Progress in Physical Geography: Earth and Environment, 35*(4), 465-492. doi:10.1177/0309133311402714

Profeti, G., & Macintosh, H. (1998). Flood management through LANDSAT TM and ERS SAR data: a case study. *Hydrological Processes, 11*(10), 1397-1408. doi:10.1002/(SICI)1099-1085(199708)11:10

Prosdocimi, M., Calligaro, S., Sofia, G., Dalla Fontana, G., & Tarolli, P. (2015). Bank erosion in agricultural drainage networks: new challenges from structure-from-motion photogrammetry for post-event analysis. *Earth Surface Processes and Landforms, 40*(14), 1891-1906. doi:10.1002/esp.3767

Rafique, R., Hennessy, D., & Kiely, G. (2011). Nitrous oxide emission from grazed grassland under different management systems. *Ecosystems, 14*(4), 563-582. doi:10.1007/s10021-011-9434-x

Rahimzadeh-Bajgiran, P., Omasa, K., & Shimizu, Y. (2012). Comparative evaluation of the Vegetation Dryness Index (VDI), the Temperature Vegetation Dryness Index (TVDI) and the improved TVDI (iTVDI) for water stress detection in semi-arid regions of Iran. *ISPRS Journal of Photogrammetry and Remote Sensing, 68*(Supplement C), 1-12. doi:10.1016/j.isprsjprs.2011.10.009

Ramsbottom, G., Horan, B., Berry, D. P., & Roche, J. R. (2015). Factors associated with the financial performance of spring-calving, pasture-based dairy farms. *J Dairy Sci, 98*(5), 3526-3540. doi:10.3168/jds.2014-8516

Rango, A., & Salomonson, V. V. (1974). Regional flood mapping from space. *Water Resources Research, 10*(3), 473-484. doi:10.1029/WR010i003p00473

Remondino, F., Spera, M. G., Nocerino, E., Menna, F., & Nex, F. (2014). State-of-the-Art in high density image matching. *The Photogrammetric Record, 29*(146), 144-166. doi:10.1111/phor.12063

Rennó, C. D., Nobre, A. D., Cuartas, L. A., Soares, J. V., Hodnett, M. G., Tomasella, J., & Waterloo, M. J. (2008). HAND, a new terrain descriptor using SRTM-DEM: Mapping terra-firme rainforest environments in Amazonia. *Remote Sensing of Environment, 112*(9), 3469-3481. doi:10.1016/j.rse.2008.03.018

Richter, A., Huallacháin, D. Ó., Doyle, E., Clipson, N., Van Leeuwen, J. P., Heuvelink, G. B., & Creamer, R. E. (2018). Linking diagnostic features to soil microbial biomass and respiration in agricultural grassland soil: a large-scale study in Ireland. *European Journal of Soil Science, 69*(3), 414-428. doi:10.1111/ejss.12551

Ridolfi, E., & Manciola, P. (2018). Water level measurements from drones: A pilot case study at a dam site. *Water, 10*(3). doi:10.3390/w10030297

Robinson, M. (1990). *Impact of improved land drainage on river flows*. Retrieved from Wallingford: http://nora.nerc.ac.uk/id/eprint/7349

Rock, G., Ries, J. B., & Udelhoven, T. (2011). *Sensitivity analysis of UAV-photogrammetry for creating digital elevation models (DEM).* Paper presented at the UAV-g 2011, Conference on Unmanned Aerial Vehicle in Geomatics, Zurich.

Rodgers, J. C., Murrah, A. W., & Cooke, W. H. (2009). The impact of Hurricane Katrina on the coastal vegetation of the Weeks Bay Reserve, Alabama from NDVI data. *Estuaries and Coasts, 32*(3), 496-507. doi:10.1007/s12237-009-9138-z

Rodriguez-Galiano, V. F., Ghimire, B., Rogan, J., Chica-Olmo, M., & Rigol-Sanchez, J. P. (2012). An assessment of the effectiveness of a random forest classifier for land-cover classification. *ISPRS Journal of Photogrammetry and Remote Sensing, 67*(Supplement C), 93-104. doi:10.1016/j.isprsjprs.2011.11.002

Roelens, J., Höfle, B., Dondeyne, S., Van Orshoven, J., & Diels, J. (2018). Drainage ditch extraction from airborne LiDAR point clouds. *ISPRS Journal of Photogrammetry and Remote Sensing, 146*, 409-420. doi:10.1016/j.isprsjprs.2018.10.014

Rogan, J., Franklin, J., Stow, D., Miller, J., Woodcock, C., & Roberts, D. (2008). Mapping land-cover modifications over large areas: A comparison of machine learning algorithms. *Remote Sensing of Environment, 112*(5), 2272-2283. doi:10.1016/j.rse.2007.10.004

Rogers, M., Baham, J., & Dragila, M. (2006). Soil iron content effects on the abililty of magnetometer surveying to locate buried agricultural drainage pipes *Applied Engineering in Agriculture, 22*(5), 701. doi:10.13031/2013.22001

Rogers, M., Cassidy, J., & Dragila, M. (2005). Ground-based magnetic surveys as a new technique to locate subsurface drainage pipes: a case study. *Applied Engineering in Agriculture, 21*(3), 421. doi:10.13031/2013.18461

Rosnell, T., & Honkavaara, E. (2012). Point cloud generation from aerial image data acquired by a quadrocopter type micro unmanned aerial vehicle and a digital still camera. *Sensors, 12*(1). doi:10.3390/s120100453

Rossiter, D. (2014). *Technical Note: Statistical methods for accuracy assesment of classified thematic maps*. Department of Earth Systems Analysis. University of Twente. Retrieved from http://www.css.cornell.edu/faculty/dgr2/teach/R/R_ac.pdf

Rouse, J. W., Haas, R. H., Schell, J. A., & Deering, D. W. (1974). *Monitoring vegetation systems in the Great Plains with ERTS*. Paper presented at the 3rd ERTS-1 Symposium, Greenbelt, Maryland. https://ntrs.nasa.gov/search.jsp?R=19740022614

Roy, S. (2013). *Remote sensing & GIS applications for drainage detection and modeling in agricultural watersheds.* (M.Sc), Indiana University Retrieved from https://scholarworks.iupui.edu/bitstream/handle/1805/4086/Roy_Thesis_Scholar.pdf?sequence=1&isAllowed=y

Ruedisili, L. C., & Logan, S. M. (1978). Locating drainage systems by magnetometer surveys *Journal of the Irrigation and Drainage Division, 104*(3), 261-273.

Ryan, M. (1974). Grassland productivity: 1. nitrogen and soil effects on yield of herbage. *Irish Journal of Agricultural Research, 13*(3), 275-291.

Sabins, F. (2007). *Remote Sensing: Principles and Applications* (Third Edition ed.). Illinois: Waveland Press.

Sahoo, P. K., Soltani, S., & Wong, A. K. C. (1988). A survey of thresholding techniques. *Computer Vision, Graphics, and Image Processing, 41*(2), 233-260. doi:10.1016/0734-189X(88)90022-9

Sandholt, I., Rasmussen, K., & Andersen, J. (2002). A simple interpretation of the surface temperature/vegetation index space for assessment of surface moisture status. *Remote Sensing of Environment, 79*(2), 213-224. doi:10.1016/S0034-4257(01)00274-7

Santos, W. J. R., Silva, B. M., Oliveira, G. C., Volpato, M. M. L., Lima, J. M., Curi, N., & Marques, J. J. (2014). Soil moisture in the root zone and its relation to plant vigor assessed by remote sensing at management scale. *Geoderma, 221*(Supplement C), 91-95. doi:https://doi.org/10.1016/j.geoderma.2014.01.006

Schilling, K. E., & Helmers, M. (2008). Effects of subsurface drainage tiles on streamflow in Iowa agricultural watersheds: Exploratory hydrograph analysis. *Hydrological Processes, 22*(23), 4497-4506. doi:10.1002/hyp.7052

Schmidt, G. L., Jenkerson, C. B., Masek, J., Vermote, E., & Gao, F. (2013). *Landsat ecosystem disturbance adaptive processing system (LEDAPS) algorithm description* (Open-File Report 2013–1057). Retrieved from https://pubs.usgs.gov/of/2013/1057/ofr13_1057.pdf

Schmugge, T. J., Jackson, T. J., & McKim, H. L. (1980). Survey of methods for soil moisture determination. *Water Resources Research, 16*(6), 961-979. doi:10.1029/WR016i006p00961

Schottler, S. P., Ulrich, J., Belmont, P., Moore, R., Lauer, J. W., Engstrom, D. R., & Almendinger, J. E. (2013). Twentieth century agricultural drainage creates more erosive rivers. *Hydrological Processes, 28*(4), 1951-1961. doi:10.1002/hyp.9738

Schoumans, O. F., Chardon, W. J., Bechmann, M. E., Gascuel-Odoux, C., Hofman, G., Kronvang, B., Rubæk, G. H., Ulén, B., & Dorioz, J. M. (2014). Mitigation options to reduce phosphorus losses from the agricultural sector and improve surface water quality: a review. *Science of The Total Environment, 468-469*, 1255-1266. doi:10.1016/j.scitotenv.2013.08.061

Schrijver, R. (2016). *Precision agriculture and the future of farming in Europe*. Retrieved from http://www.europarl.europa.eu/RegData/etudes/STUD/2016/581892/EPRS_STU(2016)581892_EN.pdf

Schulte, R., Diamond, J., Finkele, K., Holden, N. M., & Brereton, A. J. (2005). Predicting the soil moisture conditions of Irish grasslands. *Irish Journal of Agricultural and Food Research, 44*(1), 95-110.

Schulte, R., Fealy, R., Creamer, R. E., Towers, W., Harty, T., & Jones, R. J. A. (2012). A review of the role of excess soil moisture conditions in constraining farm practices under Atlantic conditions. *Soil Use and Management, 28*(4), 580-589. doi:10.1111/j.1475-2743.2012.00437.x

Schulte, R., Richards, K., Daly, K., Kurz, I., McDonald, E. J., & Holden, N. M. (2006). Agriculture, meteorology and water quality in Ireland: a regional evaluation of pressures and pathways of nutrient loss to water *Biology and Environment: Proceedings of the Royal Irish Academy, 106B*(2), 117-133.

Schulte, R., Simo, I., Creamer, R. E., & Holden, N. M. (2015). A note on the Hybrid Soil Moisture Deficit Model v2.0. *Irish Journal of Agricultural and Food Research, 54*(2), 126. doi:10.1515/ijafr-2015-0014

Schultz, B., Zimmer, D., & Vlotman, W. (2007). Drainage under increasing and changing requirements. *Irrigation and Drainage, 56*(1), S3-S22. doi:10.1002/ird.372

Scotter, D. R., & Horne, D. J. (1985). The effect of mole drainage on soil temperatures under pasture. *Journal of Soil Science, 36*(3), 319-327. doi:10.1111/j.1365-2389.1985.tb00338.x

Seibert, J., & McGlynn, B. L. (2007). A new triangular multiple flow direction algorithm for computing upslope areas from gridded digital elevation models. *Water Resources Research, 43*(4), 1-8. doi:10.1029/2006WR005128

Seneviratne, S. I., Corti, T., Davin, E. L., Hirschi, M., Jaeger, E. B., Lehner, I., Orlowsky, B., & Teuling, A. J. (2010). Investigating soil moisture–climate interactions in a changing climate: A review. *Earth-Science Reviews, 99*(3), 125-161. doi:10.1016/j.earscirev.2010.02.004

Şerban, G., Rus, I., Vele, D., Breţcan, P., Alexe, M., & Petrea, D. (2016). Flood-prone area delimitation using UAV technology, in the areas hard-to-reach for classic aircrafts: case study in the north-east of Apuseni Mountains, Transylvania. *Natural Hazards, 82*(3), 1817-1832. doi:10.1007/s11069-016-2266-4

Serbin, G., & Green, S. (2018). Open-Sourced Remote Sensing Data Management with the Irish Earth Observation (IEO) Python Module. *Preprints 2018, 2018050470*. doi:10.20944/preprints201805.0470.v1

Shalloo, L., Dillon, P., O'Loughlin, J., Rath, M., & Wallace, M. (2004). Comparison of a pasture-based system of milk production on a high rainfall, heavy-clay soil with that on a lower rainfall, free-draining soil. *Grass and Forage Science, 59*(2), 157-168. doi:10.1111/j.1365-2494.2004.00415.x

Sharma, P., Humphreys, J., & Holden, N. M. (2018). The effect of local climate and soil drainage on the environmental impact of grass-based milk production. *The International Journal of Life Cycle Assessment, 23*(1), 26-40. doi:10.1007/s11367-017-1302-2

Sharpley, A. N., Bergström, L., Aronsson, H., Bechmann, M., Bolster, C. H., Börling, K., Djodjic, F., Jarvie, H. P., Schoumans, O. F., Stamm, C., Tonderski, K. S., Ulén, B., Uusitalo, R., & Withers, P. J. A. (2015). Future agriculture with minimized phosphorus losses to waters: Research needs and direction. *Ambio, 44*(Suppl 2), 163-179. doi:10.1007/s13280-014-0612-x

Sharpley, A. N., Chapra, S. C., Wedepohl, R., Sims, J. T., Daniel, T. C., & Reddy, K. R. (1994). Managing agricultural phosphorus for protection of surface waters: issues and options. *Journal of Environmental Quality, 23*, 437-451. doi:10.2134/jeq1994.00472425002300030006x

Shukla, M. K. (2011). Introduction to soil hydrology: processes and variability of hydrological properties. In M. K. Shukla (Ed.), *Soil Hydrology, Land Use and Agriculture* (pp. 1-24). Oxfordshire: CAB International.

Singh, K. K., & Frazier, A. E. (2018). A meta-analysis and review of unmanned aircraft system (UAS) imagery for terrestrial applications. *International Journal of Remote Sensing, 39*(15-16), 5078-5098. doi:10.1080/01431161.2017.1420941

Sinha, E., Michalak, A. M., & Balaji, V. (2017). Eutrophication will increase during the 21st century as a result of precipitation changes. *Science, 357*(6349), 405. doi:10.1126/science.aan2409

Skaggs, R. W., Brevé, M. A., & Gilliam, J. W. (1994). Hydrologic and water quality impacts of agricultural drainage. *Critical Reviews in Environmental Science and Technology, 24*(1), 1-32. doi:10.1080/10643389409388459

Smedema, L., Abdel-Dayem, S., & Ochs, W. J. (2000). Drainage and Agricultural Development. *Irrigation and Drainage Systems, 14*(3), 223-235. doi:10.1023/A:1026570823692

Smedema, L., Vlotman, W., & Rycroft, D. (2004). *Modern Land Drainage*. London: CRC Press.

Snavely, N., Seitz, S. M., & Szeliski, R. (2008). Modeling the world from internet photo collections. *International Journal of Computer Vision, 80*(2), 189-210. doi:10.1007/s11263-007-0107-3

Sohrabinia, M., Rack, W., & Zawar-Reza, P. (2014). Soil moisture derived using two apparent thermal inertia functions over Canterbury, New Zealand *Journal of Applied Remote Sensing, 8*(1), 16. doi:10.1117/1.JRS.8.083624

Soliman, A., Heck, J. R., Brenning, A., Brown, R., & Miller, S. (2013). Remote sensing of soil moisture in vineyards using airborne and ground-based thermal inertia data. *Remote Sensing, 5*(8). doi:10.3390/rs5083729

Sonneveld, M. P. W., Schoorl, J. M., & Veldkamp, A. (2006). Mapping hydrological pathways of phosphorus transfer in apparently homogeneous landscapes using a high-resolution DEM. *Geoderma, 133*(1), 32-42. doi:10.1016/j.geoderma.2006.03.035

Sørensen, R., & Seibert, J. (2007). Effects of DEM resolution on the calculation of topographical indices: TWI and its components. *Journal of Hydrology, 347*(1), 79-89. doi:10.1016/j.jhydrol.2007.09.001

Soussana, J. F., Allard, V., Pilegaard, K., Ambus, P., Amman, C., Campbell, C., Ceschia, E., Clifton-Brown, J., Czobel, S., Domingues, R., Flechard, C., Fuhrer, J., Hensen, A., Horvath, L., Jones, M., Kasper, G., Martin, C., Nagy, Z., Neftel, A., Raschi, A., Baronti, S.,

Rees, R. M., Skiba, U., Stefani, P., Manca, G., Sutton, M., Tuba, Z., & Valentini, R. (2007). Full accounting of the greenhouse gas (CO2, N2O, CH4) budget of nine European grassland sites. *Agriculture, Ecosystems & Environment, 121*(1), 121-134. doi:10.1016/j.agee.2006.12.022

Srivastava, P. K., Han, D., Ramirez, M. R., & Islam, T. (2013). Machine Learning Techniques for Downscaling SMOS Satellite Soil Moisture Using MODIS Land Surface Temperature for Hydrological Application. *Water Resources Management, 27*(8), 3127-3144. doi:10.1007/s11269-013-0337-9

Stafford, J. V. (2000). Implementing Precision Agriculture in the 21st Century. *Journal of Agricultural Engineering Research, 76*(3), 267-275. doi:10.1006/jaer.2000.0577

Sweeney, J., Fabrizio, A., Brereton, A., Caffarra, A., Charlton, R., Donnelly, A., Fealy, R., Fitzgerald, J., Holden, N., Jones, M., & Murphy, C. (2008). *Climate Change – refining the impacts for Ireland*. Retrieved from http://eprints.maynoothuniversity.ie/2682/

Teagasc. (2017). Grass 10: Grassland excellence for Irish livestock. Retrieved from https://www.teagasc.ie/media/website/publications/2017/Teagasc_Grass10.pdf

Teagasc. (2018). Teagasc Heavy Soils Programme. Retrieved from www.teagasc.ie/crops/grassland/heavy-soils/publications/

Tetzlaff, B., Kuhr, P., Vereecken, H., & Wendland, F. (2009). Aerial photograph-based delineation of artificially drained areas as a basis for water balance and phosphorus modelling in large river basins. *Physics and Chemistry of the Earth, Parts A/B/C, 34*(8), 552-564. doi:10.1016/j.pce.2009.02.002

Tetzlaff, B., Kuhr, P., & Wendland, F. (2009). A new method for creating maps of artificially drained areas in large river basins based on aerial photographs and geodata. *Irrigation and Drainage, 58*(5), 569-585. doi:10.1002/ird.426

Thomas, I., Jordan, P., Mellander, P., Fenton, O., Shine, O., Ó hUallacháin, D., Creamer, R., McDonald, N., Dunlop, P., & Murphy, P. (2016). Improving the identification of hydrologically sensitive areas using LiDAR DEMs for the delineation and mitigation of critical source areas of diffuse pollution. *Science of The Total Environment, 556*, 276-290. doi:10.1016/j.scitotenv.2016.02.183

Thomas, I., Mellander, P., Murphy, P., Fenton, O., Shine, O., Djodjic, F., Dunlop, P., & Jordan, P. (2016). A sub-field scale critical source area index for legacy phosphorus management

using high resolution data. *Agriculture, Ecosystems & Environment, 233*, 238-252. doi:10.1016/j.agee.2016.09.012

Thomas, I. A., Jordan, P., Shine, O., Fenton, O., Mellander, P. E., Dunlop, P., & Murphy, P. N. C. (2017). Defining optimal DEM resolutions and point densities for modelling hydrologically sensitive areas in agricultural catchments dominated by microtopography. *International Journal of Applied Earth Observation and Geoinformation, 54*(Supplement C), 38-52. doi:https://doi.org/10.1016/j.jag.2016.08.012

Thompson, J. (2010). *Identifying subsurface tile drainage systems*

utilizing remote sensing techniques. (MA), University of Toledo, Retrieved from http://utdr.utoledo.edu/cgi/viewcontent.cgi?article=2017&context=theses-dissertations

Tlapáková, L., Žaloudík, J., & Kolejka, J. (2017). Thematic survey of subsurface drainage systems in the Czech Republic. *Journal of Maps, 13*(2), 55-65. doi:10.1080/17445647.2016.1259129

Tlapáková, L., Žaloudík, J., Kulhavý, Z., & Pelíšek, I. (2015). Use of Remote Sensing for Identification and Description of Subsurface Drainage System Condition. *Acta Universitatis Agriculturae Silviculturae Mendelianae Brunensis, 63*(5), 12. doi:10.11118/actaun201563051587

Toner, P., Bowman, J., Clabby, K., Lucey, J., McGarrigle, M. L., Concannon, C., Clenaghan, C., Cunningham, P., Delaney, J., O'Boyle, S., MacCárthaigh, M., Craig, M., & Quinn, R. (2005). *Water Quality in Ireland 2001-2003*. Retrieved from https://www.epa.ie/pubs/reports/water/waterqua/EPA_water_quality_2001-3.pdf

Torres-Sallan, G., Schulte, R. P. O., Lanigan, G. J., Byrne, K. A., Reidy, B., Simó, I., Six, J., & Creamer, R. E. (2017). Clay illuviation provides a long-term sink for C sequestration in subsoils. *Scientific Reports, 7*, 45635. doi:10.1038/srep45635

Torres-Sánchez, J., Peña, J. M., de Castro, A. I., & López-Granados, F. (2014). Multi-temporal mapping of the vegetation fraction in early-season wheat fields using images from UAV. *Computers and Electronics in Agriculture, 103*(Supplement C), 104-113. doi:10.1016/j.compag.2014.02.009

Townsend, P. A. (2002). Relationships between forest structure and the detection of flood inundation in forested wetlands using C-band SAR. *International Journal of Remote Sensing, 23*(3), 443-460. doi:10.1080/01431160010014738

Transon, J., d'Andrimont, R., Maugnard, A., & Defourny, P. (2018). Survey of hyperspectral Earth observation applications from space in the Sentinel-2 context. *Remote Sensing, 10*(2). doi:10.3390/rs10020157

Tucker, C. J. (1979). Red and photographic infrared linear combinations for monitoring vegetation. *Remote Sensing of Environment, 8*(2), 127-150. doi:10.1016/0034-4257(79)90013-0

Tuia, D., Volpi, M., Copa, L., Kanevski, M., & Munoz-Mari, J. (2011). A survey of active learning algorithms for supervised remote sensing image classification. *IEEE Journal of Selected Topics in Signal Processing, 5*(3), 606-617. doi:10.1109/JSTSP.2011.2139193

Tunney, H., Coulter, B., Daly, K., Kurz, I., Coxon, C., Jeffery, D., Mills, P., Kiely, G., & Morgan, G. (2000). *Quantification of phosphorus loss from soil to water.* Retrieved from http://hdl.handle.net/11019/1415

Tuohy, P., O' Loughlin, J., & Fenton, O. (2017). Modelling performance of a tile drainage system incorporating mole drainage. *Transactions of the ASABE, 61*(1), 169-178. doi:10.13031/trans.12203

Twele, A., Cao, W., Plank, S., & Martinis, S. (2016). Sentinel-1-based flood mapping: a fully automated processing chain. *International Journal of Remote Sensing, 37*(13), 2990-3004. doi:10.1080/01431161.2016.1192304

UN-SPIDER (2016). Recommended Practice: Flood Mapping. Space-based Information for Disaster Management and Emergency Response. Retrieved from http://www.un-spider.org/advisory-support/recommended-practices/recommended-practice-flood-mapping

Unger, I. M., Kennedy, A. C., & Muzika, R.-M. (2009). Flooding effects on soil microbial communities. *Applied Soil Ecology, 42*(1), 1-8. doi:10.1016/j.apsoil.2009.01.007

Upton, V., O'Donoghue, C., & Ryan, M. (2014). The physical, economic and policy drivers of land conversion to forestry in Ireland. *Journal of Environmental Management, 132*, 79-86. doi:10.1016/j.jenvman.2013.10.017

van den Hurk, B., Doblas-Reyes, F., Balsamo, G., Koster, R. D., Seneviratne, S. I., & Camargo, H. (2012). Soil moisture effects on seasonal temperature and precipitation forecast scores in Europe. *Climate Dynamics, 38*(1), 349-362. doi:10.1007/s00382-010-0956-2

Van Orshoven, J., Terres, J.-M., & Tóth, T. (2014). *Updated common bio-physical criteria to define natural constraints for agriculture in Europe*. Retrieved from Luxembourg: http://publications.jrc.ec.europa.eu/repository/bitstream/JRC89982/lbna26638enn.pdf

Verma, A. K., Cooke, R. A., & Wendte, L. (1996). *Mapping subsurface drainage systems with colour infrared aerial photographs.* Paper presented at the American Water Resource Association's 32nd Annual Conference and Symposium, Fort Lauderdale.

Vero, S. E., Antille, D. L., Lalor, S. T. J., & Holden, N. M. (2014). Field evaluation of soil moisture deficit thresholds for limits to trafficability with slurry spreading equipment on grassland. *Soil Use and Management, 30*(1), 69-77. doi:10.1111/sum.12093

Verstraeten, W. W., Veroustraete, F., van der Sande, C. J., Grootaers, I., & Feyen, J. (2006). Soil moisture retrieval using thermal inertia, determined with visible and thermal spaceborne data, validated for European forests. *Remote Sensing of Environment, 101*(3), 299-314. doi:10.1016/j.rse.2005.12.016

Vlcek, J., & King, D. (1983). Detection of subsurface soil moisture by thermal sensing: results of laboratory, close-range and aerial studies. *Photogrammetric Engineering and Remote Sensing, 49*(11), 1593-1597. doi:0099-1 112/83/4911-159

von Bueren, S. K., Burkart, A., Hueni, A., Rascher, U., Tuohy, M. P., & Yule, I. J. (2015). Deploying four optical UAV-based sensors over grassland: challenges and limitations. *Biogeosciences, 12*(1), 163-175. doi:10.5194/bg-12-163-2015

Wagner, W., & Pathe, C. (2005, 6-10 September 2004). *Has SAR failed in soil moisture retrieval?* Paper presented at the Proceedings of the 2004 ENVISAT & ERS Symposium, Salzburg.

Walker, J., Houser, P., & Willgoose, G. (2004). Active microwave remote sensing for soil moisture measurement: a field evaluation using ERS-2. *Hydrological Processes, 18*(11), 1975-1997. doi:10.1002/hyp.1343

Walter, M. T., Walter, M. F., Brooks, E. S., Steenhuis, T. S., Boll, J., & Weiler, K. (2000). Hydrologically sensitive areas: Variable source area hydrology implications for water quality risk assessment. *Journal of Soil and Water Conservation, 55*(3), 277-284.

Wang, L., & Liu, H. (2006). An efficient method for identifying and filling surface depressions in digital elevation models for hydrologic analysis and modelling. *International Journal of Geographical Information Science, 20*(2), 193-213. doi:10.1080/13658810500433453

Wang, X., Xie, H., Guan, H., & Zhou, X. (2007). Different responses of MODIS-derived NDVI to root-zone soil moisture in semi-arid and humid regions. *Journal of Hydrology, 340*(1), 12-24. doi:10.1016/j.jhydrol.2007.03.022

Wang, Y. (2002). Mapping extent of floods: what we have learned and how we can do better. *Natural Hazards Review, 3*(2), 68-73. doi:10.1061/(ASCE)1527-6988(2002)3:2(68)

Wang, Y., Hess, L. L., Filoso, S., & Melack, J. M. (1995). Understanding the radar backscattering from flooded and nonflooded Amazonian forests: Results from canopy backscatter modeling. *Remote Sensing of Environment, 54*(3), 324-332. doi:10.1016/0034-4257(95)00140-9

Wechsler, S. P., & Kroll, C. N. (2006). Quantifying DEM Uncertainty and its Effect on Topographic Parameters. *Photogrammetric Engineering & Remote Sensing, 72*(9), 9. doi:0099-1112/06/7209–1081

Westoby, M. J., Brasington, J., Glasser, N. F., Hambrey, M. J., & Reynolds, J. M. (2012). 'Structure-from-Motion' photogrammetry: A low-cost, effective tool for geoscience applications. *Geomorphology, 179*(Supplement C), 300-314. doi:https://doi.org/10.1016/j.geomorph.2012.08.021

Whitehead, K., & Hugenholtz, C. H. (2014). Remote sensing of the environment with small unmanned aircraft systems (UASs), part 1: a review of progress and challenges. *Journal of Unmanned Vehicle Systems, 02*(03), 69-85. doi:10.1139/juvs-2014-0006

Wingler, A., & Hennessy, D. (2016). Limitation of grassland productivity by low temperature and seasonality of growth. *Frontiers in Plant Science, 7*, 1130. doi:10.3389/fpls.2016.01130

Withers, P., Neal, C., Jarvie, P. H., & Doody, G. D. (2014). Agriculture and eutrophication: where do we go from here? *Sustainability, 6*(9). doi:10.3390/su6095853

Woledge, J., & Parsons, A. J. (1986). The effect of temperature on the photosynthesis of ryegrass canopies. *Annals of Botany, 57*(4), 487-497.

Wu, C. (2011). VisualSFM : A visual Structure from Motion system. Retrieved from http://ccwu.me/vsfm/index.html

Wu, J., Cui, Z., Sheng Victor, S., Zhao, P., Su, D., & Gong, S. (2013). A comparative study of SIFT and its variants. In *Measurement Science Review* (Vol. 13, pp. 122).

Wu, S., Li, J., & Huang, G. H. (2008). A study on DEM-derived primary topographic attributes for hydrologic applications: Sensitivity to elevation data resolution. *Applied Geography, 28*(3), 210-223. doi:https://doi.org/10.1016/j.apgeog.2008.02.006

Xiaoye, L. (2008). Airborne LiDAR for DEM generation: some critical issues. *Progress in Physical Geography, 32*(1), 31-49. doi:10.1177/0309133308089496

Xue, J., & Su, B. (2017). Significant remote sensing vegetation indices: A review of developments and applications. *Journal of Sensors, 2017*, 17. doi:10.1155/2017/1353691

Xue, Y., & Cracknell, A. P. (1995). Advanced thermal inertia modelling. *International Journal of Remote Sensing, 16*(3), 431-446. doi:10.1080/01431169508954411

Yang, X., Zhou, Q. and Melville, M. (2000) An integrated drainage network analysis system for agricultural drainage management. Part 1: the system. Agricultural Water Management, 45, 73-86.

Yao, Y., Liang, S., Cao, B., Liu, S., Yu, G., Jia, K., Zhang, X., Zhang, Y., Chen, J., & Fisher, J. B. (2018). Satellite detection of water stress effects on terrestrial latent heat flux With MODIS shortwave infrared reflectance data. *Journal of Geophysical Research: Atmospheres, 123*(20), 11,410-411,430. doi:10.1029/2018JD029011

Zandbergen, P. A. (2011). Error propagation modeling for terrain analysis using dynamic simulation tools in ArcGIS model builder. In T. Hengl, I. S. Evans, J. P. Wilson, & M. Gould (Eds.), *Geomorphometry 2011* (pp. 57-60).

Zehe, E. & Blöschl, G. (2004) Predictability of hydrologic response at the plot and catchment scales: Role of initial conditions. Water Resources Research, 40(10).

Zevenbergen, L. W., & Thorne, C. R. (1987). Quantitative analysis of land surface topography. *Earth Surface Processes and Landforms, 12*(1), 47-56. doi:10.1002/esp.3290120107

Zhang, C., & Kovacs, J. M. (2012). The application of small unmanned aerial systems for precision agriculture: a review. *Precision Agriculture, 13*(6), 693-712. doi:10.1007/s11119-012-9274-5

Zhang, D., & Zhou, G. (2016). Estimation of soil moisture from optical and thermal remote sensing: a review. *Sensors, 16*(8). doi:10.3390/s16081308

Zhao, Z., Ashraf, M. I., & Meng, F.-R. (2013). Model prediction of soil drainage classes over a large area using a limited number of field samples: A case study in the province of Nova Scotia, Canada. *Canadian Journal of Soil Science, 93*(1), 73-83. doi:10.4141/cjss2011-095

Zhu, Z., Wang, S., & Woodcock, C. E. (2015). Improvement and expansion of the Fmask algorithm: cloud, cloud shadow, and snow detection for Landsats 4–7, 8, and Sentinel 2 images. *Remote Sensing of Environment, 159*, 269-277. doi:10.1016/j.rse.2014.12.014

Appendices

A. Sentinel 1A & Sentinel 2A scenes used in Chapter 3

Full file designation	Date
S1A_IW_GRDH_1SDV_20151119T064639_20151119T064704_008670_00C535_4781	19 Nov. 2015
S1A_IW_GRDH_1SDV_20151119T064704_20151119T064729_008670_00C535_D193	
S1A_IW_GRDH_1SDV_20151119T064729_20151119T064754_008670_00C535_4397	
S1A_IW_GRDH_1SDV_20151201T064632_20151201T064657_008845_00CA1D_C9A1	1 Dec. 2015
S1A_IW_GRDH_1SDV_20151201T064657_20151201T064722_008845_00CA1D_B4FB	
S1A_IW_GRDH_1SDV_20151201T064722_20151201T064747_008845_00CA1D_2934	
S1A_IW_GRDH_1SDV_20151213T064639_20151213T064704_009020_00CEF7_C872	13 Dec. 2015
S1A_IW_GRDH_1SDV_20151213T064704_20151213T064729_009020_00CEF7_3065	
S1A_IW_GRDH_1SDV_20151213T064729_20151213T064754_009020_00CEF7_C97C	
S1A_IW_GRDH_1SDV_20151225T064631_20151225T064656_009195_00D3F4_299D	25 Dec. 2015
S1A_IW_GRDH_1SDV_20151225T064656_20151225T064721_009195_00D3F4_BC69	
S1A_IW_GRDH_1SDV_20151225T064721_20151225T064746_009195_00D3F4_E3FD	
S1A_IW_GRDH_1SDV_20160106T064638_20160106T064703_009370_00D8EE_36FF	6 Jan. 2016
S1A_IW_GRDH_1SDV_20160106T064703_20160106T064728_009370_00D8EE_F4FD	
S1A_IW_GRDH_1SDV_20160106T064728_20160106T064753_009370_00D8EE_5209	
S1A_IW_GRDH_1SDV_20160118T064630_20160118T064655_009545_00DDEB_63EB	18 Jan. 2016
S1A_IW_GRDH_1SDV_20160118T064655_20160118T064720_009545_00DDEB_872C	
S1A_IW_GRDH_1SDV_20160118T064720_20160118T064745_009545_00DDEB_2AF5	
S1A_IW_GRDH_1SDV_20160130T064637_20160130T064702_009720_00E313_D247	30 Jan. 2016
S1A_IW_GRDH_1SDV_20160130T064702_20160130T064727_009720_00E313_5D6E	
S1A_IW_GRDH_1SDV_20160130T064727_20160130T064752_009720_00E313_6CC6	
S1A_IW_GRDH_1SDV_20160211T064629_20160211T064654_009895_00E821_6FDE	11 Feb. 2016
S1A_IW_GRDH_1SDV_20160211T064654_20160211T064719_009895_00E821_8A3E	
S1A_IW_GRDH_1SDV_20160211T064719_20160211T064744_009895_00E821_B085	
S1A_IW_GRDH_1SDV_20160223T064637_20160223T064702_010070_00ED44_CA51	23 Feb. 2016
S1A_IW_GRDH_1SDV_20160223T064702_20160223T064727_010070_00ED44_E1D1	
S1A_IW_GRDH_1SDV_20160223T064727_20160223T064752_010070_00ED44_55CF	
S1A_IW_GRDH_1SDV_20160330T064630_20160330T064655_010595_00FC31_4425	30 Mar. 2016
S1A_IW_GRDH_1SDV_20160330T064655_20160330T064720_010595_00FC31_D8F4	
S1A_IW_GRDH_1SDV_20160330T064720_20160330T064745_010595_00FC31_EFAF	
S1A_IW_GRDH_1SDV_20160411T064703_20160411T064728_010770_010166_E4DE	4 April 2016
S1A_IW_GRDH_1SDV_20160411T064728_20160411T064753_010770_010166_25A9	
S1A_IW_GRDH_1SDV_20160411T064638_20160411T064703_010770_010166_EC27	
S1A_IW_GRDH_1SDV_20160704T064717_20160704T064742_011995_01282B_FE64	7 July 2016
S1A_IW_GRDH_1SDV_20160728T064718_20160728T064743_012345_013398_9509	
S1A_IW_GRDH_1SDV_20160728T064653_20160728T064718_012345_013398_A999	
S2A_OPER_PRD_MSIL1C_PDMC_20151222T161456_R023_V20151221T115730_20151221T115730	22 Dec. 2015

B. OPW hydrograph stations used in Chapter 3

Station	River	Latitude °	Longitude °
Athlone	Shannon	53.42153	-7.94076
Ballinamore	Shiven	53.48979	-8.366
Banagher	Shannon	53.19379	-7.99365
Bellagill	Suck	53.36169	-8.23855
Derrycahill	Suck	53.43176	-8.26276
Johnstons Bridge	Rinn	53.82777	-7.86275
New Bridge (Little Brosna)	Little Brosna	53.13191	-7.97574
Pollagh	Brosna	53.28135	-7.71586
Rookwood	Suck	53.56372	-8.29266
Shannonbridge	Shannon	53.27987	-8.04958

C. Met Éireann precipitation stations used in Chapter 3

Co.	Station	No.	Irish National Grid	
			E	N
Donegal	Greencastle	542	264600	440800
Monaghan	Monaghan (Castleshane)	639	272200	332500
Donegal	Carndonagh (Rocksmount) Ii	645	248400	445900
Mayo	Murrisk	1033	92700	282500
Donegal	Letterkenny (Dromore)	1043	220600	411000
Roscommon	Loughglinn	1128	163400	286000
Westmeath	Coole (Coolnagun)	1130	238400	270100
Donegal	Termon (Goldrum)	1143	212300	423800
Galway	Costelloe Fishery	1225	97500	226700
Mayo	Mulrany (Doughbeg)	1233	80900	294300
Louth	Omeath	1338	314200	316600
Mayo	Westport (Carrabawn)	1433	99400	283600
Donegal	Illies (Pollan Dam Waterworks)	1443	241400	434000
Offaly	Meelick (Victoria Lock)	1519	194600	212900
Donegal	Kilmacrennan (Massreagh)	1543	214000	420300
Donegal	Bloody Foreland	1544	185700	432700
Leitrim	Keshcarrigan G.S.	1637	203800	307700
Donegal	Crolly (Filter Works)	1641	184000	417900
Donegal	Ballybofey Navenny	1642	214600	394000
Galway	Roundstone	1725	72500	242300
Leitrim	Drumshanbo	1729	196000	312500
Mayo	Newport (Ardagh Lodge)	1733	94400	294800
Donegal	Fintown (Kingarrow)	1742	196500	405600
Galway	Portumna O.P.W.	1819	187200	204600
Mayo	Bangor Erris (Main St.)	1834	86300	323200
Louth	Ardee (St. Brigid's Hosp.)	1838	295700	290400
Donegal	Falcarragh (Lough Altan)	1844	193600	425800
Galway	Inishmore	1925	87200	210100
Mayo	Killadoon	1926	75300	271300
Westmeath	Athlone O.P.W.	1929	203900	241300
Mayo	Dooagh (Water Treatment Plant)	1934	58200	304600
Leitrim	Dromahair (Market St.)	1936	180600	331500
Donegal	Derryhenny Doochary	1941	183700	403800
Galway	Carheeny Beg	2018	144400	194300
Galway	Inishbofin	2026	55300	265500
Donegal	Kincasslagh	2041	175500	420600
Donegal	Killygordon (Ballyarrell)	2042	222300	393700
Galway	Camus	2225	96200	237200
Galway	Clifden	2226	65700	249600
Galway	Carndolla	2227	133500	239500
Westmeath	Coole-Coolure	2230	241500	269400
Leitrim	Manorhamilton (Amorset)	2236	188200	339800

Co.	Station	No.	Irish National Grid	
Donegal	Ballyshannon (Cathleen's Fall)	2237	188400	361300
Donegal	Kilclooney More	2241	171700	395900
Donegal	Quigley's Point (Three Trees)	2242	250300	429300
Mayo	Eskeragh	2335	104300	319000
Donegal	Kilcar (Cronasillagh)	2340	164900	377200
Donegal	Dungloe	2341	176400	410800
Mayo	Delphi Lodge Ii	2426	84400	266000
Mayo	Keenagh Beg	2435	103000	311000
Donegal	Ardnawark Barnesmore	2440	201500	384200
Donegal	Gweedore Weir	2441	185300	422400
Galway	Kylemore Abbey Gardens	2626	73125	259219
Galway	Ballinasloe (Derrymullen)	2628	183400	232200
Mayo	Derryhillagh	2635	108800	310200
Louth	Ardee (Boharnamoe)	2638	294100	290200
Galway	Loughrea (Rathruddy West)	2721	160100	218100
Galway	Leenane-Glanagimla	2726	89500	263000
Westmeath	Ballivor (Hill of Down)	2731	264400	254100
Mayo	Dooncarton	2734	79300	337600
Sligo	Ardtarmon	2736	159600	343400
Galway	Ballinasloe (Pollboy Lock)	2828	187700	229200
Roscommon	Athleague	2928	181800	257500
Sligo	Sligo Airport	2936	161300	336700

Co.	Station	No.	Irish National Grid	
Westmeath	Tyrrellspass	3022	240100	235500
Galway	Milltown	3027	141000	262800
Sligo	Kinsellagh	3036	173200	339400
Galway	Glenamaddy (Gortnagier)	3127	162900	261600
Sligo	Cloonacool (Lough Easkey)	3135	144600	320700
Leitrim	Rossinver Organic Centre	3140	192200	349400
Laois	Clonaslee Waterworks Ii	3222	231700	210300
Donegal	Ballyshannon (Cherrymount)	3237	190100	360400
Mayo	Straide	3335	126100	297900
Leitrim	Lough Glencar	3336	177100	343000
Louth	Clogher Head (Port)	3338	313300	289500
Offaly	Derrygreenagh	3431	249300	238200
Sligo	Easkey (Bunowna)	3436	138200	337900
Louth	Riverstown (Glenmore Upper)	3438	315500	311000
Louth	Togher (Barmeath Castle)	3538	309700	287600
Monaghan	Newbliss (Drumshannon)	3637	257300	323900
Mayo	Ballina (Shanaghy)	3735	125600	318300
Leitrim	Aughnasheelan (Miskawn)	3937	208500	315100
Cavan	Bailieboro (Duneena)	4031	264600	299900
Roscommon	Lecarrow	4129	196900	254900
Cavan	Bailieboro (Leiter)	4131	264900	298500

Co.	Station	No.	Irish National Grid	
Mayo	Laherdane (Cum)	4135	113200	310400
Monaghan	Newbliss (Crappagh)	4237	258600	321500
Westmeath	Rathwire	4331	257000	251300
Galway	Headford O.P.W.	4527	127000	247200
Mayo	Belderrig	4535	97900	341300
Westmeath	Athlone (Glynnwood)	4629	210300	239500
Mayo	Lisglennon Waterworks	4635	120200	327200
Cavan	Ballyconnell Mullaghduff	4637	228200	317700
Offaly	Corbetstown	4831	255500	240000
Mayo	Ballina (Attymass)	4835	129200	312100
Mayo	Tourmakeady (Water Treatment Wor	4927	109200	271200
Cavan	Belturbet (Naughan)	5037	236700	320700
Mayo	Derrypark	5227	101100	261600
Roscommon	Boyle (Marian Rd.)	5229	180000	302300
Sligo	Curry	5435	149400	306400
Monaghan	Shantonagh (Tooa)	5437	275300	312300
Monaghan	Clones (Dunseark)	5537	251900	322200
Mayo	Belcarra (Carrajames)	5627	119000	282200
Cavan	Tullyco (Artonagh)	5637	254200	306300
Westmeath	Collinstown (Lough Bawn)	5731	254900	270800
Sligo	Enniscrone Golf Club	5735	127500	329200
Donegal	Pettigo (Belault)	5737	207000	366200
Cavan	Killeshandra (Bawn)	5837	230000	306900

Co.	Station	No.	Irish National Grid	
Leitrim	Ballinamore (Creevy No.2)	5937	210600	311200
Roscommon	Frenchpark Callow	6129	169600	295500
Leitrim	Carrigallen-Calloughs	6237	222400	304100
Offaly	Edenderry (Ballinla)	6314	258300	231600
Cavan	Arvagh-Cormore	6337	230200	295800
Monaghan	Castleblaney_Coose	6437	280400	313100
Roscommon	Ballymore	6729	178500	299400
Roscommon	Lanesboro (Cloonadra)	6929	198600	269700

D. Landsat 8 scenes used in Chapter 3 & Chapter 4

Path/Row/Year	Scene	Date
2090232014	017	17/01/2014
2070232014	019	19/01/2014
2080222014	026	26/01/2014
2080232014	026	26/01/2014
2090222014	033	02/02/2014
2090232014	033	02/02/2014
2070222014	035	04/02/2014
2070232014	035	04/02/2014
2080222014	042	11/02/2014
2080232014	042	11/02/2014
2090222014	049	18/02/2014
2090232014	049	18/02/2014
2080222014	058	27/02/2014
2080232014	058	27/02/2014
2080222014	074	15/03/2014
2080232014	074	15/03/2014
2090222014	081	22/03/2014
2090232014	081	22/03/2014
2080222014	090	31/03/2014
2080232014	090	31/03/2014
2090232014	097	07/04/2014
2080232014	106	16/04/2014
2090222014	113	23/04/2014
2070222014	115	25/04/2014
2070232014	115	25/04/2014
2090222014	129	09/05/2014
2070232014	131	11/05/2014
2080222014	138	18/05/2014
2080232014	138	18/05/2014
2090222014	145	25/05/2014
2090232014	145	25/05/2014
2070222014	147	27/05/2014
2070232014	147	27/05/2014
2080222014	154	03/06/2014
2080232014	154	03/06/2014
2090222014	161	10/06/2014
2090232014	161	10/06/2014
2070232014	163	12/06/2014
2080232014	170	19/06/2014
2070232014	179	28/06/2014
2080222014	186	05/07/2014
2080232014	186	05/07/2014
2070232014	211	30/07/2014
2080222014	218	06/08/2014
2080232014	218	06/08/2014
2070232014	227	15/08/2014
2080222014	234	22/08/2014
2080232014	234	22/08/2014
2090222014	241	29/08/2014
2070222014	243	31/08/2014
2070232014	243	31/08/2014
2080222014	250	07/09/2014
2080232014	250	07/09/2014
2090222014	257	14/09/2014
2090232014	257	14/09/2014
2070222014	259	16/09/2014
2070232014	259	16/09/2014
2070222014	275	02/10/2014
2070232014	275	02/10/2014
2080222014	282	09/10/2014
2080232014	282	09/10/2014
2090222014	289	16/10/2014
2090232014	289	16/10/2014
2070222014	291	18/10/2014
2080222014	298	25/10/2014
2070222014	307	03/11/2014
2070232014	307	03/11/2014
2090222014	321	17/11/2014
2090232014	321	17/11/2014
2070222014	323	19/11/2014
2080232014	330	26/11/2014
2090232015	020	20/01/2015
2070222015	022	22/01/2015

Path/Row/Year	Scene	Date
2070232015	022	22/01/2015
2080232015	029	29/01/2015
2090222015	036	05/02/2015
2090232015	036	05/02/2015
2070222015	038	07/02/2015
2080222015	045	14/02/2015
2080232015	045	14/02/2015
2090222015	052	21/02/2015
2090232015	052	21/02/2015
2070222015	054	23/02/2015
2070232015	054	23/02/2015
2090222015	068	09/03/2015
2090232015	068	09/03/2015
2070222015	070	11/03/2015
2070232015	070	11/03/2015
2080222015	077	18/03/2015
2080232015	077	18/03/2015
2070232015	086	27/03/2015
2080232015	093	03/04/2015
2090222015	100	10/04/2015
2090232015	100	10/04/2015
2070222015	102	12/04/2015
2080222015	109	19/04/2015
2080232015	109	19/04/2015
2090222015	116	26/04/2015
2090232015	116	26/04/2015
2070222015	118	28/04/2015
2070232015	118	28/04/2015
2080232015	125	05/05/2015
2090222015	132	12/05/2015
2090232015	132	12/05/2015
2070222015	134	14/05/2015
2090222015	148	28/05/2015
2090232015	148	28/05/2015
2080222015	157	06/06/2015
2080232015	157	06/06/2015
2090222015	164	13/06/2015
2070222015	166	15/06/2015

Path/Row/Year	Scene	Date
2070232015	166	15/06/2015
2080222015	189	08/07/2015
2090222015	196	15/07/2015
2090232015	196	15/07/2015
2070222015	198	17/07/2015
2070232015	198	17/07/2015
2080222015	205	24/07/2015
2080222015	221	09/08/2015
2090222015	228	16/08/2015
2090232015	228	16/08/2015
2070222015	230	18/08/2015
2070232015	230	18/08/2015
2090222015	244	01/09/2015
2080222015	253	10/09/2015
2090222015	260	17/09/2015
2090232015	260	17/09/2015
2090222015	276	03/10/2015
2080222015	285	12/10/2015
2080232015	285	12/10/2015
2090222015	292	19/10/2015
2090232015	292	19/10/2015
2080222015	301	28/10/2015
2080232015	301	28/10/2015
2090222015	308	04/11/2015
2090232015	308	04/11/2015
2070222015	310	06/11/2015
2080222015	317	13/11/2015
2080232015	317	13/11/2015
2090222015	324	20/11/2015
2090232015	324	20/11/2015
2070222015	326	22/11/2015
2070232015	326	22/11/2015
2080232016	016	16/01/2016
2090222016	023	23/01/2016
2090232016	023	23/01/2016
2070222016	025	25/01/2016
2070232016	025	25/01/2016
2080222016	032	01/02/2016

Path/Row/Year	Scene	Date
2080232016	032	01/02/2016
2090222016	039	08/02/2016
2090232016	039	08/02/2016
2070222016	041	10/02/2016
2070232016	041	10/02/2016
2080222016	048	17/02/2016
2080232016	048	17/02/2016
2080222016	064	04/03/2016
2080232016	064	04/03/2016
2070222016	073	13/03/2016
2080222016	080	20/03/2016
2090222016	087	27/03/2016
2090232016	087	27/03/2016
2070222016	089	29/03/2016
2070232016	089	29/03/2016
2080222016	096	05/04/2016
2080232016	096	05/04/2016
2090232016	103	12/04/2016
2070232016	121	14/04/2016
2080222016	112	21/04/2016
2080232016	112	21/04/2016
2090222016	119	28/04/2016
2090232016	119	28/04/2016
2070222016	121	30/04/2016
2070232016	137	30/04/2016
2090222016	135	14/05/2016
2090232016	135	14/05/2016
2070222016	137	16/05/2016
2080222016	144	23/05/2016
2080232016	144	23/05/2016
2090222016	151	30/05/2016
2090232016	151	30/05/2016
2070222016	153	01/06/2016
2070232016	153	01/06/2016
2080222016	160	08/06/2016
2080232016	160	08/06/2016
2090222016	167	15/06/2016
2080222016	176	24/06/2016

Path/Row/Year	Scene	Date
2080232016	176	24/06/2016
2070232016	185	03/07/2016
2090222016	199	17/07/2016
2070222016	201	19/07/2016
2070232016	201	19/07/2016
2090222016	215	02/08/2016
2070222016	217	04/08/2016
2070232016	217	04/08/2016
2070232016	233	20/08/2016
2070222016	249	27/08/2016
2070232016	249	27/08/2016
2090222016	247	03/09/2016
2090232016	247	03/09/2016
2080222016	256	12/09/2016
2080232016	256	12/09/2016
2090222016	263	19/09/2016
2090222016	279	05/10/2016
2090232016	279	05/10/2016
2070222016	281	07/10/2016
2070232016	281	07/10/2016
2080222016	288	14/10/2016
2080232016	288	14/10/2016
2070222016	297	23/10/2016
2070232016	297	23/10/2016
2080222016	304	30/10/2016
2080232016	304	30/10/2016
2090222016	311	01/11/2016
2090232016	311	06/11/2016
2080222016	320	15/11/2016
2080232016	320	15/11/2016

E. Drainage classification script (R)

```
#####################################################################
#
# Support Vector Machine and Random Forest classification script
# Rob O'Hara
#
#####################################################################

# Package install and permissions

require (raster)
require (gtools)
require (e1071)
require (randomForest)

# Image processing

setwd("InsertYourPathHere")

img_1<- brick("InsertYourFileHere.tif")
names(img_1)<-c("Insert","Your", "File", "Names", "Here") # Rename as required
img_1.df<-na.omit(data.frame(getValues(img_1)))

img_2<- brick("InsertYourTrainingDataHere.tif ") # well drained TD
names(img_2)<-names(img_1)
img_3<- brick("InsertYourTrainingDataHere.tif ") # poorly drained TD
names(img_3)<-names(img_1)

drained.df<- na.omit(data.frame(getValues(img_2))) # generate new TD.df
undrained.df<- na.omit(data.frame(getValues(img_3))) # generate new TD.df
drained.df$drained <- "1"
undrained.df$drained <- "2"

TrainData.df <- smartbind(drained.df,undrained.df)
TrainData.df$drained <- as.factor(TrainData.df$drained)

# Support Vector Machine

setwd("InsertYourOutputPathHere")
sink("InsertYourOutputFileNameHere.txt") # Start writing to an output file

set.seed(42)
CalData <- sample(nrow(TrainData.df), round((nrow(TrainData.df) - 1) / 2, 0))
ValData <- c(1:nrow(TrainData.df))[!(c(1:nrow(TrainData.df)) %in% CalData)]
CalData.df <- na.omit(TrainData.df[CalData,])
ValData.df <- na.omit(TrainData.df[ValData,])
```

```
obj <- tune.svm(drained~., data = CalData.df, gamma = 2 ^( InsertNumericHere:
InsertNumericHere), cost = 2 ^( InsertNumericHere: InsertNumericHere))

# set limits and increments to tuning parameter (numeric; e.g. 2^(-2:5))

summary(obj)
plot(obj)
bestgamma<- as.numeric(obj$best.parameters[1])
bestcost<- as.numeric(obj$best.parameters[2])

svm.fit <- svm(drained~., data=CalData.df, gamma = bestgamma, cost = bestcost, type='C-
classification', kernel='radial',scale=T)
svm.pred <- predict(svm.fit, ValData.df[,1:InsertNumberOfBandsHere], decision.values =
TRUE) # enter number of bands as numeric
attr(svm.pred, "decision.values") [1: InsertNumberOfBandsHere]
# print decision.values for each band
svm.tab <- table(pred = svm.pred, true = ValData.df[,InsertNumberOfColumnHere])
# the columun with the classify data (0, 1 etc)

print(svm.tab)

img.fit <- best.svm(drained~., data=TrainData.df, gamma = bestgamma, cost = bestcost)
img.pred <- predict(img.fit, img_1.df) # predict the model on dataframe

img.class <- ifelse(img.pred == "1", 1, 2) # drained = 1, undrained = 2

classified_img<-brick(img_1[[1]])
values(classified_img)<- img.class

plot(classified_img)

writeRaster(classified_img, filename = InsertNameOfFileHere.tif", format="GTiff", datatype=
"INT2U", overwrite=T)
```

 # Random Forest

```
x<-TrainData.df[ ,c(1: InsertNumberOfBandsHere)] # enter number of bands as numeric

names(x)<-names(img_1)

y<-TrainData.df$drained
mtry<-tuneRF(x, y, mtryStart=as.integer(sqrt(length(y))), ntreeTry= InsertNumericHere,
stepFactor= InsertNumericHere, improve=0.05, trace=F, plot=T, doBest=F)
# set tune parameters (numeric)
best.m <- mtry[mtry[, 2] == min(mtry[, 2]), 1]

print(paste0("bestm =", best.m))
```

```
modelRF <- randomForest(x=x, y=y, mtry = best.m, ntree = InsertNumericHere, replace=T,
importance = TRUE) # try with different ntree values (default= 501)
colnames(modelRF$confusion) <- c("drained", "undrained", "class.error")
rownames(modelRF$confusion) <- c("drained", "undrained")

modelRF
varImpPlot(modelRF)
predLC <- predict(img_1, model=modelRF, na.rm=TRUE) # not img.df, make sure all bands
have same name

writeRaster(predLC, filename InsertNameOfFileHere.tif, datatype= "INT2U", format="GTiff",
overwrite=TRUE)
```

F. Flood depth & volume

After creating the SAR flood map in Chapter 3, there was an opportunity to investigate the potential depth and volume of the flood over the region. This section presents the methodology and results of this investigation. To assess the accuracy of modelled flood heights, hydrographic data from river gauge stations in the River Shannon catchment were downloaded from the Office of Public Works (OPW) website[20] (see Appendix B). River heights at the time of each SAR image were extracted from a time series of hydrograph data using R statistical software. To determine the impact of rainfall on flood extent, hourly rainfall data was downloaded for over 300 Met Éireann precipitation stations (Appendix C) and reordered, subset and aggregated into mean daily values using R statistical software.

In the absence of high-resolution elevation data over the region, a 20 m DEM with a vertical accuracy of ± 2.5 m was used to estimate flood depth and volume. The original DEM was resampled to 10 m to match the spatial resolution of Sentinel 1 using a bilinear interpolation tool in ArcGIS v.10.2.2. To quantify the impact of a 2.5 m vertical RMSE on depth and volume estimates, a Monte Carlo simulation was carried out on the resampled DEM. 2500 randomly-perturbed DEM were created using the 'spup' package (v.0.1-1) in R statistical software (v.3.2.3). Monte Carlo simulations are widely used to quantify error propagation within DEM (Heuvelink et al., 1989; Leon et al., 2014; Wechsler & Kroll, 2006; Zandbergen, 2011). They have also been used previously for flood- and surface hydrological modelling (Bodoque et al., 2016; Domeneghetti et al., 2013; S. Wu et al., 2008).

[20] http://waterlevel.ie/hydro-data/search.html?rbd=SHANNON%20RBD. Accessed 12 December 2018.

Flood depth was estimated by calculating the difference between maximum flood height and maximum elevation for flooded pixels. Flood zones were defined using the Region Group function (Generalisation toolset in ArcGIS), which grouped connected pixels under a single region identifier. Elevation heights were then extracted from the DEM using a Zonal Statistics function (Zonal toolset toolbox in ArcGIS). This calculated descriptive statistics on DEM elevations based on individual flood regions identified by the flood map. The highest recorded elevation value in each zone was assumed to to represent the maximum flood height. Using the Raster Calculator tool (Map Algebra toolset in ArcGIS), the difference between DEM elevation and maximum flood height allowed a pixel-wise estimation of flood depth (m) for each region. Depth was converted into volume (m^3) by multiplying by pixel area (100 m^2).

Estimated flood depths are illustrated in Figure A for a target area between Athlone, Co. Westmeath and Shannonbridge, Co. Offaly. Expectedly, areas closest to river channels are deeper, with decreasing depth with Euclidean distance from the channel edge. Using a Monte Carlo perturbed DEM, it was possible to illustrate the standard deviation for each pixel to indicate the potential error range present in calculations. The area depicted in Figure A is limited in extent and topographically homogeneous, yet the range of depth variability is between 1.4 m and 5.1 m. Histograms for two randomly selected points within this area of interest further exemplify the error distribution for estimated depths (Figure B). Volume was estimated at 528,863,333 m^3 [95% C.I. (482,078,000 m^3 and 575,648,500 m^3)]. In comparison, Lough Ree, the second largest lake on the River Shannon, has an estimated volume of ~650,000,000 m^3. There was no way of validating estimated flood depth and volume.

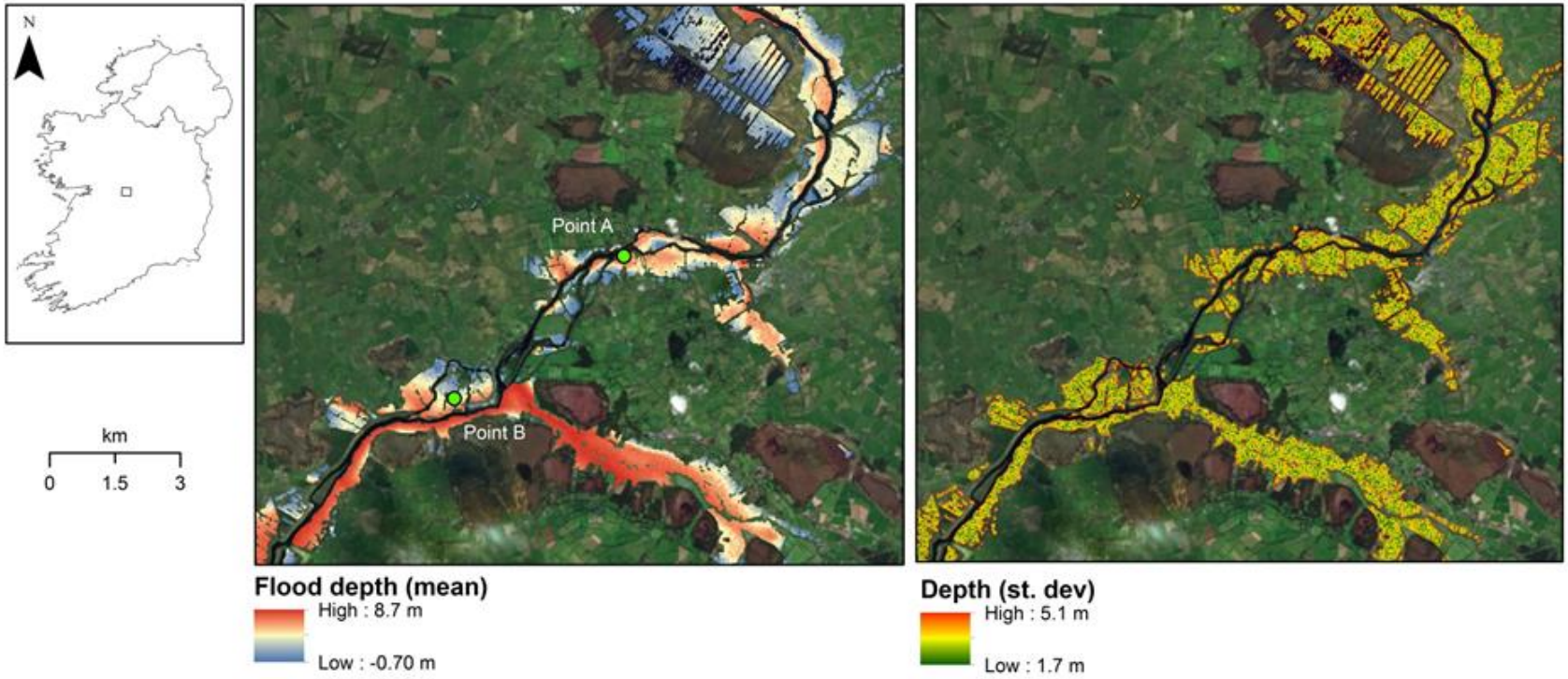

Figure A Estimated flood depth for an area at Shannonbridge, Co. Offaly. Mean and standard deviation images were compiled from 2500 Monte Carlo perturbations of a 20m DEM (vertical accuracy of ± 2.5 m)

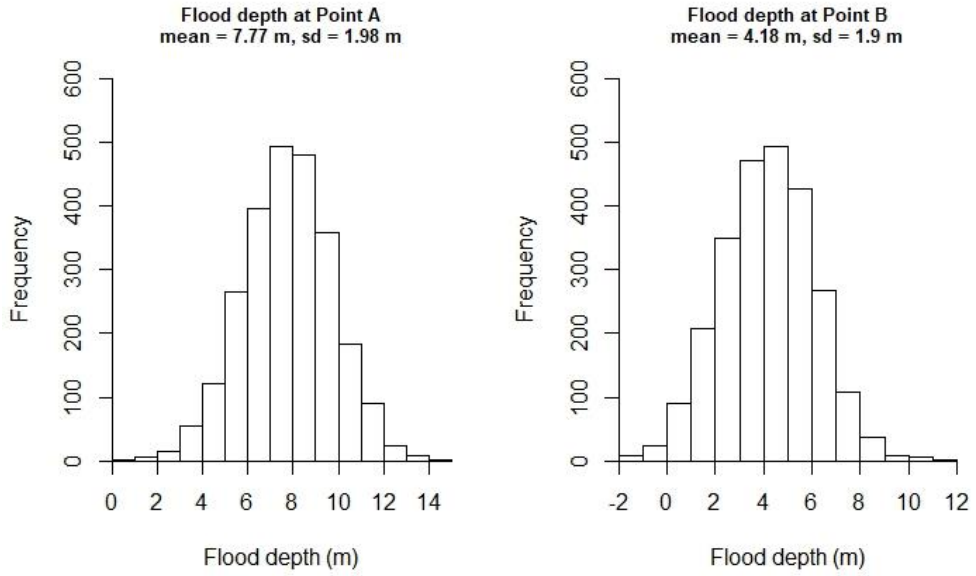

Figure B Histograms of depth estimates at the two locations marked in Figure A based on 2500 Monte Carlo simulations

Maximum river levels were recorded at ten sites in the Shannon catchment where flooding was recorded within 500 m of the station. Using regression, a significant relationship between modelled and estimated flood heights was demonstrated ($p= 0.007$; $R^2= 0.56$) (Figure C). At two locations, flood maxima were estimated to within 25 cm of measured river maxima. The greatest error was at Athlone where flood levels were overestimated by 9.70 m. A Grubbs outlier test conducted using the 'outliers' package in R (v.0.41) identified Athlone as a probable outlier ($G= 2.09$, $U= 0.45$, $p= 0.075$). Removing this station improved the regression model ($R^2 = 0.8$; $p<0.001$). The reasons why Athlone should be such an outlier is unclear. As flood levels within 500m of a river station were used for the regression. It is possible some flooding occurred on higher ground in the athlone area that casued mean values to be skewed.

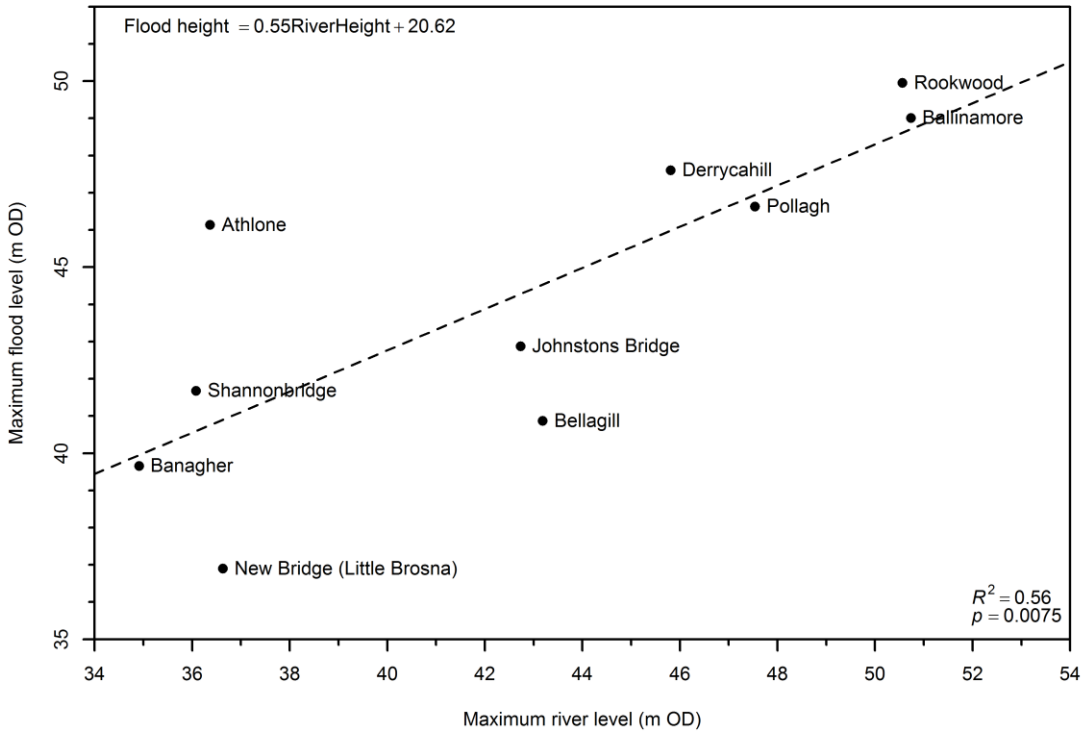

Figure C Relationship between estimated and measured river heights at 10 locations in the Shannon River Basin District.

The ArcGIS workflow that determined flood depth and volume was relatively quick to implement and could be achieved using open-source GIS software if necessary. The process could be automated within an ArcGIS model if required. The analysis suffered from a reliance on moderate spatial resolution DEM. Had a high-resolution DEM with low error been available, considerably more accurate estimations of depth and volume could be calculated. The coarse spatial resolution and high vertical error of the original DEM was undoubtedly at fault the unrealistic flood depth determinations in some areas. Nonetheless, the study highlighted to promise the Sentinel 1 mission holds for rapidly making these determinations in the future once suitable DEM and validation data is available. The use of the OPW river gauge system was a very good asset, but it was susceptible to uncertainty where flooding occurred in locations away from the river side. Floods occur when river waters break out from the river

channel and move under gravity into low lying ground. Any validation of flood waters away from river channels must rely on an independent measure of depth. If flooding of the scale of 2015-2016 continues, it would be appropriate to establish a method of measuring heights in flooded fields elsewhere in river catchments.